Shock and Release of Tantalum Studied via Molecular Dynamics and Femtosecond X-Ray Diffraction

Patrick G. Heighway

St Hugh's College

University of Oxford

A thesis submitted for the degree of

Doctor of Philosophy

Hilary 2020

For Snow

Acknowledgements

There are a great many people to whom I owe thanks for making this work possible.

I wish to thank first of all my supervisor Justin Wark, for his guidance and for the unfailing support he has given me throughout my graduate career. I thank also the members of the Wark group, past and present: David McGonegle, for his encouragement and for the many valuable insights he has offered over the years; Marcin Sliwa, without whom much of the experimental analysis in this work would not have been possible; and Matt Suggit, for introducing me to the field of shock physics during my final year as an undergraduate.

There are also a number of external collaborators to whom I am deeply grateful. I would like to thank in particular Rob Rudd, who has always been exceptionally generous with his time, and always available for a chat during my biannual pilgrimages to Livermore. Many of the release simulations in this thesis could not have been realised without his assistance. Nigel Park, too, played an integral role in much of the computational work herein, for which I am extremely thankful. I must also thank Andy Higginbotham for the many enlightening conversations we had in the early stages of my DPhil. I would further like to express my gratitude to Amy Lazicki and Martin Gorman for their being so accommodating, and giving me the opportunity to participate in their experimental work. Finally, I gratefully acknowledge the support of AWE for funding this research.

I want also to thank my friends and family, whose contribution I find difficult to articulate: I thank Stephen, whose enthusiasm for games is infectious, and Oscar and Hannah, for the critical role they have played in keeping me distracted this past year; I thank my parents, my little sister Lucy, and my littler sister Beth; and Laura, without whose inexhaustible love and dedication I would probably not have survived my first year of university, much less my DPhil.

Abstract

The response of solid matter to shock compression is complexified considerably by its strength, or its ability to withstand shear stress. Strength is challenging to measure experimentally under shock conditions and even harder to model, due to its being an extremely complicated function of the loading conditions. Our understanding of material strength and the way it manifests under dynamic loading thus remains, to a great extent, incomplete. This work presents studies of two phenomena arising from strength under the conditions of shock compression and release by means of multimillion-atom molecular dynamics simulations and femtosecond x-ray diffraction. The role of shock-induced grain interactions is first explored via simulations of elementary polycrystals. Such interactions are found to control the plasticity mechanisms activated under shock compression and the limiting shear stress state to which the polycrystal settles in the wake of the shock. A combined experimental-computational study of plastic-work heating under the conditions of shock release is then presented. An algorithm for extracting the temperature of released samples from their diffraction image is derived and verified on synthetic data. When applied to experimental data, the algorithm shows that the temperatures of shock-released tantalum foils vastly exceed those expected from a conventional isentropic release. The underlying microphysical processes responsible for the heating are then interrogated via large-scale simulations of crystals under shock and release. A heat equation is used to identify plastic-work heating owed to the sample's exceptional strength during its rapid release as the culprit, thus challenging the conventional assumption that shock release is a universally isentropic process.

Contents

List of figures

List of abbreviations

a-CNA	Adaptive common neighbour analysis
bcc	Body centred cubic
CB	Checkerboard (polycrystal)
CNA	Common neighbour analysis
DFT	Density functional theory
DXA	Dislocation Extraction Algorithm
EAM	Embedded-atom method
EOS	Equation of state
EXAFS	Extended x-ray absorption fine structure
fcc	Face centred cubic
FTFT	Fibre-texture Fourier transform
HC	Honeycomb (polycrystal)
HPC	High-performance computing
HEL	Hugoniot elastic limit
ICF	Inertial confinement fusion
LAMMPS	Large-scale Atomic/Molecular Massively Parallel Simulator
LJ	Lennard-Jones
LCLS	Linac Coherent Light Source
MD	Molecular dynamics
MEC	Matter in Extreme Conditions
RSS	Resolved shear stress
sc	Simple cubic
SVA	Slip vector analysis
TMT	Template-matching technique
VISAR	Velocity interferometer system for any reflector
XFEL	X-ray free-electron laser
XRD	X-ray diffraction

CHAPTER 1

Introduction

The study of shock-compressed matter affords us the potential to understand processes and states of matter seldom found on Earth. Revolutions in laser and x-ray technology have made it possible to compress condensed matter to millions of atmospheres within a nanosecond and simultaneously to capture in detail the evolution of its microstructure. An explosion in computational power has meanwhile enabled the use of multimillion-atom molecular dynamics simulations to predict ultrafast material evolution under shock conditions at the atomic level. Together, experiment and simulation can now give us a glimpse of the extraordinary conditions present in terrestrial planetary interiors [1, 2], during meteoric impact events [3], or in the imploding capsule of a fuel pellet at the heart of a fusion reactor [4]. As remarked by George E. Duvall [5], the study of shock physics has made clear that, while they might appear violent and chaotic, shock compression events are fundamentally orderly processes that can be analysed, comprehended, and controlled, and all of which obey the same simple conservation laws first written down by William Rankine and Pierre Henri Hugoniot 150 years ago [6, 7].

1.1 Inception of the field

Shock physics as a distinct field of scientific inquiry was born in the 1940s at Los Alamos National Laboratory. Early into its nuclear program, it became apparent that the successful development of a plutonium weapon would demand a level of understanding of material behaviour at extreme pressures and deformation rates that did not yet exist. The ensuing period of intense research during the years leading up to the termination of the Second World War [8] left scientists at Los Alamos with an unprecedented capability to load materials explosively – but precisely – to several hundred thousand atmospheres, and accurately to diagnose their pressure and density. Given impetus by the Manhattan project's success and an influx of new researchers, the Laboratory sponsored a renewed experimental campaign in which

the novel shock-compression techniques developed during wartime were brought to bear on fundamental scientific questions about the behaviour of solids in this newly accessible pressure regime. The following decade saw the publication of a number of seminal papers [9–12] culminating in a review by Rice, McQueen, and Walsh [13] in 1958 introducing the scientific community at large to this new branch of physics.

The results coming out of Los Alamos were not received without challenge. In 1956, Dennison Bancroft, Eric Peterson, and Stanley Minshall reported that by analysing the splitting of a shock wave into three fronts in an explosively driven iron sample, they could prove the existence of a polymorphic transition in iron at 13 GPa[1] [11]. This was the first evidence that a solid-solid phase transition could take place in less than a microsecond. Within weeks of Bancroft *et. al.*'s publication appearing in the Journal of Applied Physics, its editor received a letter from Nobel laureate Percy W. Bridgman, the leading high-pressure scientist of the time, communicating that he had conducted an experiment of his own, wherein he had quasistatically loaded an iron sample up to 17.5 GPa, and watched for a discontinuity in its resistivity that might indicate a phase transition. Bridgman reported that he could find no evidence of any such transition [14], and did not miss the opportunity to express his doubts about the extent to which the shock community could really claim to understand shock wave structure. It was another five years before this disparity between the static and dynamic measurements of compressed iron was finally reconciled by two chemical engineers, Anthony Balchan and Harry Drickamer, who, upon performing an experiment similar to that of Bridgman, observed a sudden jump in iron's resistivity at a pressure of (13.3 ± 0.2) GPa [15]. Bancroft, and by extension shock physics, were vindicated[2]. It was as a result of this controversy that the legitimacy of the huge volume of high-pressure equation-of-state data obtained from shock-compression techniques [9, 12, 18] came to be widely recognised. It was thus that an early collision between the established field of static high-pressure research and the nascent field of shock physics led in large part to the latter's acceptance as a credible scientific discipline.

[1] 1 GPa = 10^4 bar.

[2] Following this episode, Bridgman embraced the shock compression technique, writing in one of his last works that he should like to see static and dynamic loading methods combined [16]. Hybrid loading experiments have indeed been realised since (see for instance Ref. [17]).

1.2 Historical development

The landscape of shock physics has changed substantially since its origin, particularly in terms of the mechanisms used to drive shocks, the diagnostics used to characterise them, and the models used to understand them. Many of these advances are owed to technological innovations, of which the most important is arguably the creation of the laser, which can play the role of both driver and diagnostic. The following section recaps the major landmarks in the progression of shock physics.

The earliest compression experiments performed at Los Alamos used explosives as their drive mechanism. By either placing an explosive lens in direct contact with the sample [12], or by using one to launch a flyer plate at several kilometres per second toward the sample [18], transient pressures of order 100 GPa could be induced. While scientists at Los Alamos had honed this method to an exact science, the maximum pressures attainable via explosive loading were ultimately limited by the explosive's detonation velocity. This ceiling was broken through with the invention of the two-stage gas gun [19] in 1957. Such a gun uses an explosive to propel a piston into an antechamber containing a light gas, which it compresses to around ten thousand atmospheres. The pressurised gas suddenly tears open a rupture disk at the far side of the chamber, behind which is an evacuated barrel containing a projectile to which the gas then rapidly transfers kinetic energy. A hypervelocity impact between the projectile and a target near the muzzle, whose relative velocity can approach 10 $\mathrm{km\,s^{-1}}$ [20], may generate pressures as high as 1 TPa[3] [22].

In the 1960s, a fundamentally different means of shock wave generation became available in the form of *laser ablation*. If a target is illuminated by an extremely intense laser pulse, the concentration of the energy deposited into its surface is great enough to convert it from a solid into a dense, high-pressure plasma. As the plasma rushes away from the target, it imparts a strong impulse to the solid material below it, and thus launches a compression wave into the target. High-power laser facilities allowing compression to pressures exceeding 100 GPa now exist worldwide[4]; the very largest laser systems [built primarily for the purposes of conducting inertial confine-

[3] For comparison, the pressure at Earth's core is thought to be around 0.35 TPa [21].

[4] To generate beams of this intensity without destroying the internal optical components of the laser itself requires a technique called chirped pulse amplification (CPA) [23], wherein one first 'stretches' the laser pulse, amplifies it, and then recompresses it immediately before it encounters the target. So important was CPA for the realisation of high-power lasers that its inventors, Donna Strickland and Gérard Mourou, were awarded the 2018 Nobel Prize in Physics.

ment fusion (ICF) research] can comfortably realise shock pressures of several [24] to tens [25] of terapascals. Laser compression platforms further have the advantages of being able to operate at high repetition rates[5], and their ability to accommodate tailored compression profiles via temporal shaping of the pulse. Small lasers have also found a role in the velocity interferometer system for any reflector (VISAR), a diagnostic now widely used to track the rear-surface velocity of shocked targets, replacing the contact-pin arrays used in the first half of the 20$^{\text{th}}$ century.

Experimental shock physics has been further transformed by a series of innovations in x-ray science that have made x-ray crystallography on ultrafast timescales practicable. The first x-ray diffraction image of a sample under shock compression was not obtained until 1970. In 1967, Quintin Johnson and coworkers showed that by using a powerful 'flash' x-ray tube, they could obtain diffraction patterns from lithium fluoride (LiF) crystals within a nanosecond interval – nine orders of magnitude faster than conventional techniques [27]. Three years later, the same team used this technology to record a diffraction peak from the (200) plane of a LiF target shocked to 13 GPa within a 20 ns experimental window [28], thus obtaining conclusive evidence that crystalline order can exist behind a shock front. By 1989, *in situ* x-ray diffraction had been pushed into the subnanosecond regime by Justin Wark and coworkers. It was by that time realised that the dense plasmas generated by laser ablation emit intense line radiation in the x-ray region over a timescale comparable to the duration of the laser pulse [29]. Wark *et. al.* exploited this, using one arm of the ICF-class laser Janus to create x-ray bursts of 100 ps duration from a 'backlighter' target, which were allowed to illuminate silicon targets shock compressed simultaneously with Janus' other arm [30]. By varying the delay between the two beams, time-resolved images of the Si targets' (111) diffraction peak could be obtained at different stages in their evolution, allowing a 'movie' of their strain evolution to be constructed. Laser-plasma x-ray sources have since been used extensively at many international facilities [31–33], and in fact provided the first *in situ* diffraction measurement of the polymorphic phase transition in iron at 13 GPa [31]. A third step change in x-ray source brightness came about with the activation of the Linac Coherent Light Source (LCLS) in 2009. LCLS is the world's first hard x-ray

[5] The DiPOLE100 laser, for example, built at the Central Laser Facility (UK) and soon to be installed at European XFEL (Germany), will be capable of launching shocks with strengths of several hundred gigapascals ten times a second [26].

free electron laser (XFEL), a machine that generates an exceptionally bright beam of x-rays by rapidly 'wiggling' an incident stream of relativistic electrons. In 2013, Despina Milathianaki and coworkers used the LCLS to capture with unprecedented temporal resolution the evolution of shock-compressed copper using x-ray bursts of only 48 fs duration [34]. XFELs have thus made it possible to take snapshots of a shock-loaded solid's atomic structure over timescales shorter even than the period over which its constituent atoms execute thermal oscillations.

Concurrent to these experimental developments has been an ongoing increase in accessible computational power, and the advent of high-performance computing (HPC), whose benefits have of course been felt in many fields of modern physics. For shock physicists, the greatest benefits have arguably been the realisation of two computationally intensive simulation techniques: *density functional theory* (DFT), a computational framework used to estimate the electronic structure of condensed phases of matter; and *molecular dynamics* (MD) (the main technique employed in this thesis), a simulation method that models matter at the level of its con-

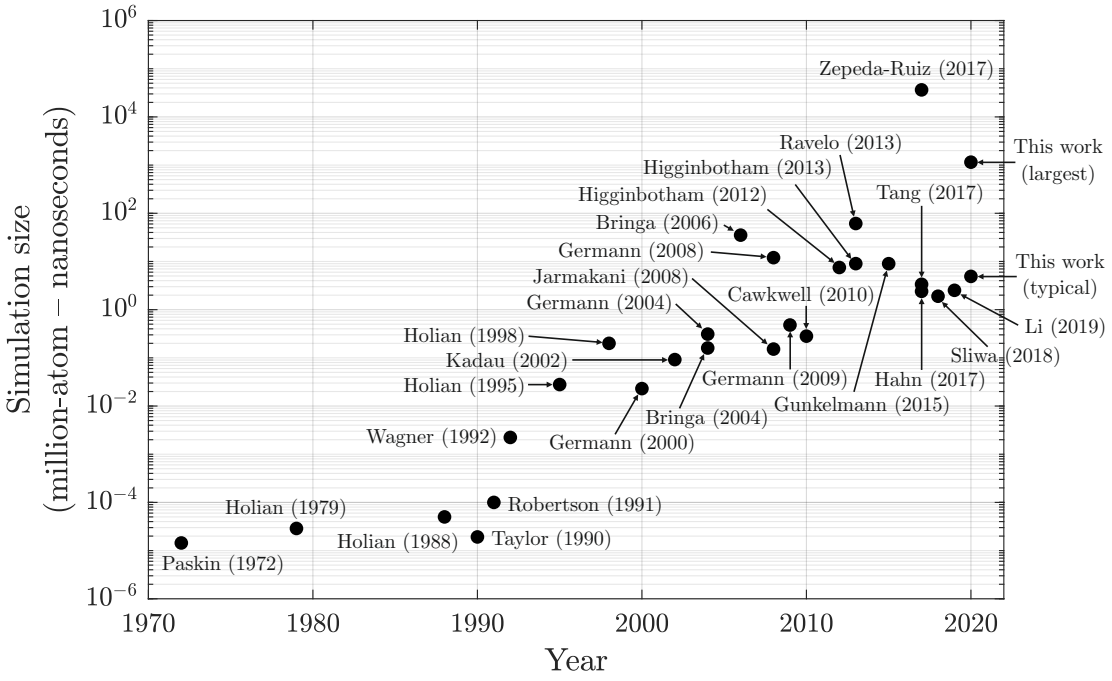

FIG. 1.1. The size of representative classical molecular dynamics simulations (expressed as the product of the number of atoms and the time for which they were simulated) modelling dynamic loading since 1970. Reasonable estimates have been made for studies employing Lennard-Jones units. Data taken from Refs. [35–60] (cited in chronological order).

stituent atoms by solving numerically the classical equations of motion governing their dynamics. The earliest MD simulations of shock-compressed matter performed between c. 1970 and 1990 (pioneered by Brad Lee Holian [36, 37, 61]) were severely hampered by their computational cost, which only allowed systems of a few thousand atoms to be modelled for perhaps tens of picoseconds. Such constraints on a simulated system's size are now known to artificially inhibit certain means of deformation [62]. It was in the 1990s that a rapid proliferation of supercomputing and distributed computing facilities raised the manageable system size from thousands to millions of particles (see Fig. 1.1). One can now routinely model micron-scale materials over hundreds of picoseconds, exactly the spatiotemporal scales pertinent to shock compression. MD has since been able to reproduce a number of shock-induced phenomena observed in experiment, including the phase transition in iron originally observed by Bancroft [44], the inelastic collapse of silicon [63], and the shock-induced rotation of tantalum [64].

1.3 Material strength

The physics of crystalline matter undergoing dynamic compression is made particularly rich by the phenomenon of strength. Under weak loading, a crystal can accommodate the imposed deformation elastically, which is to say that it will return to its original size and shape once the sample unloads. However, when shock-compressed above its elastic limit, the crystal will flow somewhat like a liquid (albeit in a highly restricted manner) to relieve the shear stress accumulated during compression. This is known as plastic deformation. Flow of this kind continues until the shear stress drops below an ultimate limiting value known as the material strength. Strength is responsible for a number of interesting behaviours: it is well-known to cause shock waves to split into elastic and plastic fronts [10]; it can suppress the Rayleigh-Taylor instability [65]; and it can in fact shift the position of phase boundaries [66]. Strength is also challenging to measure experimentally, and exceptionally difficult to model, depending as it does on temperature and pressure, on the amount of deformation accumulated, and the deformation rate. To construct a complete model for material strength in the kind of extreme conditions accessible via shock compression remains

one of shock physics' greatest challenges.

This thesis details studies of two further phenomena ultimately attributable to strength that have received little serious attention to date, namely the roles of grain interactions and of plastic-work heating under dynamic loading conditions. The material of study throughout will be tantalum, an archetypal body-centred-cubic crystal that makes an ideal testbed for our understanding of strength due to its complex plastic behaviour and lack of phase transitions. The principal means of investigation is via large-scale molecular dynamics simulations, whose ability to explain the lattice-level processes at work during shock compression is unmatched.

1.4 Thesis layout and role of the author

The nature of high-energy-density research is such that large collaborative efforts are often required, and this is certainly true of the work described in this thesis. Much of the data studied herein was acquired either at national experimental facilities like LCLS (where the experiments are by necessity carried out by a team of researchers and staff scientists) or using exceptionally powerful external HPC resources that cannot typically be found in a university environment. The analysis of this data, too, was accomplished with the aid of many invaluable contributions from the author's colleagues and collaborators. The following section summarises the content of the thesis, and makes clear which parts are the original work of the author, and which can be credited to other researchers.

Chapter 2 outlines the background theory underlying the research presented in this thesis. It is divided into four sections describing the basics of crystal plasticity, x-ray diffraction, shock waves, and molecular dynamics simulations. Its content is derived from a number of textbooks (references to which are provided at the start of the chapter) and various other sources that are cited as and when they are used.

Chapter 3 describes the postprocessing techniques used to extract information from molecular dynamics simulations. The attributions for the techniques in the order in which they are presented are as follows. The Voronoi code is the work of Chris Rycroft. The elastic deformation gradient code is the work of the author. The two Fourier transform codes described are heavily based on a code written by

Andrew Higginbotham. The original common neighbour analysis (CNA) technique was conceived by J. Dana Honeycutt, the adaptive version (a-CNA) by Alexander Stukowski; the implementation used here was written by the author. The vacancy-counting algorithm and code is the work of the author. The dislocation extraction algorithm (DXA) is the work of Alexander Stukowski and coworkers. The slip vector analysis (SVA) and template-matching technique (TMT) were conceived and implemented by the author, though similar methods have been derived independently in the past. The elastic deformation gradient, vacancy-counting, SVA, and TMT codes all employ a neighbour-list code originally written by Andrew Higginbotham. The simulation presented at the end of the chapter, which demonstrates the postprocessing techniques in action, was performed by the author.

Chapter 4 describes a molecular dynamics simulation campaign designed to elucidate the physics of grain interactions under shock conditions. The behaviour of two elementary types of tantalum polycrystal under shock compression is compared with that of a single-crystal analogue, and used to isolate the additional physics that manifests when grains are allowed to exert forces on one another. It is shown that grain interactions partially control the plasticity mechanisms active under shock compression, and bring about an additional means of shear stress relaxation. The original motivation and concept for the study were formulated by Matthew Suggit, Justin Wark, David McGonegle, and Andrew Higginbotham. The simulations were designed and analysed by the author. While many of the simulations were executed on a computing cluster at Oxford, the largest polycrystal simulations were executed by Nigel Park using HPC resources at AWE (and their output analysed by the author). The work in this chapter is published in Physical Review Materials [67].

Chapter 5 presents the results of an experiment in which the temperature of shock-loaded tantalum foils is measured after their release from the shock state by use of *in situ* x-ray diffraction. The experimental geometry, the targets probed, and the diagnostics used are described. The algorithm used to extract temperatures from the targets' diffraction pattern is derived and verified on synthetic data from large-scale molecular dynamics simulations. The algorithm is then applied to real data, and used to show the temperatures vastly exceed that expected from an isentropic release. Some small-scale simulations that reproduce the gross features of the

experimental data are finally presented and discussed. The experiment described was performed by Christopher Wehrenberg, David McGonegle, Cynthia Bolme, Andrew Higginbotham, Amy Lazicki, Hae Ja Lee, Bob Nagler, Hye-Sook Park, Bruce Remington, Damian Swift, and Justin Wark. The experimental data was preprocessed using codes by David McGonegle. The temperature extraction algorithm was derived independently by Marcin Sliwa and the author. The validation of the algorithm using molecular dynamics was performed by the author. Application of the algorithm to the experimental data and calculation of the attendant errors was the sole work of Marcin Sliwa. The design and analysis of the simulations presented at the end of the chapter are the work of the author.

Chapter 6 is a continuation of the previous chapter in which the excessive heating suffered by tantalum foils after shock release is studied in detail via large-scale molecular dynamics simulations. The temperature evolution of releasing tantalum crystals is interpreted using a heat equation, which contains contributions from thermoelastic cooling, plastic-work heating, and effects arising from crystal defects. The variation of the heating with depth below the crystal's surface is further analysed. The simulations were designed and analysed by the author, with the aid of many helpful suggestions provided by Justin Wark and David McGonegle. The simulations were executed by Robert Rudd using the HPC resources at Lawrence Livermore National Laboratory. The essential parts of this chapter and of Chapter 5 are published in Physical Review Letters [68].

Chapter 7 summarises the conclusions drawn from the thesis and speculates on routes for further work.

1.5 Relevant publications

1. **P. G. Heighway**, M. Sliwa, D. McGonegle, C. Wehrenberg, C. A. Bolme, J. Eggert, A. Higginbotham, A. Lazicki, H. J. Lee, B. Nagler, H.-S. Park, R. E. Rudd, R. F. Smith, M. J. Suggit, D. Swift, F. Tavella, B. A. Remington, and J. S. Wark, *Nonisentropic Release of a Shocked Solid*. Phys. Rev. Lett. **123**, 245501 (2019).

2. **P. G. Heighway**, D. McGonegle, N. Park, A. Higginbotham, and J. S. Wark,

Molecular dynamics simulations of grain interactions in shock-compressed highly textured columnar nanocrystals. Phys. Rev. Mater. **3**, 083602 (2019).

3. M. Sliwa, D. McGonegle, C. Wehrenberg, C. A. Bolme, **P. G. Heighway**, A. Higginbotham, A. Lazicki, H. J. Lee, B. Nagler, H.-S. Park, R. E. Rudd, M. J. Suggit, D. Swift, F. Tavella, L. Zepeda-Ruiz, B. A. Remington, and J. S. Wark, *Femtosecond X-Ray Diffraction Studies of the Reversal of the Microstructural Effects of Plastic Deformation during Shock Release of Tantalum.* Phys. Rev. Lett. **120**, 265502 (2018).

CHAPTER 2

Background theory

The following chapter lays out the theory underlying the work in this thesis. It is divided into four sections: Sec. 2.1 explains what a crystal is and how it deforms when subjected to stress; Sec. 2.2 reviews the basics of x-ray diffraction and the operating principle of a free-electron laser; in Sec. 2.3, the fundamentals of shock physics are presented; and Sec. 2.4 describes the molecular dynamics simulation technique. Most of the material herein can be found in textbooks [69–73]; any that cannot will be referenced at the appropriate point in the text.

2.1 Crystal plasticity

2.1.1 Crystal structure

A crystal is a solid whose constituent atoms or molecules form a periodic structure. This structure can be expressed as a structural motif (or *basis*) that is repeated at every point on an infinite array (known as the *lattice*). The underlying lattice can be constructed by taking all integral linear combinations of an appropriately chosen set of noncoplanar *primitive lattice vectors* $\{\mathbf{a}_i\}$:

$$\mathbf{R}_{\text{lattice}} = n_1\mathbf{a}_1 + n_2\mathbf{a}_2 + n_3\mathbf{a}_3, \tag{2.1}$$

where n_1, n_2, and n_3 are integers, and $\mathbf{a}_1 \cdot (\mathbf{a}_2 \times \mathbf{a}_3) \neq 0$. The primitive lattice vectors form the edges of a parallelepiped called the *primitive unit cell*. When such a cell and its contents are repeated at every lattice point given by Eq. (2.1), they exactly fill all space, and form an infinite crystal structure. Note that the choice of unit cell for a given lattice type is not unique. As shown in Fig. 2.1, it is possible to construct other primitive unit cells that also tessellate perfectly and contain exactly one lattice point. Alternatively, one can construct bigger unit cells enclosing multiple lattice points that only tessellate when translated by certain, non-primitive lattice vectors.

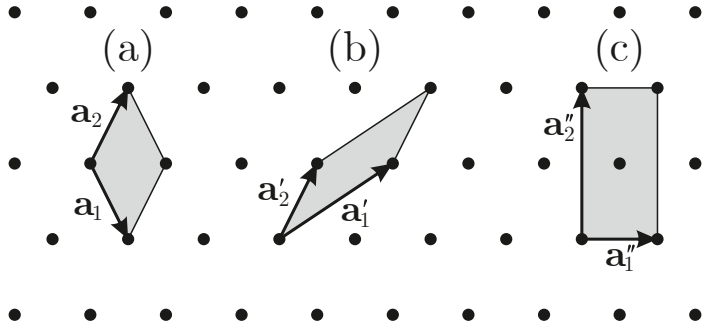

FIG. 2.1. A two-dimensional lattice constructed from primitive lattice vectors $\mathbf{a}_1$ and $\mathbf{a}_2$, and several of its possible unit cells. Cells (a) and (b) are primitive unit cells, and (c) is a larger, conventional unit cell containing two lattice points.

The virtue of using this larger *conventional unit cell* is that the way it tessellates with its neighbours is often more intuitive, and it can be chosen such that it possesses the same symmetry as the lattice it describes.

Lattices can be divided into several categories according to their symmetries. One of the broadest categories is the so-called *lattice system*, of which there are seven. Each system contains all lattices sharing the same set of *point groups*, i.e. groups of symmetry operators that leave one common point in the lattice unchanged, and map all other points onto one another. Every lattice belonging to the cubic lattice system, for example, is invariant under the same five point groups, common to all of which are the four threefold rotation operators about the body diagonals that are characteristic of cubic symmetry. Certain of these lattice systems may be further subdivided according to the *space groups* under which they are invariant, which comprise both pointlike symmetry operations and translations (and compositions thereof). This distinction allows the cubic lattice system to be further decomposed

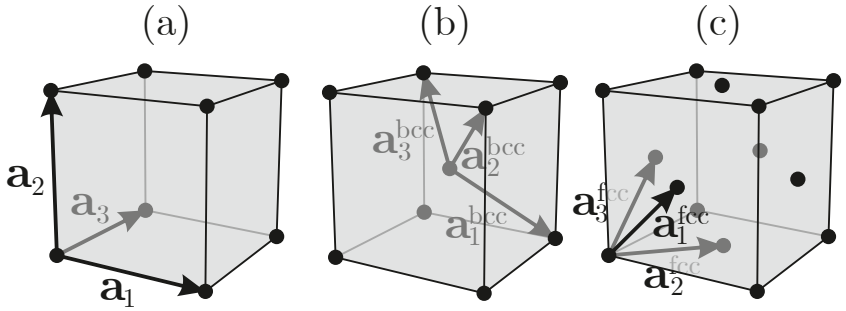

FIG. 2.2. Conventional unit cells for the (a) simple-cubic, (b) body-centred-cubic, and (c) face-centred-cubic lattices.

into the *simple-cubic* (sc), *face-centred-cubic* (fcc), and *body-centred-cubic* (bcc) lattices, whose conventional unit cells are shown in Fig. 2.2. When differentiated by space groups, one finds that 14 distinct three-dimensional lattice types exist, which are conventionally called *Bravais lattices* after Auguste Bravais, the first to enumerate them in 1848 [74]. For detailed discussions of crystallographic space groups, and their rather complex taxonomy, the reader is referred to Refs. [75, 76].

The crystal basis is the set of atoms or molecules positioned around each Bravais lattice point. The position of any atom α in the crystal may be expressed as

$$\mathbf{x}_\alpha = \mathbf{R}_{\text{lattice}} + \mathbf{r}_{\text{basis}}, \tag{2.2}$$

where $\mathbf{r}_{\text{basis}}$ gives the location of α within its unit cell. Fig. 2.3 shows how some familiar crystals can be built using an fcc lattice convolved with an appropriately chosen basis. Tantalum, the metal of study in this thesis, has a plain bcc crystal structure. This is to say that its structure can simply be described using a bcc

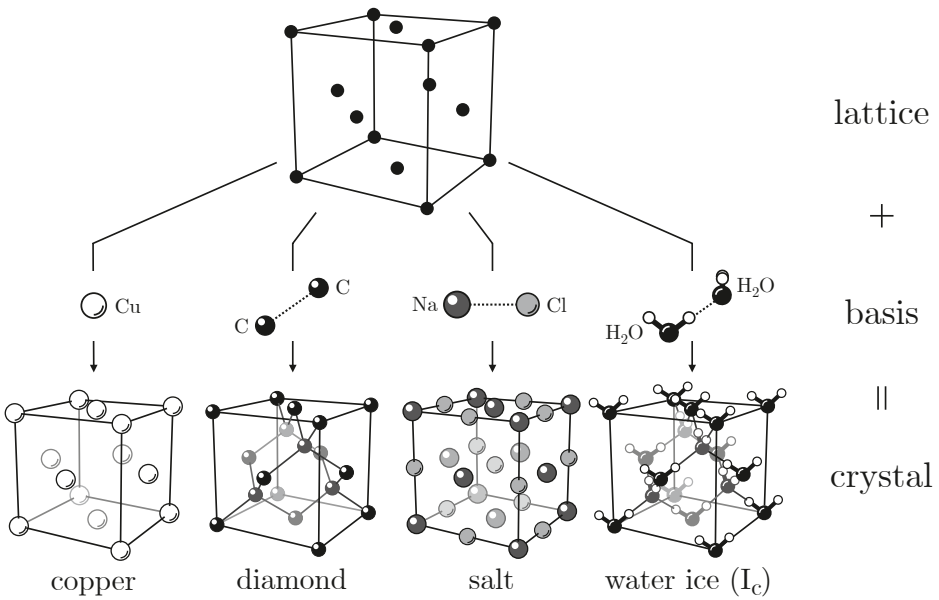

FIG. 2.3. Examples of crystal structures with an underlying fcc lattice. Copper has a plain fcc structure, with one Cu atom at each lattice site. Diamond has a basis of two C atoms displaced by $\frac{1}{4}[111]$. The relatively rare cubic form of ice has an analogous structure. Rock salt comprises sodium and chlorine atoms arranged on fcc lattices separated by $\frac{1}{2}[100]$.

lattice with an atom situated at each lattice point:

$$\mathbf{R}_{\text{lattice}} = n_1\mathbf{a}_1^{\text{bcc}} + n_2\mathbf{a}_2^{\text{bcc}} + n_3\mathbf{a}_3^{\text{bcc}}, \tag{2.3a}$$

$$\mathbf{r}_1 = \mathbf{0}, \tag{2.3b}$$

where $\{\mathbf{a}_i^{\text{bcc}}\}$ is the set of bcc primitive lattice vectors. However, as noted above, this formulation is not particularly intuitive. Instead, we will use the conventional description of bcc crystals, which is as a simple cubic lattice with a two-atom basis:

$$\mathbf{R}_{\text{lattice}} = n_1\mathbf{a}_1 + n_2\mathbf{a}_2 + n_3\mathbf{a}_3, \tag{2.4a}$$

$$\mathbf{r}_1 = \mathbf{0}, \quad \mathbf{r}_2 = \frac{1}{2}(\mathbf{a}_1 + \mathbf{a}_2 + \mathbf{a}_3), \tag{2.4b}$$

where $\{\mathbf{a}_i\}$ denotes the set of orthogonal sc lattice vectors pictured in Fig. 2.2(a).

2.1.2 Directions and planes

Vectors expressing lattice directions or atomic coordinates are conventionally expressed in terms of the chosen lattice vectors as $[uvw]$, where

$$[uvw] \equiv u\mathbf{a}_1 + v\mathbf{a}_2 + w\mathbf{a}_3. \tag{2.5}$$

Since the indices u, v, and w are not comma-separated, an overbar is usually used to denote a negative index, e.g. -2 would be rendered $\bar{2}$. A family of symmetrically equivalent directions is denoted using angled brackets. For instance, the set of vectors joining an atom to its eight nearest neighbours in a bcc crystal would, with our choice of lattice vectors, be expressed as $\frac{1}{2}[111], \frac{1}{2}[\bar{1}11], \frac{1}{2}[1\bar{1}1], \ldots \equiv \frac{1}{2}\langle 111\rangle$.

In many cases, however, it is more useful to think of a crystal not as a set of points, but as a set of planes. The most widely used system for enumerating lattice planes employs *Miller indices* to express their intersections with the unit cell axes. Let the coordinate system be chosen such that one lattice plane of interest contains the origin O, as in Fig. 2.4. The next adjacent plane, whatever its orientation and spacing, will intercept the unit cell axes at the positions $\mathbf{a}_1/h$, $\mathbf{a}_2/k$, and $\mathbf{a}_3/l$, where

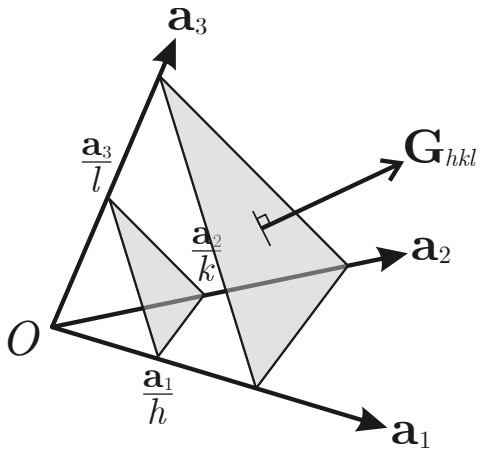

FIG. 2.4. A set of lattice planes denoted by Miller indices (hkl) and their intersections with the primitive lattice vectors $\{\mathbf{a}_i\}$. Also shown is their associated reciprocal lattice vector $\mathbf{G}_{hkl}$, to which their surfaces are normal.

the Miller indices h, k, and l are strictly integer values[6]. The set of planes described by these Miller indices is denoted as (hkl). By analogy with the notation for lattice directions, families of symmetrically equivalent lattice planes are denoted with curly brackets, e.g. $(100), (010), (001), (\bar{1}00), ... \equiv \{100\}$.

2.1.3 The reciprocal lattice

Suppose the normal to the plane (hkl) can be expressed generally as

$$\mathbf{G}_{hkl} = h\mathbf{b}_1 + k\mathbf{b}_2 + l\mathbf{b}_3, \tag{2.6}$$

where $\{\mathbf{b}_i\}$ is a set of appropriately chosen noncoplanar vectors. From Fig. 2.4, we see that the vector joining (say) $\mathbf{a}_1/h$ to $\mathbf{a}_2/k$ must be normal to $\mathbf{G}_{hkl}$. So,

$$0 = \left(\frac{\mathbf{a}_2}{k} - \frac{\mathbf{a}_1}{h}\right) \cdot (h\mathbf{b}_1 + k\mathbf{b}_2 + l\mathbf{b}_3) \tag{2.7a}$$

$$= \left[\frac{h}{k}(\mathbf{a}_2 \cdot \mathbf{b}_1) + \frac{l}{k}(\mathbf{a}_2 \cdot \mathbf{b}_3) - \frac{k}{h}(\mathbf{a}_1 \cdot \mathbf{b}_2) - \frac{l}{h}(\mathbf{a}_1 \cdot \mathbf{b}_3)\right] + [\mathbf{a}_2 \cdot \mathbf{b}_2 - \mathbf{a}_1 \cdot \mathbf{b}_1] \tag{2.7b}$$

[6] The limiting case of (e.g.) $h = 0$ means the plane intercepts the vector $\mathbf{a}_1$ at infinity, which is to say, not at all.

To make certain that the contents of both brackets vanish for any h, k, and l, the set of vectors $\{\mathbf{b}_i\}$ can be chosen such that

$$\mathbf{a}_i \cdot \mathbf{b}_j = C\delta_{ij}, \tag{2.8}$$

where δ_{ij} is the Kronecker delta, and C is some arbitrary constant whose value (which determines the *magnitude* of the vector $\mathbf{G}_{hkl}$) can be chosen freely. For reasons that will become clear later, it is convenient to define $\mathbf{G}_{hkl}$ such that its length is equal to $2\pi/d_{hkl}$, where d_{hkl} is the separation of the planes it describes. This distance can be calculated by projecting a vector joining points on adjacent planes onto the unit normal. Applying this reasoning to the points $\mathbf{0}$ and $\mathbf{a}_1/h$ gives

$$\frac{2\pi}{G_{hkl}} = \left(\frac{\mathbf{a}_1}{h} - \mathbf{0}\right) \cdot \frac{\mathbf{G}_{hkl}}{G_{hkl}} \tag{2.9a}$$

$$\implies 2\pi = C. \tag{2.9b}$$

In order that each $\mathbf{b}_j$ satisfy the relation $\mathbf{a}_i \cdot \mathbf{b}_j = 2\pi\delta_{ij}$, the following construction can be used:

$$\mathbf{b}_1 = 2\pi \frac{\mathbf{a}_2 \times \mathbf{a}_3}{\mathbf{a}_1 \cdot (\mathbf{a}_2 \times \mathbf{a}_3)}, \tag{2.10a}$$

$$\mathbf{b}_2 = 2\pi \frac{\mathbf{a}_3 \times \mathbf{a}_1}{\mathbf{a}_2 \cdot (\mathbf{a}_3 \times \mathbf{a}_1)}, \tag{2.10b}$$

$$\mathbf{b}_3 = 2\pi \frac{\mathbf{a}_1 \times \mathbf{a}_2}{\mathbf{a}_3 \cdot (\mathbf{a}_1 \times \mathbf{a}_2)}. \tag{2.10c}$$

These are known as the *reciprocal lattice vectors*. When all possible linear superpositions of them are taken together, i.e. when one considers every possible vector $\mathbf{G}_{hkl}$ of the form given by Eq. (2.6), one obtains another lattice called the *reciprocal lattice*. It provides an alternative expression of the original lattice in terms of the planes formed by its constituent points, and it is vital in the context of crystallography, as will be shown in Sec. 2.2.

An interesting property of the reciprocal lattice vectors is that they identically

satisfy the following relation for every real lattice vector $\mathbf{R} = [uvw]$:

$$e^{i\mathbf{G}\cdot\mathbf{R}} = e^{i(hkl)\cdot[uvw]} \tag{2.11a}$$

$$= e^{2\pi i(hu+kv+wl)} \tag{2.11b}$$

$$= 1. \tag{2.11c}$$

This identity will be used in Sec. 2.2.1 to derive the conditions for x-ray diffraction.

2.1.4 Single crystals and polycrystals

Only rarely do real crystal samples have a perfect, continuous crystal structure that extends all the way to their surface. Most macroscopic crystalline solids are actually an aggregate of a huge number of relatively small *crystallites* (or *grains*) called a *polycrystal*. The atoms within each grain are arranged on their own lattice, but the crystallographic orientation of each grain differs from that of its neighbours. The surfaces where adjacent grains meet are called *grain boundaries*, and the local atomic arrangement on such a boundary necessarily differs from that of a perfect crystal, as illustrated in Fig. 2.5. Grain boundaries are thus an example of an extended *crystal defect*, i.e. an interruption of the ordinary crystal structure. Several other species of crystal defect will be encountered in this thesis. A polycrystal composed of nanometre-scale grains is sometimes called a *nanocrystal*.

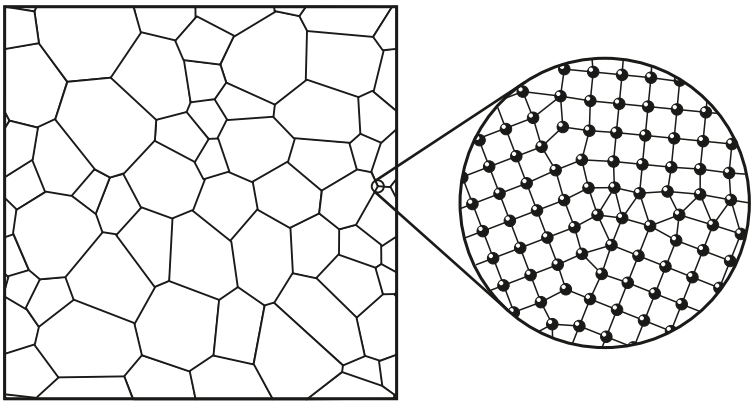

FIG. 2.5. Diagram of a cross-section of a polycrystal, with solid lines indicating grain boundaries. Shown also is a closeup of a junction between three grains illustrating local atomic disorder at the grain boundaries.

The term *texture* refers to the statistical distribution of grains in a polycrystal. Their *crystallographic texture* describes their distribution of orientations, while their *morphological texture* refers to how their shapes are distributed. It is known that under ambient conditions at least, a crystal's texture influences many of its macroscopic physical properties, such as its strength, conductivity, and refractive index [77]. The role of texture in a crystal's response to shock compression, meanwhile, is relatively poorly understood due to its being difficult to diagnose. Chapter 4 of this thesis explores the influence of texture on a shock-loaded crystal's stress and strain state during shock compression, the theory for which will now be introduced.

2.1.5 Stress

To understand how a crystal structure deforms when subjected to the extreme forces attending shock loading, it is necessary first to formalise the concepts of mechanical stress and strain.

Consider an homogeneous substance that is divided in two by a plane with outward unit normal $\hat{\mathbf{n}}$. For an isotropic substance, like an ideal gas, the outward force acting on any unit area of this plane (known as the *traction*) is uniquely determined by the scalar pressure p:

$$\mathbf{T}_{\hat{\mathbf{n}}} = \hat{\mathbf{n}}\, p. \tag{2.12}$$

That is, the force always acts normal to the plane, and the total force exerted per unit area (or *stress*) is independent of the plane's orientation. In an anisotropic material like a crystal, however, the magnitude of the traction can vary depending on the direction of $\hat{\mathbf{n}}$. Moreover, there is no guarantee that the traction will be normal to the plane on which it acts, which is to say that a crystal can support *shear stress*. To account for the crystal's being *nonhydrostatic*, we must replace the scalar p with the *Cauchy stress tensor* σ, which is defined such that

$$\mathbf{T}_{\hat{\mathbf{n}}} = \hat{\mathbf{n}} \cdot \sigma. \tag{2.13}$$

To constrain fully the nine components of σ, one can calculate the tractions acting on three mutually perpendicular planes (with outward normals $\hat{\mathbf{1}}$, $\hat{\mathbf{2}}$, and $\hat{\mathbf{3}}$), and

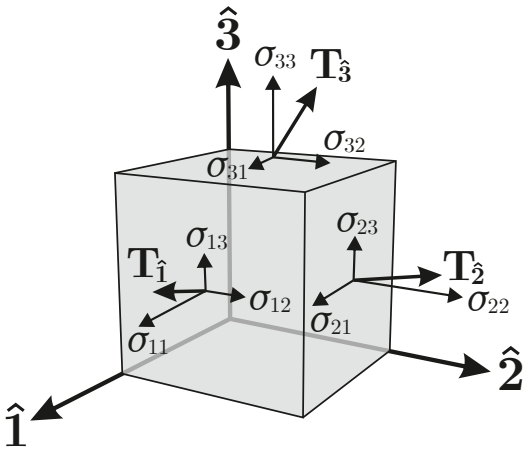

FIG. 2.6. Tractions acting on a material element and their resolution into components along orthogonal coordinate axes, which define the Cauchy stress tensor elements σ_{ij}.

resolve each traction in those same three directions:

$$\sigma_{nm} = [\mathbf{T}_{\hat{\mathbf{n}}}] \cdot \hat{\mathbf{m}} \tag{2.14a}$$

$$= \begin{pmatrix} \sigma_{11} & \sigma_{12} & \sigma_{13} \\ \sigma_{21} & \sigma_{22} & \sigma_{23} \\ \sigma_{31} & \sigma_{32} & \sigma_{33} \end{pmatrix}. \tag{2.14b}$$

Element σ_{11}, for instance, gives the stress acting normal to the plane aligned with direction $\hat{\mathbf{1}}$, while σ_{23} denotes the shear stress acting along the $\hat{\mathbf{3}}$ direction on the plane normal to $\hat{\mathbf{2}}$ (see Fig. 2.6). In mechanical equilibrium, it turns out that σ must be symmetric (i.e. $\sigma_{ji} = \sigma_{ij}$) if angular momentum is to be conserved. The stress tensor therefore comprises six independent elements under static conditions.

If σ is known, it is possible to resolve the stress acting on any plane in any direction. As it is ultimately the complete shear stress state of the crystal that determines which deformation modes will be activated by the shock loading process, knowing σ is key to predicting and understanding its response. This idea will be developed further in Sec. 2.1.8.

The sign convention used throughout this thesis treats positive normal stresses as being compressive, and negative stresses as tensile. Whenever the equivalent scalar

pressure p is quoted, the following definition is being used:

$$p = \frac{1}{3}\left(\sigma_{11} + \sigma_{22} + \sigma_{33}\right). \tag{2.15}$$

This pressure is frame-independent, as it is proportional to the trace of σ.

2.1.6 Strain

When subjected to stress, the shape, size, and orientation of a crystal may change. The following section outlines the kinematics used to quantify the extent and nature of this deformation.

Suppose that each element of a material, with initial position $\mathbf{X}$, moves to position $\mathbf{x}$ after deformation. We assume that the deformation is 'well-behaved', in the sense that $\mathbf{x} = \mathbf{x}(\mathbf{X})$ is a smooth, differentiable function of the initial coordinate $\mathbf{X}$. The remapping is usually expressed in terms of a displacement field $\mathbf{u}(\mathbf{X})$:

$$\mathbf{x}(\mathbf{X}) = \mathbf{X} + \mathbf{u}(\mathbf{X}). \tag{2.16}$$

If $\mathbf{u}$ is a constant, the material experiences a rigid body translation. For a material to experience actual deformation, the displacement field must be inhomogeneous (though this is a necessary rather than a sufficient condition, as we will see). Locally, the warping engendered by the variation of $\mathbf{u}$ is characterised by the *deformation gradient tensor* $F(\mathbf{X})$, which is defined as

$$F = \frac{\partial \mathbf{x}}{\partial \mathbf{X}} \tag{2.17a}$$

$$= I + \frac{\partial \mathbf{u}}{\partial \mathbf{X}}. \tag{2.17b}$$

Since any of the three components of the displacement field can vary in any of the three spatial dimensions, F generally has $3 \times 3 = 9$ nontrivial elements, i.e. it is a second-rank tensor, like σ. The utility of F is made more apparent when one considers how the separation of two nearby points in the material transforms following deformation. Suppose their initial displacement, $\mathbf{R} = \mathbf{X}_2 - \mathbf{X}_1$ is sufficiently small that the curvature of the displacement field $\mathbf{u}$ is locally negligible. Then their

separation after deformation reads

$$\mathbf{r} = \mathbf{x}_2 - \mathbf{x}_1 \tag{2.18a}$$
$$= (\mathbf{X}_2 - \mathbf{X}_1) + [\mathbf{u}(\mathbf{X}_2) - \mathbf{u}(\mathbf{X}_1)] \tag{2.18b}$$
$$= (\mathbf{X}_2 - \mathbf{X}_1) + \left[\mathbf{u}(\mathbf{X}_1) + \frac{\partial \mathbf{u}(\mathbf{X}_1)}{\partial \mathbf{X}}(\mathbf{X}_2 - \mathbf{X}_1) - \mathbf{u}(\mathbf{X}_1)\right] \tag{2.18c}$$
$$= \left[I + \frac{\partial \mathbf{u}(\mathbf{X}_1)}{\partial \mathbf{X}}\right]\mathbf{R} \tag{2.18d}$$
$$\mathbf{r} = F\mathbf{R}. \tag{2.18e}$$

Thus, the deformation gradient is simply the linear operator that transforms undeformed line elements into deformed ones.

However, $F \neq I$ does not necessarily imply that the material has 'deformed' – in principle, F could represent a rigid body rotation, in which case neither the size nor the shape of the material changes. To 'factor out' any reorientation encoded by F, one can calculate its *polar decomposition*. Such a decomposition expresses F as either a pure *strain* followed by a rotation, or vice versa, as in Fig. 2.7:

$$F = RU \tag{2.19a}$$
$$= VR, \tag{2.19b}$$

where R is a rotation operator, and $U = U^T$ and $V = V^T$ are the so-called right and left *stretch tensors*, respectively. These tensors encode that part of the mapping that leads to actual deformation of the material, and so contributes to internal stress. Tensor U expresses the strain in a frame that rotates with the material, while V gives the strain in the 'laboratory' frame. Note that since the stretch tensors are symmetric, they each contain six independent elements, like σ; the rotation matrix R takes the remaining three of F's nine degrees of freedom.

There exist many different measures of strain that can be derived from the stretch tensor(s). Perhaps the most common measure is the *engineering* (or sometimes the *Biot*) *strain*. The elements of the engineering strain tensor e are defined such that

$U = I + e$, that is,

$$U_{ij} = \begin{pmatrix} 1+e_{11} & e_{12} & e_{13} \\ e_{12} & 1+e_{22} & e_{23} \\ e_{13} & e_{23} & 1+e_{33} \end{pmatrix}. \tag{2.20}$$

The on-diagonal elements e_{ii} are the *normal strains*, and the off-diagonal components $e_{ij} \equiv \frac{1}{2}\gamma_{ij}$ are the *shear strains*. Their meaning becomes clearer when one considers how two initially perpendicular line elements in the 12 plane transform under the action of a two-dimensional stretch tensor. If these elements are at first described by the vectors $\mathbf{P} = (l_0, 0)$ and $\mathbf{Q} = (0, l_0)$, after deformation they read

$$\mathbf{p} = \left[(1+e_{11})l_0,\ \frac{1}{2}\gamma_{12}l_0\right], \tag{2.21}$$

$$\mathbf{q} = \left[\frac{1}{2}\gamma_{12}l_0,\ (1+e_{22})l_0\right]. \tag{2.22}$$

In the absence of shear, then, the normal strains e_{11} and e_{22} simply give the fractional

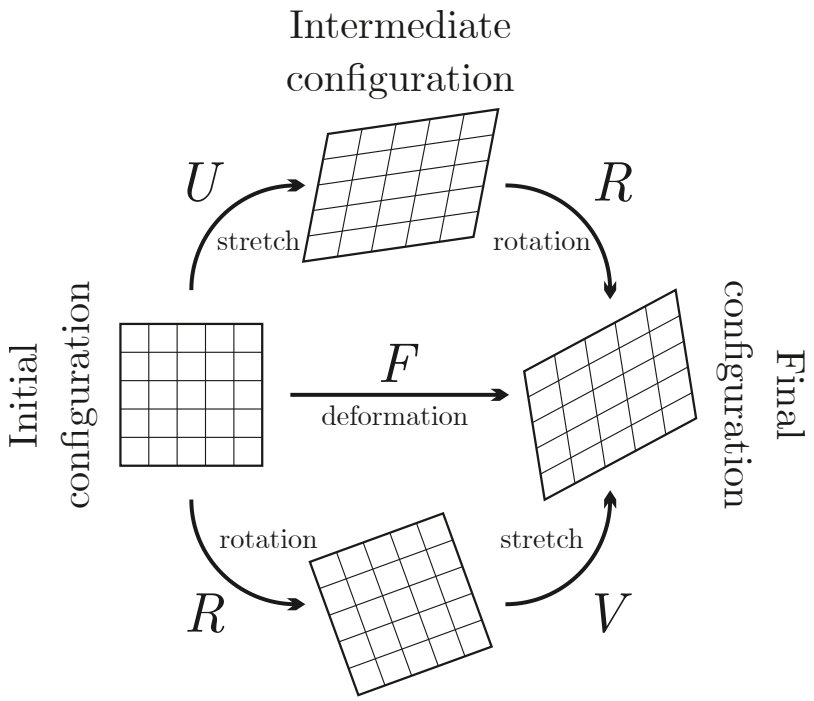

FIG. 2.7. A two-dimensional material element before and after application of a deformation gradient F. Shown also are intermediate configurations obtained by applying either the stretch U first (followed by a rotation R) or the rotation R first (followed by a stretch $V \neq U$). The strains chosen to generate this figure were $e_{11} = 0.2$, $e_{22} = -0.10$, and $\gamma_{12} = 20 \times \pi/180$. The rotation angle was 20°.

changes in the length of sample along their respective coordinate axes. In a state of pure shear, meanwhile, one can show using the dot product of $\mathbf{p}$ and $\mathbf{q}$ that the change in angle δ made between the line elements satisfies

$$\cos\left(\frac{\pi}{2} - \delta\right) = \frac{2 \times \frac{1}{2}\gamma_{12}}{1 + (\frac{1}{2}\gamma_{12})^2}. \tag{2.23}$$

To leading order, then,

$$\delta = \gamma_{12}. \tag{2.24}$$

In some circumstances, it is more natural to use the *true strain* ε, whose normal components are defined such that a small change in the material's *current* length l effects a strain of

$$d\varepsilon = \frac{dl}{l} \tag{2.25}$$

$$\implies \varepsilon = \ln\left(\frac{l}{l_0}\right) \tag{2.26}$$

Since the equivalent engineering strain e would be $(l - l_0)/l_0$,

$$\varepsilon = \ln(1 + e). \tag{2.27}$$

The two strain measures converge in the limit of infinitesimal deformations. All strains quoted throughout this thesis are true strains. As with stress, we will adopt a sign convention that means compressive strains (i.e. those leading to a reduction in volume) are denoted as positive.

2.1.7 Elasticity and plasticity

The preceding section described strain in an entirely 'microstructure-agnostic' sense. That is, it was ignorant of how strain is actually realised in crystalline matter at the atomic level. The next few sections illustrate the two fundamentally different ways a crystal can accommodate an imposed strain, namely by either elastic or plastic deformation. To illustrate the physics, we will follow the progress of a single cubic crystal as it undergoes compression up to and then beyond its yield point.

Consider the region of crystalline matter pictured in Fig. 2.8(a). It has an sc structure, and has its $\langle 100 \rangle$ directions aligned with the coordinate axes. The region in question spans 16 unit cells along the z direction (which will be the loading axis), and so has a total initial length of $L_0 = 16\,a$, where $a = \|\mathbf{a}_3\|$. We imagine that the crystal pictured constitutes only a small part of a much larger sample, which is to say that it is surrounded on all sides by identical crystalline matter. By symmetry, this means the pictured region cannot expand in the transverse directions (or *barrel*) in response to loading. This is known as *lateral confinement*. Now suppose that the ends of the crystal are slowly (quasistatically) forced together along the z direction through a distance $\Delta L(t)$. How will the crystal respond?

Initially, the compression simply causes the crystal's interplanar spacing parallel to the loading direction to decrease, as shown in Fig. 2.8(b). Such deformation is described as *elastic*. Elastic deformation is reversible, which is to say that if the ends of the crystal were returned to their original positions, the final configuration

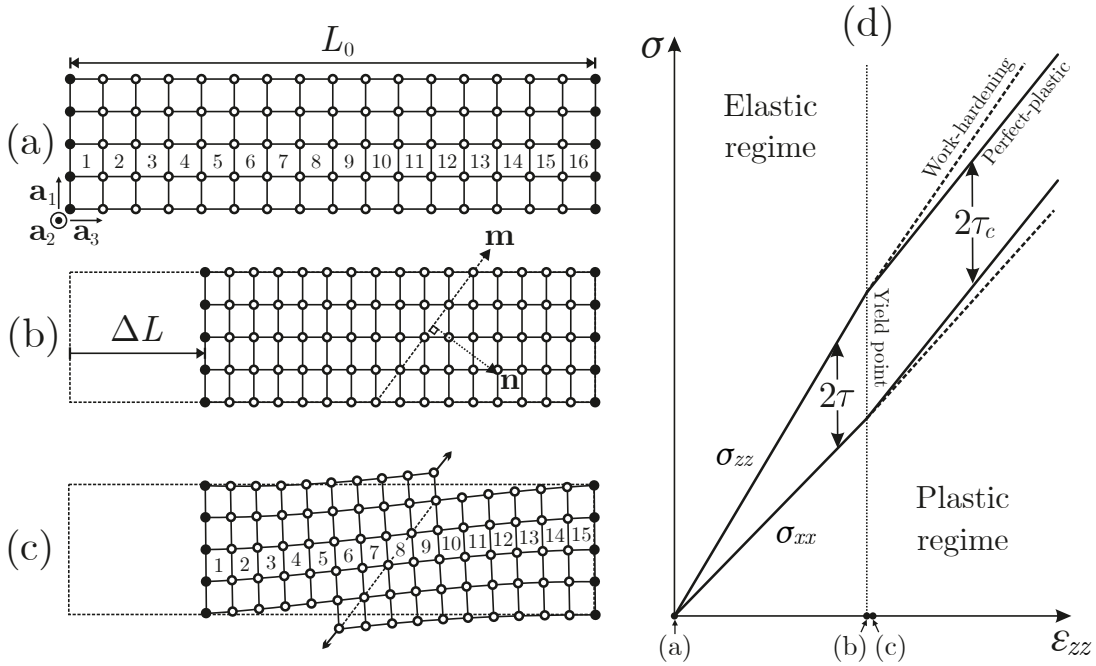

FIG. 2.8. Yield behaviour of a single cubic crystal uniaxially compressed along the z direction. (a) The crystal's initial configuration. (b,c) The crystal's configuration immediately before and after the yield point. On reaching strain $e_{zz} = \Delta L/L_0$, the crystal yields on a $\hat{\mathbf{n}} = (\bar{1}01)$ plane, undergoing shear motion along the $\hat{\mathbf{m}} = [101]$ direction. (d) Normal stresses along x and z as a function of applied longitudinal strain. The crystal yields when the shear stress $\tau = \frac{1}{2}(\sigma_{zz} - \sigma_{xx})$ reaches critical value τ_c. Beyond this point the limiting shear stress likely grows with strain due to work hardening.

of the crystal would be the same as before compression.

In the elastic regime, the crystal's stress state (which is fundamentally governed by the spacing and angles made between atoms) is a unique function of the applied strain. To leading order, the relation between stress and strain is linear:

$$\sigma_{ij} = C_{ijkl}\varepsilon_{kl}. \tag{2.28}$$

Here, C is the fourth-rank *stiffness tensor* containing the crystal's various elastic moduli. Generally speaking, C comprises some $3^4 = 81$ elements. As explained in previous sections, however, both σ and ε only contain six independent elements each in equilibrium, which reduces the number of independent elements in C to 36. This makes it practicable to express the constitutive relation between σ and ε using *Voigt notation*, in which the stress and strain are written as vectors and the stiffness tensor as a 6×6 matrix:

$$\begin{pmatrix} \sigma_{xx} \\ \sigma_{yy} \\ \sigma_{zz} \\ \sigma_{yz} \\ \sigma_{xz} \\ \sigma_{xy} \end{pmatrix} = \begin{pmatrix} C_{11} & C_{12} & C_{13} & C_{14} & C_{15} & C_{16} \\ C_{21} & C_{22} & C_{23} & C_{24} & C_{25} & C_{26} \\ C_{31} & C_{32} & C_{33} & C_{34} & C_{35} & C_{36} \\ C_{41} & C_{42} & C_{43} & C_{44} & C_{45} & C_{46} \\ C_{51} & C_{52} & C_{53} & C_{54} & C_{55} & C_{56} \\ C_{61} & C_{62} & C_{63} & C_{64} & C_{65} & C_{66} \end{pmatrix} \begin{pmatrix} \varepsilon_{xx} \\ \varepsilon_{yy} \\ \varepsilon_{zz} \\ \varepsilon_{yz} \\ \varepsilon_{xz} \\ \varepsilon_{xy} \end{pmatrix}. \tag{2.29}$$

When one further takes into account the manifold symmetries of a cubic crystal, one finds that only three of the above moduli are actually independent of one another. For our sample for which the $\langle 100 \rangle$ directions are aligned with the coordinate axes, the constitutive relation reduces to

$$\begin{pmatrix} \sigma_{xx} \\ \sigma_{yy} \\ \sigma_{zz} \\ \sigma_{yz} \\ \sigma_{xz} \\ \sigma_{xy} \end{pmatrix} = \begin{pmatrix} c_{11} & c_{12} & c_{12} & 0 & 0 & 0 \\ c_{12} & c_{11} & c_{12} & 0 & 0 & 0 \\ c_{12} & c_{12} & c_{11} & 0 & 0 & 0 \\ 0 & 0 & 0 & c_{44} & 0 & 0 \\ 0 & 0 & 0 & 0 & c_{44} & 0 \\ 0 & 0 & 0 & 0 & 0 & c_{44} \end{pmatrix} \begin{pmatrix} 0 \\ 0 \\ \varepsilon_{zz} \\ 0 \\ 0 \\ 0 \end{pmatrix}, \tag{2.30}$$

where the minuscule c's denote the three independent *cubic elastic constants*, and $\varepsilon_{zz} = \ln(1 + \Delta L/L_0)$. The normal stresses thus scale with ΔL according to $\sigma_{zz} = c_{11}\varepsilon_{zz}$ and $\sigma_{xx} = \sigma_{yy} = c_{12}\varepsilon_{zz}$, with the latter scaling somewhat slower since $c_{12} < c_{11}$.

The purely elastic response cannot continue without limit. Consider the $(\bar{1}01)$ plane pictured in Fig. 2.8(b), whose normal is given approximately by $\hat{\mathbf{n}} = \frac{1}{\sqrt{2}}(-1, 0, 1)$. According to Eq. (2.13), the traction acting on this plane reads

$$\mathbf{T}_{\hat{n}} = \left(-\frac{1}{\sqrt{2}}, 0, \frac{1}{\sqrt{2}}\right) \cdot \begin{pmatrix} \sigma_{xx} & 0 & 0 \\ 0 & \sigma_{xx} & 0 \\ 0 & 0 & \sigma_{zz} \end{pmatrix} \tag{2.31a}$$

$$= \frac{1}{\sqrt{2}} \left(-\sigma_{xx}, 0, \sigma_{zz}\right). \tag{2.31b}$$

The component of this traction acting in the [101] direction, which can be approximated as $\hat{\mathbf{m}} = \frac{1}{\sqrt{2}}(1, 0, 1)$, is

$$\tau = \frac{1}{2}(\sigma_{zz} - \sigma_{xx}) > 0. \tag{2.32}$$

So, although the shear stresses acting on the planes normal to the coordinate axes might be zero, there is considerable shear stress acting on this inclined $(\bar{1}01)$ plane, and indeed on *every* plane oblique to the loading axis[7]. While a solid can tolerate some degree of shear, there will come a point at which the shear stress acting on some plane reaches a critical value τ_c, beyond which the attendant deformation can no longer be accommodated elastically. If further loaded above this *elastic limit*, the crystal will either fracture, or it will deform *plastically*.

An illustration of the deformation the crystal might suffer just after yielding is given in Fig. 2.8(c). In this instance, the shear stress acting on one of the crystal's $(\bar{1}01)$ planes has built to such a level that it temporarily fails, and allows an entire block of the crystal to slide over another. This plastic deformation mode sees atoms immediately above and below the *slip plane* become displaced by a whole lattice vector. This changes the deformation state of the crystal in two important ways.

[7] For any nontrivial stress state, the shear acting on almost any plane in almost any direction is nonzero. However, in shock physics the shear stress $\tau = \frac{1}{2}(\sigma_{zz} - \sigma_{xx})$ acting on planes at 45° to the loading direction is often called *the* shear stress. These planes suffer the greatest shear stress of any plane for the largely diagonal stress state present under shock conditions.

First, note that by undergoing this coordinated slipping motion, the crystal has actually succeeded in changing the number of atomic planes in each direction: where once it spanned 16 unit cells along z, it now spans only 15. The atoms are thus allowed to move apart in the loading direction. Conversely, the number of transverse crystal planes [of the type (100)] locally increases from four to five. As the crystal is laterally confined, this causes the atoms to bunch together along the x direction. The result of this reconfiguration is to decrease σ_{zz} and to increase σ_{xx}, which, according to Eq. (2.32), relieves the very shear stress driving the deformation. As long as the crystal can keep flowing plastically, then, the shear stress τ cannot grow any higher than the material's *strength* τ_c. Often, the strength of a metal increases with the amount of plastic deformation it has undergone [as pictured in Fig. 2.8(d)], a phenomenon known as *work hardening*. This hardening results from interactions between *dislocations*, which will be described in the next section.

Second, we see that the material in proximity to the slip plane has rotated slightly. When the crystal slips, the blocks of material above and below the slip plane become laterally displaced from one another. Such displacement is forbidden, however, by the fact that the crystal region is laterally confined. To compensate, the crystal rotates in the vicinity of the slip plane, with the sense of the rotation being such that the slip direction (in this case, [101]) rotates away from the loading axis.

In the plastic regime, it is necessary to distinguish which parts of the deformation are owed to irreversible, plastic deformation, and which are purely elastic. This is conventionally done with a multiplicative *elastoplastic decomposition*, in which the total deformation gradient F is expressed as

$$F = F^e F^p. \tag{2.33}$$

In essence, the plastic deformation gradient F^p first maps each atom into its new unit cell, then the elastic deformation gradient F^e distorts and rotates the unit cell to reproduce the final atomistic configuration. It is F^e, then, that actually tells us how neighbouring atoms are arranged, and so what kind of forces they exert on one another. Therefore the constitutive relation in Eq. (2.28) should be amended to

$$\sigma = C\varepsilon^e, \tag{2.34}$$

where ε^e refers to the elastic portion of the total strain, obtained from the polar decomposition of F^e.

Fig. 2.8(c) gave only one example of how plastic deformation might be realised in a compressed crystal. In reality, there is almost always more than one means of deforming available to any given crystal, and the nature and multiplicity of these deformation modes depends on the crystal structure. In the following sections, descriptions of the two plasticity mechanisms prevalent in bcc crystals like tantalum will be given, along with a discussion of dislocations, the mediators of plastic flow.

2.1.8 Dislocations

Were it really the case that entire blocks of a crystal slid past one another like rigid bodies during plastic deformation, as Fig. 2.8 suggests, the typical strength of a metal would be of order $G/(2\pi)$ [78], where G is the shear modulus. The notional strength of tantalum, for example, for which $G = 69$ GPa [79], would therefore be around 11 GPa. Tantalum actually yields between 0.18 and 0.40 GPa [80, 81]. A more nuanced theory of plasticity that can account for this vast discrepancy was first put forward in 1934 in separate papers by Egon Orowan [82], Michael Polanyi [83], and G. I. Taylor [84]. The authors posited that atoms in a slip plane do not in fact move as one, but piecemeal. That is, there should exist a boundary within the slip plane that separates atoms that have slipped from those that have not, and grows as plastic deformation proceeds. The arrangement of the atoms in the immediate vicinity of such a boundary would necessarily deviate from the usual crystal structure, which is to say that the boundary would constitute a linelike crystal defect. Taylor named these defects *dislocations*. By localising slip to the vicinity of the dislocation, one only has to break a few atomic bonds at a time to realise plastic deformation, rather than having to break every atomic bond in the plane simultaneously. The existence of dislocations, which was unambiguously confirmed in 1955 via electron microscopy[8] [88], thus explains the surprisingly low strength of the typical metal.

[8] Earlier observations of dislocations do exist: the earliest, in fact, may have come from Obreimov and Shubnikov in 1926 [85–87], who, upon viewing a deforming salt crystal under polarised light, noticed the rapid transmission of 'sharp bright lines' (indicating distorted material) from one side of the sample to the other. Taylor cited these observations in his 1934 paper [84].

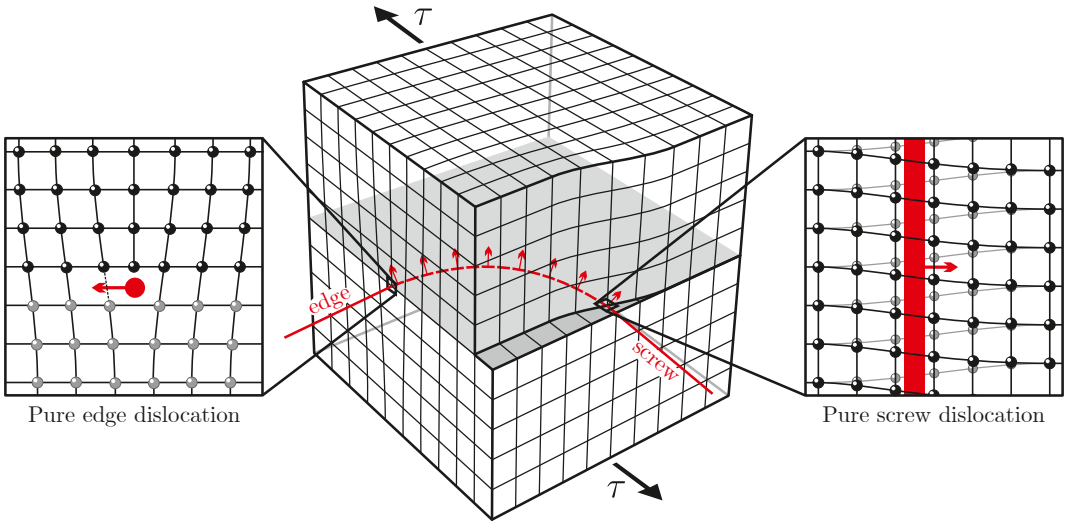

FIG. 2.9. Section of a dislocation loop (red) moving in a slip plane (grey) mediating shear deformation in a block of sc crystal under the action of shear stress τ. Left: edge dislocation viewed along the direction of the loop. Atoms below the slip plane are coloured grey. The atomic bond rendered as a dashed line will be broken when the dislocation next moves. Right: screw dislocation viewed from above the slip plane.

Fig. 2.9 illustrates part of a dislocation loop mediating shear deformation in a block of simple-cubic crystal. The arrangement of the atoms in the core of the dislocation differs dramatically depending on where along the dislocation loop one looks. At its leading edge, atoms are slipping directly into unslipped material, meaning the atoms above the slip plane are to some extent 'bunched up'. Indeed, when one views the crystal along the direction of the loop, it appears as if an extra plane of atoms has been inserted (left of Fig. 2.9). This segment of the dislocation is called an *edge*. On the sides of the dislocation loop, meanwhile, the atoms slip parallel to the dislocation direction. This portion of the dislocation is referred to as a *screw*, so-called because the atomic planes perpendicular to the dislocation form a helter-skelter-like pattern (right of Fig. 2.9). Segments of the dislocation that are neither parallel nor perpendicular to the slip direction are said to be of *mixed* character. The character of a dislocation segment profoundly influences properties such as its mobility under shear stress and the long-range stress field it generates. Interestingly, screw dislocations uniquely can engage in *cross-slip*, meaning they can transfer between different slip planes.

The most fundamental property of a dislocation is its *Burgers vector* $\mathbf{b}$. It is the lattice vector by which nearby atoms are displaced during slip. The Burgers vector

of any given dislocation can be deduced using a construction formulated by Frederick Frank [89] (based on earlier work by Johannes Burgers [90]). Far from a dislocation, the local atomic arrangement is still consistent with a crystal structure, so the lattice vector joining one unit cell to another is well-defined. If one draws a closed circuit around the dislocation that passes exclusively through this 'good' material, and adds up the lattice vectors used to traverse the circuit, one will find that the result is nonzero. That sum is equal to $\mathbf{b}$. An example of a *Burgers circuit* enclosing an edge dislocation is shown in Fig. 2.10. The Burgers vector essentially quantifies the direction and strength of the plastic deformation carried by the dislocation.

Plastic flow at the macroscopic level is realised by the concerted motion of many millions of dislocations. According to the classic kinematic equation of Orowan [91], a collection of dislocations moving in a given slip plane at average speed ν can accommodate a plastic strain rate of

$$\dot{\varepsilon}^p = \rho_D \|\mathbf{b}\| \nu, \tag{2.35}$$

where ρ_D, the dislocation density, is defined as the total length of dislocation present per unit volume:

$$\rho_D = \frac{L_D}{V}. \tag{2.36}$$

Most any metal sample will already contain a population of dislocations, whose density might vary between around 10^8 cm^{-2} (if it has previously been *annealed*,

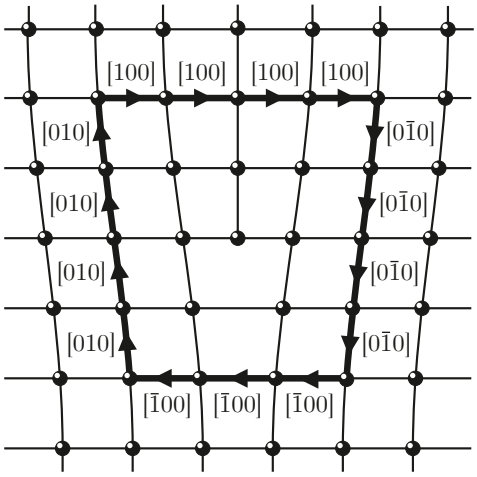

FIG. 2.10. Burgers circuit drawn around an edge dislocation with Burgers vector $\mathbf{b} = [100]$.

or raised to a high temperature and allowed to cool) and 10^{12} cm^{-2} (if it has been *cold-worked*, i.e. deliberately subjected to plastic deformation beforehand). Often, the extreme plastic strain rates brought about by shock compression and release are too great to be realised by the pre-existing dislocation population, necessitating the creation of new dislocations. At relatively low strain rates, dislocations are primarily generated from other defects – grain boundaries can act as dislocation sources, as can other dislocations. If these *heterogeneous nucleation* processes are unavailable, or are simply too slow, the crystal may resort to *homogeneous* nucleation, in which dislocation loops are spontaneously generated from perfect, crystalline material.

A laterally confined crystal must usually slip in more than one direction to relieve shear stress on all of its planes. It is observed, though, that crystals do not slip in arbitrary directions, nor on arbitrary planes. In bcc crystals like tantalum, slip takes place only in the $\frac{1}{2}\langle 111\rangle$ directions, i.e. along the shortest possible lattice vectors. The planes to which the dislocations are confined are usually of the types $\langle 112\rangle$, $\langle 110\rangle$, and $\langle 123\rangle$. A slip direction and slip plane taken together define a *slip system*. Which of these systems will be activated on compression can be often predicted by calculating the *resolved shear stress* τ_{RSS} acting upon them. This is the component of the shear stress acting on plane (hkl) in the $[uvw]$ direction, calculated as usual using Eq. (2.14a):

$$\tau_{\mathrm{RSS}} = \frac{[(hkl)\cdot\sigma]\cdot[uvw]}{\|(hkl)\|\|[uvw]\|}. \tag{2.37}$$

Plastic flow will take place most rapidly on slip systems with the greatest resolved shear stress, and in fact can only take place if τ_{RSS} exceeds the material's strength τ_c. This is known formally as *Schmid's law*[9].

2.1.9 Twinning

The discussion so far has been based around the assumption that when a crystal yields, the atoms above and below the plane on which it fails suffer displacement by a whole lattice vector. This does not have to be the case. *Deformation twinning* is an alternative plasticity mechanism which, in bcc crystals, causes atoms in a {211}-

[9] Literature on the Schmid law often expresses the resolved shear stress as $\tau_{\mathrm{RSS}} = \sigma\cos(\phi)\cos(\lambda)$, where ϕ and λ are the angles made by the slip direction and slip plane normal with the compression direction. This represents a special case of Eq. (2.37) where all stresses but the longitudinal stress σ_{zz} are zero, which is not applicable for a shock-compressed, laterally confined crystal.

type plane to move by only $\frac{1}{6}\langle 111\rangle$ relative to the planes adjacent to it. As illustrated in Fig. 2.11, this results in a reversal of the crystal's *stacking sequence*. Ordinarily, a bcc crystal can be built from an infinite repeating stack of six distinct $\{211\}$ planes, labelled A to F, in the order $ABCDEFAB$ ... . Twinning locally reverses this stacking sequence, such that it might read $ABCDEFAFEDC$ ... . The result is the formation of a reoriented crystal region called a *twin* that forms a mirror image of the original crystal, from which it is separated by a *twin* (or sometimes *habit*) *plane*. This plane constitutes a two-dimensional defect, like a grain boundary.

Twinning, too, is realised by the propagation of dislocations. Since their Burgers vector constitutes only a fraction of a lattice vector, they are referred to as *partial dislocations*, to distinguish them from the *perfect dislocations* that mediate slip.

When forced to deform plastically, tantalum responds via a mixture of dislocation slip and deformation twinning. The relative abundance of each plasticity agent is sensitive to the loading conditions: at higher temperatures, for example, slip tends to become dominant, while twinning increases at higher strain rates. Combined with its lack of phase transitions, this rich behaviour makes tantalum an ideal candidate for studying crystal plasticity under high strain-rate and high pressure conditions.

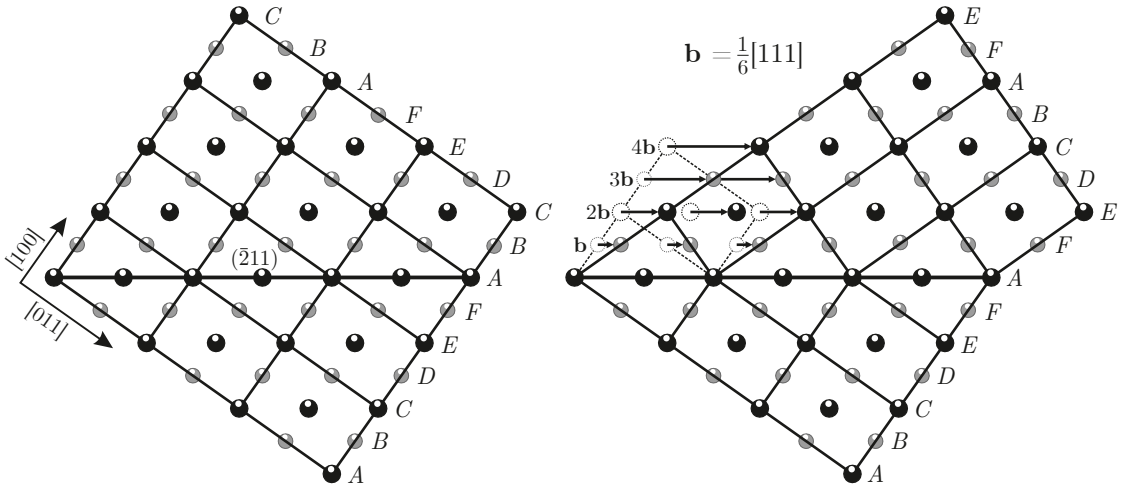

FIG. 2.11. Left: an ideal bcc crystal viewed along the $[01\bar{1}]$ direction. Black and grey atoms belong to separate $(01\bar{1})$ planes. The crystal can be thought of as a repeating stack of inequivalent $(\bar{2}11)$ planes labelled A-F. Right: the same crystal after deformation twinning. Successive $(\bar{2}11)$ planes are displaced by Burgers vector $\mathbf{b} = \frac{1}{6}[111]$ relative to those adjacent to them, resulting in a local reversal of the stacking sequence.

2.2 X-ray diffraction

When illuminated by hard x-rays, whose wavelength $\lambda \sim 1$ Å is comparable to the separation of its constituent atoms, a crystal behaves much like a three-dimensional diffraction grating, and scatters the incident radiation into a discrete set of directions. The resulting diffraction pattern is directly related to the arrangement of the crystal's atoms. This simple observation was first demonstrated experimentally in 1912 by Max von Laue, and so transformed the field of crystallography. There now exist sources of x-rays so powerful that diffraction images of an evolving sample may be obtained with subpicosecond exposure times, allowing the structure of even a crystal relaxing in the wake of a shock wave to be resolved. The following section reviews the basic theory of x-ray crystallography, and the diffraction geometry used in the experiment studied as part of this thesis.

2.2.1 The Laue condition

Fundamentally, x-rays scatter from a crystal's electrons. Consider, then, a single electron with equilibrium position $\mathbf{x}$ that is illuminated by a plane electromagnetic wave whose amplitude at $\mathbf{x}$ is the real part of

$$\psi_0(\mathbf{x}, t) = A(t)e^{i\mathbf{k}_0 \cdot \mathbf{x}}, \tag{2.38}$$

where $A(t) = A_0 e^{-i\omega t}$ and $\mathbf{k}_0$ is the incident wavevector, whose direction gives the propagation direction of the wave and whose magnitude is related to its wavelength by $k = \|\mathbf{k}_0\| = 2\pi/\lambda$. Let us assume the electron reradiates the incident wave in all directions like an ideal point source, and that it does so elastically, so that the wavelengths of the incident and emergent waves are equal. The amplitude of the emergent wave at some point $\mathbf{r}$ is therefore proportional to

$$\psi = \frac{A(t)e^{i\mathbf{k}_0 \cdot \mathbf{x}}}{\|\mathbf{r} - \mathbf{x}\|} e^{ik\|\mathbf{r}-\mathbf{x}\|}. \tag{2.39}$$

Now suppose we are interested only in the *far-field* limit, i.e. at locations a great distance from the crystal in which the electron lives. This means that, for any elec-

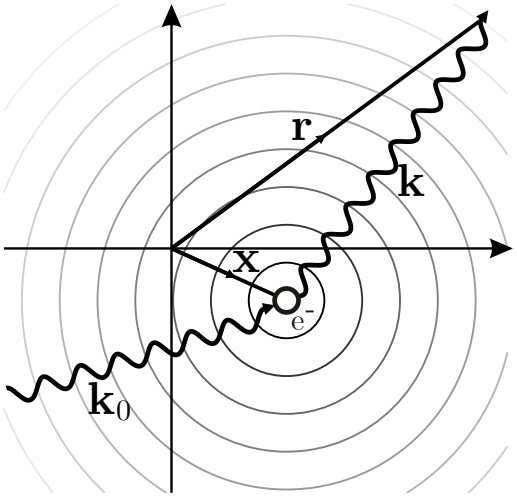

FIG. 2.12. A single electron isotropically reradiating a plane electromagnetic wave with incident wavevector $\mathbf{k}_0$, as observed along the $\hat{\mathbf{r}}$ direction.

tron under consideration, $\|\mathbf{r}\| \gg \|\mathbf{x}\|$. We are therefore justified in approximating $\|\mathbf{r}-\mathbf{x}\|$ using the leading order of the Taylor expansion:

$$(\mathbf{r}-\mathbf{x})^2 = \mathbf{r}^2 - 2\,\mathbf{r}\cdot\mathbf{x} + \mathbf{x}^2 \tag{2.40a}$$

$$\approx \mathbf{r}^2\left(1 - \frac{2\,\mathbf{r}\cdot\mathbf{x}}{\mathbf{r}^2}\right) \tag{2.40b}$$

$$\implies \|\mathbf{r}-\mathbf{x}\| \approx r\left(1 - \frac{\mathbf{r}\cdot\mathbf{x}}{r^2}\right). \tag{2.40c}$$

We may thus approximate Eq. (2.39) as

$$\psi \approx \frac{A(t)e^{i\mathbf{k}_0\cdot\mathbf{x}}}{r} e^{ik(r-\hat{\mathbf{r}}\cdot\mathbf{x})}, \tag{2.41}$$

where $\hat{\mathbf{r}} = \mathbf{r}/r$. Collecting terms that only involve $\mathbf{x}$, one finds

$$\psi = \frac{A(t)e^{ikr}}{r} \times e^{-i[(k\hat{\mathbf{r}})-\mathbf{k}_0]\cdot\mathbf{x}}. \tag{2.42}$$

The combination $k\hat{\mathbf{r}}$ we rename $\mathbf{k}$, which is effectively the wavevector of that part of the scattered wave propagating along $\hat{\mathbf{r}}$.

To calculate the scattering amplitude for an entire crystal, one simply adds together the waves scattered by every one of its electrons. Therefore if the local electron density at point $\mathbf{x}$ is $\rho(\mathbf{x})$, the total scattering intensity is, up to some

constant of proportionality, given by

$$\Psi(\mathbf{k}-\mathbf{k}_0) = \int d^3\mathbf{x}\ \rho(\mathbf{x}) e^{-i(\mathbf{k}-\mathbf{k}_0)\cdot\mathbf{x}}, \tag{2.43}$$

which is nothing more than the Fourier transform (FT) of the sample's electron density. It turns out that for an infinite crystalline solid, the scattering amplitude above is nonzero only at a discrete set of scattering vectors, which can be seen as follows. The integral over all space may be re-expressed as the sum of integrals over an infinite set of tessellating unit cells:

$$\Psi(\mathbf{k}-\mathbf{k}_0) = \sum_{\mathbf{R}} \int_{\mathrm{UC}} d^3\mathbf{r}\ \rho(\mathbf{r}-\mathbf{R}) e^{-i(\mathbf{k}-\mathbf{k}_0)\cdot(\mathbf{r}-\mathbf{R})}. \tag{2.44}$$

Here, $\mathbf{R}$ is a real lattice vector [of the form given by Eq. (2.1)], and the variable of integration $\mathbf{r}$ is restricted to a single unit cell (UC). Since the crystal is by definition spatially periodic, so too is its electron density ρ, which is to say that $\rho(\mathbf{r}) = \rho(\mathbf{r}-\mathbf{R})$. Eq. (2.44) may therefore be expressed as

$$\Psi(\mathbf{k}-\mathbf{k}_0) = \left[\sum_{\mathbf{R}} e^{i(\mathbf{k}-\mathbf{k}_0)\cdot\mathbf{R}}\right] \left[\int_{\mathrm{UC}} d^3\mathbf{r}\ \rho(\mathbf{r}) e^{-i(\mathbf{k}-\mathbf{k}_0)\cdot\mathbf{r}}\right]. \tag{2.45}$$

The scattering intensity therefore separates into two components, the first being governed by the underlying lattice structure, the second depending on the details of the electron distribution within the unit cell. The latter term, which is referred to as the *structure factor*, determines whether the arrangement of basis atoms and the shape of the electron density clustered around them (expressed by the *atomic form factor*) is such as to give constructive interference between emerging x-rays. The structure and atomic form factors will be discussed further in Sec. 2.2.3.

The first term in Eq. (2.45), meanwhile, which is simply the FT of the lattice, places a very strong constraint on the scattered wavevectors at which any diffraction is actually visible. If the scattering vector $\mathbf{G} = \mathbf{k} - \mathbf{k}_0$ is chosen arbitrarily, the chances are that the scattered waves from different unit cells will combine incoherently, i.e. the contribution of every cell will likely interfere destructively with that of another cell somewhere else in the crystal. The only way to guarantee that Ψ will

not be vanishingly small is to demand that every scattered wave is in phase:

$$e^{i\mathbf{G}\cdot\mathbf{R}} = 1. \tag{2.46}$$

Comparing this condition with Eq. (2.11), we conclude that, for there to be appreciable scattering intensity into direction $\mathbf{k}$, the scattering vector $\mathbf{G}$ must be a reciprocal lattice vector $\mathbf{G}_{hkl}$:

$$\mathbf{k} - \mathbf{k}_0 = \mathbf{G}_{hkl}. \tag{2.47}$$

This is known as the *Laue condition*.

2.2.2 The Bragg condition

The same geometric constraint between the incident and emergent rays can be reached by assuming that successive planes of atoms effectively 'reflect' the incident wave. Fig. 2.13 shows two atomic planes with separation d illuminated by a wave with wavelength λ that is incident at angle θ to its surface. Some fraction of the beam is diffracted by the first plane, the remainder transmitted; of that transmitted beam, some fraction is diffracted by the second plane, and so on.

For constructive interference between successive emergent rays to take place, their path difference, which is equal to segment PQ in Fig. 2.13, must be an integer multiple of λ. Since the segment $RP = 2d$,

$$2d\sin\theta = n\lambda. \tag{2.48}$$

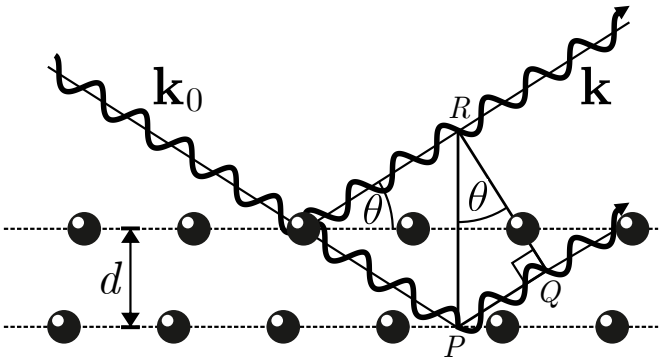

FIG. 2.13. Adjacent atomic planes with separation d coherently 'reflecting' an incident plane wave at Bragg angle $\theta = \lambda/2d$.

This is the *Bragg condition*.

The Bragg and Laue conditions are in fact equivalent. Fig. 2.14 pictures the constraint between $\mathbf{k}$ and $\mathbf{k}_0$ expressed by the Laue condition. As shown in Sec. 2.1.3, $\mathbf{G}_{hkl}$ encodes the set of atomic planes with separation $d = 2\pi/G_{hkl}$ and surface normal $\mathbf{G}_{hkl}/G_{hkl}$. The Laue condition essentially identifies this set of planes as being responsible for the diffraction. The angles made by the incident and scattered wavevectors with these planes are equal, and are shown in Fig. 2.14 to be given by

$$k \sin\theta = \frac{1}{2} G_{hkl}. \tag{2.49}$$

Replacing G_{hkl} with $2\pi/d$ and k with $2\pi/\lambda$ yields

$$\lambda = 2d \sin\theta. \tag{2.50}$$

The angular relation between the $\mathbf{k}_0$, $\mathbf{k}$, and $\mathbf{G}$ predicted by Laue condition is therefore identical to that given by the Bragg condition. The higher-order solutions to Eq. (2.47) ($n = 2, 3, ...$) can be understood as coming from reciprocal lattice vectors constituting integral multiples of $\mathbf{G}_{hkl}$, which are normal to the same planes.

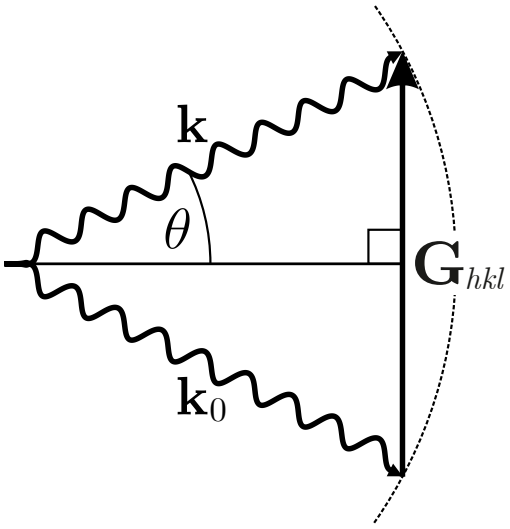

FIG. 2.14. Pictorial representation of the Laue condition, with the Bragg angle θ shown.

2.2.3 The structure factor

Eq. (2.45) expresses the diffraction intensity from a crystal as the product of the FT of the underlying lattice (which, as just established, is nonzero only at points in the reciprocal lattice) and that of the electron density within the unit cell:

$$\Psi(\mathbf{G}) \propto \delta^{(3)}\left(\mathbf{G}-\mathbf{G}_{hkl}\right) \times \left[\int_{\mathrm{UC}} d^3\mathbf{r}\ \rho(\mathbf{r}) e^{-i\mathbf{G}\cdot\mathbf{r}}\right]. \tag{2.51}$$

The latter term, which is called the *structure factor* $S(\mathbf{G})$, determines whether the arrangement of the electrons in the unit cell is conducive to diffraction or not:

$$S(\mathbf{G}) = \int_{\mathrm{UC}} d^3\mathbf{r}\ \rho(\mathbf{r}) e^{-i\mathbf{G}\cdot\mathbf{r}}. \tag{2.52}$$

In principle, it is possible to express the structure factor as a discrete sum over contributions from individual basis atoms, which can be seen as follows. One first expresses the electron density at any point as a linear superposition of the electron distributions surrounding every atom in the crystal. This sum can be calculated by adding up contributions from different basis atoms within each unit cell, and then summing over unit cells. That is to say that the local electron density reads

$$\rho(\mathbf{r}) = \sum_{j,\mathbf{R}} \rho_j(\mathbf{r}-\mathbf{r}_j-\mathbf{R}), \tag{2.53}$$

where $\mathbf{r}_j$ is the position of basis atom j within its unit cell, and ρ_j expresses the electron distribution that surrounds it. Inserting this sum into Eq. (2.52) yields

$$S(\mathbf{G}) = \sum_j \left[\sum_{\mathbf{R}} \left(\int_{\mathrm{UC}} d^3\mathbf{r}\ \rho_j(\mathbf{r}-\mathbf{r}_j-\mathbf{R}) e^{-i\mathbf{G}\cdot\mathbf{r}}\right)\right]. \tag{2.54}$$

We now imagine that for each term in the outer sum, we can shift our origin of coordinates such that there is a basis atom located at the origin. By introducing the change of variable $\mathbf{y}_j = \mathbf{r} - \mathbf{r}_j$, we find

$$S(\mathbf{G}) = \sum_j e^{-i\mathbf{G}\cdot\mathbf{r}_j} \left[\sum_{\mathbf{R}} \left(\int_{\mathrm{UC}} d^3\mathbf{y}_j\ \rho_j(\mathbf{y}_j-\mathbf{R}) e^{-i\mathbf{G}\cdot\mathbf{y}_j}\right)\right]. \tag{2.55}$$

Now, given that we are only concerned with scattering vectors that satisfy the Laue condition, we can insert 'for free' a factor of $e^{i\mathbf{G}\cdot\mathbf{R}} = 1$ into the inner sum, meaning Eq. (2.55) can just as well be written

$$S(\mathbf{G}) = \sum_j e^{-i\mathbf{G}\cdot\mathbf{r}_j} \left[\sum_{\mathbf{R}} \left(\int_{\mathrm{UC}} d^3\mathbf{y}_j \; \rho_j(\mathbf{y}_j - \mathbf{R}) e^{-i\mathbf{G}\cdot(\mathbf{y}_j - \mathbf{R})} \right) \right]. \tag{2.56}$$

We now employ the inverse of the logic that took us between Eqs. (2.43) and (2.44): the sum of integrals over tessellating unit cells is an integral over all space. Hence

$$S(\mathbf{G}) = \sum_j e^{-i\mathbf{G}\cdot\mathbf{r}_j} \int d^3\mathbf{y}_j \; \rho_j(\mathbf{y}_j) e^{-i\mathbf{G}\cdot\mathbf{y}_j}. \tag{2.57}$$

The phase-weighted integral of the electron density surrounding basis atom j is known as its *atomic form factor* f_j:

$$f_j(\mathbf{G}) = \int d^3\mathbf{y} \; \rho_j(\mathbf{y}) e^{-i\mathbf{G}\cdot\mathbf{y}}. \tag{2.58}$$

It expresses the amplitude of the signal scattered into wavevector $\mathbf{k}_0 + \mathbf{G}$ by an isolated atom of the type j. In real terms, the effect of the atomic form factor is to attenuate the diffraction intensity from a crystal at large values of $\|\mathbf{G}\|$ (i.e. at large scattering angles), owing to the decreased coherence between scattering from different regions of each atom's electron cloud.

Generally, then, the structure factor for a crystal can be expressed by the sum

$$S(\mathbf{G}) = \sum_j f_j(\mathbf{G}) e^{-i\mathbf{G}\cdot\mathbf{r}_j}. \tag{2.59}$$

For monatomic crystals, the atomic form factors for different basis atoms are identical, and the structure factor simplifies to

$$S(\mathbf{G}) = f(\mathbf{G}) \sum_j e^{-i\mathbf{G}\cdot\mathbf{r}_j}. \tag{2.60}$$

Depending on the arrangement of the basis atoms, the structure factor can vanish for certain reflections, even if $\mathbf{G}$ is a reciprocal lattice vector. If the coordinates of

the j^{th} basis atom are expressed as $[u_j v_j w_j]$, Eq. (2.60) becomes

$$S(\mathbf{G}) = f(\mathbf{G}) \sum_j e^{-i(h\mathbf{b}_1+k\mathbf{b}_2+l\mathbf{b}_3)\cdot(u_j\mathbf{a}_1+v_j\mathbf{a}_2+w_j\mathbf{a}_3)} \tag{2.61a}$$

$$= f(\mathbf{G}) \sum_j e^{-2\pi i(hu_j+kv_j+lw_j)}, \tag{2.61b}$$

using $\mathbf{a}_i \cdot \mathbf{b}_j = 2\pi\delta_{ij}$. A crystal with a simple-cubic structure has a single basis atom located at [000], and thus $S(\mathbf{G})$ reduces to $f(\mathbf{G})$, meaning all reflections are permitted. For a bcc crystal like tantalum, however, a second basis atom is located at $[\frac{1}{2}\frac{1}{2}\frac{1}{2}]$, so the structure factor becomes

$$S_{\text{bcc}}(\mathbf{G}) = f(\mathbf{G}) \left[1 + e^{-i(h+k+l)\pi}\right] \tag{2.62a}$$

$$\propto 1 + (-1)^{h+k+l}. \tag{2.62b}$$

The interference between the two basis atoms in a bcc crystal is therefore such that reflections for which $h+k+l$ is odd are 'forbidden'. The criterion that $h+k+l$ be even for diffraction to be visible is known as a *selection rule*. Each crystal structure has its own set of selection rules. With our choice of lattice vectors[10], the planes with the smallest scattering angles in tantalum are labelled {011}, {200}, and {211}.

2.2.4 The Ewald sphere

The Laue condition tells us that when a crystal is illuminated by an x-ray source with wavevector $\mathbf{k}_0$, we should only expect to see diffraction into a discrete set of wavevectors $\mathbf{k} = \mathbf{k}_0 + \mathbf{G}$, where $\mathbf{G}$ is a reciprocal lattice vector adhering to any selection rules relevant to the crystal in question. The conditions for diffraction, then, are actually rather exacting. This problem is best visualised using a construction called the *Ewald sphere*. To do so, one first draws the crystal's reciprocal lattice, as in Fig. 2.15(a). If the scattering is elastic, any emergent wavevector $\mathbf{k}$ must sit on the surface of a sphere with radius k. If the centre of this sphere is not drawn on the origin, but at $-\mathbf{k}_0$, then its surface represents the locus of all possible elastic

[10] These systematic absences are in a sense artificial, because we deliberately chose to use a unit cell whose edges are not *primitive* lattice vectors – if instead we used $\{\mathbf{a}_i^{\text{bcc}}\}$ from the outset, *all* reflections would be permitted (and the meaning of the Miller indices would change).

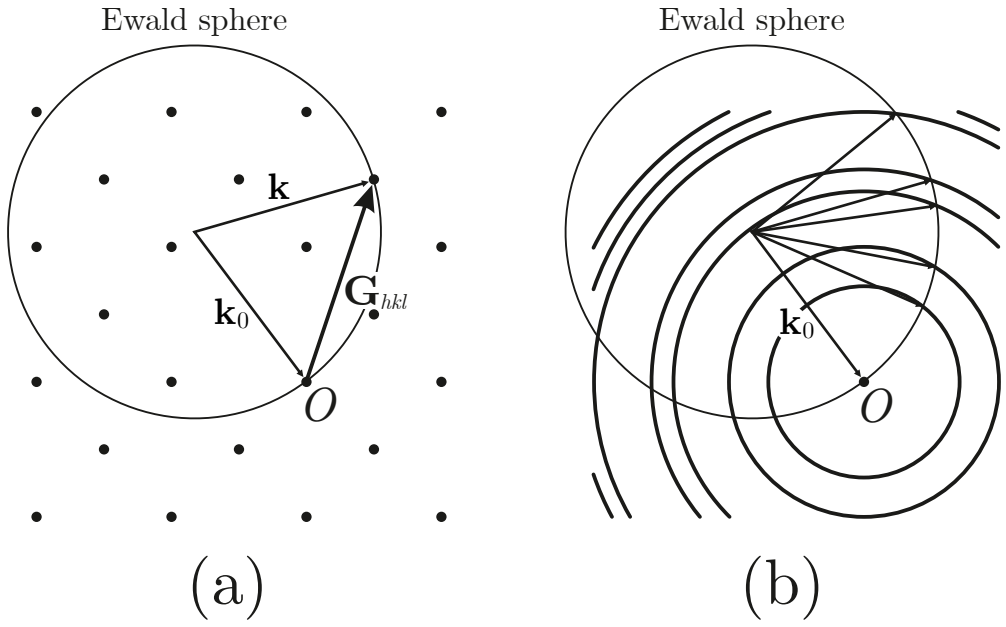

FIG. 2.15. Ewald construction for a two-dimensional (a) single crystal and (b) untextured polycrystal illuminated by a monochromatic x-ray source with wavevector $\mathbf{k}_0$.

scattering vectors $\mathbf{k} - \mathbf{k}_0$ in the reciprocal lattice coordinate system. The Laue condition demands that $\mathbf{k} - \mathbf{k}_0$ be equal to a reciprocal lattice vector for constructive interference to take place. Thus, wherever the sphere intersects a reciprocal lattice point, coherent diffraction will occur.

A cursory glance at Fig. 2.15(a) is enough to show that an intersection between the Ewald sphere and the reciprocal lattice is unlikely to happen by chance. That is to say that if one were to aim a monochromatic x-ray beam at an arbitrarily oriented single crystal, one would probably not observe a diffraction pattern. A number of diffraction techniques and geometries have been developed to make the Laue condition easier to satisfy. One approach is to mount the crystal on an adjustable stage so that it can be rotated and brought to meet the Laue condition as in Fig. 2.15(a). Another approach is to use an x-ray source with a range of wavevectors. This can be achieved either by using a diverging-beam geometry, in which a pointlike source of x-rays is allowed to diverge and strike the target at a range of incidence angles, or by using a polychromatic source that contains a finite range of wavelengths. In the Ewald construction, these two methods essentially introduce a continuum of Ewald spheres that cover a much larger volume of the reciprocal lattice.

Complementary to all of these techniques is *powder diffraction*. Here, one does

not study a monocrystalline sample, but a polycrystal composed of a huge number of randomly oriented crystallites. The notion is that every possible crystallographic orientation will be represented by a crystallite somewhere in the crystal. This means that for every family of crystal planes, there will exist a set of those planes with the correct orientation to satisfy the Laue condition. The geometry can again be visualised using the Ewald construction. Since the reciprocal lattice of a powderlike sample is essentially a superposition of the lattices of all of its constituent grains, it will comprise a set of concentric spheres. As shown in Fig. 2.15(b), this means one is guaranteed to observe a diffraction peak from every type of crystal plane, provided its spacing d permits a solution to the Bragg condition. Each family of planes scatters light into a cone with opening angle 4θ, which, when recorded on a flat detector, forms a circular pattern known as a *Debye-Scherrer ring*. The spacing of each plane can then be ascertained directly from the Bragg condition [$d = \lambda/(2\sin\theta)$], allowing one to place to constraints on the possible crystal structure.

2.2.5 Fibre diffraction

The previous section showed that x-ray diffraction patterns are relatively easily obtained from polycrystalline samples. However, by opting for a powder sample, one sacrifices some of one's ability to detect any rotation that might ensue due to plastic deformation. Suppose the sample were to undergo deformation twinning. A twin in a single crystal represents a distinct crystallographic orientation with its own novel set of scattering vectors. If the alignment of the twin and the incident x-ray beam are just so, one might therefore be able to observe a brand new diffraction peak that provides an unambiguous experimental signal of deformation twinning. In a powderlike sample, however, a crystallite with the same orientation as the new twin already exists. What one wants is a sample whose character falls somewhere between that of a single crystal and a powderlike polycrystal, with sufficiently many grain orientations that diffraction can be observed without needing to carefully orient that sample, but few enough orientations that rotated crystallites are distinct.

An ideal candidate for such a sample is a fibre-textured polycrystal. A *textured* polycrystal is any one whose distribution of orientations is not completely random.

A powder sample would be described as untextured, while a single crystal has the strongest texture possible. A *fibre* texture is one in which every grain has the same crystallographic direction closely aligned with one particular axis, but whose azimuthal orientation about that axis is random. The reciprocal lattice vectors of such a crystal therefore form a cylindrically symmetric 'ring system' that is likely to intersect the Ewald sphere at several points.

Fig. 2.16 compares the Ewald construction for a fibre-textured target with those of a single crystal and a powderlike polycrystal. It is useful at this point to introduce the *Polanyi sphere*. It is the locus of all *possible* reciprocal lattice vectors of a given type (say {011}). The intersection between the Ewald and Polanyi spheres thus represents all potential solutions to the Laue condition for that type of scattering vector. In a single crystal, the Polanyi surface is obviously very sparsely populated by reciprocal lattice vectors, and so the Laue condition is generally not met. By contrast, the Polanyi surface is completely occupied in a powderlike sample, and so the Laue condition is satisfied everywhere on the intersection between the Ewald and Polanyi spheres. The situation for the fibre-textured crystal is intermediate. The Laue condition is indeed met in several places along the spheres' intersection, wherever one of the reciprocal rings crosses it. The resulting diffraction pattern is not an entire Debye-Scherrer ring, but a set of discrete diffraction peaks. Any

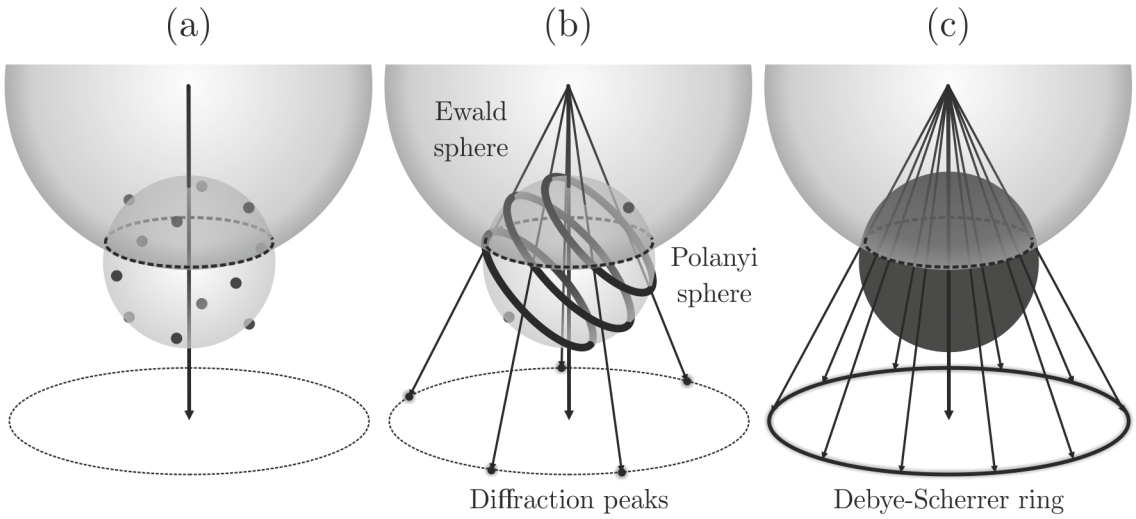

FIG. 2.16. Ewald constructions for a three-dimensional (a) single crystal, (b) fibre-textured polycrystal, and (c) untextured polycrystal illuminated by a monochromatic x-ray beam. The Polanyi surface in this case represents the locus of all possible {011} scattering vectors. The polycrystal in (b) has a [011] fibre texture.

reorientation of the grains caused by plastic deformation will change the 'latitude' of the rings on the Polanyi surface and hence the position of the diffraction peaks around the ring, allowing slip and twinning to be detected via x-ray diffraction.

2.2.6 X-ray free-electron lasers

A revolution in x-ray science was triggered with the activation of the world's first hard X-ray Free Electron Laser (XFEL), the Linac Coherent Light Source (LCLS), a source of radiation with a spectral brightness one billion times greater than that of its predecessors and a bandwidth of order 10^{-3} [92]. These extraordinary machines, of which only a few exist[11], can produce high-quality diffraction images of a sample with only a few femtoseconds' exposure. This unprecedented temporal resolution means XFELs uniquely are able to capture ultrafast processes occurring at the atomic level, of which crystal plasticity under shock conditions is a prime example.

At the front end of an XFEL is a beam of electrons travelling at speed $v \sim c$. The beam is directed into a periodic arrangement of alternating magnetic dipoles called an *undulator*. As each electron traverses the undulator, it experiences a time-

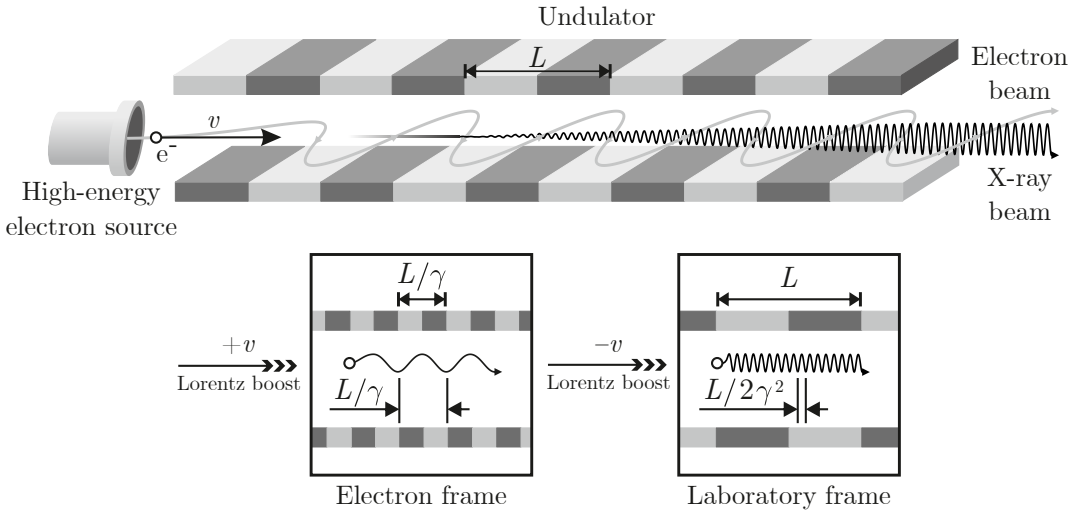

FIG. 2.17. Schematic of a free-electron laser. Relativistic electrons pass through a series of magnets with period L causing them to oscillate rapidly in the transverse direction and thus emit intense x-ray radiation in the forward direction. In its own frame of reference, each electron radiates light with wavelength L/γ, which is Doppler shifted to $\lambda = L/(2\gamma^2)$ in the laboratory frame. A Lorentz factor of $\gamma = 3$ was used to generate this figure.

[11] At the time of writing, five hard XFELs are currently operational: LCLS in the USA, SACLA in Japan, European XFEL in Germany, PAL-XFEL in Korea, and SwissFEL in Switzerland [93].

varying Lorentz force from the spatially periodic transverse magnetic field and so oscillates in directions perpendicular to the beam. As the electron accelerates it emits radiation whose wavelength in the frame of the undulator is given by [94]

$$\lambda = \frac{L}{2\gamma^2}\left(1 + \frac{1}{2}K^2\right), \tag{2.63}$$

where L is the period of the undulator, $\gamma = (1 - v^2/c^2)^{-1/2}$ is the beam's Lorentz factor, and K parametrises the strength of the undulator field. The leading-order approximation to Eq. (2.63), $\lambda \sim L/(2\gamma^2)$, can be understood as arising from two relativistic effects. First, from the electron's perspective, the undulator is Lorentz contracted by a factor γ, meaning the radiation emitted in the electron's frame of reference only has wavelength L/γ. When one boosts back into the undulator's frame, the radiation emitted in the forward direction is further Doppler shifted by a factor 2γ. Thus, if one sends electrons with GeV energies ($\gamma \sim 10^4$) through an undulator with a spatial period of order centimetres, they will produce hard x-rays with wavelengths of order Ångstroms.

In what sense, then, is an XFEL a laser? Initially, each electron in the beam emits radiation independently of its neighbours. The phase relation of waves from different electrons is therefore essentially random, meaning the resultant x-ray beam is incoherent. However, as the intensity of the radiation field grows, it begins to exert appreciable Lorentz forces on the very electrons producing it. It transpires that the nature of the interaction is such as to cause the electrons to cluster together into *microbunches* along the beam axis, whose period equals λ. As electrons bunch together, they emit more coherently, thus increasing the intensity of the radiation field, thus augmenting the bunching effect, and so on. This feedback loop, much like the one active in a conventional laser, exponentially amplifies the x-ray beam's intensity as it propagates along the undulator axis. Eventually, enough energy is extracted from the electrons that they begin to fall behind – and thus draw energy out of – the radiation field; beyond this point, the x-ray beam intensity saturates.

2.3 Shock physics

Almost all solids become harder to compress at higher density, meaning their local sound speed increases with pressure. If a compression wave is launched into a solid, then, its peak will travel faster than its foot. The wave will thus steepen and, if given a sufficiently long runway, eventually form a steplike discontinuity[12] in density, pressure, and energy called a *shock wave*. It is largely thanks to dynamic loading techniques like shock compression that we are able to access the extreme pressures and temperatures that would otherwise be present only in planetary and stellar interiors. The following section gives an overview of the basic theory underpinning the propagation of one-dimensional shock waves, and the release waves that ensue after a shock encounters a free surface.

2.3.1 The Rankine-Hugoniot conditions

The Rankine-Hugoniot conditions are the fundamental equations expressing the conservation of mass, momentum, and energy across a shock front. When supplemented by sufficiently many constitutive relations (see Sec. 2.3.2), the connections between the density, stress, and energy of the material either side of the shock these relations provide fully constrain the set of states that can be achieved via shock compression.

The equations are traditionally derived by envisaging a column of material of cross-sectional area A and initial mass density ρ_0 that is struck by a 'piston' travelling

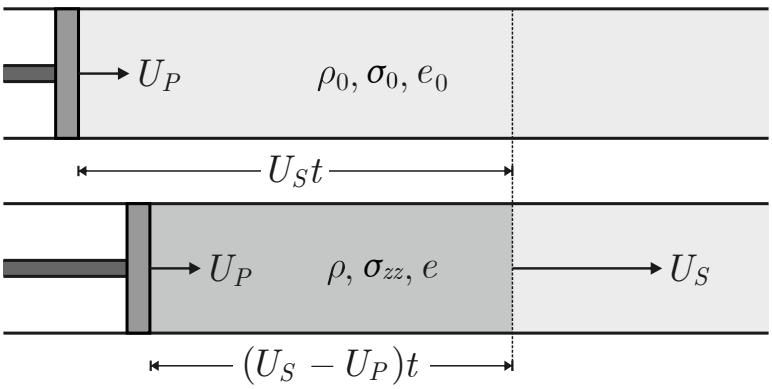

FIG. 2.18. A piston driving a shock wave into a compressible medium.

[12] Real shocks always have a finite width set by the viscosity of the medium [95].

at constant speed U_P, resulting in the creation of a shock wave travelling at speed $U_S > U_P$. It is assumed that the material is both laterally confined by and thermally insulated from its surroundings, so that neither mass nor energy[13] can escape into the transverse directions. By time t, the shock wave has travelled through a distance $U_S t$. The material between this front and the piston, which previously occupied volume $A \times U_S t$, now occupies only $A \times (U_S - U_P)t$, where $U_P t$ is the distance travelled by the piston in time t. So, by the conservation of mass,

$$\rho_0 \times [AU_S t] = \rho \times [A(U_S - U_P)t], \tag{2.64}$$

where ρ is the density of the material behind the shock front. Eliminating At gives the first Rankine-Hugoniot equation:

$$\rho_0 U_S = \rho(U_S - U_P). \tag{2.65}$$

The stress jump across the shock front can be constrained by applying Newton's second law. The net force applied to the compressed region is $(\sigma_{zz} - \sigma_0)A$, where σ_{zz} and σ_0 are the longitudinal normal stresses either side of the shock. The impulse delivered by this force can be equated with the momentum gained by the compressed material, whose final velocity is equal to the piston velocity U_P:

$$[(\sigma_{zz} - \sigma_0)A] \times t = [\rho_0 U_S A t] \times U_P. \tag{2.66}$$

Factoring out At as before gives the second relation:

$$\sigma_{zz} - \sigma_0 = \rho_0 U_S U_P. \tag{2.67}$$

Finally, note that the work done on the material by the piston, $[\sigma_{zz}A] \times [U_P t]$, is, by virtue of the adiabaticity condition, equal to its change in energy. If the internal energy per unit mass before and behind the shock front are e_0 and e, respectively,

[13] The adiabatic assumption is usually justified for a shock-loading scenario simply because the timescale is so short as to prevent any substantial thermal conduction from taking place.

the conservation of energy can be expressed as

$$[\sigma_{zz}A] \times [U_P t] = \left[(\rho_0 U_S A t)e + \frac{1}{2}(\rho_0 U_S A t)U_P^2\right] - [(\rho_0 U_S A t)e_0 + 0] \tag{2.68a}$$

$$\implies \sigma_{zz}U_P = \rho_0(e - e_0)U_S + \frac{1}{2}\rho_0 U_S U_P^2. \tag{2.68b}$$

The product $U_S U_P$ on the right-hand side can be eliminated using Eq. (2.67):

$$\sigma_{zz}U_P = \rho_0(e - e_0)U_S + \frac{1}{2}(\sigma_{zz} - \sigma_0)U_P; \tag{2.69}$$

$$\frac{1}{2}(\sigma_0 + \sigma_{zz}) = \rho_0(e - e_0)\frac{U_S}{U_P}. \tag{2.70}$$

The ratio U_S/U_P can be expressed via Eq. (2.65) as $\rho/(\rho - \rho_0)$, so

$$\frac{1}{2}(\sigma_0 + \sigma_{zz}) = (e - e_0)\frac{\rho\rho_0}{\rho - \rho_0}. \tag{2.71}$$

Finally, we re-express the densities as volumes per unit mass $V \equiv 1/\rho$, giving the conventional form of the third Rankine-Hugoniot equation:

$$e - e_0 = \frac{1}{2}(\sigma_0 + \sigma_{zz})(V_0 - V). \tag{2.72}$$

2.3.2 The Hugoniot

If the ambient pressure and density of the material before the shock are known, then there are essentially six 'unknowns' in the Rankine-Hugoniot system of equations: the shock stress (σ_{zz}) and specific volume (V), the particle and shock velocities (U_P and U_S), and the initial and final energies (e_0 and e). The Rankine-Hugoniot relations themselves remove three degrees of freedom. Two more can be eliminated by the material's equation of state (EOS), which relates its energy $e = e(p, V)$ in thermodynamic equilibrium to its volume and pressure. *If* one can reasonably make the approximation $\sigma_{zz} = p$ for the material in question, one is left with only one unknown variable, of which all other variables can be treated as dependent functions. One can thus obtain the shock pressure as a function of specific volume:

$$p = p(V; p_0, V_0). \tag{2.73}$$

This function is called *the Hugoniot*. It describes the locus of thermodynamic states in the stress-volume plane that are accessible via shock compression. Note that the system does not pass through all intermediate shock states on its way to (p, V), but jumps to that point discontinuously. A typical Hugoniot is illustrated in Fig. 2.19.

If the crystal supports significant shear stress following shock compression, one cannot substitute σ_{zz} for p, and the EOS alone cannot uniquely determine the Hugoniot. To close the system of equations, one requires an extra constraint in the form of a strength model, which can relate the longitudinal stress to the hydrostatic pressure via the shear stress $\tau = \frac{3}{4}(\sigma_{zz} - p)$. Constructing such a model is difficult. Material strength varies with density, temperature, strain rate, and dislocation density, *all* of which vary substantially during shock compression. Moreover, acquiring experimental measurements of strength with which to evaluate a given model is challenging – indeed, it is increasingly common practice to appeal instead to first-principles simulation techniques to provide synthetic data to which to fit model parameters. The pursuit of a strength model that is robust over the breadth of extreme conditions accessible via shock compression has produced a multitude of models of varying complexity (see for example Refs. [96–98]), and remains an area of intense research.

If one is primarily interested in ascertaining the shock pressure, though, and is not too concerned with the energy densities, it is possible to solve only the first two

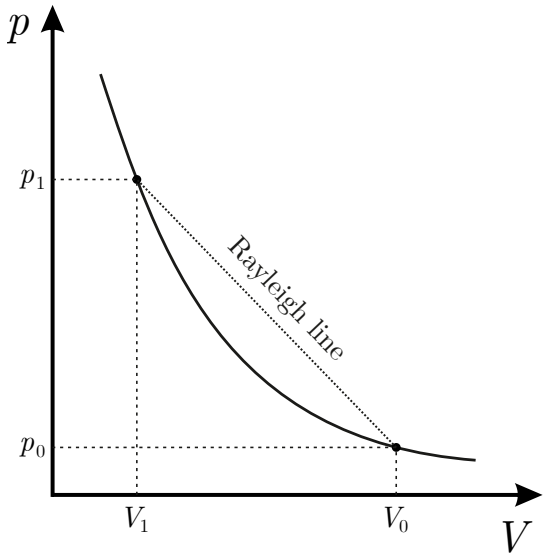

FIG. 2.19. A typical Hugoniot curve showing the locus of pressure-volume states achievable via shock compression. The line connecting the initial and final states in the (p, V) plane is called the Rayleigh line.

Rankine-Hugoniot equations with the aid of a so-called 'shock EOS', which is an empirical relation between the shock and particle velocities of the form

$$U_S = C_0 + SU_P, \tag{2.74}$$

where C_0 is the ambient bulk sound speed, and S is a material-dependent parameter of order unity. This linear dependence of U_S on U_P holds for a remarkably wide range of shock pressures for most metals. By substituting the expression above for U_S into Eqs. (2.65) and (2.67) and then eliminating U_P between the two resultant equations, the following common expression for $\sigma_{zz}(V)$ can be obtained:

$$\sigma_{zz} - \sigma_0 = \frac{C_0^2(V_0 - V)}{[V_0 - S(V_0 - V)]^2}. \tag{2.75}$$

2.3.3 Two-wave structures in solids

In Sec. 2.1.7, it was shown that the constitutive response of a crystal changes radically when it is loaded above its yield point, as it probably will be in a shock-compression experiment. It turns out that this has some interesting consequences for the structure of shock waves in crystalline matter.

A simple model for the normal stress $\sigma_{zz}(V)$ along the Hugoniot may be built if one neglects for a moment the heating that results from shock compression, and assumes the stresses can be described with reasonable accuracy by the linear elasticity relation provided by Eq. (2.34). If for sake of argument we assume once again the $\langle 100 \rangle$ directions are aligned with the coordinate axes, differential changes to the normal stresses and strains are connected via

$$\begin{pmatrix} d\sigma_{xx} \\ d\sigma_{xx} \\ d\sigma_{zz} \end{pmatrix} = \begin{pmatrix} c_{11} & c_{12} & c_{12} \\ c_{12} & c_{11} & c_{12} \\ c_{12} & c_{12} & c_{11} \end{pmatrix} \begin{pmatrix} d\varepsilon^e_{xx} \\ d\varepsilon^e_{xx} \\ d\varepsilon^e_{zz} \end{pmatrix}. \tag{2.76}$$

Suppose the volume of the crystal decreases by $dV > 0$. Below the yield point, the

elastic strain state is uniaxial ($d\varepsilon^e_{zz} = dV$, $d\varepsilon^e_{xx} = 0$), thus

$$d\sigma_{zz} = c_{11} dV. \tag{2.77}$$

Above the yield point (which in this context is called the *Hugoniot elastic limit* or HEL), shear stress is prevented from accumulating further by plastic deformation. That is, if one neglects work hardening, the changes in strain must be such that

$$d\tau = \frac{1}{2}(d\sigma_{zz} - d\sigma_{xx}) = 0. \tag{2.78}$$

One can show from Eq. (2.76) that $d\sigma_{xx} = d\sigma_{zz}$ requires that $d\varepsilon^e_{xx} = d\varepsilon^e_{zz}$. So, using the fact that in the differential limit $dV = 2d\varepsilon^e_{xx} + d\varepsilon^e_{zz} = 3d\varepsilon^e_{zz}$, the rate at which the longitudinal stress increases above the yield point is given by

$$d\sigma_{zz} = 2c_{12} d\varepsilon^e_{xx} + c_{11} d\varepsilon^e_{zz} \tag{2.79a}$$

$$= \frac{1}{3}\left(c_{11} + 2c_{12}\right) dV. \tag{2.79b}$$

Together, Eqs. (2.77) and (2.79) tell us that the Hugoniot has a kink at the HEL:

$$\left.\frac{d\sigma_{zz}}{dV}\right)_{\text{elastic}} = c_{11}, \tag{2.80}$$

$$\left.\frac{d\sigma_{zz}}{dV}\right)_{\text{plastic}} = \frac{1}{3}(c_{11} + 2c_{12}). \tag{2.81}$$

Since the off-diagonal elastic constant c_{12} is less than c_{11} (reflecting the fact that each normal stress is relatively weakly coupled to the 'other' normal strains), these equations tell us the gradient of the Hugoniot is steeper below the elastic limit than above. Physically, this means the crystal is *effectively* more compressible above its yield point. This is because a crystal that plastically deforms 'shares' the uniaxial compression among all three normal elastic stress components rather than loading it all onto ε^e_{zz}, meaning σ_{zz} increases more slowly for a given change in volume. Thus, the Hugoniot temporarily shallows at the HEL, as illustrated in Fig. 2.20.

What does this mean for the shock wave structure? If one eliminates U_p between the first two Rankine-Hugoniot equations [Eqs. (2.65) and (2.67)], one obtains the

following expression for U_S:

$$U_S(\sigma_{zz}) = V_0 \left(\left| \frac{\sigma_{zz} - \sigma_0}{V - V_0} \right| \right)^{\frac{1}{2}}. \tag{2.82}$$

The expression inside the modulus is the gradient of the so-called *Rayleigh line*, which connects the initial and shocked states in the stress-volume plane. Consider shock state A shown in Fig. 2.20, for which $0 < \sigma_A \leq \sigma_{\text{HEL}}$. Its speed $U_S(\sigma_A)$ is determined by the slope of the line segment OA, which will increase with shock stress (due to the tendency of c_{ij} to increase with density) until reaching a maximal value U_S^e at the HEL (labelled E), which is given by

$$U_S^e = V_0 \left(\left| \frac{\sigma_{\text{HEL}} - \sigma_0}{V_{\text{HEL}} - V_0} \right| \right)^{\frac{1}{2}}. \tag{2.83}$$

Now suppose the shock stress slightly *exceeds* the HEL. The inset of Fig. 2.20 shows that the slope of the Rayleigh line for such a shock state is less than that of the segment OE. Therefore a shock with a strength marginally exceeding the HEL actually travels slower than a weaker shock at the HEL itself. So, if a crystal is loaded to state B such that $\sigma_{\text{HEL}} < \sigma_B$, its shock wave will split into two: the crystal will first undergo elastic compression behind a shock front moving at speed U_S^e, and will then deform plastically behind a front moving at speed $U_S^p < U_S^e$ whose speed *in the rest frame of the elastically compressed material* is given by the slope of the line segment EB. This two-wave structure is shown in the right of Fig. 2.20. The region between the elastic and plastic fronts is called the *elastic precursor*.

However, if the shock stress is raised further yet, the decreasing compressibility of the crystal will cause the slope of the Rayleigh line to increase until the speed of the plastic front exceeds that of the elastic front. There therefore exists a threshold shock stress σ_{OD} above which no elastic precursor exists, and the shock wave comprises once again a single front. At the threshold, the elastic and plastic shock speeds are equal. In the frame of the elastic precursor, the elastic front travels at speed $U_S^e - U_P^e$, which, according to Eq. (2.65), is

$$U_S^e - U_P^e = \frac{V_{\text{HEL}}}{V_0} U_S^e \tag{2.84a}$$

$$= \frac{V_{\mathrm{HEL}}}{V_0} V_0 \left(\left| \frac{\sigma_{\mathrm{HEL}} - \sigma_0}{V_{\mathrm{HEL}} - V_0} \right| \right)^{\frac{1}{2}}. \tag{2.84b}$$

Equating this with the plastic wave speed calculated from the Rayleigh line, we find

$$V_{\mathrm{HEL}} \left(\left| \frac{\sigma_{\mathrm{HEL}} - \sigma_0}{V_{\mathrm{HEL}} - V_0} \right| \right)^{\frac{1}{2}} = V_{\mathrm{HEL}} \left(\left| \frac{\sigma_{\mathrm{OD}} - \sigma_{\mathrm{HEL}}}{V_{\mathrm{OD}} - V_{\mathrm{HEL}}} \right| \right)^{\frac{1}{2}}. \tag{2.85}$$

Hence, the threshold stress may be found graphically by extrapolating the Rayleigh line between the unshocked and HEL states, and finding its intersection with the Hugoniot, as shown in Fig. 2.20. A shock driven at stress $\sigma_C > \sigma_{\mathrm{OD}}$ is said to be 'overdriven', and comprises a single plastic front.

The crystals modelled in this thesis will not contain the pre-existing dislocation networks that are found in real metal samples, and must therefore rely on homogeneous nucleation to create the dislocations needed to mediate plastic flow. The shear stress required to create dislocations in a defect-free tantalum crystal is substantial (around 10 GPa [54]), meaning we should anticipate a large HEL and thus clear two-wave splitting even at shock pressures of 60 GPa or so.

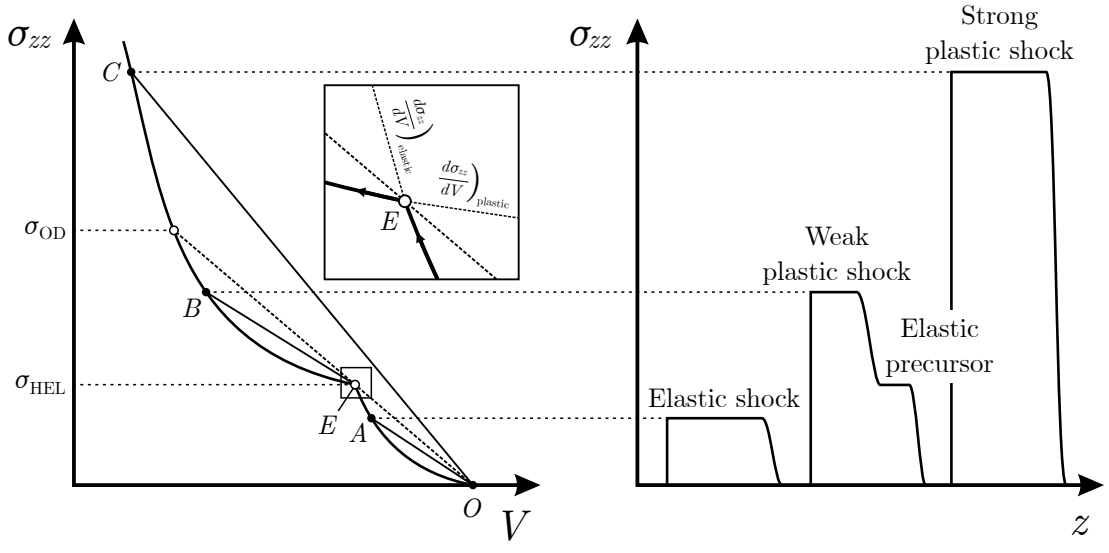

FIG. 2.20. Left: Hugoniot for a crystal with a large Hugoniot elastic limit (HEL). Inset: kink in the stress-volume relation at the yield point E. Right: stress profiles in crystals compressed to various pressures. Crystals loaded below the elastic limit to state A exhibit a purely elastic shock wave. Crystals loaded to state B between the HEL and the overdrive (OD) stress exhibit a two-wave structure comprising elastic and plastic fronts. Crystals loaded to state C above the OD stress contain only a single plastic shock wave.

2.3.4 Shock release

Clearly, a shock wave can only propagate so long as there is more material for it to travel into. When the shock wave inevitably reaches the end of the sample (at a moment referred to as *breakout*), it encounters a free surface at zero pressure that is unable to support the high stress state behind the shock. Consequently, the free surface immediately releases from the shock state and allows a counterpropagating rarefaction wave to be launched back into the sample, as illustrated in Fig. 2.21. In direct contrast to a shock, the foot of a release wave travels *behind* its faster-moving peak, causing it gradually to broaden with time. The strain rate within a release fan therefore falls with increasing distance from the free surface, allowing a wide range of strain-rate regimes to be accessed via shock release. Like a shock, a release wave can exhibit a two-wave structure in which the crystal initially releases elastically and subsequently yields. Note that it is possible to observe a two-wave structure on release even if the shock preceding it is overdriven. The study of shock release constitutes a substantial part of this thesis – the experimental and computational facets of the study will be found in Chapters 5 and 6, respectively.

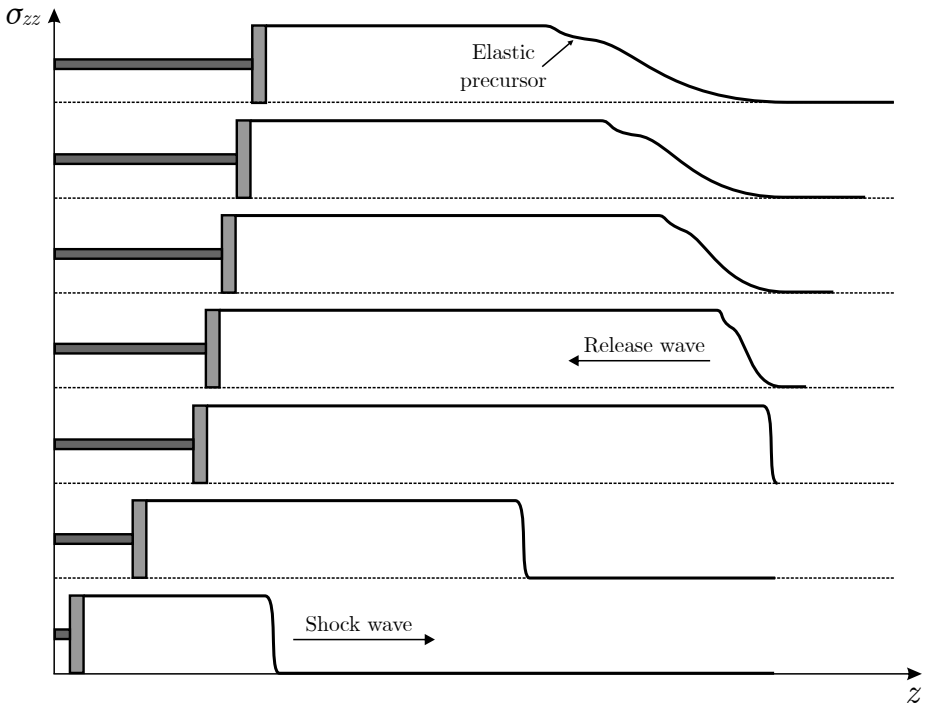

FIG. 2.21. Schematic illustration of stress profiles in a crystal undergoing shock and subsequent release back to the ambient pressure state.

2.3.5 Laser compression

For many, high-power lasers are the drive mechanism of choice for dynamic compression studies. Not only have pulsed lasers achieved the greatest laboratory pressures of any mechanism to date, but they offer the highest shot rate, and exceptional flexibility in the achievable loading paths – one can realise compression not only by a single shock, but also by multiple shocks, ramp-compression waves, and combinations thereof. The laser pulse itself acts as the 'piston', maintaining the pressure at the target's surface via a process known as laser ablation, which works as follows.

A fraction of the leading edge of the pulse is first absorbed by the target, turning its surface into a thin layer of plasma. Since laser-compression experiments are conducted under near-vacuum conditions, the incipient plasma can rapidly expand, forming a low density region between the target and the incoming beam known as a *corona*. The laser can propagate some way into this corona before it encounters a *critical surface*, beyond which the plasma's density is so high that it absorbs the beam. Most of the beam's energy is thus deposited a finite distance from the solid surface. Conduction must carry this energy from the critical surface to the target, which heats its surface and so generates more plasma, thus sustaining the ablation process. The plasma rushing away from the surface exerts a reaction force on the material below it (to conserve momentum), and it is this force that drives the shock.

A high-power laser of 'moderate' size can deliver around 10 J of energy to a drive spot of 100 μm radius within about 10 ns. The typical beam intensity on-target is

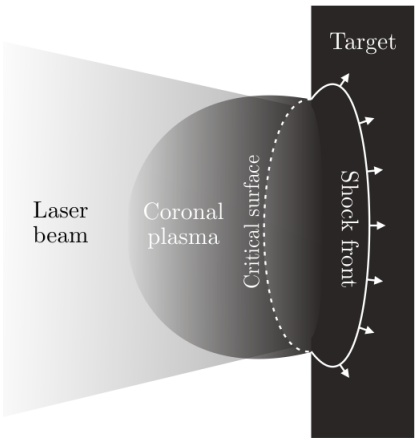

FIG. 2.22. Schematic depiction of the laser-ablation process.

thus $I = 10\ \mathrm{J}/(10\ \mathrm{ns})/[\pi \times (100\ \mu\mathrm{m})^2] \sim 10^{12}\ \mathrm{W\,cm^{-2}}$. At these intensities and above, the principle mechanism by which the plasma consumes energy from the beam is via *inverse bremsstrahlung* [99]. In this absorption regime, the pressure at the surface of a sample composed of element ${}^{\mathrm{A}}_{\mathrm{Z}}\mathrm{X}$ is predicted to scale as

$$p = p_0 \left(\frac{A}{2Z}\right)^{1/3} \left(\frac{1}{\lambda}\right)^{2/3} \left(\frac{I}{10^{14}}\right)^{2/3} \mathrm{Mbar}, \tag{2.86}$$

where I is the on-spot beam intensity in $\mathrm{W\,cm^{-2}}$, λ its wavelength in microns, and p_0 is a dimensionless prefactor thought to be 10 or so [100–102]. The attainable pressure is thus largely material agnostic, and is instead governed by the properties of the drive laser. The most commonly used laser in this field is the neodymium-glass laser, which emits near-infrared light at 1 053 nm. Plasmas tend to absorb higher-frequency radiation more efficiently, so the beam is often *frequency-doubled* with an anharmonic conversion crystal. According to Eq. (2.86), a frequency-doubled neodymium laser operating at an irradiance of at least $10^{12}\ \mathrm{W\,cm^{-2}}$ can easily generate shocks with pressures of order 1 Mbar (= 100 GPa).

2.4 Molecular dynamics

The goal of molecular dynamics and other atomistic techniques like it is to model matter at the level of its constituent particles. Such techniques are extremely versatile, as they make possible the detailed investigation of a host of microphysical processes, such as radiation damage, thin-film growth, protein folding, phase transitions, and, indeed, crystal plasticity. Clearly, the quantum-mechanical nature of matter is inescapable at the atomic level. It is well-known, however, that the complexity of the Schrödinger equation renders even its numerical solution intractable for all but the smallest of quantum systems. Molecular dynamics aims to provide a purely classical model of large collections of atoms that faithfully models their interactions, but whose computational cost is exponentially lower than its quantum equivalent. This chapter explains the basic principles underlying the molecular dynamics simulation technique.

2.4.1 Physical basis

The complete description of a crystal at the atomic level is given by its wavefunction Ψ, which in the ground state is the solution to the time-independent version of the Schrödinger equation:

$$\hat{H}\Psi(\mathbf{r}_1, \mathbf{r}_2, ..., \mathbf{R}_1, \mathbf{R}_2, ...) = E_0\Psi(\mathbf{r}_1, \mathbf{r}_2, ..., \mathbf{R}_1, \mathbf{R}_2, ...). \tag{2.87}$$

The wavefunction depends on both the electronic coordinates $\{\mathbf{r}_1, \mathbf{r}_2, ...\} = \mathbf{r}$ and on the nuclear coordinates $\{\mathbf{R}_1, \mathbf{R}_2, ...\} = \mathbf{R}$. The Hamiltonian $\hat{H}$ includes contributions from the electronic and nuclear kinetic energies, and from the ion-ion, ion-electron, and electron-electron Coulomb interactions:

$$\begin{aligned}\hat{H} = &-\sum_\alpha \frac{\hbar^2}{2M_\alpha}\nabla_\alpha^2 - \sum_i \frac{\hbar^2}{2m_e}\nabla_i^2 \\ &+ \frac{e^2}{4\pi\varepsilon_0}\Bigg(\underbrace{\sum_{\alpha,\beta>\alpha}\frac{Z_\alpha Z_\beta}{\|\mathbf{R}_\alpha - \mathbf{R}_\beta\|}}_{\text{ion-ion}} - \underbrace{\sum_{\alpha,j}\frac{Z_\alpha}{\|\mathbf{R}_\alpha - \mathbf{r}_j\|}}_{\text{ion-electron}} + \underbrace{\sum_{i,j>i}\frac{1}{\|\mathbf{r}_i - \mathbf{r}_j\|}}_{\text{electron-electron}}\Bigg),\end{aligned} \tag{2.88}$$

where m_e is the electron rest mass, and M_i and Z_i are the mass and atomic number of the i^{th} ion, respectively. Eq. (2.88) in its exact form cannot be solved, so one has to make some judicious approximations to make its solution tractable. The first and most important simplification made in almost all atomistic simulation techniques is the *Born-Oppenheimer approximation*. It recognises that since each electron is at least three orders of magnitude lighter than any of the nuclei, and therefore moves several thousand times faster, it essentially sees the ions as static. That is to say that the electrons can adapt practically instantaneously to any perturbation to the nuclear coordinates caused by (say) thermal motion, which they perceive as laughably slow. The evolution of the electron distribution can therefore be treated as being quasistatic – at any instant of time, the electrons assume the lowest-energy state for the current nuclear configuration.

In the above picture, the wavefunction Ψ can be partially separated into a nuclear

part $\phi_N(\mathbf{R})$ and an electronic part $\phi_e(\mathbf{r};\mathbf{R})$, where the latter satisfies the equation

$$\left[-\sum_i \frac{\hbar^2}{2m_e}\nabla_i^2 + \frac{e^2}{4\pi\varepsilon_0}\left(-\sum_{\alpha,j}\frac{Z_\alpha}{\|\mathbf{R}_\alpha - \mathbf{r}_j\|} + \sum_{i,j>i}\frac{1}{\|\mathbf{r}_i - \mathbf{r}_j\|}\right)\right]\phi_e(\mathbf{r};\mathbf{R}) = E_e(\mathbf{R})\phi_e(\mathbf{r};\mathbf{R}). \tag{2.89}$$

Here, the nuclear degrees of freedom $\mathbf{R}$ serve only to *parametrise* the potential landscape in which the electrons move, and thus their ground-state energy $E_e(\mathbf{R})$. The dynamics of the nuclei can in turn be calculated from their effective potential energy $E(\mathbf{R})$, which comprises their actual pairwise interaction energy *and* the energy of the electron distribution binding them together:

$$E(\mathbf{R}) = \frac{e^2}{4\pi\varepsilon_0}\sum_{\alpha,\beta>\alpha}\frac{Z_\alpha Z_\beta}{\|\mathbf{R}_\alpha - \mathbf{R}_\beta\|} + E_e(\mathbf{R}). \tag{2.90}$$

The second main approximation used in molecular dynamics is that the nuclei obey classical mechanics, i.e. their trajectories are governed by Newton's laws of motion. This approximation relies on a corollary of the *Ehrenfest theorem* stating that a particle will closely follow a classical trajectory if its wavefunction is strongly localised (which is true of sufficiently massive nuclei). Under this assumption, the position of each nucleus evolves according to

$$M_\alpha\frac{d^2\mathbf{R}_\alpha}{dt^2} = -\frac{\partial E(\mathbf{R}_1,\mathbf{R}_2,...)}{\partial\mathbf{R}_\alpha}. \tag{2.91}$$

The nuclear coordinates will henceforth be renamed $\mathbf{x}$ for consistency with the rest of the thesis.

To implement Eq. (2.91), one first needs to calculate the electronic energy function $E_e(\mathbf{x})$ by solving Eq. (2.89). Though it now only describes electrons, Eq. (2.89) is still a many-body Schrödinger equation and therefore cannot be solved exactly. It is possible to obtain good approximations for the electronic wavefunction and its associated energy using computational techniques (perhaps the most widely used of which in this field is DFT), which is exactly what is done in so-called *quantum molecular dynamics* (QMD) (see for examples the studies in Refs. [103, 104]). However, calculating the internuclear forces using quantum mechanics is not only

computationally demanding but also highly inefficient – most ions in a crystal spend most of their time displaced only slightly from their equilibrium positions, exploring only a tiny volume of the crystal's total configuration space, meaning one ends up performing very similar calculations over and over again. The third simplification employed in *classical* molecular dynamics is to approximate the potential $E(\mathbf{x})$ using analytic functions that capture the shape of the potential landscape obtained from the full quantum calculations, but can be evaluated far quicker.

2.4.2 Interatomic potentials

The accuracy of the potential energy function $E(\mathbf{x})$ governing the forces between ions is of course essential, as it encodes almost all of the crystal's physics. The simplest expression of a crystal's energy employs *pair potentials*, in which the total energy is simply a sum over the interaction energies of pairs of neighbouring ions. Perhaps the most widely known of these is the Lennard-Jones (LJ) potential, which expresses the interaction energy between two nearby neutral atoms as

$$E_{\mathrm{LJ}}(x) = \epsilon \left[\left(\frac{x_0}{x} \right)^{12} - 2 \left(\frac{x_0}{x} \right)^{6} \right], \tag{2.92}$$

where x is their separation, x_0 is their equilibrium separation in isolation, and ϵ expresses the energy required to break their bond. The LJ potential, which is pictured in Fig. 2.23, has two components: the terms which scales as $-x^{-6}$ models the relatively long-range attractive force owed in this case to the van der Waals interaction; and the repulsive x^{-12} term captures the atoms' extreme aversion to having their electron clouds forced to overlap. Though it is popular due to its computational simplicity, the LJ potential is fundamentally unsuited to modelling metals simply because it is a pair potential. It is known that crystals modelled under a pair potential always assume a close-packed structure (frequently fcc), meaning open structures like bcc tantalum are impossible to reproduce. Moreover, pair potentials identically predict that $c_{12} = c_{44}$, while for tantalum these elastic moduli appear in the ratio $c_{12}/c_{44} \approx 2$ [105], as they do for most transition metals. To accurately model metallic bonding, the potential must incorporate many-body effects.

One of the most common many-body potentials is derived from the embedded-

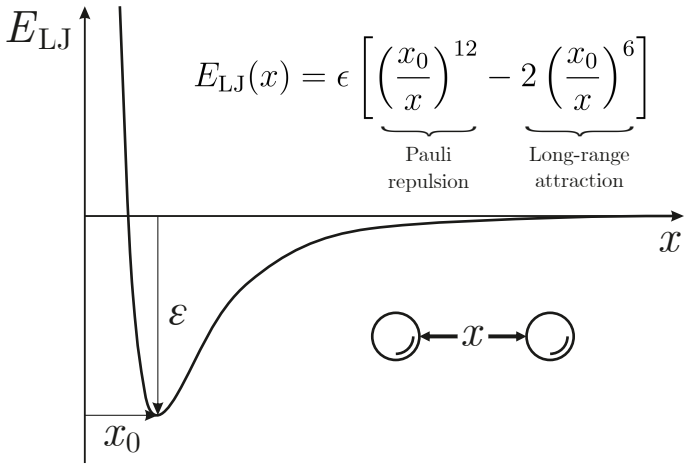

FIG. 2.23. Functional form of the pairwise Lennard-Jones potential $E_{\mathrm{LJ}}(x)$.

atom method (EAM) [106]. In the EAM scheme, the energy of ion α is expressed in the semiempirical form

$$E_{\mathrm{EAM}}(\mathbf{x}) = F(\bar{\rho}_\alpha) + \frac{1}{2}\sum_{\beta\neq\alpha} \phi(x_{\alpha\beta}), \tag{2.93}$$

where ϕ is a spherically symmetric pairwise interaction energy between α and nearby ion β (from which it is separated by distance $x_{\alpha\beta} = \|\mathbf{x}_\alpha - \mathbf{x}_\beta\|$), and F is the so-called embedding energy, which quantifies the binding energy the ion has by virtue of its being immersed in a background 'sea' of valence electrons of local density $\bar{\rho}_\alpha$, with which it varies nonlinearly. This density is in turn expressed as a sum of contributions from nearby atoms within some appropriately chosen cutoff radius:

$$\bar{\rho}_\alpha = \sum_{\beta\neq\alpha} w(x_{\alpha\beta}); \tag{2.94}$$

The function $w(r)$ thus gives the electron density a distance r from each ion. For high-pressure applications where experimental data may be scarce, the functions F, ϕ, and w are frequently fitted to structural data obtained from DFT calculations, as was the case for the Ravelo EAM potentials used to model tantalum throughout this thesis [54]. While more costly than the LJ potential, EAM potentials are still relatively computationally cheap, and are therefore suitable for application to large-scale MD simulations that may involve many millions of atoms.

2.4.3 Integration scheme

The classical equation of motion governing the trajectory of each atom cannot be solved analytically due to the sheer number of interactions it participates in, meaning its motion must be calculated numerically. To this end, many classical molecular dynamics codes use the *velocity Verlet algorithm*, an integration scheme that explicitly evaluates both atomic positions and velocities. To recap, the acceleration experienced by ion α is given by

$$\mathbf{a}_\alpha(t) = -\frac{1}{M_\alpha}\frac{\partial E[\mathbf{x}(t)]}{\partial \mathbf{x}_\alpha}, \tag{2.95}$$

which can be evaluated if the crystal's configuration $\mathbf{x}$ at time t is known. The position of each ion after a small increment of time δt is calculated simply using the first few terms of the Taylor expansion, which read

$$\mathbf{x}_\alpha(t+\delta t) = \mathbf{x}_\alpha(t) + \frac{d\mathbf{x}_\alpha(t)}{dt}\delta t + \frac{1}{2}\frac{d^2\mathbf{x}_\alpha(t)}{dt^2}(\delta t)^2 + \mathcal{O}(\delta t^3) \tag{2.96a}$$

$$= \mathbf{x}_\alpha(t) + \mathbf{v}_\alpha(t)\delta t + \frac{1}{2}\mathbf{a}_\alpha(t)(\delta t)^2 + \mathcal{O}(\delta t^3). \tag{2.96b}$$

Applying a similar expansion to the velocity yields

$$\mathbf{v}_\alpha(t+\delta t) = \mathbf{v}_\alpha(t) + \mathbf{a}_\alpha(t)\delta t + \frac{1}{2}\frac{d\mathbf{a}_\alpha(t)}{dt}(\delta t)^2 + \mathcal{O}(\delta t^3). \tag{2.97}$$

The jerk $\dot{\mathbf{a}}_\alpha(t)$ is not evolved explicitly by the algorithm, but can be calculated on-the-fly using

$$\mathbf{a}_\alpha(t+\delta t) = \mathbf{a}_\alpha(t) + \frac{d\mathbf{a}_\alpha(t)}{dt}\delta t + \mathcal{O}[(\delta t)^2], \tag{2.98}$$

where $\mathbf{a}_\alpha(t+\delta t)$ can be estimated by substituting the extrapolated coordinates $\mathbf{x}_\alpha(t+\delta t)$ into Eq. (2.95) for the acceleration. Substituting this into Eq. (2.97) gives

$$\mathbf{v}_\alpha(t+\delta t) = \mathbf{v}_\alpha(t) + \mathbf{a}_\alpha(t)\delta t + \frac{1}{2}\left[\frac{\mathbf{a}_\alpha(t+\delta t) - \mathbf{a}_\alpha(t)}{\delta t}\right](\delta t)^2 + \mathcal{O}[(\delta t)^3] \tag{2.99a}$$

$$= \mathbf{v}_\alpha(t) + \frac{1}{2}\left[\mathbf{a}_\alpha(t) + \mathbf{a}_\alpha(t+\delta t)\right] + \mathcal{O}[(\delta t)^3]. \tag{2.99b}$$

Together, the three equations approximating the trajectories read

$$\mathbf{x}_\alpha(t+\delta t) = \mathbf{x}_\alpha(t) + \mathbf{v}_\alpha(t)\delta t + \frac{1}{2}\mathbf{a}_\alpha(t)(\delta t)^2, \tag{2.100a}$$

$$\mathbf{a}_\alpha(t+\delta t) = -\frac{1}{M_\alpha}\frac{\partial E[\mathbf{x}(t+\delta t)]}{\partial \mathbf{x}_\alpha}, \tag{2.100b}$$

$$\mathbf{v}_\alpha(t+\delta t) = \mathbf{v}_\alpha(t) + \frac{1}{2}\left[\mathbf{a}_\alpha(t) + \mathbf{a}_\alpha(t+\delta t)\right]\delta t. \tag{2.100c}$$

Note that the values of $\mathbf{a}_\alpha(t+\delta t)$ are stored and used for $\mathbf{a}_\alpha(t)$ on the next iteration.

The velocity Verlet algorithm is often chosen for MD applications as it tends to conserve energy well over long time periods, and it only requires one expensive force calculation per iteration. The limiting factor in all numerical algorithms is the choice of timestep δt, which must be small enough that truncation errors do not accrue too quickly, but large enough that one does not require too many iterations to reach the desired simulation duration. Shock simulations are unforgiving in this regard because of the steep velocity gradient at the shock front – if δt is too large, atoms moving close to U_P just behind the front will move far too close to the stationary atoms ahead of them before the repulsive force they exert on one another can register. On the next timestep, their extreme proximity will cause them to exert enormous forces on one another, causing them to fly apart and 'blow up' the crystal. To avoid this, the timestep is typically restricted to no more than one femtosecond for shock applications, which is what will be used throughout this thesis.

2.4.4 Ensembles

Applied as is, the integration scheme described in the previous section simulates a system drawn from the *microcanonical ensemble*. That is, the crystal's particle number (N), volume (V), and energy (E) are conserved (the latter to within numerical precision, at least). These are often the most appropriate conditions for shock compression simulations, the purpose of which is to recreate the response of material embedded deep within a much larger pressurised sample that prevents its volume from changing, over timescales too short for significant thermal conduction to occur. Even so, reference will occasionally be made in this thesis to other ensembles (e.g. NVT, NPT) that are helpful when establishing the crystal's initial pressure and

temperature conditions before the simulation proper begins.

Temperature control is possible with the aid of a *Nosé-Hoover thermostat*. In this scheme, a viscosity-like term is appended to each ion's equation of motion whose magnitude and sign is coupled to the system-wide temperature T:

$$M_\alpha \frac{d\mathbf{v}_\alpha(t)}{dt} = -\frac{\partial E[\mathbf{x}(t)]}{\partial \mathbf{x}_\alpha} - M_\alpha \gamma(t)\mathbf{v}_\alpha(t), \tag{2.101}$$

$$\frac{d\gamma(t)}{dt} = \frac{3Nk_B}{Q}\left(T - T_0\right). \tag{2.102}$$

If the current temperature exceeds the target temperature T_0, the friction coefficient γ grows in magnitude and thus drains kinetic energy from the system, decreasing its temperature. Conversely, the thermostat acts so as to propel the ions if $T < T_0$. The parameter Q expresses the 'inertia' of the thermal bath with which the system is effectively in contact, and thus controls the timescale over which the temperature relaxes. It can be shown formally that the Nosé-Hoover thermostat produces a system whose trajectory is consistent with the *canonical* (or NVT) ensemble [107]. An analogous barostat can be simultaneously defined that couples each ion's coordinates to the current pressure in order to steer the system towards a desired stress state, and thus sample instead from the NPT ensemble.

An alternative means of controlling the crystal's temperature is via a *Langevin thermostat*. Here, the crystal is placed in contact not with a heat bath but with a kind of solvent with which it makes collisions. The equation of motion of ion α is amended to

$$M_\alpha \frac{d\mathbf{v}_\alpha(t)}{dt} = -\frac{\partial E[\mathbf{x}(t)]}{\partial \mathbf{x}_\alpha} - \Gamma\mathbf{v}_\alpha(t) + S(t), \tag{2.103}$$

where Γ is a damping constant, and S is a stochastic driving force whose statistics are such that

$$\langle S(t)\rangle = 0, \tag{2.104}$$

$$\langle S(t)S(t')\rangle = 2\Gamma k_B T_0\, \delta(t - t'). \tag{2.105}$$

The ratio of the damping and driving terms is such that the crystal will eventually reach the target temperature T_0.

2.4.5 The LAMMPS code

All MD simulations presented in this thesis were performed using LAMMPS (the Large-scale Atomic/Molecular Massively Parallel Simulator) developed at Sandia National Laboratories [108]. The code allows molecular systems comprising millions of atoms to be simulated by using a great number of processors working in parallel, each of which is responsible for evolving the trajectories of a subset of atoms.

The input to LAMMPS is a script containing a list of high-level commands. The essential commands are those reflecting the three key ingredients of any MD code: one needs to create a set of atoms to simulate, which means specifying a list of initial positions and velocities; one needs to choose an interatomic potential to simulate their interactions; and one needs to define a numerical integration scheme (LAMMPS uses velocity Verlet by default) and its timestep (1 fs for our purposes) to advance the atomic coordinates through time. Other commands might include: specification of the system's boundary conditions, which determines how atoms at the periphery of the simulation box behave; the mechanism used to shock-compress the system; or the physical variables the program should write out, and how often to do so.

The output of LAMMPS may consist of any number of microscopic or macroscopic quantities. The safest approach to MD (that is, the approach that minimises the chances of one's having to repeat a very computationally expensive simulation) is periodically to write a file containing the current coordinates, velocities, forces, and so on, of every atom in the system. This way, one retains all information about the system at the chosen timesteps, and one can derive any property of the crystal one wants. It is this post-processing step that is the difficult part of MD – how does one convert millions of lines of atomic properties into meaningful information? The number of analysis techniques employed in this thesis is enough to warrant a separate discussion, which can be found in the next chapter.

CHAPTER 3

Analysis methods for molecular dynamics simulations

3.1 Introduction

It is essential to be able to translate the output of molecular dynamics simulations (which typically takes the form of many millions of lines of per-atom variables) into macroscopic observables from which meaningful predictions or comparisons with experiment can be made. In this regard, the inherently microscopic description given by molecular dynamics, and other atomistic methods like it, is both a blessing and a curse. In one sense, one knows absolutely everything about the modelled system, insofar as one knows the precise position and velocity of every one of its constituent atoms at every instant of time; and in another sense, one knows nothing, in that anything of which one could conceivably make an experimental measurement must be derived from these phase-space coordinates. Calculation of these observables ranges in difficulty from fairly painless (for e.g. density and temperature) to surprisingly complicated (for e.g. plastic strain and dislocation density). In any case, getting information out of MD requires more work on the user's part (or perhaps on the part of a benevolent developer) than for many other, higher–length-scale simulation techniques. Critical reviews of the most popular postprocessing techniques in use today may be found in Refs. [109–111].

In this chapter, the methods used here to convert the atomistic data yielded by MD into useful information will be presented. Note that the methods are categorised according to their usage in this thesis, and it should be appreciated that many of them can actually serve multiple functions – for instance, the Fourier transform will eventually be used here to infer the crystal's elastic strain state, but reciprocal-space techniques can also yield information about crystal reorientation [53, 57], melting behaviour [52], and stacking fault density [112]. In the final part of the chapter, every method described will be used to interrogate a small block of tantalum undergoing

controlled uniaxial compression until it yields plastically, in order to provide a central resource where every technique can be seen in action.

3.2 Temperature

The temperature of an atomistic configuration can be derived most easily by invoking the equipartition theorem [113]. The theorem states that for an equilibrium classical system with Hamiltonian H, the following relation holds for any pair of degrees of freedom, X_m and X_n:

$$\left\langle X_m \frac{\partial H}{\partial X_n} \right\rangle = \delta_{mn} k_B T. \tag{3.1}$$

Here, the $\langle \cdot \rangle$ operator denotes an ensemble average. For an isolated monatomic crystal modelled under the microcanonical ensemble, the Hamiltonian reads

$$H = \sum_{\alpha=1}^{N} \frac{1}{2} m \mathbf{v}_\alpha^2 + E(\mathbf{x}), \tag{3.2}$$

where the former term is just the sum of the atoms' kinetic energies, and the latter is their total interatomic potential energy, which depends only on their positions. When applied to the i^{th} component of atom α's velocity, Eqs. (3.1) and (3.2) yield

$$m\langle [\mathbf{v}_\alpha]_i^2 \rangle = k_B T. \tag{3.3}$$

Evaluating the ensemble average of $[\mathbf{v}_\alpha]_i^2$ for a given atom (which, according to the ergodic hypothesis, can be realised simply by time-averaging its trajectory over a sufficiently long period) may be inconvenient if one wishes to track the evolution of T over the short timescales ($\sim$ ps) characteristic of the shock regime. As a workaround, the single-particle time average is commonly replaced by an instantaneous average over a local group of atoms:

$$\langle \cdot \rangle \to \frac{1}{M} \sum_{\alpha=1}^{M} \cdot \,. \tag{3.4}$$

The idea is that every atom within a macroscopically homogeneous volume has the same velocity distribution, but is at a different stage in its trajectory. Thus, by sampling a set of atomic velocities at an instant of time, one is effectively sampling

the same distribution at many different moments, and is thus, by proxy, performing a time average. The greater the number of particles sampled (M), and the more components of velocity exploited, the more accurate one's estimate of T becomes. Usually, Eq. (3.3) would be applied to all three velocity components and combined:

$$T = \frac{m}{3Mk_B} \sum_{\alpha=1}^{M} \mathbf{v}_\alpha^2. \tag{3.5}$$

However, to avoid having to worry about correcting for the centre-of-mass longitudinal velocity component (U_P) introduced by shock compression, the temperatures quoted throughout this thesis will be calculated using only the transverse velocities:

$$T = \frac{m}{2Mk_B} \sum_{\alpha=1}^{M} \left([\mathbf{v}_\alpha]_x^2 + [\mathbf{v}_\alpha]_y^2 \right). \tag{3.6}$$

The similarity of this 'two-dimensional temperature' and the traditional temperature given by Eq. (3.5) has been verified on crystals with temperatures up to 3000 K.

3.3 Stress

The virial theorem states that for a stable mechanical system (i.e. one whose binding forces are strong enough to keep its constituent particles confined to some finite volume V), the following relations hold for $i, j = x, y, z$:

$$\left\langle \sum_{\alpha=1}^{N} [\mathbf{x}_\alpha]_i [\mathbf{f}_\alpha]_j \right\rangle + 2 \left\langle \sum_{\alpha=1}^{N} \frac{1}{2} m [\mathbf{v}_\alpha]_i [\mathbf{v}_\alpha]_j \right\rangle = 0, \tag{3.7}$$

where $\mathbf{f}_\alpha$ is the total force acting on atom α. By separating the per-atom force $\mathbf{f}_\alpha$ into contributions from neighbouring atoms and from a confining boundary enclosing the system [114], the virial theorem can be used to show that the macroscopic stress tensor σ reads

$$\sigma_{ij} = \frac{1}{V} \left[\left\langle \sum_{\alpha=1}^{N} m [\mathbf{v}_\alpha]_i [\mathbf{v}_\alpha]_j \right\rangle + \frac{1}{2} \left\langle \sum_{\alpha=1}^{N} \sum_{\beta \neq \alpha} [\mathbf{x}_{\alpha\beta}]_i [\mathbf{f}_{\alpha\beta}]_j \right\rangle \right], \tag{3.8}$$

where $\mathbf{f}_{\alpha\beta}$ is the force exerted on atom α by atom β, and $\mathbf{x}_{\alpha\beta}$ is their relative displacement. The virial stress comprises two parts: the first is a kinetic, gaslike component that captures the momentum conveyed by the particles as they oscillate and recoil from one another; and the second is a potential, solidlike stress that accounts for the average interaction force each particle exerts on those nearby it due to their proximity. As one might expect, the latter stress dominates in a shocked crystal – for instance, when tantalum is loaded to 100 GPa, only 1% of that pressure is owed to the thermal, gaslike component.

The formulation of the macroscopic stress given by Eq. (3.8) naturally leads to the definition of the widely used and more versatile per-atom virial stress tensor σ_α:

$$\sigma_\alpha = \frac{1}{\Omega_\alpha}\left[m(\mathbf{v}_\alpha \otimes \mathbf{v}_\alpha) + \frac{1}{2}\sum_{\beta\neq\alpha}(\mathbf{x}_{\alpha\beta} \otimes \mathbf{f}_{\alpha\beta})\right], \tag{3.9}$$

where Ω_α is the volume occupied by the atom (which can be calculated from the Voronoi tessellation, see Sec. 3.4.1). Defined this way, the stress within any region is related to the stresses experienced by its constituent atoms by $\sigma = \langle \frac{1}{V}\sum_\alpha \Omega_\alpha \sigma_\alpha \rangle$, which reduces intuitively to $\langle \frac{1}{N}\sum_\alpha \sigma_\alpha \rangle$ if every atom occupies the same volume $\Omega = V/N$. As with temperature, care must be taken to exclude any centre-of-mass velocity components from Eq. (3.9), which would yield spurious results [115]. For this reason, the gaslike stress component will be calculated using the two-dimensional temperature defined in Eq. (3.6).

3.4 Strain

3.4.1 Voronoi analysis

The Voronoi decomposition of an atomistic configuration partitions the volume it occupies into a set of tessellating polyhedra called Voronoi cells. Within each cell is contained exactly one atom, and that cell constitutes the locus of points that are closer to that atom than to any other. The shape of the polyhedron enclosing each atom characterises completely the arrangement of its neighbours, and can therefore be used (after being distilled into a small set of characteristic numbers, like the

number of faces or vertices the cell has, the number of faces with exactly five edges, and so on) to identify the local crystal structure [116–118]. Here, the Voronoi tessellation will be used to calculate the effective volume Ω_α occupied by each atom [which may be used to calculate the virial stress using Eq. (3.9)], and, by extension, the volume $V = \sum_\alpha \Omega_\alpha$ occupied by extended groups of atoms, from which the volumetric strain suffered by the crystal can be deduced. All decompositions here were performed with the open-source code VORO++ by Rycroft [119].

3.4.2 Elastic deformation gradient

In the shock regime, where crystals are expected to show considerable strength, it is essential to be able to measure not only total volumetric strain, but also individual components of strain suffered along each axis of the unit cell. To this end, one can employ the per-atom elastic deformation gradient F^e_α. It may be defined as the linear operator that maps some atom α's neighbour vectors in an ambient, stress-free state onto its neighbour vectors following deformation, as illustrated in Fig. 3.1:

$$F^e_\alpha \mathbf{R}_{\alpha\beta} = \mathbf{x}_{\alpha\beta}. \tag{3.10}$$

In other words, if $\mathbf{x}_{\alpha\beta}$ is the vector joining atom α to neighbouring atom β after deformation has taken place, then $\mathbf{R}_{\alpha\beta}$ would be the displacement of atom β from α if one relaxed all stresses on the crystal. To calculate F^e_α, one requires at least three independent equations of the form above, each of which will provide three constraints on the nine elements of F^e_α. For instance, if one knows the position of three neighbouring atoms (labelled by $\beta = 1, 2, 3$) and their ambient displacements, one can express three such vector equations simultaneously via the matrix equation

$$F^e_\alpha \begin{pmatrix} \mathbf{R}_{\alpha 1} & \mathbf{R}_{\alpha 2} & \mathbf{R}_{\alpha 3} \end{pmatrix} = \begin{pmatrix} \mathbf{x}_{\alpha 1} & \mathbf{x}_{\alpha 2} & \mathbf{x}_{\alpha 3} \end{pmatrix}, \tag{3.11}$$

where $(\mathbf{u} \quad \mathbf{v} \quad \mathbf{w})$ is the 3×3 matrix whose columns are the vectors $\mathbf{u}$, $\mathbf{v}$, and $\mathbf{w}$. This equation is sufficient to determine uniquely F^e_α:

$$F^e_\alpha = \begin{pmatrix} \mathbf{x}_{\alpha 1} & \mathbf{x}_{\alpha 2} & \mathbf{x}_{\alpha 3} \end{pmatrix} \begin{pmatrix} \mathbf{R}_{\alpha 1} & \mathbf{R}_{\alpha 2} & \mathbf{R}_{\alpha 3} \end{pmatrix}^{-1}. \tag{3.12}$$

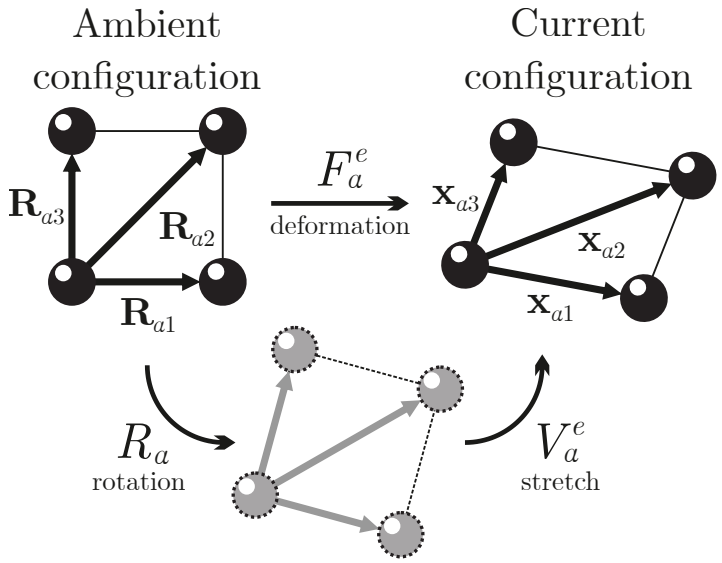

FIG. 3.1. Transformation of atom α's nearest-neighbour vectors under the action of elastic deformation gradient F_α^e. Shown also is its polar decomposition, in which the unit cell passes through an intermediate state via a rotation R_α followed by an elastic stretch V_α^e.

Depending on which of atom α's neighbours one uses in Eq. (3.12), one may obtain slightly different results due to effects that cause F_α^e to be nonaffine, like sharp strain gradients or thermal fluctuations. To mitigate such effects, F_α^e will be taken as the arithmetic mean of all possible elastic deformation gradients calculable from α's 14 nearest and next-nearest neighbours, of which 232 exist for a bcc crystal.

The elastic deformation gradient encodes information about not only the pure strains applied to the unit cell, but also its reorientation. To deconvolve these two effects, one can calculate a polar decomposition of F_α^e. The decomposition used throughout this thesis reads

$$F_\alpha^e = V_\alpha^e R_\alpha, \tag{3.13}$$

where R_α is the rotation matrix, and the symmetric matrix V_α^e is the so-called left stretch tensor. The engineering elastic strain in the computation cell basis is related trivially to the stretch tensor by $e_\alpha^e = V_\alpha^e - I$, which may then be converted to the true, compressive elastic strain via $\varepsilon_\alpha^e = -\ln(1 + e_\alpha^e)$. The per-atom elastic strain can then be volume-averaged in order to calculate the macroscopic elastic strain state ε^e of any given region of interest. For the majority of this thesis (until Chapter 6), the e-superscript will be dropped, as elastic strain is generally the only type of strain to which explicit reference will be made.

To implement Eq. (3.10) for the elastic deformation gradient, two preliminary steps are required. First, one must exclude from the computation defective atoms (i.e. those that do not retain a crystalline environment after shock loading) for which F_α^e cannot uniquely be defined. Sec. 3.5.1 describes the adaptive common neighbour analysis routine used to identify and reject noncrystalline material before the calculation begins. Second, one must have a consistent means of assigning to each of α's current neighbours an ideal neighbour vector, i.e. of assigning to each $\mathbf{x}_{\alpha\beta}$ an $\mathbf{R}_{\alpha\beta}$. A description of the template matching technique used to do so can be found in Sec. 3.5.5.

3.4.3 The Fourier transform

In the shock-compression experiments performed at facilities like LCLS, one does not have direct access to the target's atomic coordinates as one does in MD. One can, however, observe a slice of its *reciprocal* lattice by using x-ray diffraction. If the wavevector of the incident x-ray beam is $\mathbf{k}_0$, the diffraction intensity from a monatomic target at wavevector $\mathbf{k}$ is proportional to the intensity of its reciprocal lattice at the point $\mathbf{q} = \mathbf{k} - \mathbf{k}_0$, which is just the modulus of its Fourier transform:

$$|F(\mathbf{q})|^2 = \left| \sum_{\alpha=1}^{N} e^{-i(\mathbf{k}-\mathbf{k}_0)\cdot\mathbf{x}_\alpha} \right|^2 . \tag{3.14}$$

Given a crystal's reciprocal-space representation, it is possible to infer its elastic strain state using the fact that the reciprocal lattice vectors $\{\mathbf{G}_i\}$ at which $I(\mathbf{q}) = |F(\mathbf{q})|^2$ is maximal transform according to $\mathbf{G}_i \to [(F^e)^T]^{-1}\mathbf{G}_i$ [120]. This reasoning can be applied just as well to a real crystal as to a synthetic one modelled using MD, whose reciprocal-space intensity can be calculated directly from its atomic coordinates using Eq. (3.14).

The work in this thesis is strongly motivated by the desire to understand how fibre-textured polycrystals respond to shock compression. A fibre texture is one for which every grain has a particular axis (in our case, [011]) closely aligned with a common direction called the fibre axis, but whose orientation around this direction is distributed approximately randomly. To simulate and then calculate synthetic

diffraction data from a true polycrystalline aggregate is often prohibitively expensive. In Ref. [121], fibrelike x-ray diffraction patterns were generated from simulations of a single crystal by first calculating its scattering intensity in reciprocal space, and then rotating the pattern around the z axis and continuously integrating up the result to emulate diffraction from an axially symmetric polycrystal. This hugely relaxes the computational requirements to simulate a full pattern, but not enough for the hundred-million-atom simulations performed here. For this reason, we will opt not to integrate numerically the scattering intensity around z, but to integrate analytically the scattering *amplitude*. The expression for this fibre-texture Fourier transform (FTFT) (a full derivation of which is given in Appendix A) reads

$$F_{\mathrm{FT}}(\mathbf{q}) \propto \sum_{\alpha} J_0\left(q_\rho \rho_\alpha\right) e^{-iq_z z_\alpha}, \tag{3.15}$$

where $q_\rho = \sqrt{q_x^2 + q_y^2}$ and $\rho_\alpha = \sqrt{x_\alpha^2 + y_\alpha^2}$ are effectively radial coordinates, and J_0 is the zeroth-order Bessel function of the first kind. Physically, the expression above is obtained by imagining that every atom in the original grain is swept around the z axis into a continuous ring of atoms – this is the atomistic configuration that would result if all of the grains in a fibre-textured polycrystal directly overlapped. The FTFT is therefore only an approximation of the real diffraction signal. However, it is also only slightly more expensive than the plain Fourier transform $\sum_\alpha \exp(-i\mathbf{q}\cdot\mathbf{r}_\alpha)$. It has further been confirmed that the locations of the Bragg peaks for homogeneously strained crystals predicted by the FTFT coincide with the locations predicted by geometrically solving the Laue condition.

3.5 Defects

3.5.1 Common neighbour analysis

Common neighbour analysis (CNA) [122] is one of the most frequently used methods for identifying the local structure of an atomistic configuration. The central idea is as follows: first, take the atom under consideration and find all of its neighbours; then, for one of those neighbouring atoms, identify *its* neighbours; next, find all the

atoms that are common to both neighbour lists; finally, extract from those common neighbours a set of indices that characterise the nature of their bonding. Such indices might include the total number of common neighbours, the number of bonds that exist between them, or the longest chain of bonded atoms that can be formed among them. Taken together, these indices give a 'fingerprint' that is unique to each crystal structure. CNA can thus separate a crystal into its various phases, or, as will be done here, distinguish crystalline from defective material. Fig. 3.2 illustrates what a crystal visualised using CNA might look like.

The one free parameter in the CNA routine is the cutoff radius r^{cut}, or the maximum separation two atoms can have and still be considered 'bonded'. In order that the method be robust to the large changes in density that shock compression and release can cause, this cutoff radius should be chosen for each atom individually based on the density of its environment. To do so, one can first infer the local lattice constant a_α using the displacements of the atoms nearest α. The expression appropriate for a bcc crystal reads

$$a_\alpha = \frac{1}{14}\left(\sum_{\beta=1}^{8}\frac{2}{\sqrt{3}}\|\mathbf{x}_{\alpha\beta}\| + \sum_{\beta=9}^{14}\|\mathbf{x}_{\alpha\beta}\|\right). \tag{3.16}$$

The first sum runs over the 8 nearest neighbours in the 1$^{\text{st}}$ coordination shell (displaced on average by $\|1/2\,\langle 111\rangle\| = \sqrt{3}/2\,a_\alpha$), while the second sum accounts for the 6 next-nearest neighbours in the 2$^{\text{nd}}$ coordinate shell (displaced by $\|\langle 100\rangle\| = a_\alpha$). The cutoff is then placed between the 2$^{\text{nd}}$ and 3$^{\text{rd}}$ shells, i.e. $r_\alpha^{\text{cut}} = 1/2\,(1+\sqrt{2})a_\alpha$. This technique is known as adaptive common neighbour analysis (a-CNA) [109]. By dynamically calculating r^{cut} in this way, one can filter defective atoms from shock-compressed or shock-releasing crystals without needing to manually select a cutoff to suit the pressure-dependent density.

CNA is known to fail at temperatures approaching the (pressure-dependent) melt temperature T_M, where it frequently misidentifies crystalline material as defective due to the sporadic breaking of bonds caused by strong thermal fluctuations [117]. In this thesis, CNA will only be applied to crystals for which $T < 0.5\,T_M$.

3.5.2 Cluster analysis

Once a population of atoms has been divided into those that are crystalline and those that are defective, bonded groups of atoms of the same species can be identified. A deformation twin, for instance, comprises a group of hundreds or perhaps thousands of crystalline atoms separated from its host by planes of defective atoms that constitute the twin boundaries. A twin therefore constitutes a single 'cluster' of nondefective atoms. Similarly, the core of an isolated dislocation loop is formed of a long chain of connected defective atoms immersed entirely in a nondefective host, and so constitutes a single 'cluster' of a different sort. Cluster analysis allows one rapidly to separate an atomistic configuration into its component grains, twins, and other defect structures, making the crystal far easier to analyse and visualise.

In this thesis, cluster analysis will be used to identify and (very approximately) enumerate vacancy defects. If one generates a population spectrum of the clusters in a shock-loaded crystal, point defects like vacancies or self-interstitials, and indeed any aggregates thereof, tend to be found in the range of roughly 10 to 100 atoms. A single vacancy defect in a bcc crystal, for instance, comprises a connected group of

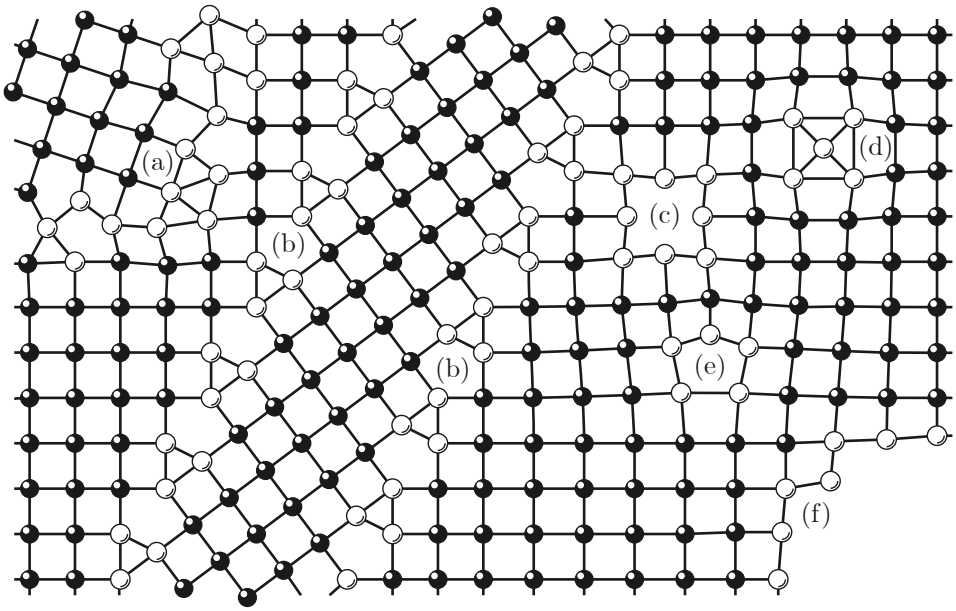

FIG. 3.2. A highly defective crystal viewed using CNA. Atoms whose environments are inconsistent with any anticipated crystal structure are deemed defective, and coloured white. CNA thus reveals the presence of (a) grain boundaries, (b) twin boundaries, (c) point vacancies, (d) interstitials, (e) dislocations, and (f) free surfaces.

14 defective atoms surrounding an empty lattice site, whereas a divacancy may be formed of between 28 atoms (two single vacancy clusters tangentially touching) and 22 atoms (for a true divacancy comprising two adjacent empty sites). These vacancies are easily distinguished from other, far larger defect structures like dislocations, twin boundaries, and grain boundaries, which consist of hundreds to thousands of connected noncrystalline atoms. One can exploit this 'stratification' of the cluster population spectrum to identify the vacancies in an atomistic configuration without actually needing to verify that empty lattice sites are present. If the number of defective clusters containing n atoms is $C(n)$, the vacancy count is approximately

$$N_v \approx C(14) + \sum_{n=15}^{n_{\max}} \left\lceil \frac{n}{14} \right\rceil C(n), \tag{3.17}$$

where $n_{\max}$ is an upper limit taken to be around 100 or so. All of the clusters comprising 39 defective atoms, for example, would be interpreted as 3 marginally interpenetrating vacancy clusters comprising 14 defective atoms each, and would thus contribute $\lceil 39/14 \rceil C(39) = 3\,C(39)$ vacancies to N_v. This method is crude, and will generally underestimate the number of vacancies present, because any vacancy attached to a much larger defective structure like a dislocation network is 'absorbed' into its associated cluster, and thus evades detection. However, it is also fast, and is adequate for the purposes of this thesis.

It is noted that the vacancy-counting method described above cannot actually distinguish vacancies from other point defects, such as self-interstitials, which also comprise clusters of ten defective atoms or so. The reason Eq. (3.17) is referred to as a 'vacancy' count is because vacancies tend to be far more abundant than interstitials under the loading conditions considered in this thesis. The underlying physical reason for this asymmetry will be addressed in Chapter 6.

3.5.3 Dislocation extraction algorithm

Once a crystal has been partitioned into clusters, a surface of 'interface atoms' can be constructed that separates the defective atoms from their crystalline host, and thus encloses entirely the crystal's defect content. The dislocation extraction algorithm

(DXA) [123, 124] is a routine that locates and characterises full dislocations by searching for the thin, tubelike parts of this interface. The algorithm first constructs a circuit around one such tube by joining together atoms on the interface; if the narrow defect enclosed by the tube is a true dislocation, the vector sum of the crystallographic vectors joining the atoms in the loop is non-zero, and yields the dislocation's Burgers vector. The Burgers circuit can then be swept along the tube, allowing the dislocation line it encloses to be traced out and stored in an array. The DXA can thus create an explicit line representation of a dislocation network within an atomistic configuration. In this thesis, the DXA will be used mainly to calculate the dislocation density ρ_v as a function of time, though a sample visualisation of a dislocation network will be shown in Sec. (3.6).

3.5.4 Slip vector analysis

The DXA provides a time-resolved picture of the dislocation content of a crystal. Slip vector analysis (SVA) is a complementary technique (originally formulated by Zimmerman *et. al.* in the context of nanoindentation [125]) that allows one to view the slip planes, stacking faults and twins 'traced out' by dislocations as they propagate. This is achieved by identifying atoms whose neighbours have suffered permanent displacement from their original sites in the unit cell, i.e. those that have participated in a plastic flow event. The displacement vectors of the neighbours may be used to infer the Burgers vector of the dislocation responsible, while its plane(s) of motion may be determined by visualising the structure formed by the slipped atoms. In brief, the algorithm used here first generates a 'heatmap' of the displacement vectors (whose maxima will be located at the Burgers vectors of the dislocations generated on compression), and then assigns atoms to slip or twin planes according to which of these maxima their particular neighbour displacements are found close to.

To illustrate the principle of SVA, Fig. 3.3(a) shows a bcc crystal that has undergone plastic flow on nearby $(\bar{2}11)$ planes. Two atoms are highlighted: atom s, which is located in proximity to a slip plane; and atom t, found in a twin. Each atom is distinguished by the particular combination of displacements of its eight nearest neighbours. For atom s, three neighbours are displaced by $1/2\,[111]$, while

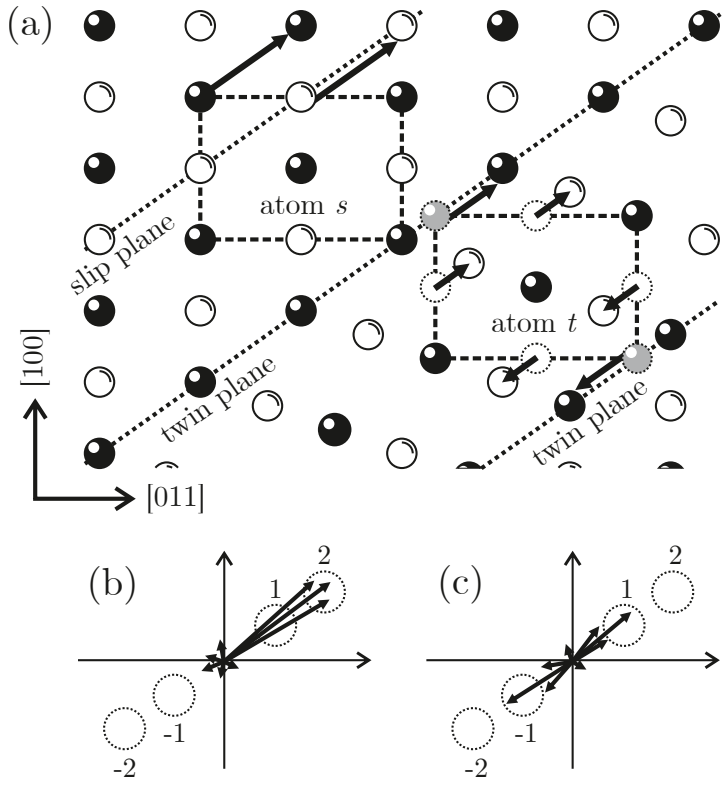

FIG. 3.3. Slip signatures for atoms in proximity to slip and twin events. (a) shows an ideal bcc crystal viewed along the $[01\bar{1}]$ direction. Black and white atoms belong to separate $(01\bar{1})$ planes. Atom s is located on a slip plane, atom t in a twin. Arrows indicate the change in displacement of each atom's eight nearest neighbours following compression. (b) and (c) show these same changes (plus thermal noise) centred on a common origin for atoms s and t respectively. Each atom is characterised by the bins (labelled ± 1 and ± 2) into which their neighbour displacements fall.

five suffer only thermal displacement. For atom t, two neighbours are displaced by $\pm 1/3\,[111]$, four by $\pm 1/6\,[111]$ and two by [000]. With these signatures, one can identify the slip or twin event in which the atom has participated.

In traditional SVA, the displacements of the central atom's neighbours are collapsed into a single metric called the slip vector $\mathbf{s}_\alpha \propto \sum_\beta \mathbf{u}_{\alpha\beta}$, where $\mathbf{u}_{\alpha\beta}$ is the displacement suffered by neighbour β in the frame of α, the central atom. While this step simplifies the resultant signature by reducing its dimensionality, it also renders the method unable to detect atoms located in deformation twins, for which $\mathbf{s}_\alpha$ vanishes. This issue will be circumvented by retaining information about the individual displacements of each atom's neighbours, in such a way that slip and twinning can be treated equivalently.

The first step is to establish the set of neighbour displacements frequently ob-

served in the sampling region. Taking each atom as the central atom in turn, one calculates the change in relative position of the atoms with which it was coordinated before deformation. Let the trajectory of some atom γ be denoted by $\mathbf{x}_\gamma(t)$. The change in displacement of neighbour β from the central atom α, as of time t, is

$$\mathbf{u}_{\alpha\beta} = [\mathbf{x}_\beta(t) - \mathbf{x}_\alpha(t)] - [\mathbf{x}_\beta(0) - \mathbf{x}_\alpha(0)] \tag{3.18a}$$

$$= \mathbf{x}_{\alpha\beta} - \mathbf{X}_{\alpha\beta}. \tag{3.18b}$$

Here, the index β runs over central atom α's initial neighbours. One then generates a three-dimensional density plot of the set of all neighbour displacements $\{\mathbf{u}_{\alpha\beta}\}$. The displacements will cluster around a discrete set of points corresponding to the Burgers vectors of the dislocations generated on compression. We can define a set of spherical bins located at these points with centres $\{\mathbf{b}_i\}$ and radii $\{r_i\}$. The finite radii of the bins account for both thermal noise and modulations in density and orientation. Since the density plot is necessarily centrosymmetric ($\mathbf{u}_{\alpha\beta} = -\mathbf{u}_{\beta\alpha}$), bin n is always implicitly paired with a second bin $-n$ located at $-\mathbf{b}_n$, as shown in Figs. 3.3(b,c). While it is not necessary to define the bins with the aid of a density plot if one has knowledge of the deformation modes *a priori*, doing so tends to increase the accuracy with which the atoms are classified.

The second step is to associate each atom with a plasticity mechanism according to the bins into which its neighbour displacements fall. Displacement $\mathbf{u}_{\alpha\beta}$ is said to belong to bin n if $\|\mathbf{u}_{\alpha\beta} - \mathbf{b}_n\| \leq r_n$. If none of the bins are occupied, the central atom is assigned to slip event 0, denoting an atom that has not undergone plastic flow. If only bins $\pm n$ are occupied, the atom is assigned to event n. If more than one type of bin is occupied, the atom is deemed unresolvable. To identify twinned atoms, for which more than one type of displacement exists, we ensure there are only bins located at either $\pm 1/3\,[111]$ *or* $\pm 1/6\,[111]$; the former is preferable as the latter frequently overlaps the broad peak located at [000].

SVA has the advantage of being able to detect both dislocation slip and deformation twinning, but the technique suffers at high shock pressure. The more plastic deformation a crystal has suffered, the greater the probability of its atoms having participated in multiple plastic flow events. This causes the bins nearest the origin

to empty out into the surrounding volume. Any atom located at the intersection between slip planes and twins can thus escape detection. The following section describes a complementary algorithm with which we can detect deformation twins (but not slip planes) reliably at higher pressures.

3.5.5 Template matching technique

The material within a deformation twin has a radically different crystallographic orientation to that of its host crystal. If one can somehow deduce the orientation of each atom's environment (by, say, working out the directions of the local $\langle 100 \rangle$ basis vectors), one can tell whether it belongs to a deformation twin, without having to know the crystal's deformation history as in SVA. Here, the crystal's orientation will be calculated using a template-matching algorithm, in which each of atom α's current neighbour displacement vectors $\mathbf{x}_{\alpha\beta}$ is independently matched to an ideal neighbour vector in a set of template bcc unit cells according to their cosine similarity (not unlike the study in Ref. [126]). The implementation of this technique, depicted schematically in Fig. 3.4, is performed as follows.

One first specifies the set of 14 ambient neighbours vectors $\{\mathbf{B}_i^{(0)}\} = \mathcal{B}_0$ that describe the 1$^{\text{st}}$ and 2$^{\text{nd}}$ bcc coordination shells for the host orientation. In anticipation of the onset of deformation twinning, M further twin bases $\mathcal{B}_{1,2,\ldots,M}$ are also constructed. The elements of each twin basis are constructed by reflecting the elements of $\mathcal{B}_0$ in the corresponding twin plane with unit normal $\hat{\mathbf{m}}$:

$$\mathbf{B}_i^{(m)} = \mathbf{B}_i^{(0)} - 2(\mathbf{B}_i^{(0)} \cdot \hat{\mathbf{m}})\hat{\mathbf{m}}. \tag{3.19}$$

A separate set of $M + 1$ candidate bases must be constructed for each grain under consideration. Then, taking each basis in turn, we assign each of the central atom's 14 nearest and next-nearest neighbours to an ideal neighbours vector. Vector $\mathbf{x}_{\alpha\beta}$ is paired with the ideal vector with which it subtends the smallest angle, or equivalently, the vector with which it has maximal cosine similarity. Formally,

$$\mathbf{R}_{\alpha\beta}^{(m)} = \underset{\mathbf{B}_i^{(m)} \in \mathcal{B}_m}{\arg\max}\, \mathrm{sim}(\mathbf{x}_{\alpha\beta}, \mathbf{B}_i^{(m)}), \tag{3.20}$$

where

$$\mathrm{sim}\,(\mathbf{u},\mathbf{v}) = \frac{\mathbf{u}\cdot\mathbf{v}}{\|\mathbf{u}\|\|\mathbf{v}\|}. \tag{3.21}$$

We then determine the basis that best describes the local unit cell of α. The basis chosen is the one that maximizes the total cosine similarity $\sum_{\beta=1}^{14}\mathrm{sim}(\mathbf{x}_{\alpha\beta},\mathbf{R}_{\alpha\beta}^{(m)})$. If the pairing of current and ideal neighbours vectors is not one-to-one for a given basis, that basis is excluded from consideration. If none of the bases provide one-to-one mappings, the atom is deemed unresolvable and is excluded from the computation.

By matching the local unit cell to one of the twin bases in this way, this template matching technique (TMT) provides a time-resolved picture of the deformation twins in a shock-loaded crystal, which nicely complements the DXA. Note that in addition to providing a means of detecting deformation twins, the TMT also naturally provides the set of ideal neighbour vectors $\mathbf{R}_{\alpha\beta}$ with which the elastic deformation gradient F_α^e can be calculated via Eq. (3.10).

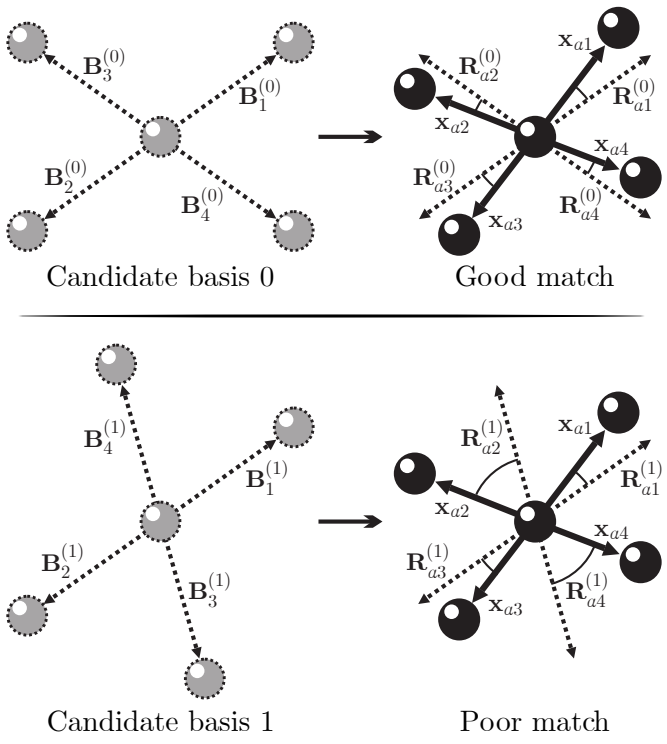

FIG. 3.4. Schematic depicting the template matching technique. Left: two candidate bases representing the host and twin orientations with associated ideal neighbours vectors $\{\mathbf{B}_i^{(0)}\}$ and $\{\mathbf{B}_i^{(1)}\}$ respectively. Right: pairing-off of the ideal neighbours vectors and the current neighbours displacements $\{\mathbf{x}_{\alpha\beta}\}$ according to cosine similarity for central atom α. In this case, basis 0 would be deemed more consistent because the total angle subtended by its paired vectors is smaller.

3.6 Example: Application to ⟨100⟩ tantalum

Given the number of postprocessing techniques used in this thesis, it may be informative for the reader first to see them all applied simultaneously to a single, simple simulation. Here, we will examine the plastic response of a block of monocrystalline tantalum that is steadily compressed until it yields, and is subsequently allowed to evolve under fixed-volume conditions. Note that the actual physics of the deformation will not be discussed in detail, since the purpose of this section is only to exhibit the characterisation techniques.

The crystal analysed here is a $100 \times 100 \times 100$ unit cell ($33.9 \times 33.9 \times 33.9$ nm^3) block of tantalum with its [100], [010], and [001] directions aligned with the x, y, and z computational cell axes, respectively. The cell is subjected to periodic boundary conditions on each of its faces, so that atoms just above (say) the lower yz face interact with those immediately below the upper yz face. The crystal is created with 75 point vacancies distributed randomly throughout its bulk, and a void at its centre of 10 nm radius – the void provides an easy nucleation site for dislocations, so

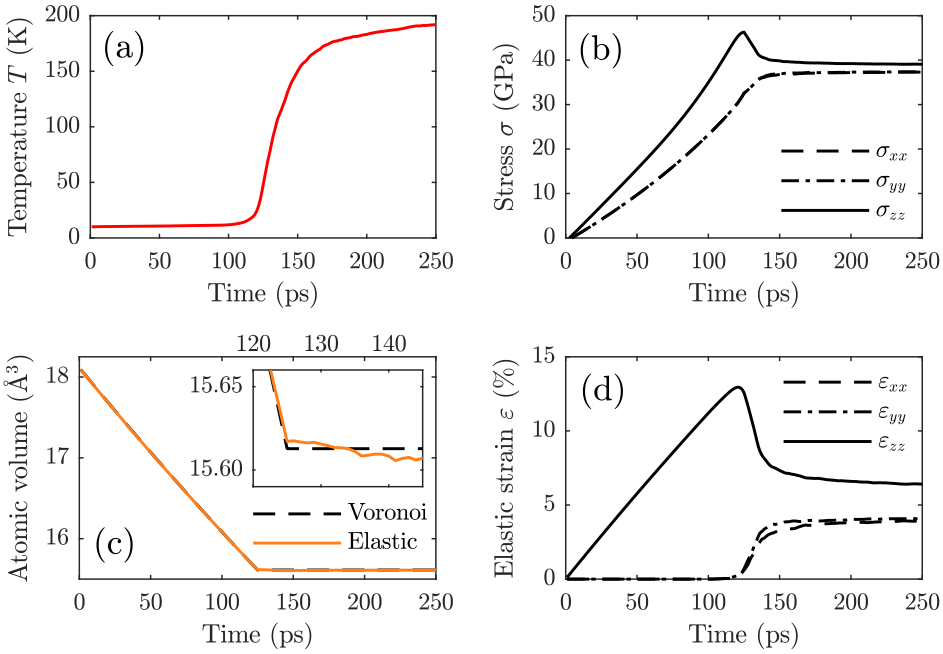

FIG. 3.5. Evolution of (a) temperature, (b) stress, (c) per-atom volume, and (d) elastic strain for a tantalum crystal compressed along [001]. Two volume calculations are given in (c), the first being taken directly from the crystal's Voronoi tessellation, the second from the determinant of the average elastic deformation gradient F^e.

that the crystal does not yield quite as 'catastrophically' as it would do if dislocations had to nucleate homogeneously, i.e. in the bulk. A low initial temperature of 10 K is chosen to make classification of the defects cleaner. The cell is uniaxially compressed along the z direction for 125 ps until it reaches 116% ambient density. The crystal is then held at constant volume and allowed to evolve for a further 125 ps.

Plotted in Fig. 3.5 are the temperature, stress, volume, and elastic strain of the crystal as functions of time. During the loading phase, the elastic strain along z increases linearly while the transverse strains ε_{xx} and ε_{yy} remain at zero. In other words, all that happens is the (001) planes move closer together. The volume decrease inferred from this purely uniaxial strain matches precisely that calculated from the Voronoi tessellation of the crystal, as shown in Fig. 3.5(c). Meanwhile, the stresses along the computational cell axes steadily increase, with σ_{zz} leading, and the transverse stresses lagging behind slightly (the difference being governed by the crystal's Poisson ratio ν). As the longitudinal and transverse stresses drift apart, shear stress accumulates until reaching a critical value at $t \approx 125$ ps, at which point the loading is deliberately arrested. Hereafter, several things happen. First, ε_{zz} suddenly decreases [i.e. the (001) planes move apart], and the two transverse strains increase. Fig. 3.5(c) shows that this strain evolution takes place almost exactly isochorically, which is to say that the unit cell changes shape, but not size. At the same time, the longitudinal and transverse stresses converge, meaning the shear stresses acting on the crystal relax. We also observe that the temperature of the crystal rises sharply. This behaviour (as will be explored extensively in this thesis) is all symptomatic of plastic deformation.

The defect detection methods outlined in Sec. 3.5 can now be used to understand how plastic deformation is realised. SVA (Sec. 3.5.4) can identify both slip planes and deformation twins by classifying atoms according to the displacement suffered by their neighbours; the heatmap used to locate the neighbour-displacement bins in shown in Fig. 3.6. As expected, the displacements cluster around the $\frac{1}{2}\langle 111\rangle$ vectors (which are associated with full slip), and also around $\frac{1}{3}\langle 111\rangle$ and $\frac{1}{6}\langle 111\rangle$ (which stem from deformation twinning). TMT (Sec. 3.5.5) provides a second, independent means of identifying twins; the twin bases were obtained by reflecting

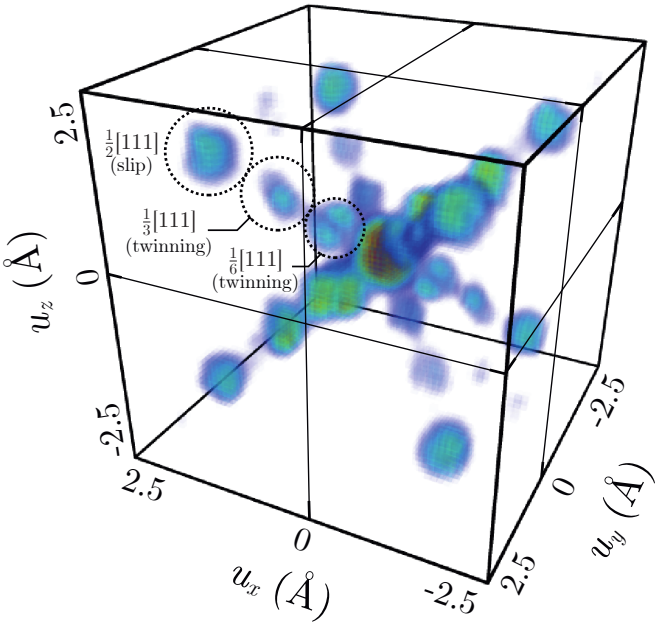

FIG. 3.6. Three-dimensional density plot showing the distribution of slip vectors in single-crystal tantalum with its ⟨100⟩ directions collinear with the computational cell axes. Dashed circles indicate the position and radius of the bins used to implement the SVA.

the host basis in the $(11\bar{2})$, (112), $(\bar{1}12)$, and $(1\bar{1}2)$ twinning planes[14].

Fig. 3.7 shows a composite visualisation of the defect evolution, the key features of which are as follows. Before the crystal yields, the only defective atoms present are those at the surface of vacancies and the central void. By $t = 110$ ps, two dislocation loops have been emitted from the void (leaving in their wake planes of slipped atoms, as seen in the SVA), which travel along the ⟨111⟩ directions towards the corners of the simulation cell. At this stage, the plastic flow is highly localised, meaning the small amount of shear stress it relieves does not register in the stress-strain curves plotted in Fig. 3.5. At $t = 119$ ps, we start seeing profuse production of deformation twins (visible via both SVA and TMT), which by 123 ps occupy a considerable fraction of the crystal. This is the point at which yield proper begins. By 250 ps, deformation twins and full dislocations pervade the entire crystal, and have reached a stable state in which they are unable to bring about any further relief of shear stress. We also observe that, by this time, the population of point vacancies has increased enormously (a point to which we will return in Chapter 6). Shown in

[14] Although there are 12 distinct {112} twin planes in a bcc crystal, there exist only four distinct twin orientations. For example, the $(11\bar{2})$, $(1\bar{2}1)$ and $(\bar{2}11)$ twins (which all share the $\frac{1}{6}$[111] Burgers vector) have exactly the same orientation, so any one of them can be chosen to perform the reflection in.

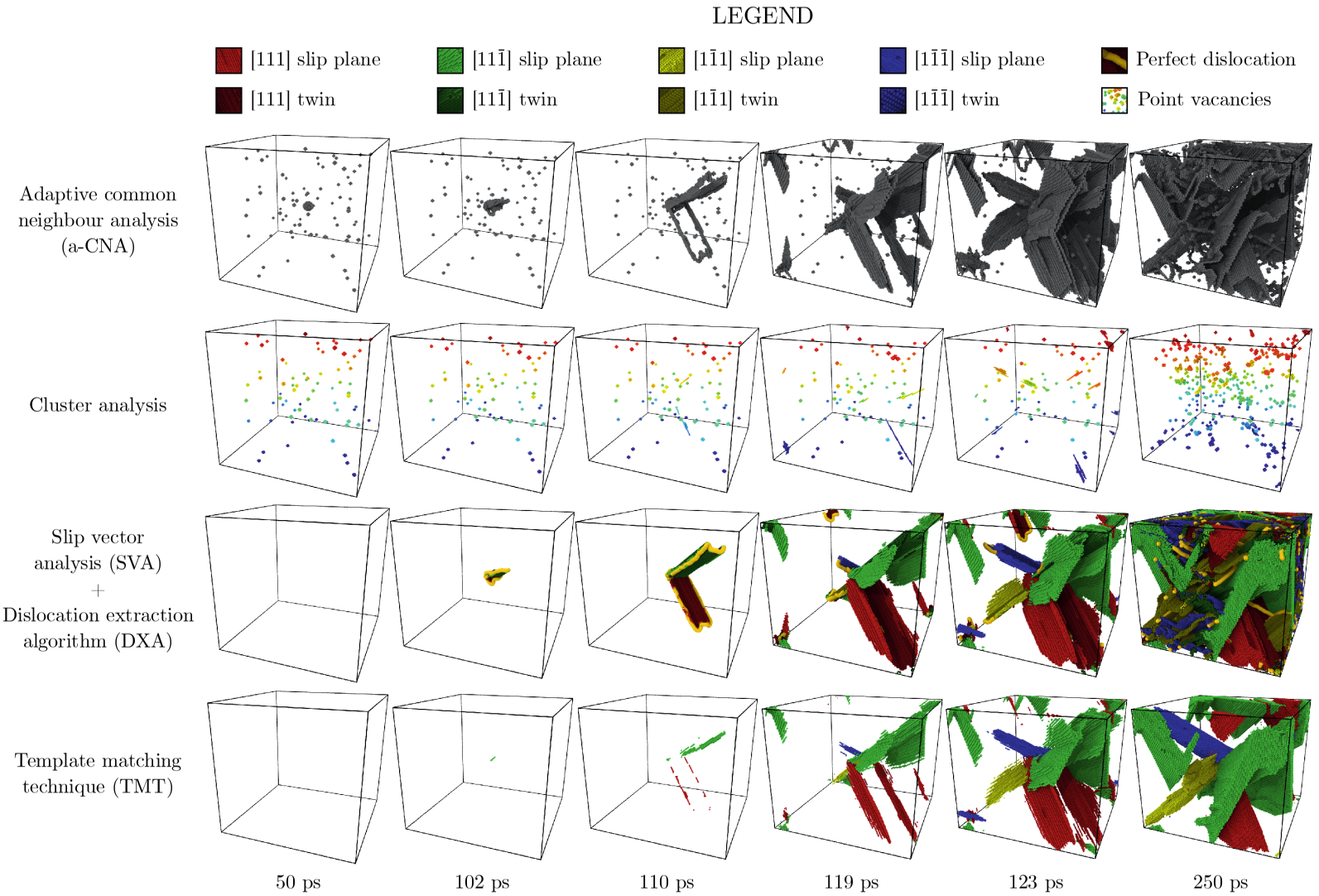

FIG. 3.7. Visualisation of defects in a block of monocrystalline tantalum with its ⟨100⟩ directions aligned with the computational cell axes at various stages of deformation (left to right). Row one shows defective atoms identified by a-CNA, highlighting point vacancies, full dislocations, and deformation twin boundaries indiscriminately. Row two shows point vacancies isolated using cluster analysis. Row three shows slip planes and deformation twins viewed using SVA, and dislocations using the DXA. Row four shows twins viewed via TMT.

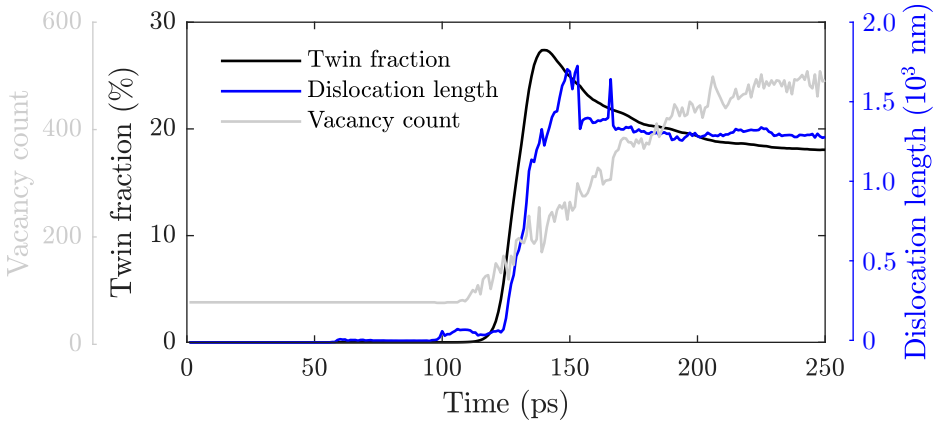

FIG. 3.8. Defect populations in 10 K tantalum loaded along [001] to 116% ambient density.

Fig. 3.8 is the population of point vacancies [deduced using Eq. (3.17)], deformation twins (from TMT), and full dislocations (from DXA) as functions of time. The shortcomings of the vacancy-counting method are evident: the profile is noisy, and starts increasing too early, likely due to the algorithm misinterpreting 'debris' from nascent twin boundaries as defect clusters. The overall trend it suggests, however, is likely trustworthy. In summary, the techniques described in Sec. 3.5 allow us to distinguish and quantify the three species of defect present in this ⟨100⟩ tantalum crystal, and so better understand its behaviour after yield.

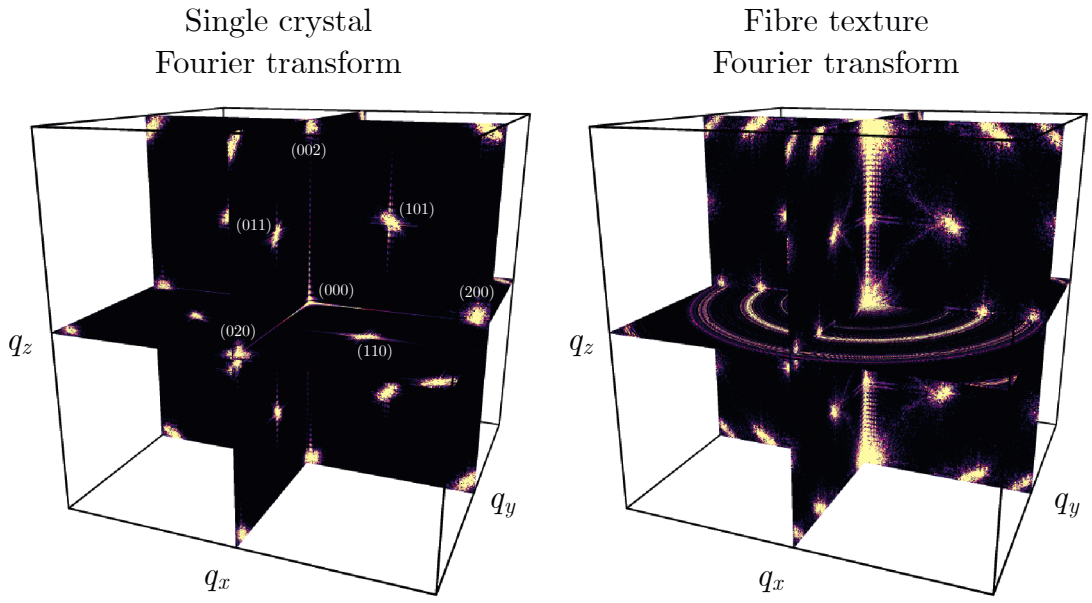

FIG. 3.9. Fourier transforms of host material from a single tantalum crystal with its ⟨100⟩ directions aligned with the cell axes. The plain Fourier transform and the fibre-textured analogue defined by Eq. (3.15) are shown on the left and right, respectively.

Finally, shown in Fig. 3.9 is the FTFT of the crystal calculated at $t = 250$ ps, alongside the plain, single-crystal Fourier transform for comparison. Atoms identified as belonging to twins by the TMT, which bring about many extra diffraction peaks due to their different orientations, have been excluded from the computation for clarity. We see that the intensity of the plain Fourier transform is strongly localised around the reciprocal lattice vectors for a bcc crystal (which, as expected, form an fcc lattice). In the FTFT analogue, each peak is swept into a ring, imitating the distribution of reciprocal lattice vectors present in an axially symmetric, fibre-textured polycrystal. In Chapter 5, it will be shown that synthetic diffraction patterns generated from the FTFT compare favourably with real diffraction data, confirming the Fourier transform's role as an indispensable interpretative tool that allows MD to make direct contact with dynamic compression experiments.

CHAPTER 4

Simulations of grain interactions during shock compression

4.1 Introduction

When a polycrystal is compressed, the grains of which it is composed cannot deform as they would do in isolation, but must generally do so in such a way as to accommodate the presence of their neighbours[15]. This is to say that every grain must interact with those adjacent to it. Over the past several decades, extensive experimental and material modelling efforts have revealed a host of physical effects that can be directly attributed to interactions between grains, including changes to local orientation [127–135] and strain [135–139], generation of additional dislocations [140–143], and alteration of the macroscopic yield strength [127, 128, 144, 145]. The vast majority of work to date has been performed in the context of quasistatic loading, where inertial forces between grains are negligible. By comparison, very little consideration has been given to the physics of grain interactions under the conditions of shock loading. In this chapter, the results of large-scale molecular dynamics simulations are presented demonstrating that the enormous stresses one grain exerts on its neighbours alter the way they plastically deform, and further allow them to reach a state of shear stress lower than material strength would ordinarily permit.

4.1.1 Studies undertaken to date

The modelling of grain interactions under quasistatic loading conditions began in earnest just before the end of the 20$^{\text{th}}$ century. Prior to this time, the two extant species of polycrystal model, namely Taylor-type[16] [146–149] and self-consistent

[15] This assertion is true provided the boundaries between the grains do not fail.

[16] Here, Taylor-type refers to any model underpinned by an assumption of strain homogeneity. This includes Taylor's original prescription, in which every strain component is constant throughout the aggregate, and variations thereof such as the relaxed constraints approach, where select strain components are allowed to vary.

models [144, 150–152], were both incapable of faithfully treating interactions between grains; the former class could not guarantee that adjacent grains were in mechanical equilibrium, while the latter class could do so, but only in an average, mean-field sense. With rapid increases in readily-available computing power, it became possible to move beyond these statistical models and seek numerical, full-field solutions, in which the stress and strain tensors are solved for on a discrete grid with sub-grain resolution (with e.g. the finite element method [153]) in such a way that grain interactions are automatically incorporated. The first studies capitalising on these new numerical techniques quickly established that while statistical models could correctly predict the gross behaviour of quasistatically deformed polycrystals, certain effects could only be explained with recourse to grain interactions. Such effects included: additional rotations [127, 129], retrograde rotations [129, 145], and the formation of otherwise inexplicable textures [130]; the appearance of large intragranular orientation gradients, i.e. grain fragmentation [132, 134, 137]; and loss of correlation between each grain's initial orientation and its plastic strain state following loading [136, 137]. Becker and Panchanadeeswaran [129] accounted for observations such as these by postulating two abstract 'forces' that compete to control each grain's evolution: the first is intrinsic to the grain itself, and compels it to behave as it would do in isolation; the second is exerted upon the grain by its neighbourhood, and forces it to undergo additional deformation to maintain compatibility and equilibrium with its neighbours at its boundaries. Subsequent statistical analyses suggested that, under certain circumstances, the latter force is actually dominant [136, 138]. These computational studies have thus illustrated the significance of grain interaction effects, and although they were undertaken within the context of quasistatic loading, there is every reason to believe the same phenomena must manifest on some level in the shock regime.

In more recent years, a number of computational studies of multicrystals under shock-loading conditions have been undertaken with the aid of large-scale molecular dynamics (MD) simulations [57, 154–161]. A small subset of these studies have focused on elucidating the physics of grain interactions, typically by modelling simple bicrystalline samples. These investigations have clearly demonstrated that during shock compression, grain interactions take on a dynamic nature due to the abrupt-

ness of the loading. Park [155] performed shock-compression simulations of a nickel bicrystal with its grain-boundary-normal perpendicular to the shock, and showed that when the shock front in one grain outpaces that in its neighbour, the former can laterally precompress the latter due to the transient stress gradients induced over the boundary within the elastic precursor. In a similar study of copper, Luo *et. al.* [156] further showed that under high-symmetry conditions, lateral compression waves can coalesce at the centre of the lagging grain, generating a moving 'focus' at which the stress concentration is exceptionally high. One can speculate on the basis of investigations such as these that the ability of one grain to radically affect the stress state of its neighbours through dynamic interactions could have profound consequences for the manner in which each plastically deforms. The purpose of this study is to build on these previous works, and identify dynamic grain interaction effects in nanocrystals comprising more than two crystallites.

4.1.2 Fibre-textured targets

This study is concerned with interactions in a particular class of bcc polycrystal whose grains are characterised by i) a columnar morphology and ii) a fibrelike crystallographic texture, in which every grain has the same crystallographic direction closely aligned with its long axis (in this instance, [011]). The reasons for doing so are twofold. First, the response of these polycrystals when shock-compressed along their fibre axis is relatively simple – the high aspect ratio of the crystallites means that interactions between grains take place almost exclusively in directions normal to the shock, while the fibre texture ensures the shock front progresses at approximately the same speed in every grain, meaning shock broadening effects are minimized. These polycrystals thus provide us with an uncomplicated environment in which to study the fundamentals of grain interactions. Second, tantalum targets with this morphological and crystallographic texture (which can be procured via vapour deposition) have already been successfully used to reveal the lattice-level dynamics that take place during shock compression [162] and subsequent release [59] using *in situ* XRD measurements. Moreover, as an axis of twofold rotational symmetry, the [011] fibre axis is particularly interesting from a grain-interaction point

of view, because each grain will exhibit elastic and plastic anisotropy in directions normal to the shock. Bcc tantalum has been chosen here to provide better contact with the aforementioned experiments, but it is stressed that the fundamental grain interaction physics that will be illustrated is not peculiar to this element.

4.2 Simulation setup

To study the response of nanocrystalline tantalum (Ta) to shock compression, large-scale MD simulations using the LAMMPS code [108] and the EAM Ta1 potential constructed by Ravelo *et. al.* [54] were employed. This potential was tailored to reproduce the mechanical and thermodynamic properties of Ta at the megabar pressure scale. It successfully predicts the equation of state, elastic constants, and Hugoniot temperatures obtained from *ab initio* calculations [54], as well as several experimentally determined high-pressure relations, including the pressure-volume curve at ambient temperature [163, 164], the locus of shock states in the U_S - U_P plane [165], and the melt curve [166].

The polycrystals simulated comprise tessellating prismatic grains whose long axes are aligned with z, the direction along which the shock wave is launched. The bases of the prisms constitute the front and rear surfaces of the polycrystal, while the lateral faces make up the grain boundaries (GBs). We will investigate two columnar geometries labelled the checkerboard (CB) and the honeycomb (HC), as depicted in Fig. 4.1. The former contains four grains with approximately square cross-sections, the latter six grains with hexagonal cross-sections. The minimum transverse dimensions of the grains in the CB and HC geometries are 21.5 nm and 21.8 nm respectively. Both geometries span 1 122 nm (i.e. 4 800 [011] lattice spacings) in the compression direction. Periodic boundary conditions (PBCs) are applied to each polycrystal's xz- and yz-faces, while the z direction is left aperiodic.

The orientations of the grains are chosen so as to emulate a fibre texture. In each geometry, there exists a central grain whose [100], [01$\bar{1}$] and [011] axes are aligned with the x, y and z directions, respectively. The orientations of the adjacent grains are related to that of the central grain by rotations about z. For the CB geometry, the misorientation angle is 90°. This angle is chosen to maximise the

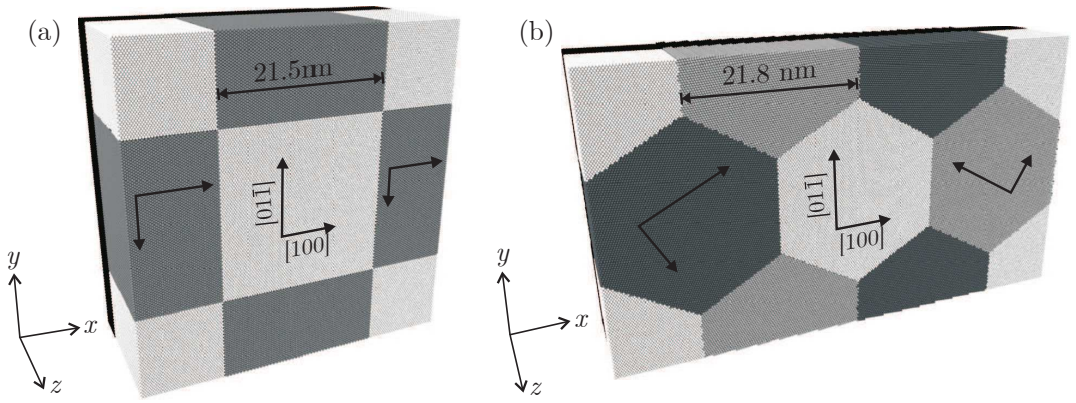

FIG. 4.1. Front end of the computational cells used in MD simulations of shock-compressed columnar polycrystals, visualised using OVITO [167]. (a) depicts the checkerboard (CB) geometry, (b) the honeycomb (HC). All grains have their [011] crystallographic axis aligned with z, the loading direction; the azimuthal orientation of each grain is indicated by the directions of the [100] and [01$\bar{1}$] axes. Grains with the same shading share the same orientation. The piston is depicted in black at the rear of the cells.

degree of anisotropy over the GBs, and exaggerate the magnitude of the stress gradients induced by shock-loading that cause the grains to interact. The analysis will be focused primarily on the CB geometry, though comparisons will be made with the less contrived HC geometry, for which the misorientation is only 60°. While the morphology and texture of these nanocrystals is highly idealised, they may serve as informative models, as they exhibit the basic physics relevant to a polycrystal in a way that is amenable to simple analysis.

To equilibrate the nanocrystals prior to loading efficiently, their translational symmetry along z can be exploited: rather than relaxing the crystals in their entirety, we first construct and relax a fully periodic supercell 9.4 nm in thickness, and subsequently replicate the cell 120 times in the z direction to bring the system up to its full dimensions. The supercells are first simulated under the microcanonical (NVE) ensemble with a 300 K Langevin thermostat to absorb the heat released from the GBs. Relaxation is then performed under isothermal-isobaric (NPT) conditions for 50 ps to anneal the GBs and bring the pressure to 0 GPa. Following the pressure correction, the system is time-integrated for a further 25 ps under the canonical (NVT) ensemble (i.e. without pressure control); if the pressure has drifted by more than 1 kbar following this interval, an additional NPT run is executed. This process is iterated until the pressure stabilises.

The equilibrated supercell is then replicated in the compression direction, and the PBCs on the xy-faces of the simulation cell are relaxed. The full polycrystal is run under the NVE ensemble with a weak Langevin thermostat for 50 ps to damp out the pressure waves released from the front and rear surfaces. A final 50 ps period of relaxation without thermostatting concludes the equilibration. The polycrystals typically converge with residual pressures of order 10 bar and temperatures deviating from 300 K by no more than 0.1 K. The only crystal defects present following relaxation are the front and rear free surfaces, and the GBs.

In order to isolate the influence of one grain on another, we will also examine MD simulations of single crystals with the same orientation as the central grain in the nanocrystals. By comparing the response of monocrystals and polycrystals subjected to the same shock conditions, we can understand precisely how the stress and strain state of the grains is altered by virtue of their being situated in a polycrystal. The full dimensions of the single crystals are $24.8 \times 24.8 \times 1\,122$ nm^3. They are relaxed in the same manner as the polycrystals, and are also periodic in x and y.

The single- and polycrystals are shock-loaded under the NVE ensemble with a 1 fs timestep, using a 'piston' instantaneously accelerated to constant velocity $\mathbf{U}_P = (0, 0, U_P)$. The piston is simply a group of atoms whose motion is completely unperturbed by interatomic forces. Time integration proceeds until the compression wave reaches the end of the simulation cell. Note that the shock velocity U_S, and therefore the breakout time, is identical for every grain because each one has its [011] direction parallel to the loading axis.

4.3 Single crystal response

It is instructive first to establish how [011] Ta responds to shock compression at the level of a single grain, that is, in the absence of polycrystalline effects. To do so, we will study the behaviour of monocrystals shock-compressed to at least 40 GPa (the HEL for a crystal modelled under the Ta1 potential shocked along [011] [54]) that are periodic in directions normal to the shock. These monocrystals serve as the 'control group' with which we will eventually compare polycrystals loaded under similar shock conditions in order to isolate the additional physics introduced by

intergranular interactions. We should primarily be interested in establishing whether the response of these [011] single crystals is (given their low rotational symmetry about z) markedly different in the two directions normal to the shock, both during the plastic relaxation phase and in the steady state that follows. As Sec. 4.4 will show, a grain that exhibits transverse anisotropy of this sort is bound to interact with its neighbours.

Let us identify the plasticity mechanisms activated in [011] Ta under shock compression by means of SVA (see Sec. 3.5.4). Fig. 4.2(a,b) shows cross-sections of the slip-vector heatmap in the xz- and xy-planes obtained from a single crystal shocked to 40 GPa. Atoms whose slip vectors are found in proximity to labelled peaks in the heatmap are shown in Fig. 4.2(c,d) for representative regions of the crystal. The SVA reveals that plastic deformation occurs in two stages.

The first is characterised by a combination of dislocation slip and deformation twinning of the types $[111](\bar{2}11)$ and $[\bar{1}11](211)$. That twinning of this kind operates in rapidly strained [011] Ta is well-known, having been extensively observed in MD [54, 59, 121, 162, 168, 169] and in experiment, both *ex-post-facto* [169–171] and, more recently, *in-situ* via time-resolved XRD [59, 162]. The deformation twins nucleate first, and are then partially replaced by perfect dislocations, which are able to accommodate the same shear strain as the twins without the large energy cost associated with their surfaces. In our coordinate system, the shearing motion associated with these mechanisms takes place exclusively in the xz-plane. The second stage of deformation, whose onset is delayed with respect to the first, involves dislocation slip in directions $[11\bar{1}]$ and $[\bar{1}1\bar{1}]$, which are situated in the xy-plane (i.e. normal to the shock). Fig. 4.2(d) shows that the slipped atoms left in the wake of these dislocations form a relatively complicated structure. This is because the dislocations mediating slip during this latter stage of flow have predominantly screw-like character, so they are permitted to cross-slip between planes; dislocations with Burgers vector $\frac{1}{2}[11\bar{1}]$, for instance, can be observed moving on planes $(2\bar{1}1)$, (101), and $(\bar{1}21)$. These two stages of deformation exhaust the four distinct $\langle 111 \rangle$ directions in which a bcc crystal is inclined to flow.

The key observation supplied by the SVA is that the crystallographic inequivalence of the crystal's two transverse directions is clearly manifested in the way it

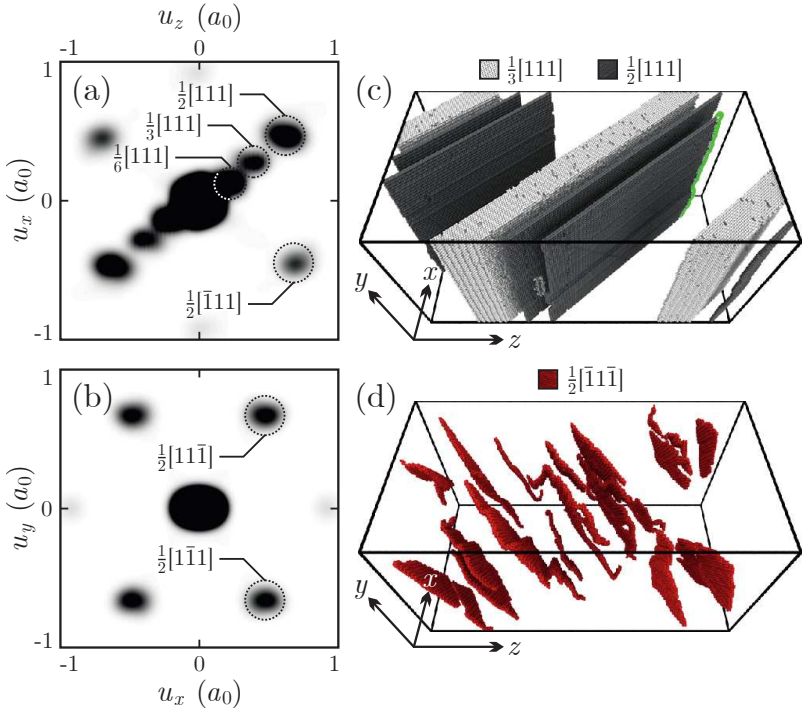

FIG. 4.2. Visualisation of the plasticity mechanisms active in $24.8 \times 24.8 \times 1\,122$ nm^3 monocrystalline Ta shocked along [011] to 40 GPa via SVA. (a) Cross-section of the slip-vector heatmap in the xz-plane, showing plasticity mechanisms belonging to the first stage of deformation. Visible are peaks from dislocation slip (Burgers vectors $\frac{1}{2}[111]$ and $\frac{1}{2}[\bar{1}11]$) and deformation twinning (Burgers vector $\frac{1}{6}[111]$). Note that the twins generate peaks at both $\frac{1}{6}[111]$ and $\frac{1}{3}[111]$; only the latter is used in the SVA algorithm. (c) Atoms contributing to selected peaks in the heatmap, which form slip planes (dark grey) and deformation twins (light grey). The dislocation preceding one of the slip planes, detected using the DXA, can be seen in green at the right of the image. (b,d) Similar analysis for the second stage of deformation, which is characterised by slip with associated Burgers vectors $\frac{1}{2}[11\bar{1}]$ and $\frac{1}{2}[\bar{1}1\bar{1}]$.

plastically deforms: while the first stage of deformation is characterised by flow in the xz-plane, there exists no similar mechanism allowing flow in the yz-plane – the crystal must instead settle for relatively sedate flow in the xy-plane. The transverse components of stress σ_{xx} and σ_{yy}, coupled as they are to separate plasticity mechanisms, must therefore evolve at different rates. To verify this, atoms that have participated in plastic flow events are shown alongside the local components of stress and elastic strain (expressed in the computational cell basis) in Fig. 4.3. This allows us to give a detailed account of how each plasticity mechanism alters the stresses perpendicular to the shock, and thus how the plastic and elastic aspects of the crystal's deformation are coupled.

The compression wave is led by an elastic precursor within which the crystal suffers uniaxial strain by 10% along z. The normal stresses increase to around half of their final values within this elastic zone in the order $\sigma_{zz} > \sigma_{xx} > \sigma_{yy}$, as is expected from the crystal's elastic moduli[17] [172]. Resolved shear stress (RSS) τ accumulates most rapidly on the $[111](\bar{2}11)$ and $[\bar{1}11](211)$ systems [for which $\tau = \sqrt{2}/3\,(\sigma_{zz}-\sigma_{xx})$], hence the triggering of the first stage of plastic relaxation. The attendant flow in the xz-plane allows the crystal to expand along z and collapse along x, causing stresses σ_{xx} and σ_{zz} to converge; the lattice spacing along y, meanwhile, remains unchanged. The systems under the greatest RSS following the first stage of deformation are $[11\bar{1}](\bar{2}1\bar{1})$ and $[\bar{1}1\bar{1}](21\bar{1})$ [for which $\tau = \sqrt{2}/3\,(\sigma_{xx}-\sigma_{yy})$], followed closely by the set $[11\bar{1}](1\bar{1}0)$, $[11\bar{1}](\bar{1}0\bar{1})$, $[\bar{1}1\bar{1}](\bar{1}\bar{1}0)$, and $[\bar{1}1\bar{1}](\bar{1}01)$ [$\tau = 1/\sqrt{6}\,(\sigma_{xx}-\sigma_{yy})$)] i.e. those involving transverse slip; these shear stresses are actually enhanced beyond the values they assume within the precursor by the first deformation mode, which causes σ_{xx} to increase. The transverse slip systems become active several tens of picoseconds after the first set and allow the crystal to collapse along the y-direction, thus relieving most of the remaining shear stress that the first stage of deformation could not. The stress state to which the fully relaxed portion of the crystal converges is slightly nonhydrostatic, supporting residual shear stresses of order 1 GPa (see the left inset of Fig. 4.3(b)). The difference between the transverse stresses $\sigma_{xx} - \sigma_{yy}$ is thus finite throughout the deformation, and can in fact reach values as extreme as 10 GPa between the two stages of deformation.

At higher shock pressures, the response of the crystal is qualitatively similar: flow takes place rapidly in the [111] and $[\bar{1}11]$ directions, and relatively slowly in the $[11\bar{1}]$ and $[\bar{1}1\bar{1}]$ directions. There do exist differences in certain aspects of the deformation as the shock pressure increases; for instance, the delay between the onset of the first and second stages of deformation shrinks to zero. Also, the number of stable deformation twins rapidly decreases, as observed by Ravelo *et. al.* [54], and dislocation slip comes to be the dominant means of plastic relaxation. However, the crystal's underlying twofold rotational symmetry about z is obviously preserved,

[17] One can show by rotating the stiffness tensor into a frame in which [100], $[01\bar{1}]$, and [011] are aligned with the computational cell axes (see Appendix B) that, in a state of uniaxial strain along [011] by ε_{zz}, the stresses are given by $\sigma_{xx} = c_{12}\varepsilon_{zz}$, $\sigma_{yy} = [(c_{11}+c_{12})/2 - c_{44}]\,\varepsilon_{zz}$, and $\sigma_{zz} = [(c_{11}+c_{12})/2 + c_{44}]\,\varepsilon_{zz}$, where the $\{c_{ij}\}$ are the cubic elastic constants. If the ambient lattice constants for tantalum are used ($c_{11} = 264\,\text{GPa}$, $c_{12} = 160\,\text{GPa}$, $c_{44} = 82\,\text{GPa}$ [105]), we correctly predict that $\sigma_{zz} > \sigma_{xx} > \sigma_{yy}$.

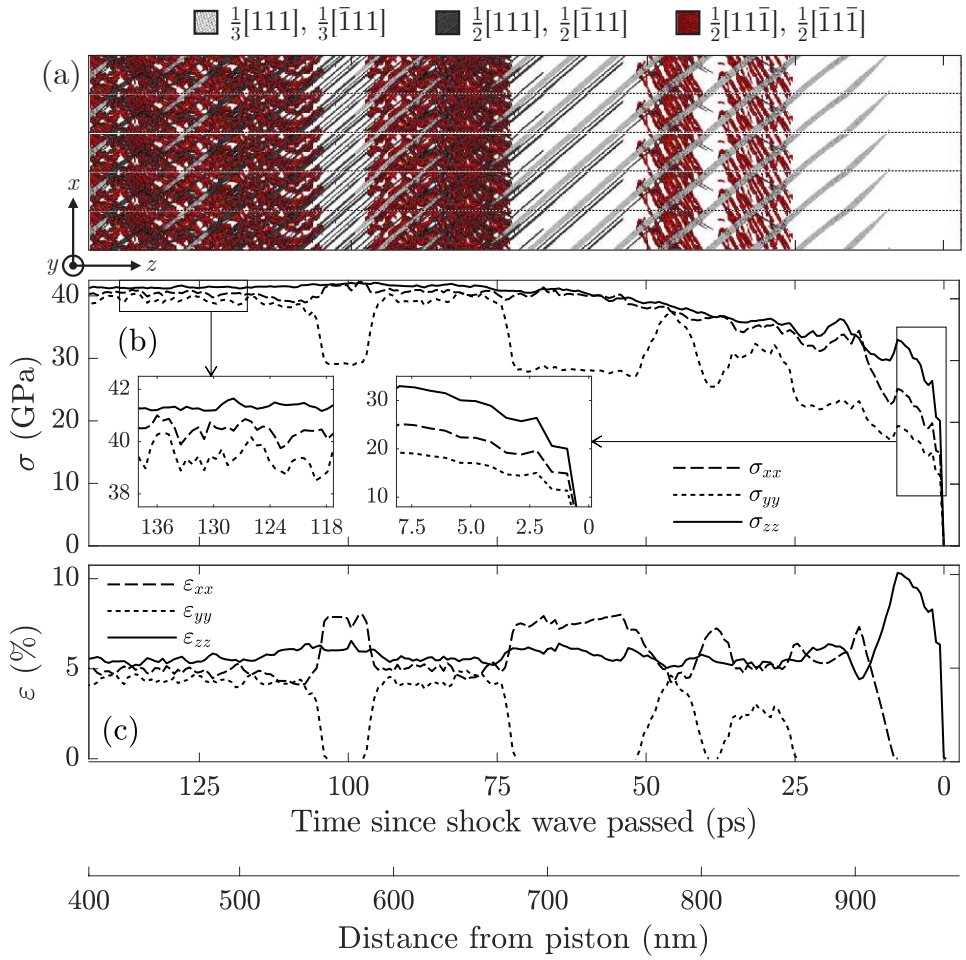

FIG. 4.3. Visualisation of the plasticity mechanisms active in monocrystalline Ta shocked to 40 GPa along [011] (the positive z-direction), alongside profiles of the stresses and elastic strains. Subfigures (a-c) are plotted on the same scale. The z-coordinate is primarily expressed in terms of the local time since the compression front passed; the secondary axis shows the distance from the piston generating the shock. (a) Atoms that have participated in plastic flow events, identified via SVA (as in Fig. 4.2). Visible are planar deformation twins and slip planes with associated Burgers vectors in the xz-plane (light and dark grey, respectively), and nonplanar slip planes with Burgers vectors in the xy-plane (red). Periodic images of the cell have been added in the x-direction for clarity. (b) Stresses along the computational cell axes averaged over the cross-section of the crystal. Left and right insets show the late-time stresses and stresses within the elastic precursor, respectively. (c) Elastic strains in the computational cell basis. Positive strains denote compression.

and so it continues to assume an anisotropic transverse stress state during and after plastic relaxation up to pressures as high as 1 Mbar. Fig. 4.4 shows the average deviatoric stresses and elastic strains, defined by $\sigma' = \sigma - \frac{1}{3}\,\mathrm{Tr}[\sigma]I$ and $\varepsilon' = \varepsilon - \frac{1}{3}\,\mathrm{Tr}[\varepsilon]I$, respectively, within the fully relaxed region of monocrystals compressed to between 40 and 100 GPa. The steady-state transverse stress anisotropy $\sigma_{xx} - \sigma_{yy}$

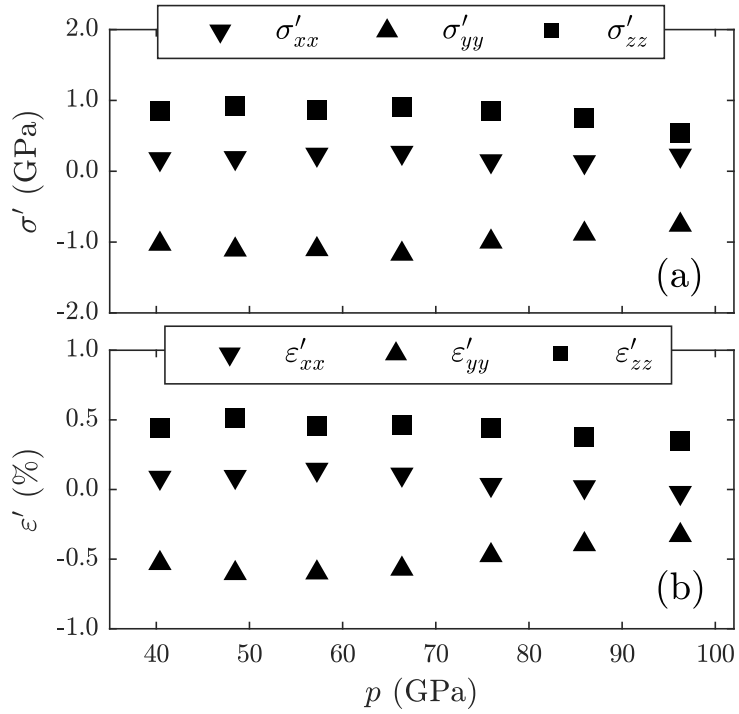

FIG. 4.4. (a) Steady-state deviatoric stresses of monocrystalline Ta shocked along [011] to between 40 and 100 GPa. (b) Corresponding deviatoric elastic strains.

over this pressure range takes values between 1.0 and 1.5 GPa. This anisotropy manifests in the elastic strain state of the crystal as a persistent difference between ε_{xx} and ε_{yy} whose magnitude (approximately 0.5%) is comparable to the traditional shear strain $\varepsilon_S - \varepsilon_T \equiv \varepsilon_{zz} - (\varepsilon_{xx} + \varepsilon_{yy})/2$. Further reduction of the stress anisotropy is prevented by material strength, or more specifically the shear stress required to effect plastic flow along $[11\bar{1}]$ and $[\bar{1}1\bar{1}]$.

To summarise, single-crystal tantalum shocked along [011] generally assumes an anisotropic stress state in the plane normal to the shock, due to each component of transverse stress being coupled to different plasticity mechanisms. The anisotropy may reach values as high as 10 GPa during the course of plastic relaxation, and falls to no lower than 1 GPa in the steady state due to material strength. We will now go on to consider the consequences of transverse stress anisotropy at the level of a single grain for the evolution of a polycrystal composed of many such grains.

4.4 Polycrystal response below the HEL

It was shown in Sec. 4.3 that a laterally confined Ta crystal shocked above its HEL along [011] will reach a state in which $\sigma_{xx} \neq \sigma_{yy}$. Suppose we were to construct a columnar polycrystal from several such compressed monocrystals by rotating each through some angle about z and then tessellating them in the xy-plane. It is clear that such a polycrystal would in general be mechanically unstable: if one were to move along any given direction in the xy-plane, the normal stress components σ_{xx} and σ_{yy} would change whenever one passed from one grain to another, because each grain is anisotropic in the transverse plane. In other words, the presence of transverse stress anisotropy at the level of each individual grain necessarily implies the existence of stress gradients over the grain boundaries. The polycrystal would thus fail to satisfy the stability criterion $\nabla \cdot \sigma = 0$ in the vicinity of the grain boundaries, causing nearby material to experience a net force and therefore accelerate. The equilibrium stress state of grains in the polycrystal must therefore differ from the state they assume in isolation. Moreover, one should expect the stress gradients over the grain boundaries in such a polycrystal temporarily to assume extremely large values during the course of its deformation, causing neighbouring grains to interact strongly with one another. To elucidate this basic physics, let us first consider the response of a polycrystal loaded below its HEL.

The simulation involves uniaxially compressing a 46.7-nm long, fully periodic supercell with the CB geometry by 5% along the z direction by instantly rescaling every atom's z coordinate by 0.95. The cell was simulated under an NVE ensemble for 200 ps, during which time it oscillates about a mechanically stable state (as explained below). To hasten the convergence of the crystal to its steady state, a weak Langevin thermostat was applied after several tens of picoseconds, which damps out large-scale oscillations while maintaining the system's temperature.

Shown in Fig. 4.5(a,b) are the difference between the spatially averaged transverse stresses, $\Delta\sigma = \sigma_{xx} - \sigma_{yy}$, and the transverse elastic strain component ε_{xx} for the central grain of the supercell as functions of time. We see that the transverse stress anisotropy $\Delta\sigma$ oscillates about a value close to zero, which can be understood as follows. The compression of the crystal at $t = 0$ instantaneously effects a stress state in

which $\Delta\sigma = 2.1$ GPa. That the two transverse stresses are unequal is a consequence of the transverse directions ([100] and [01$\bar{1}$]) being crystallographically inequivalent; identical behaviour was seen in the elastic precursor of shock-compressed single crystals in Sec. 4.3. Now, the rotational symmetry of the CB geometry is such that σ_{yy} in grain 1 is equal to σ_{xx} in grain 2, as indicated schematically in Fig. 4.5(c). There thus exist at $t = 0$ stress gradients over the grain boundaries. Atoms on the boundaries between grains 1 and 2 therefore experience a net force in the x direction. Consequently grain 1 expands along its [100] axis, allowing σ_{xx} to decrease. By symmetry, the central grain also contracts along the y-direction (since grain 3 expands along its own [100] axis), causing σ_{yy} to increase. The effect of this transverse

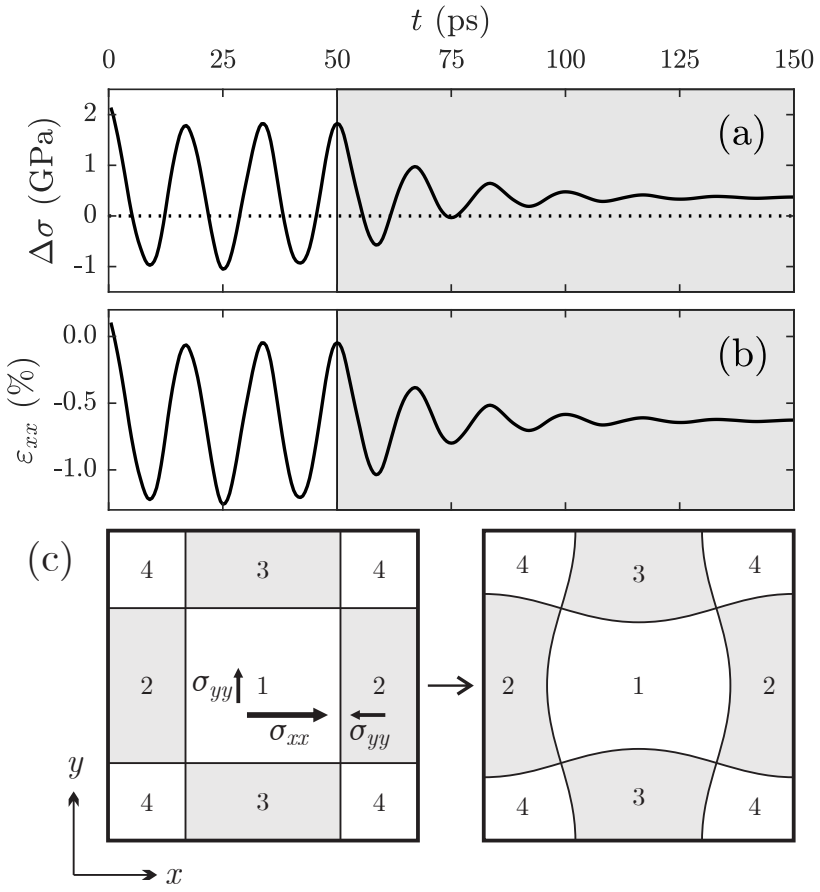

FIG. 4.5. (a) Transverse stress anisotropy $\Delta\sigma = \sigma_{xx} - \sigma_{yy}$ for grain 1 of a CB polycrystal instantaneously strained by 5% along z at $t = 0$. (b) Transverse elastic strain component ε_{xx} for the same grain. Note that $\varepsilon < 0$ denotes expansion. Shaded regions indicate where oscillations are damped by a Langevin thermostat. (c) Schematic cross-section of the CB polycrystal at $t = 0$ ps and $t = 150$ ps (left and right images, respectively), showing the (greatly exaggerated) expansion of each grain along its local [100] axis in response to the stress gradients induced over their boundaries by the compression.

elastic deformation is to relax the stress gradients over the grain boundaries, and in so doing cause σ_{xx} and σ_{yy} to converge. The grain then overshoots the state of mechanical equilibrium (for which $\Delta\sigma \approx 0$ GPa) due to its inertia, and subsequently executes something close to simple harmonic motion (SHM). Once the motion has been damped out by the thermostat, the residual stress state in each grain is such that $\Delta\sigma$ is only 0.38 GPa.

What we are seeing here is the relief of shear stress not by plastic, but elastic deformation. This means of relaxation is available only to a polycrystal, for the following reasons. Both a single crystal and a polycrystal that are laterally confined have fixed transverse dimensions. For the single crystal, this means that any change in transverse lattice spacing is necessarily reliant on plastic flow; only by changing the number of crystal planes can their spacing be made to change. The polycrystal, by contrast, is subject to no such limitation: individual grains may undergo elastic strain transverse to the shock without the aid of plasticity mechanisms, provided they do so in such a way that the sum of their strains vanishes. In this instance, grain 1 is allowed to expand along [100] by grain 2's contraction along $[01\bar{1}]$. Note also that this 'cooperative' deformation is able to relax the transverse stress anisotropy to a greater degree than the corresponding plasticity mechanism can: while $\Delta\sigma$ was limited to at least 1.0 GPa for the single crystals studied in Sec. 4.3 (specifically by the shear stress required to effect flow in the $[11\bar{1}]$ or $[\bar{1}1\bar{1}]$ directions), the difference here is no more than 0.4 GPa. The polycrystal can thus reach a state of lower shear stress than the individual grains of which it is composed could in isolation.

However, while it is more efficient than plastic flow, the elastic relaxation mechanism cannot eliminate the transverse stress anisotropy entirely. To understand why this is, we need to consider the full stress state of the crystal. Fig. 4.6 shows the variation in the xy plane of not only ε_{xx} and σ_{xx} but also the off-diagonal stress tensor component σ_{xy}, before and after the stress gradients have relaxed. We see that as the supercell relaxes the transverse strain field ε_{xx} becomes less homogeneous, the transverse stress σ_{xx} more so – the system moves from the *isostrain* or *Voigt condition* [173] towards the *isostress* or *Reuss limit* [174]. Yet, while the difference between σ_{xx} in adjacent grains clearly decreases following relaxation, it does not vanish. In fact, towards the upper and lower boundaries of each grain, σ_{xx}

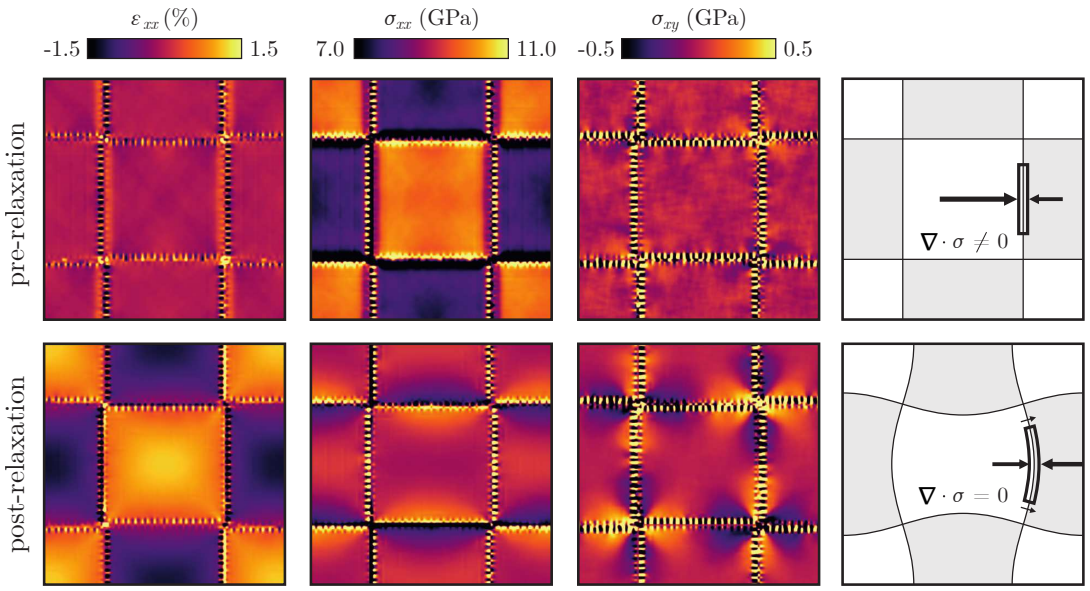

FIG. 4.6. Cross-sections of a CB polycrystal instantaneously strained by 5% along z at $t = 0$ both before and after relaxation of the resultant stress gradients (upper and lower rows, respectively), showing spatial variation of the fields ε_{xx}, σ_{xx}, and σ_{xy}. Panes in the rightmost column depict the tractions acting on a material element straddling the grain boundary between grains 1 and 2 before and after the grains have undergone their (greatly exaggerated) deformation.

differs only slightly from the value it assumed before relaxation. This frustration is caused by material either side of the grain boundaries being driven in different directions: grain 1, for instance, 'wants' to expand along x, while grain 3 wants to contract. This generates shear (off-diagonal) stresses in the vicinity of the boundary that are particularly strong at the corners of the grains, where the spatial gradients of the atomic displacement field are greatest. A material element straddling a grain boundary therefore experiences additional tractions on those of its faces that are perpendicular to the boundary; an example of such an element is depicted in Fig. 4.6 at the interface between grains 1 and 2. The tractions provide a countervailing force that opposes the normal stress gradient over the boundary, such that

$$[\nabla \cdot \sigma]_x = \partial_x \sigma_{xx} + \partial_y \sigma_{xy} = 0. \tag{4.1}$$

The crystal is thus able to tolerate normal stress gradients over its grain boundaries, which frustrates relaxation of the transverse stress anisotropy $\Delta\sigma$.

Furthermore, the efficiency of the elastic relaxation mode (i.e. how far short of

the Reuss limit the supercell falls) depends on the geometry of the polycrystal. Shown in Fig. 4.7 is a comparison of the off-diagonal stress field σ_{xy} for the CB and HC geometries post-relaxation. Note that σ_{xy} in the central grain is both less localized and of greater magnitude in the HC geometry than in the CB. The typical normal stress gradients $\partial_x\sigma_{xx}$ and $\partial_y\sigma_{yy}$ required to balance gradients in σ_{xy} are therefore correspondingly larger, meaning relaxation of $\Delta\sigma$ is frustrated to a greater degree – the average transverse stress anisotropy in the HC geometry falls to only 0.66 GPa. The increased frustration suffered by grains in the HC geometry is caused by their deformation being constrained by the presence of six (rather than only four) neighbours. The elastic relaxation mechanism in the HC is, however, still more efficient than the corresponding plasticity mechanism.

Finally, it is important to appreciate the timescale P over which the elastic deformation occurs. Fig. 4.5 showed that the polycrystal adapts to the imposed stress gradients within 5 ps. To identify the property of the crystal that allows it to respond this rapidly, we can use simple dimensional arguments to construct the functional form of P. The relaxation timescale must depend on the elastic constants $\{C_{ij}\}$, as these determine the magnitude of the stresses induced in the crystal when it is elastically deformed to a given extent; it must also depend on the mass density ρ, as this dictates the rate at which the crystal can locally respond to stresses of a given magnitude; and it must depend on the transverse dimension of the grains, L, because it takes a finite time for the stress waves generated at the grain boundaries to propagate into the bulk of the grains. The only dimensionally

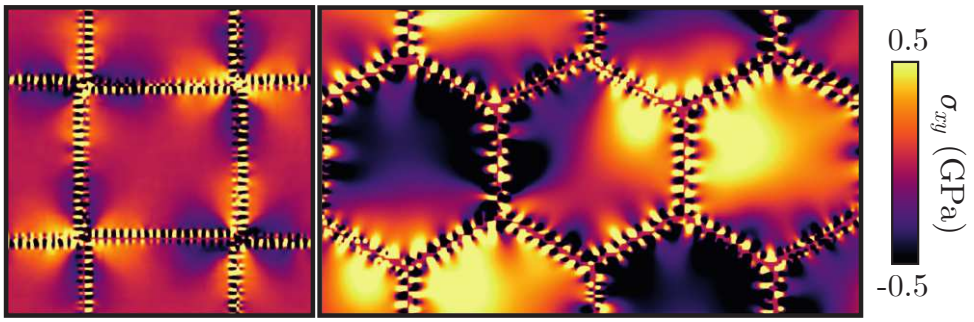

FIG. 4.7. Comparison of the off-diagonal stress field σ_{xy} for (left) CB and (right) HC polycrystals strained by 5% along z following relaxation of the induced stress gradients.

consistent combination of these variables reads

$$P = \left(\frac{\rho}{\sum_{ij} \alpha_{ij} C_{ij}} \right)^{\frac{1}{2}} L, \tag{4.2}$$

where $\{\alpha_{ij}\}$ is a set of dimensionless constants, presumably of order unity. Of the variables appearing in Eq. (4.2), L is arguably the most important. For most metals, the square root (which strongly resembles the inverse of a sound speed), ranges between 10^{-3} sm^{-1} (e.g. for lead [175]) and 10^{-4} sm^{-1} (e.g. for beryllium [176]), and cannot be pushed far beyond this range by shock compression unless the loading is extreme (i.e. to several TPa [177]). The grain size, meanwhile, can in principle span three orders of magnitude, from nm to μm, depending on the way the polycrystal is prepared. It is therefore L that is primarily responsible for setting the relaxation timescale, which for a nanocrystal is of order picoseconds.

To verify the linear dependence of P on L suggested by dimensional analysis, a set of instantaneous compression simulations similar to those discussed above were performed on CB supercells with grain sizes in the range 8.1 nm $\leq L \leq$

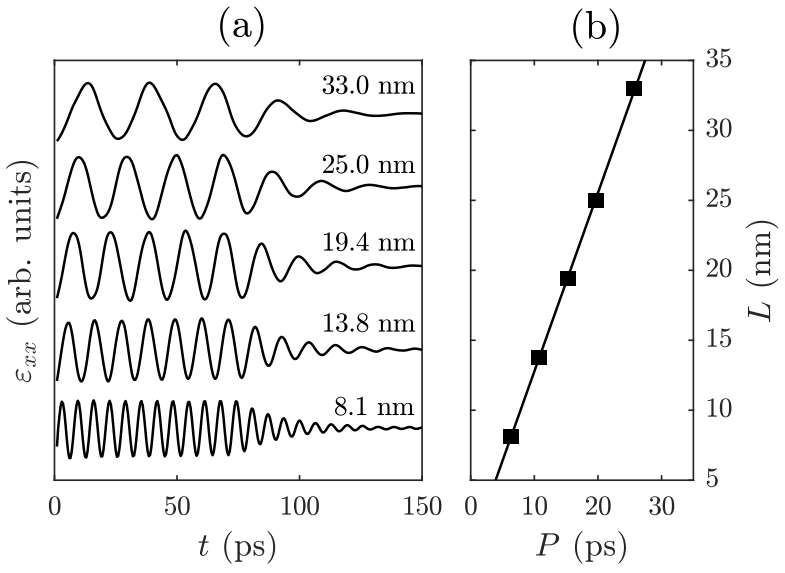

FIG. 4.8. (a) Evolution of the transverse strain component ε_{xx} for the central grain of uniaxially strained CB polycrystals of various sizes. Each profile, which is labelled by the corresponding grain size L, has been vertically offset for clarity. Motion is damped by a Langevin thermostat after 75 ps. (b) Oscillation period P as a function of grain size L. Shown also is the line of best fit obtained from a linear least-squares regression analysis with intercept fixed at zero.

33.0 nm. The variation of ε_{xx} with time for grain 1 is shown for each of these supercells in Fig. 4.8(a). By Fourier transforming each strain profile and identifying the frequency component with the greatest intensity, one can compute the variation of the oscillation period P with L. The results, plotted in Fig. 4.8(b), show that the proportionality predicted by Eq. (4.2) is indeed borne out in the simulations.

That the grains in an elastically compressed nanocrystal interact over only a few picoseconds is significant, because plastic flow takes place in a shock-loaded single crystal over a comparable timescale. If the nanocrystal were loaded above its HEL, then, these two mechanisms should take place concurrently. As we will see shortly, this allows the mechanisms to combine 'non-linearly', in the sense that the elastic deformations can actually activate or deactivate plasticity mechanisms, depending on the shock pressure.

In summary, we have found that when a columnar polycrystal is uniaxially compressed below its HEL, its constituent grains elastically expand and contract normal to the loading axis in order to relax the stress gradients that are induced over its grain boundaries. Relaxation of these stress gradients reduces the degree of transverse stress anisotropy $\Delta\sigma = \sigma_{xx} - \sigma_{yy}$ within each grain. The efficiency of this elastic relaxation is limited to a greater extent in the HC than the CB geometry, but for both geometries this mechanism still relieves transverse shear stress more efficiently than the corresponding plastic deformation mode can. The nanocrystals studied here relax within picoseconds, i.e. at a rate comparable to that of plastic flow. We will now consider the full elastoplastic response of columnar polycrystals shock-compressed above their HEL.

4.5 Polycrystal response above the HEL

Having seen how a single grain undergoes plastic deformation in isolation, and how a polycrystal responds to transverse stress anisotropy, we are in a position to understand the full elastoplastic response of a shock-compressed polycrystal. The most conspicuous features of the crystal's dynamic response will first be discussed, first just above the single-crystal HEL at 40 GPa, and then at higher pressures of 60 GPa and above. We will then compare the equilibrium mechanical state of the CB and

HC polycrystals with that of the isolated single crystals.

4.5.1 Slip deactivation at low pressure

It was shown in Sec. 4.4 that grains in an elastically loaded, fibre-textured, columnar polycrystal deform normal to the loading axis due to the stresses they exert on one another. These interactions relieved the shear stress associated with the transverse stress anisotropy $\Delta\sigma$. This same shear stress was relieved by dislocation slip in the $[\bar{1}11]$ and $[\bar{1}1\bar{1}]$ directions in the isolated grains discussed in Sec. 4.3. Dislocation slip of this kind and intergranular interactions therefore *compete* when the polycrystal is shock-compressed above its HEL. To demonstrate this, Fig. 4.9 shows the slipped atoms within a cross-section of a CB polycrystal shocked to 40 GPa, alongside plots of the stress and elastic strain variation along the length of the central grain. The wave structure is substantially different to that within the single crystal shocked to the same pressure, as will now be explained.

Within the elastic precursor, the normal stresses initially increase in the order $\sigma_{zz} > \sigma_{xx} > \sigma_{yy}$, exactly as they did in the single crystal. However, the transverse stresses σ_{xx} and σ_{yy} almost immediately start to converge due to the grains interacting with one another; in response to the stress gradients over its boundaries, grain 1 expands along x, and contracts along y. At the rear of the elastic zone, the average transverse stress anisotropy $\Delta\sigma$ has vanished entirely due to this elastic relaxation, as shown in the right inset of Fig. 4.9(b). The crystal subsequently undergoes slip and twinning in the [111] and $[\bar{1}11]$ directions due to the difference between σ_{xx} and σ_{zz}, just as the single crystal did, causing the crystal to collapse along x (i.e. the [100] direction). This deformation mechanism alone is sufficient to relieve the majority of the remaining shear stress, and so no further plastic flow takes place. The second stage of deformation that was observed in the isolated single crystals is thus conspicuously absent.

The fact that the CB polycrystal does not yield in the $[11\bar{1}]$ and $[\bar{1}1\bar{1}]$ directions at low shock pressure is a consequence of intergranular interactions. Since the interactions cause σ_{xx} and σ_{yy} to converge, and thus serve the same purpose as slip along $[11\bar{1}]$ and $[\bar{1}1\bar{1}]$, they render these latter plasticity mechanisms unnecessary. Phrased

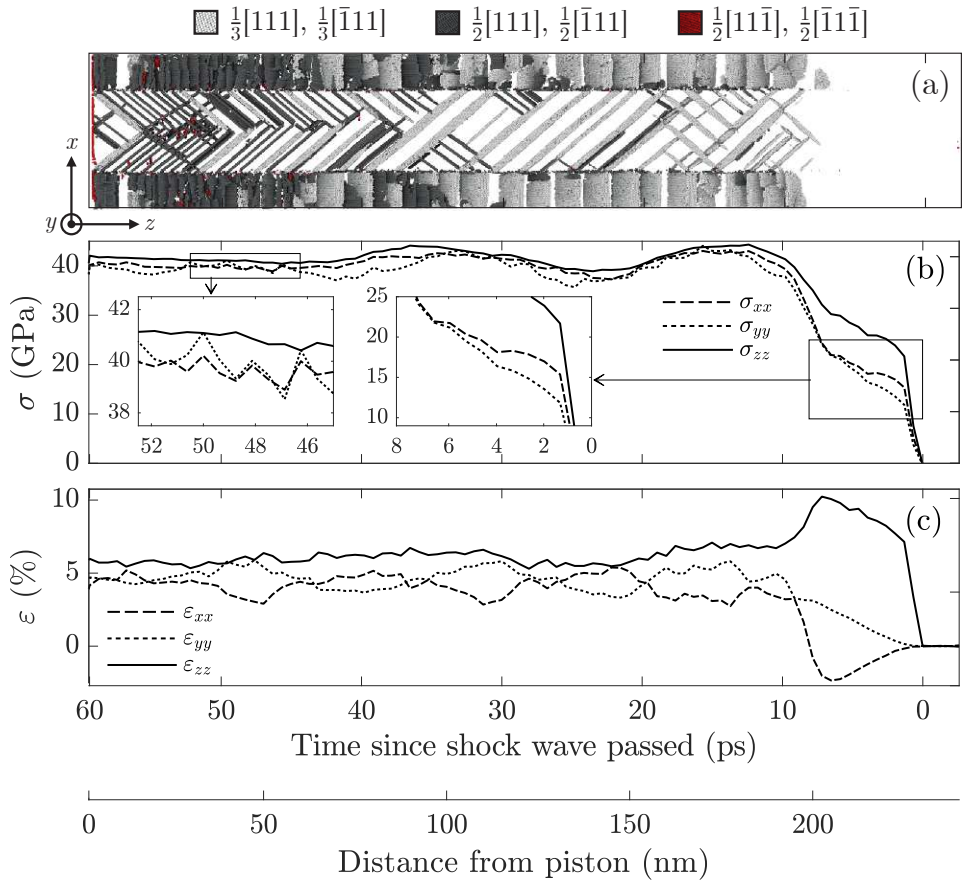

FIG. 4.9. Response of the CB geometry at 40 GPa. (a) Atoms that have undergone plastic flow. Visible are planar deformation twins and slip planes with associated Burgers vectors in the xz-plane (light and dark grey, respectively). The central grain is grain 1, that on the outside is grain 2. (b) Stresses in the central grain. Left and right insets show late-time stresses and stresses within the precursor, respectively. (c) Elastic strains.

another way, the collapse along the y-direction (i.e. $[01\bar{1}]$) that was permitted in the isolated grains by the second stage of plastic deformation can instead be realised by purely elastic compression of each grain by its neighbours. Note that the elastic relaxation mechanism is only able to replace plastic flow because it takes place so quickly – the nucleation of $\frac{1}{2}[\bar{1}11]$ and $\frac{1}{2}[\bar{1}1\bar{1}]$ dislocations takes at least 25 ps at 40 GPa, while the grains can elastically deform normal to the shock within 5 ps.

The second stage of plastic deformation is also suppressed in the HC geometry, though to a lesser extent. While $\frac{1}{2}[11\bar{1}]$ and $\frac{1}{2}[\bar{1}1\bar{1}]$ dislocations are almost entirely absent in the CB geometry, there do exist several such dislocation loops stemming from the grain boundaries in the HC geometry. However, their growth is quickly arrested before they can traverse the grains by the shear stress relief provided by

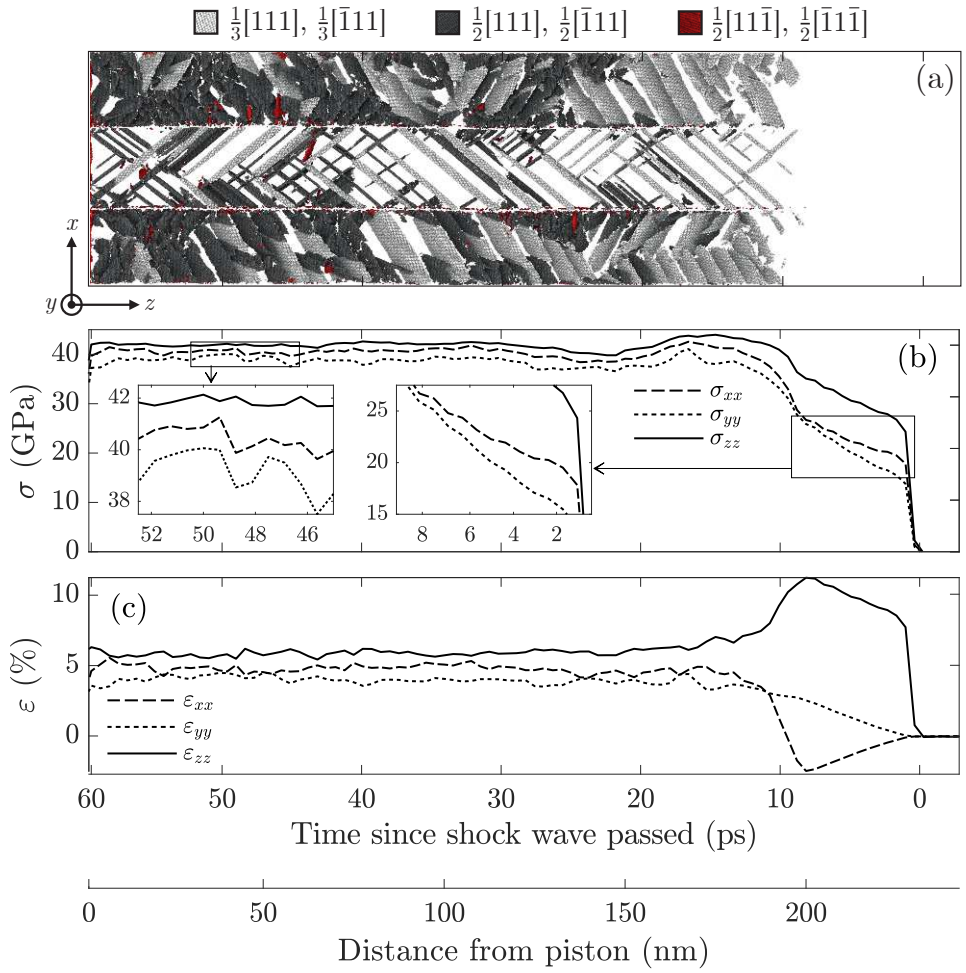

FIG. 4.10. Response of the HC geometry at 40 GPa. (a) Atoms that have undergone plastic flow. Visible are planar deformation twins and slip planes with associated Burgers vectors in the xz-plane (light and dark grey, respectively), and – to a limited degree – nonplanar slip planes with associated Burgers vectors in the xy-plane (red). (b) Stresses in the central grain. Left and right insets show late-time stresses and stresses within the elastic precursor, respectively. (c) Elastic strains.

elastic deformation, so the bulk of the grains remain devoid of $\frac{1}{2}[11\bar{1}]$ and $\frac{1}{2}[\bar{1}1\bar{1}]$ dislocations, as shown in Fig. 4.10. That grains in the HC geometry must rely partially on conventional plastic deformation seems consistent with the observation that elastic deformation is less efficient at relieving shear stress in this latter geometry.

4.5.2 Twinning activation at higher pressure

It was noted in Sec. 4.4 that the stress gradients formed over the grain boundaries in an elastically compressed polycrystal do not relax monotonically, but oscillate

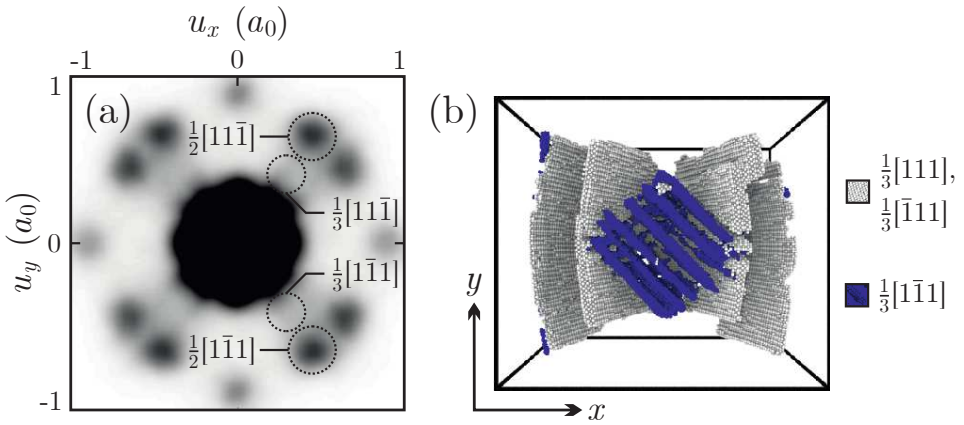

FIG. 4.11. Visualisation of deformation twins in polycrystalline Ta with the CB geometry shocked along [011] to 60 GPa. (a) Cross-section of the slip-vector heatmap in the xy plane. Visible are peaks from dislocation slip in the $[11\bar{1}]$ and $[\bar{1}1\bar{1}]$ directions and (very weakly) the new, transverse deformation twins with Burgers vectors in those same directions. Note the plot is a superposition of slip vectors from all four grains, hence its approximate fourfold rotational symmetry about the origin. (b) Atoms forming the transverse twins (blue) alongside the conventional twins with habit planes $(\bar{2}11)$ and (211) (white) viewed along the loading axis, identified not via SVA but TMT (see Sec. 3.5.5).

about an equilibrium value due to the inertia of the grains. It is thus possible for the transverse stress anisotropy $\Delta\sigma$, and so the shear stress associated with it, to change sign temporarily. If the crystal is shocked with sufficient strength, the inverted shear stress can in fact trigger a new variant of deformation twinning.

Shown in Fig. 4.11(a) is a cross-section of the slip-vector heatmap in the xy plane taken from a CB polycrystal shock-compressed to 60 GPa. The clearest features of the plot are the eight peaks surrounding the origin that correspond to transverse slip in the $[11\bar{1}]$ and $[\bar{1}1\bar{1}]$ directions. The four peaks for which $|u_y| > |u_x|$ (which were previously observed in Fig. 4.2 for the single crystal) come from grains 1 and 4, the other four from grains 2 and 3. In addition to these peaks, it is also possible (though barely) to discern patches of intensity at locations corresponding to $\frac{1}{3}[11\bar{1}]$ and $\frac{1}{3}[\bar{1}1\bar{1}]$, suggesting that deformation twinning of a previously unobserved type is taking place. However, the contrast of these twin peaks at this high shock pressure is extremely poor (for the reasons discussed in Sec. 3.5.4), making reliable identification of the twinned atoms via the SVA technique impractical. For this reason, we will identify the new 'transverse twins' with the complementary template-matching technique described in Sec. 3.5.5, assuming habit planes $(\bar{2}1\bar{1})$ and $(21\bar{1})$. The atoms constituting the transverse twins in the central grain are shown in blue

in Fig. 4.11(b), alongside the 'conventional twins' with habit planes $(\bar{2}11)$ and (211) for reference. Note that the transverse twins form only near the centre of the grain.

To understand how these twins nucleate, we need to know how the shear stress applied to their habit planes varies in the wake of the shock. Fig. 4.12 shows once again the slipped and twinned atoms within a cross-section of the CB polycrystal shocked to 60 GPa on the same scale as the stress and elastic strain profiles for host atoms in the central grain. Just behind the compression front, σ_{zz} and σ_{xx} increase at nearly the same rate, their difference being kept small by continuous plastic flow in the [111] and $[\bar{1}11]$ directions, while σ_{yy} 'lags' as usual due to there being no plastic flow along y. As before, the central grain elastically expands along

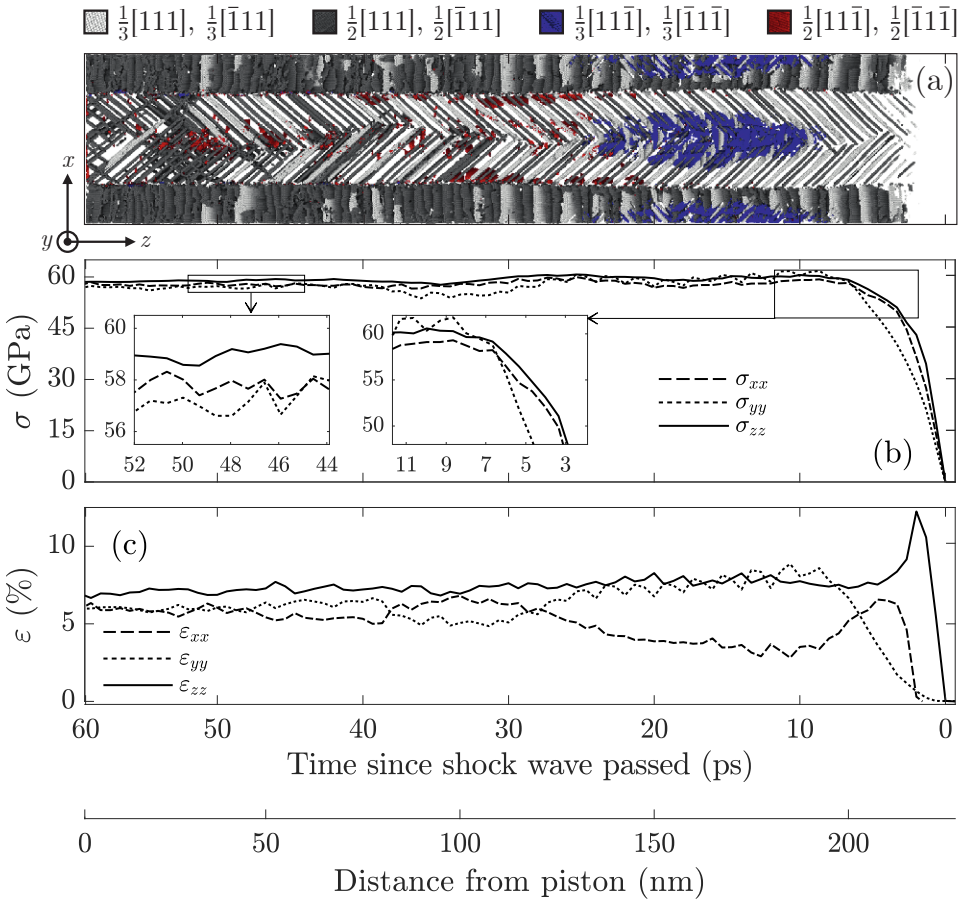

FIG. 4.12. Response of the CB geometry at 60 GPa. (a) Atoms that have undergone plastic flow. Visible are planar deformation twins and slip planes with associated Burgers vectors in the xz-plane (light and dark grey, respectively), and deformation twins with Burgers vectors in the xy-plane (blue), present between 130 and 180 nm from the piston. (b) Stresses in the central grain. Left and right insets show late-time stresses and inversion of the stress state, respectively. (c) Elastic strains.

x and contracts along y in response to the huge stress gradients formed over the grain boundaries, which assume peak values of 10 GPa at around 5 ps compression time, allowing σ_{yy} to converge to σ_{xx}. Crucially, the grain continues to expand once $\sigma_{xx} - \sigma_{yy} \approx 0$ GPa due its inertia, so the transverse stress anisotropy changes sign, as shown in the right inset of Fig. 4.12(b). However, rather than reaching -10 GPa, as might be expected from the SHM-like behaviour of the supercells described in Sec. 4.4, the growth of $\Delta\sigma$ is suddenly arrested at 10 ps once it reaches -2 GPa. At this instant, the resolved shear stress acting on the $(\bar{2}1\bar{1})$ and $(21\bar{1})$ planes is apparently great enough to trigger transverse deformation twinning.

It is the reversal of the sign of $\Delta\sigma$, then, that causes the transverse twins to form. That the crystal refuses to twin when $\Delta\sigma = 10$ GPa, but twins profusely the moment it reaches -2 GPa, is consistent with the so-called *twinning-antitwinning asymmetry* that is characteristic of bcc crystals [178–181]. Were the crystal to relieve transverse shear stress via deformation twinning when $\sigma_{xx} > \sigma_{yy}$, it would have to do so by *antitwinning*, in which adjacent atomic planes move not by the usual $\mathbf{b} = \frac{1}{6}[111]$, but by $-2\mathbf{b}$. Antitwinning is acted against by a large energy barrier, and is thus suppressed under typical stress conditions in Ta loaded along [011]. If ever σ_{yy} exceeds σ_{xx}, though, the sense of the shear stress is such that flow would instead be realised via the usual twinning path. Deformation twinning in this sense, which requires motion through only $\|\frac{1}{6}[111]\|$, has a comparatively small activation energy [54], and thus ensues copiously in the inverted transverse stress state. The process can be understood perhaps most intuitively with an analogy: conventional deformation twins, with habit planes $(\bar{2}11)$ and (211), are formed when the grains are compressed along their [011] axis by the shock; in much the same way, transverse deformation twins, with habit planes $(\bar{2}1\bar{1})$ and $(21\bar{1})$, are formed when the grains are compressed along their local $[01\bar{1}]$ axis by their rapidly expanding neighbours.

It should be stressed, however, that the propensity of the CB polycrystal to undergo transverse twinning is most likely an artefact of its high symmetry. HC polycrystals shocked to a similar pressure do not exhibit profuse twinning of this sort, despite the fact that the *average* stress conditions present in the wake of the shock are comparable (i.e. $\Delta\sigma$ approaches -2 GPa) . The absence of transverse twins in the HC geometry is demonstrated in Fig. 4.13. It seems that the comparatively

low symmetry of this latter geometry gives rise to a delocalized transverse shear stress field whose magnitude is nowhere sufficient to trigger transverse twinning. By contrast, the highly contrived arrangement of grains in the CB polycrystal is such that, when the grains overshoot the mechanically stable state and enter an inverted stress state, shear stress is strongly concentrated at the grain centre. So intense is the concentration, in fact, that at shock pressures exceeding 75 GPa the transverse twinning becomes catastrophic: the closely spaced twins actually coalesce, and form a stable, rhombic grain bounded by planes of the type $(\bar{2}1\bar{1})$ and $(21\bar{1})$. In a real polycrystalline target, then, transverse deformation twinning would likely

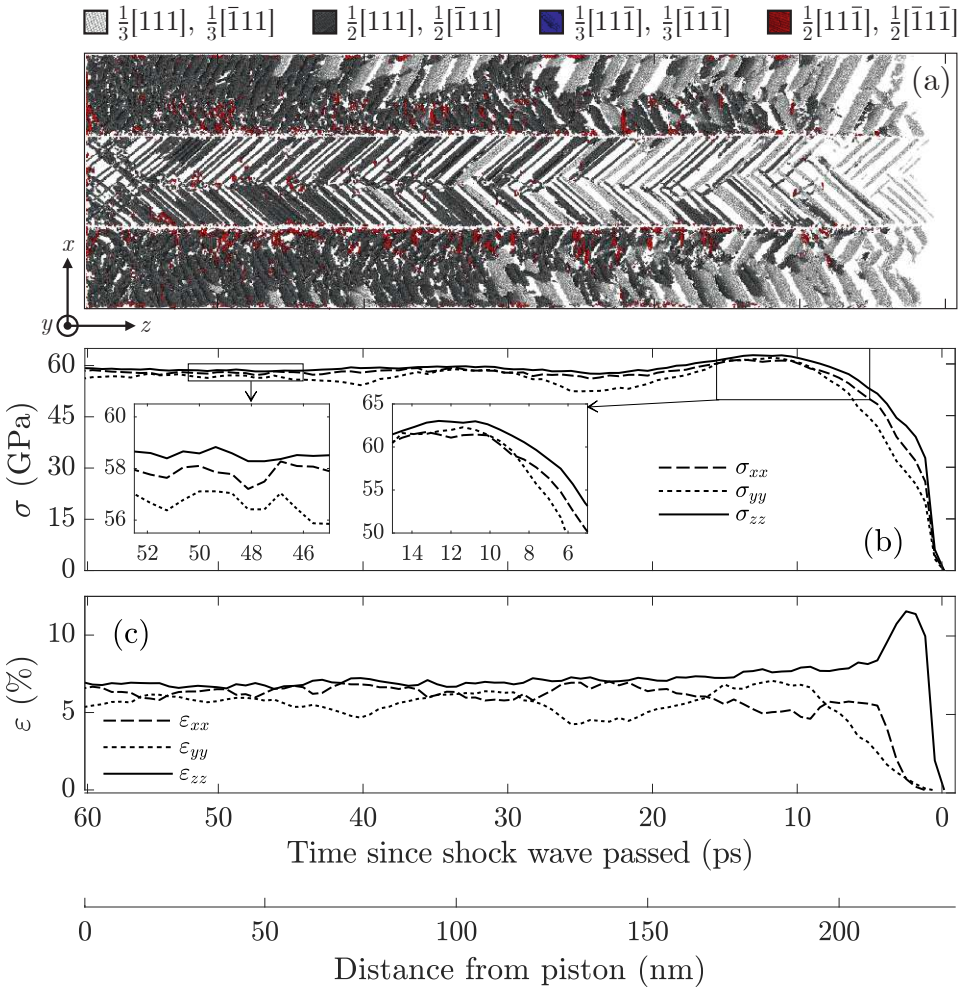

FIG. 4.13. Response of the HC geometry at 60 GPa. (a) Atoms that have undergone plastic flow. Visible are planar deformation twins and slip planes with associated Burgers vectors in the xz-plane (light and dark grey, respectively). (b) Stresses in the central grain. Left and right insets show late-time stresses and inversion of the stress state, respectively. (c) Elastic strains.

be confined to small regions whose grain configuration locally resembles that of a checkerboard polycrystal.

4.5.3 Equilibrium mechanical state

We saw in Sec. 4.4 that when grains are allowed to expand and contract elastically in directions normal to the loading axis, they can reach a state of lower transverse stress anisotropy $\Delta\sigma$ than laterally confined grains loaded above their HEL. Specifically, $\Delta\sigma$ was limited to at least 1.0 GPa by material strength in the single crystals, while σ_{xx} and σ_{yy} could converge to within 0.4 GPa for the elastically loaded polycrystals with the CB geometry. In the section that follows, we will see whether the relief of $\Delta\sigma$ by elastic deformation is still efficient in the plastic regime, and how the efficiency differs between the CB and HC geometries. The transverse *strain* anisotropy $\Delta\varepsilon = \varepsilon_{xx} - \varepsilon_{yy}$ will also be considered, which is crucial if one is to make connections with experiment, because the difference (or lack thereof) between elastic strain components can in principle be extracted directly from diffraction data.

The steady-state stresses and elastic strains were obtained by averaging over the portion of the central grain nearest the piston within which the stress and strain profiles were approximately uniform. At low pressures, the profiles suffer some additional nonuniformity due to the grains continuing to execute small SHM-like oscillations even after plastic flow has ceased. The crystals are sufficiently long, though, that the average is taken over at least five oscillation periods, so the additional variation in σ and ε stemming from the SHM averages to a negligible value. At higher pressures, the sampling region was deliberately truncated so as to avoid the region of the crystal nearer the shock front that has undergone transverse twinning, which will be treated as an artefact.

The steady-state transverse stress and strain anisotropies $\Delta\sigma$ and $\Delta\varepsilon$ are shown in Fig. 4.14 for both the single-crystal control group and polycrystals with the CB and HC geometries over the pressure range 40 to 100 GPa. In all instances, grains in the CB polycrystal exhibit lower transverse stress anisotropy than the laterally confined monocrystals do. The elastic relaxation mechanism described in Sec. 4.4 is therefore still able to relieve transverse shear stress to a greater extent than

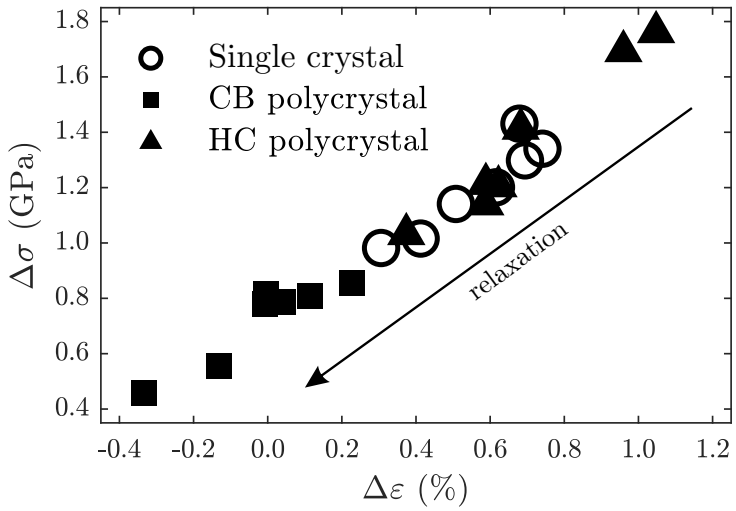

FIG. 4.14. Steady-state transverse stress and strain anisotropies for single crystals and for the central grain of CB and HC polycrystals shocked to between 40 and 100 GPa.

transverse slip in the plastic regime, at least for the CB geometry. However, it is clear that the efficiency of elastic relaxation is much reduced above the HEL: most of the data points taken from the CB geometry lie only slightly below the 1.0 GPa single-crystal limit, and only one of them approaches the limiting value of 0.4 GPa that was reached under elastic loading conditions.

The reduction in efficiency is even more conspicuous in the HC geometry: overall, $\Delta\sigma$ is no lower in the HC polycrystals than in the single-crystal control group, and is in fact markedly *higher* in two instances. There were indications in Sec. 4.4 that the cooperative relaxation mechanism is less effective in the HC than in the CB geometry: Fig. 4.7 showed that, below the HEL, the HC geometry can tolerate relatively large stress gradients due to the countervailing tractions provided by the off-diagonal shear stress σ_{xy}. Fig. 4.15 shows analogous plots of the off-diagonal stress field for CB and HC polycrystals shocked to 60 GPa (i.e. above their HEL). The plots were obtained by calculating $\sigma_{xy}(x, y)$ for notionally relaxed 50-nm-thick cross-sections of the polycrystals every 0.1 ps for 2.5 ps, and then taking the time average – the averaging process somewhat mitigates the considerable noise caused by the thermal fluctuations and spatial inhomogeneities that manifest above the HEL. Once again, we see that shear stress relief is frustrated to a greater degree in the HC geometry owing to the presence of a comparatively intense off-diagonal stress

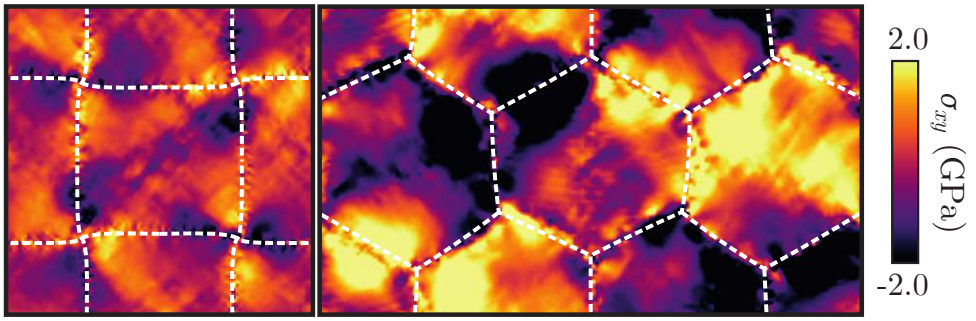

FIG. 4.15. Comparison of the off-diagonal stress field σ_{xy} for (left) CB and (right) HC polycrystals shocked to 60 GPa along z following relaxation of the induced stress gradients. Dashed white lines indicate the approximate locations of the grain boundaries.

field. It is perhaps surprising, though, that the cooperative relaxation mechanism is apparently *completely* ineffectual above the HEL. It is possible that the flow stress of the HC polycrystals is being enhanced by the presence of their grain boundaries (something referred to as the *Hall-Petch effect* [182, 183]) to such an extent that the cooperative relaxation mechanism is effectively nullified. Further simulations, perhaps of polycrystals with a range of grain sizes, would be necessary to verify this.

The strain anisotropy $\Delta\varepsilon$, meanwhile, follows much the same pattern as $\Delta\sigma$: as the difference between σ_{xx} and σ_{yy} decreases, so too does that between ε_{xx} and ε_{yy}. In fact, when $\Delta\sigma$ drops below 0.8 GPa, the difference between the transverse elastic strains actually changes sign. This conspicuous signature of grain interactions could, given an elastic strain extraction technique of sufficient precision, be verified experimentally, assuming the polycrystal in question is well-represented by the CB geometry; conversely, no such signature would exist if the HC geometry were the better representation. Whether or not grain interactions could be observed experimentally via this route therefore depends intimately on the manner in which the grains in the target are oriented and coordinated.

To conclude, it is found that when a laterally confined single crystal and a CB polycrystal are shock-loaded to between 40 and 100 GPa, the grains in the polycrystal always reach a state of lower transverse stress anisotropy, which is reflected in their elastic strain state. By contrast, the stress state of grains in the HC geometry is not significantly different from the state they would assume if they were laterally confined. The efficiency of the elastic relaxation mechanism is thus dependent on the geometry of the polycrystal.

4.6 Discussion

The analysis above has demonstrated that the behaviour of crystallites in a fibre-textured nanocrystal differs profoundly from that of their single-crystal analogues under shock compression. The salient difference between the nanocrystalline and monocrystalline samples, which was discussed in Sec. 4.4 and will be reiterated here, is one of kinematic freedom. An ideal single crystal is translationally symmetric in directions normal to the loading axis. Thus the global constraint of lateral confinement to which it is subjected during uniaxial shock compression must also apply locally; the crystal is *everywhere* laterally confined. It is for this reason that any change in the monocrystal's transverse elastic strain state must be realised via plastic flow. When one moves to an aggregate, translational symmetry is broken, and so lateral confinement need not be respected locally. This permits the grains in the aggregate to respond to shear stresses elastically via interactions with their neighbours, which gives rise to the novel effects described in Sec. 4.5, namely the absence of transverse slip at low pressures, the presence of transverse twinning at high pressures, and relaxation of stress anisotropy in the plane normal to the shock.

Clearly, these predictions should be treated with caution. In an effort to render them amenable to simple analysis and to make as clear as possible their grain interactions, the elementary polycrystals studied here were deliberately constructed with highly idealised morphologies and textures. The price of this simplification was the introduction of a number of artificial behaviours, including coherent oscillation of the grains, and catastrophic transverse twinning in the CB geometry above 60 GPa. Note also that the CB geometry likely exaggerates the extent of the lateral relaxation permitted by grain interactions, because its grains are arranged in such a way that the degree to which the relaxation of one grain frustrates that of its neighbours is minimal. It is not obvious, then, whether the closure of the gap between the transverse strains seen in the CB geometry would be seen in a real polycrystal – one would expect *a priori* that the HC geometry would provide a better representation of a typical target, in which case interactions would make no perceptible difference to the strain anisotropy. Whatever the case, one should anticipate that interaction effects in a real target will be subtler than the CB polycrystals would suggest.

Nevertheless, it is possible to draw a number of qualitative conclusions from this study whose applicability extends beyond the particular targets considered here. First, the grain interactions that take place under shock conditions are clearly dynamic in nature. Their time dependence was made apparent in Sec. 4.4, in which it was shown that the timescale over which neighbouring crystallites interact scaled with the transverse grain size L due to the finite propagation speed of stress waves generated at the grain boundaries. In a similar vein, the transverse twinning observed at higher shock pressures was directly caused by the inertial forces exerted on each grain by its rapidly expanding neighbours. Second, it was shown that grain interactions can radically alter the crystal's stress state. The typical size of the changes to the transverse stresses caused by interactions is comparable to the strength of the stress gradients produced over the grain boundaries by the uniaxial compression, which in the shock regime is frequently of order gigapascals. Since the stress state governs the RSS acting on any given slip or twinning system, grain interactions also influence which of these systems are active, and hence control the dislocation content of the crystal during shock compression. That grain interactions are able partially to govern stress, strain, and defect evolution means they are worthy of inclusion in any predictive model that seeks to recreate material behaviour to better than first order, and they certainly warrant further study in their own right.

4.7 Conclusion

Multimillion-atom molecular dynamics simulations of mono- and nanocrystalline tantalum shock-compressed to between 40 and 100 GPa have been performed. By comparing their response, one can identify a number of physical effects that may be ascribed to interactions between neighbouring grains. We saw that adjacent grains undergo cooperative elastic deformation normal to the shock due to the gigapascal-scale stresses they exert on one another, and are thus able to reach a state of reduced shear stress and strain that would otherwise be made inaccessible by material strength. We further saw that the stress changes precipitated by grain interactions are able to activate and deactivate conventional plasticity mechanisms depending on the shock pressure, and, as a corollary, have some degree of control over the disloca-

tion content of the crystal during compression. In brief, this analysis has shown that the pervasive influence of grain interactions under shock-loading conditions must not be underestimated, and surely deserves further computational study.

CHAPTER 5

Temperature of shock-released tantalum from x-ray diffraction

5.1 Introduction

A shock wave propagating through any sample of finite size will eventually encounter one of its free surfaces. This unconfined boundary, at which the normal stress must be zero[18], is completely unable to support the state of high stress imposed by the shock. Consequently, a rarefaction wave is launched back into the sample that allows it gradually to release to ambient pressure. It is commonly accepted that decompression of this sort takes place isentropically, and is thus attended by a substantial reduction in temperature owing to the thermoelastic effect [184]. This assumption is espoused by a number of textbooks on shock physics [185–188], and is regularly employed in studies interpreting the behaviour of shock-releasing materials [9, 189–195], in many cases without scrutiny or justification. In the following chapter, the results of an experiment are presented in which the post-breakout temperatures of laser-shocked tantalum foils are deduced from their thermal strains via *in situ* x-ray diffraction, and are found to greatly exceed those expected from an isentropic expansion. These results challenge the current consensus that shock release is isentropic.

5.1.1 The assumption of isentropic release

When a substance undergoes adiabatic deformation, two mechanisms dominate the evolution of its internal energy: work may be done on the material by its surroundings (or vice versa) as it changes volume, allowing internal energy to be transferred to and from the substance mechanically; and dissipative processes may manifest, which irreversibly convert macroscopic kinetic energy to internal energy. Uniaxial

[18] Anything comparable to or less than atmospheric pressure ($\approx 10^{-4}$ GPa) is zero as far as shock physics is concerned.

shock release represents an interesting case in which these two mechanisms fight against one another – a releasing crystal constantly loses internal energy via the mechanical work it must exert as it expands, while internal dissipation (in the form of plastic work) vies to pump some fraction of that energy back in. The assertion that release is isentropic is essentially a statement that the energy supplied by dissipation is dwarfed by the energy lost through expansion.

On what physical grounds would one base such an assertion? For a metal, the magnitude of the dissipative heating term is dictated by the substance's resistance to shear flow, i.e. its mechanical strength τ [65, 196, 197]. The rate at which a material does work on its surroundings as it expands, meanwhile, is proportional to the instantaneous pressure p. Hence, for a metal, the ratio of the dissipative and expansive work terms is characterised by the dimensionless ratio $\hat{\tau} = \tau/p$. To claim that release is isentropic, then, is to claim that the typical flow stress during release is negligible compared to the overall stress scale at which the flow is taking place.

This might seem at first sight to be a reasonable assumption to make in the shock regime, as it appears the reduced flow stress $\hat{\tau}$ can be made arbitrarily small simply by scaling up the shock pressure. Indeed, this is essentially the historical argument that was used to establish the isentropic treatment of release. In their pioneering work of 1955 on obtaining equations of state from shock wave measurements, Walsh and Christian [9] prefaced their discussion with the following statements: "Since shock pressures are several hundred times the yield points of the materials involved, an ordinary 'fluid' type equation of state is assumed ... this assumption precludes the explicit treatment of effects arising from the material rigidity which, however, are felt to play a negligible role in the description of the states in the present pressure range". These sentiments are echoed in the comprehensive text of Zel'dovich and Raizer (first published in 1964), whose treatment of shock release in solids [185] is preceded by the following: "We shall also assume that the shock wave is not too weak, so that we can neglect effects associated with the strength of the solid ... this assumption [that the stress is isotropic] is valid when the pressure is large in comparison with the ultimate strength, the critical shear stress, etc.". Simply put, these authors were arguing that the reduced flow stress $\hat{\tau}$ falls as one pushes further into the shock regime, thereby establishing the isentropic picture of release that is

used extensively today.

It is implicit in the treatments of both Walsh and Christian [9] and Zel'dovich and Raizer [185] that the flow stress itself is not significantly altered by the shock-loading process. While there may have been little reason to doubt this at the time, there is now a substantial body of evidence to suggest that material strength increases dramatically in the shock regime, due to a confluence of several physical effects.

First, it is now well-established that the yield stress of a metal increases significantly with pressure. At the extreme densities accessible via shock compression, an atom in the core of a gliding dislocation must pass considerably closer to its neighbours during a slip event than it would do under ambient conditions. The nearer the atoms are forced to pass, the greater the associated energy cost, and so the larger the *Peierls barrier* the dislocation must overcome in order to continue moving. Diamond anvil cell studies have demonstrated that when compressed to pressures of around half a megabar, this pressure-hardening effect alone[19] can elevate a crystal's flow stress by several gigapascals [198–201].

Contemporary methods have also made it clear that work hardening becomes extreme in the shock regime. During the reversed plastic flow that takes place during shock release [48, 59], the motion of each dislocation is impeded by an extremely dense tangle (or *forest*) of neighbouring dislocations left in the wake of the shock, whose density, according to MD simulations, can easily reach 10^{13} cm^{-2} at shock pressures of tens of gigapascals [47, 54, 112]. By using dislocation dynamics simulations to estimate the strength of the interaction between impinging dislocations, one can infer that defect densities of this magnitude will cause work hardening on the order of gigapascals [98].

The third effect contributing to the enhancement of strength in the shock regime is its extraordinary scaling with strain rate. In the quasistatic limit, the mobility of a metal's dislocations is owed primarily to the action of thermal fluctuations, which occasionally give the dislocations a helpful kick over the otherwise insurmountable Peierls barrier. In such a regime, the flow stress scales logarithmically (i.e. slowly) with strain rate. However, once the imposed strain rate surpasses around 10^4 s^{-1} [97], the rapidly moving dislocations transition from the thermal activation to the

[19] Some caution is required when interpreting the results of these DAC studies, as not all of them explicitly separate the hardening owed purely to pressure from that due to work hardening.

so-called *phonon drag* regime, under which they encounter strong resistance to their motion via the scattering of phonons. The flow stress thence scales linearly and rather quickly with strain rate, and is expected to reach the gigapascal scale in the ultrahigh strain-rate regime ($\dot{\varepsilon}^p \gtrsim 10^7$ s^{-1}) [97, 202]. Note that although the strain rates present in a broadening rarefaction fan are admittedly somewhat lower than those behind the shock itself, if the target is small enough (on the scale of microns, say), the fan will still be relatively steep, and thus release will still be extremely rapid. This point will be explored in greater detail in Chapter 6.

When one considers the cooperation of these three strengthening mechanisms, one is given ample reason to doubt the premise that shock release is always isentropic.

5.1.2 Temperature as a route to diagnosis

Given a sample of material that has just released from the shock state, how might one deduce whether or not it did so isentropically? A crystal that releases nonisentropically does so because it experiences substantial heating via internal dissipation. One's first thought, then, might be to assess the temperature of the crystal, and compare its value with that calculated assuming an isentropic release (which can be done, for instance, using the Grüneisen formalism [203]). How best to measure the temperature of shock-compressed condensed matter is actually something of an open question. The most widely used diagnostic technique is currently optical pyrometry, in which the temperature of a sample (or that of its surface, at least) is calculated from the intensity of the thermal radiation it emits. This method's main shortcoming is that it is heavily reliant on one's knowing the sample's emissivity, which is likely to be altered by the shock compression process itself. EXAFS, another established thermometric technique [204], exploits the oscillatory structure exhibited by the x-ray absorption coefficient close to an absorption edge to infer a material's temperature. While thought to be more accurate than pyrometry in the temperature range pertinent to the solid state, EXAFS is also relatively imprecise. Two further diagnostics exploiting the Debye-Waller effect [205, 206] and the inelastic scattering of x-rays by phonons [207] are actively being explored as possible means of resolving the temperature measurement problem.

In the experiment described in this chapter, a rather different and somewhat ad hoc temperature diagnostic technique will be used that exploits the high-quality x-ray diffraction data provided by an XFEL. The underlying reasoning is very simple. Using Bragg's law, one can calculate the distance between any set of diffracting crystal planes from the angle at which they scatter the incident x-ray beam. It is therefore possible to deduce the crystal's volume from its diffraction pattern. Since the released crystal is no longer under pressure, any change to its volume must be attributed to thermal expansion[20]. Hence, if one knows the crystal's thermal expansion coefficient, one can deduce its temperature after release. In the following chapter, the results of an experiment will be presented in which this method is used to infer the temperature of fibre-textured tantalum foils that have released from a megabar shock state. The temperature extraction algorithm (a full derivation and verification of which will be presented) predicts that the foils' temperature is completely inconsistent with a standard isentropic release, and thus challenges the textbook treatment of this fundamental thermodynamic process.

5.2 Experimental setup

The experiment described in this chapter was executed at the Matter in Extreme Conditions (MEC) endstation of the Linac Coherent Light Source (LCLS) facility. The MEC instrument allows one to load samples dynamically to hundreds of gigapascals by exposing them to a high-power optical laser, and simultaneously to illuminate them with an exceptionally bright x-ray beam, from which one can obtain time-resolved diffraction images of the sample in its compressed state. A schematic of the experimental setup is shown in Fig. 5.1.

5.2.1 MEC laser system

The long-pulse laser system at MEC comprises four high-power, frequency-doubled (527 nm) neodymium-glass pulsed optical lasers whose beams may be overlapped at a spot between 100 and 250 μm in diameter on a target's surface. The energy carried by the beams, which ranges between around 5 and 25 J, is deposited into this tiny

[20] Things are actually a little more complicated than this, as we shall see.

area over the course of 5 to 10 ns. The resulting compression wave launched into the target [which Eq. (2.80) suggests will have a strength of order 1 Mbar = 100 GPa] generally requires a finite distance over which to steepen into a steady shock, which can easily be accommodated for by placing a few microns of ablator material between the lasers and the target proper (see Sec. 5.2.2 below). The ablation pressure supporting the shock is sustained for as long as the surface plasma continues to absorb energy from the optical drive beam, which, as noted, lasts around 10 ns.

5.2.2 Target design

A schematic cross-section and closeup image of the multilayer targets used here is shown in Fig. 5.2. The target proper is a 6-μm-thick foil of fibre-textured polycrystalline tantalum. These foils are fabricated via vapour deposition onto a thin silica substrate at an elevated temperature of 450°. The temperature and crystallographic

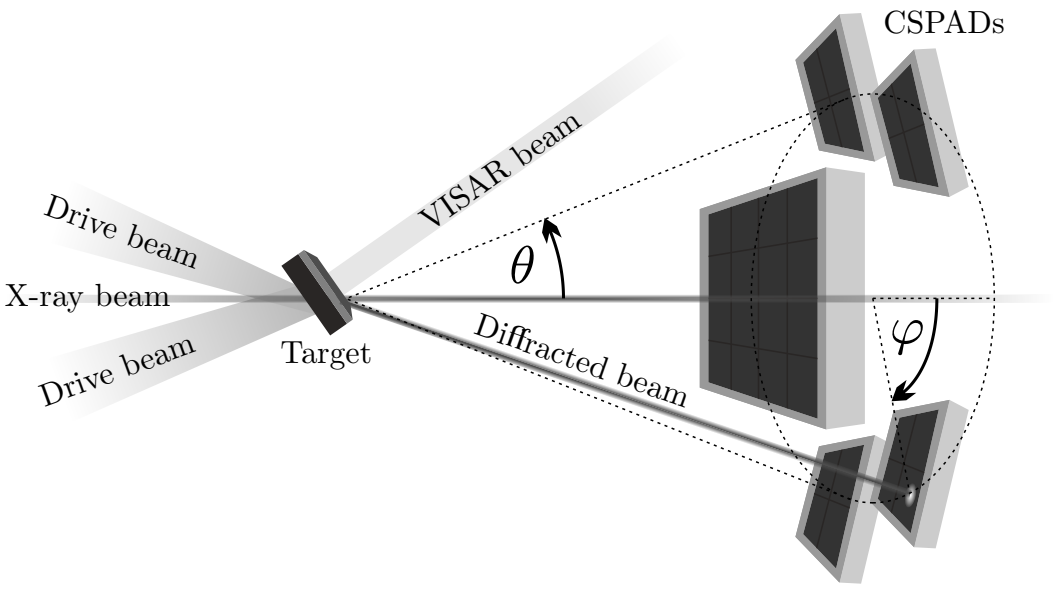

FIG. 5.1. Experimental configuration for release studies of polycrystalline tantalum. Optical drive beams launch a shock of megabar strength into a target comprising a 50-μm-thick polyimide ablator and a 6-μm-thick fibre-textured tantalum foil. The target is probed with 50-fs pulses of 9.6 keV x-rays whose resulting diffraction pattern is recorded by a set of Cornell-SLAC pixel array detectors (CSPADs) [208]. A velocity interferometer system for any reflector (VISAR) [209] is used to monitor the foil's rear surface velocity. A beam diffracted at angles θ and φ is shown for reference.

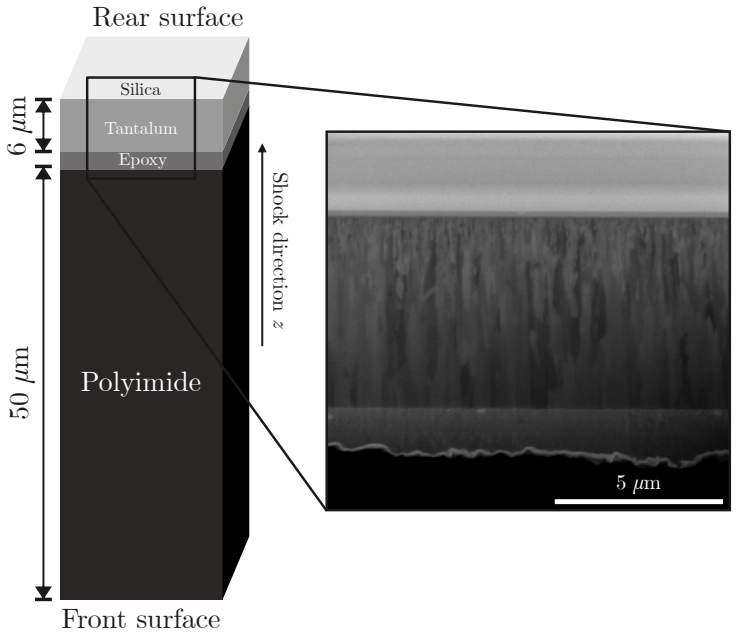

FIG. 5.2. Cross-section and high-resolution image (obtained via scanning electron microscopy) of a typical layered target. A [011]-fibre-textured, 6-μm-thick polycrystalline tantalum foil is grown on a thin SiO_2 substrate and subsequently attached with a layer of epoxy to a 50-μm-thick layer of polyimide. This foil happens to have failed to delaminate from its silica substrate, which ordinarily would not be present during the experiment.

orientation of the substrate are such that the deposited tantalum forms long, thin grains whose [011] directions are closely aligned (to within 1°) with the substrate's surface normal, but whose orientations around this axis are approximately randomly distributed. When the foils are cooled to room temperature after reaching their required thickness, the mismatch between their thermal expansion coefficient and that of silica causes the substrate to delaminate from the foil. When driven, the shock wave travels along the foil's surface normal. This means each grain is compressed along its [011] direction, like the crystals simulated in the previous chapter.

Attached to the front surface of the tantalum foils is a 50-μm-thick layer of polyimide. The purpose of the ablator is twofold. First, it provides the compression wave generated by the optical lasers with a 'runway' over which to steepen into a steady shock before entering the tantalum foil. The ablator also gives adequate time for smoothening out of any irregularities in the shape of the shock front, which are caused by the speckle pattern of the drive laser spot. Actually, 50 μm of ablator is more than long enough to regularise the shock – the reason the ablator is so thick compared to the foil is that, when the shock wave reaches the polyimide-tantalum

interface, a counterpropagating secondary shock wave is launched back into the ablator. This reverberation will run along the length of the ablator and back again, and subsequently enter the foil, complicating its compression state. For this reason, the polyimide layer is made thick enough that the tantalum foil will have undergone its full shock-release load cycle before the reverberation can reach it.

5.2.3 LCLS x-ray source

The primary diagnostic for this experiment is x-ray diffraction. The XFEL at LCLS produces 50-fs-long pulses of monochromatic[21] x-rays in a beam with a transverse dimension of only 20 μm. The x-ray spot is aligned to the centre of the optical laser spot, as shown in Fig. 5.3, thus allowing one to probe the uniaxially compressed portion of the target behind the shock front. The diffracted signal is collected by a number of Cornell-SLAC Pixel Array Detectors (CSPADs) [208] placed around the

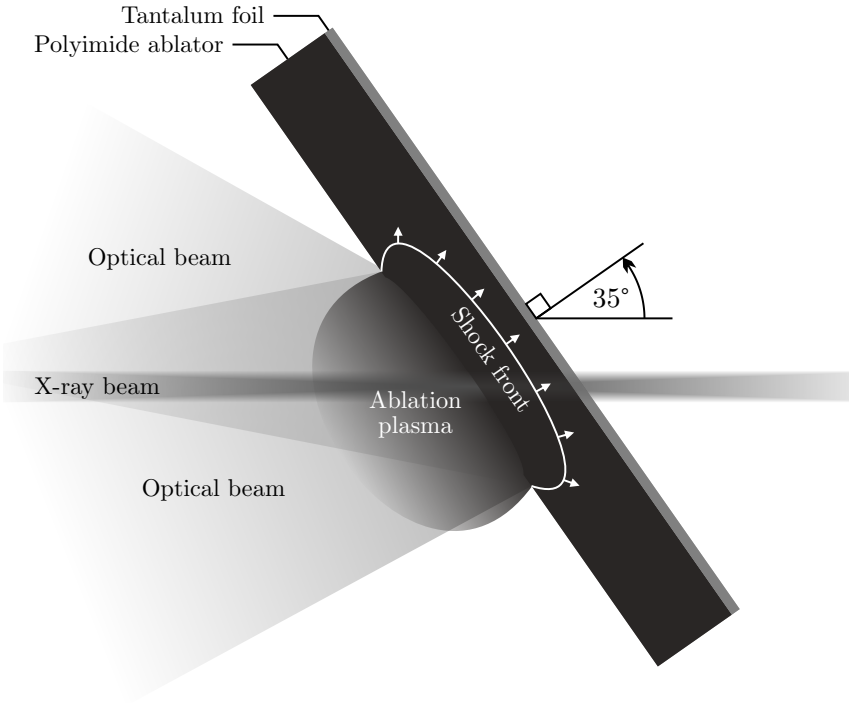

FIG. 5.3. Closeup of the target-beam interaction region. Energy deposited by the high-intensity optical beams drives ablation of the target's front surface, thus generating a shock wave that is approximately planar over the width of the optical spot (of order 100 μm). The shocked region is probed by an intense x-ray beam of around 20 μm diameter. The target thicknesses and various beam diameters are shown approximately to scale.

[21] The typical bandwidth of the beam is just 0.2% of its central frequency.

target within the interaction chamber. The intensity of the signal across the surface of the detectors will be expressed using (θ, φ)-coordinates, where 2θ is the angle made by the direction of the incident beam with the vector joining the target to the position on the detector, and φ is the azimuthal coordinate expressing the position of the detector 'around' the incident beam – these angles are illustrated in Fig. 5.1. The length of time after activating the optical laser beams one waits before firing the XFEL can be varied, allowing one to obtain time-resolved diffraction images of the target at different stages during shock and subsequent release.

LCLS can provide x-rays with energies anywhere between 2.5 and 12 keV. The energy chosen for this experiment represents a tradeoff between two competing criteria. Broadly speaking, higher frequency photons are preferable, for two reasons: one can probe a greater volume of reciprocal space with a higher-energy beam, i.e. one can in principle measure a greater number of diffraction peaks, allowing one better to constrain the strain state of the target; and the x-ray absorption cross-section decreases quickly with increasing energy (notionally according to an inverse cube law [210]), meaning higher-energy x-rays are more penetrative and thus give a stronger diffraction signal. However, one also needs to account for the presence of tantalum's L-edges (located at approximately 9.9, 11.1, and 11.7 keV), above which the absorption cross-section jumps by a factor of 2.5 [211]. The energy chosen for this experiment was $E_\nu = 9.6$ keV, which is the highest energy one can obtain while still safely avoiding the first L-edge at 9.9 keV.

Although the majority of the x-ray beam is confined to the 20-μm-wide spot centred on larger optical drive spot, scattering in the beryllium lenses that focus the beam generates a weak 'halo' of x-rays that fall well outside the drive spot. This halo thus always diffracts from unshocked material. While the ambient diffraction peaks generated by the halo might ordinarily be considered a nuisance, they are actually quite helpful for our purposes, because they provide a 'calibrant' from which the volume change undergone by the foil following release can be deduced.

5.2.4 VISAR

The secondary diagnostic is VISAR [209], a technique that uses laser interferometry to monitor the velocity of the rear surface of the target. Shock breakout is marked by a sudden increase in the free-surface velocity and thus has a clear signature in the VISAR trace. The time at which shock release begins (relative to the moment at which the drive lasers were fired) can thus be found, and used to judge when to fire the XFEL beam so as to catch the sample while it is releasing. The post-breakout free-surface velocity deduced from VISAR can also be used to infer the shock pressure in the foil, using pretabulated Hugoniot data (i.e. the U_P - p relation).

5.3 Representative release data

Shown in Fig. 5.4(a) is an archetypal shock-release XRD image of a target loaded to 190 GPa taken approximately 0.5 ns after shock breakout. The CSPADs capture scattering intensity from the three most widely spaced families of bcc atomic planes, namely {011}, {200}, and {211}. Despite its being polycrystalline, we see that the sample generates diffraction peaks that are highly localised in the azimuthal direction. This, as explained in Sec. 2.2.5, is owed to the strong fibre texture of the foils, which restricts the distribution of crystallographic orientations represented in the sample and thus confines the scattering signal to narrow arcs along the Debye-Scherrer ring. The feature of the data in which we are interested here is that each scattering peak is dispersed over a broad range of θ (i.e. Bragg) angles. This is because under release conditions one observes diffraction from a distribution of density states. To illustrate this idea, consider the $\{01\bar{1}\}$ peaks depicted in Figs. 5.4(b-c). Shortly before shock breakout [Fig. 5.4(b)], the x-ray beam is most strongly scattered with a Bragg angle of 18.2° that exceeds the ambient Bragg angle (16.1°) due to the crystal's being compressed. This can be understood with reference to the Bragg condition, which states that the angle of scattering from a given set of crystal planes, 2θ, increases as their transverse separation d decreases according to $\sin\theta = \lambda/2d$. As the crystal starts to rarefy following shock breakout [Fig. 5.4(c)], its interplanar spacings increase, causing the diffraction intensity to shift back to

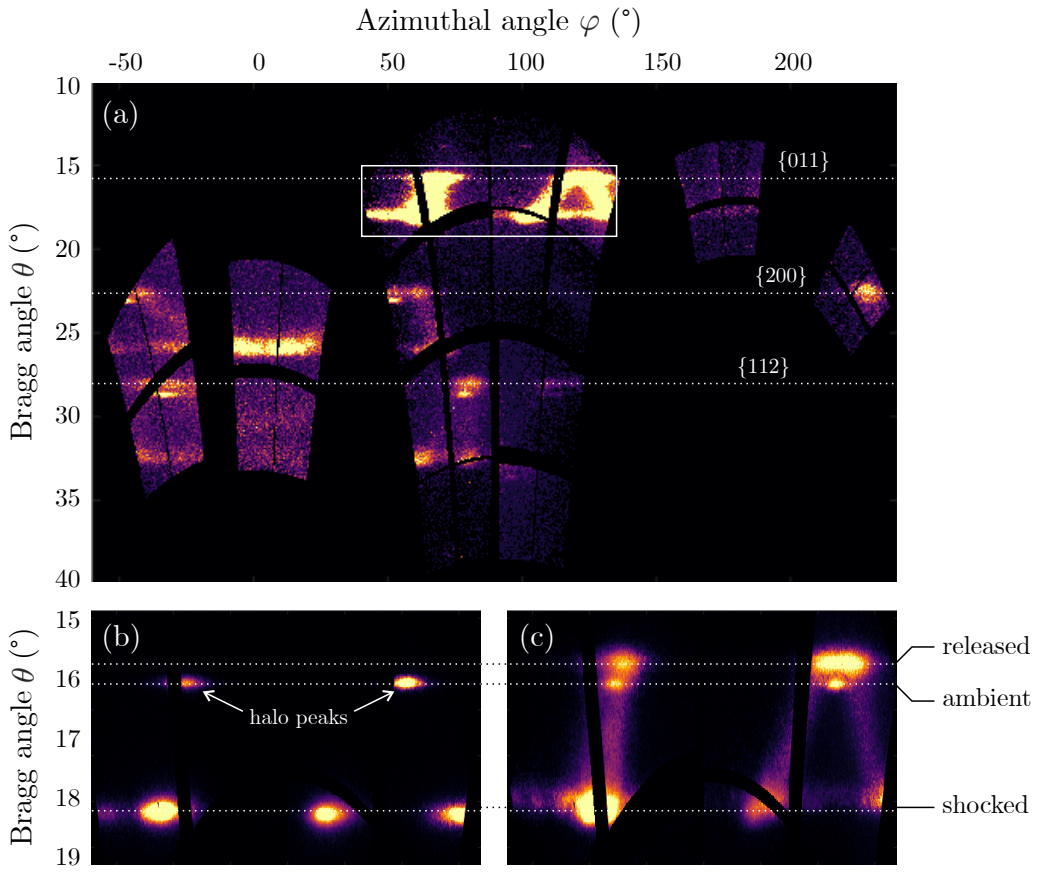

FIG. 5.4. Representative x-ray diffraction data from fibre-textured tantalum shocked to 190 GPa. (a) Data collected during release by the full set of CSPADs, showing the {011}, {200}, and {112} peaks. (b) and (c) show closeups of the {011} peaks shortly before and after breakout, respectively. Peaks arising from shocked, released, and unshocked material illuminated by the halo are indicated.

lower values of 2θ, until finally reaching a limiting value of 15.7° when the crystal has fully released. Since the top and tail of a release wave are separated by a considerable distance (unlike in a shock), we see appreciable diffraction not only from shocked and released material, but from the gamut of intermediate density states.

What is interesting is that the Bragg angle to which the signal returns once the rarefaction process is complete is lower even than that from ambient material. This can readily be seen in Fig. 5.4(c) by comparing the lowermost θ value taken by diffraction signal from the release fan with that of the halo peaks. According to Bragg's law, this overall decrease in scattering angle indicates that the fully released material is less dense than it was before it was shocked[22]. What is the origin of

[22] A study by Turneaure and Gupta [212] showed that the decreased scattering angle of the peak parallel to the loading direction can be explained by material strength, and does not necessarily

this expansion? We know that the free-surface boundary condition imposed by the sample's unconfined rear surface forces the normal stress σ_{zz} within the released portion of the sample to fall to zero. The expansion we observe relative to the ambient state is not caused by tensile stress, then, but must be largely thermal in origin. This is to say that the targets are 'hot' following shock-release.

It should be noted that, in and of itself, the observation that the targets undergo net heating during a shock-and-release load cycle is not surprising. However, precisely *how* hot the targets are after release depends on the nature of the shock-release process. Suppose the sample has initial pressure $p_1 = 0$, temperature T_1, and entropy $S_1 = S(p_1, T_1)$. Fig. 5.5 illustrates the thermodynamic paths taken by the sample as it progresses between the ambient, shocked, and released states, which are labelled 1, 2, and 3, respectively. Upon shock compression to some pressure $p_2 > p_1$, the sample's entropy increases to $S_2 > S_1$, and its temperature follows suit. What happens when the sample subsequently releases from this shock state? Assuming the release process proceeds adiabatically, the change in entropy suffered by the sample is zero at the very least, and thus $S_3 \geq S_2$ (the equality holding in the special case

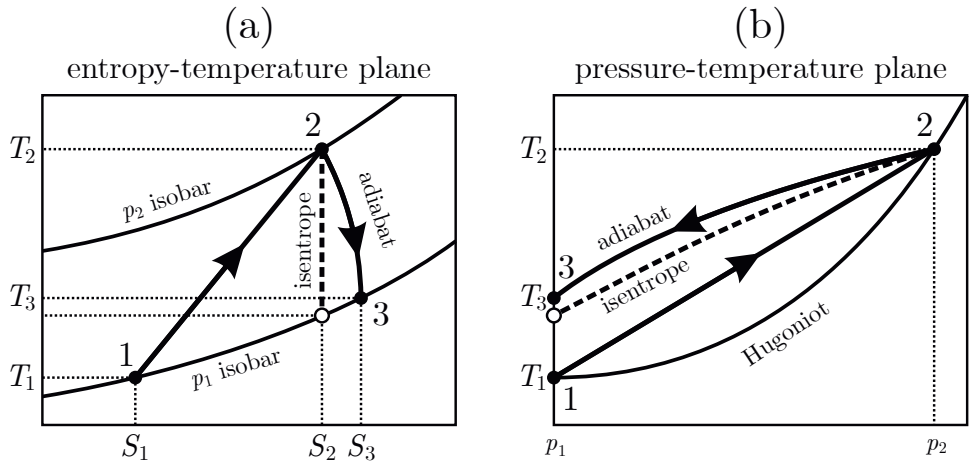

FIG. 5.5. Schematic depictions of the thermodynamic path taken by a crystal undergoing shock and subsequent release in (a) the entropy-temperature plane and (b) the pressure-temperature plane. In state i, the crystal has pressure p_i, temperature T_i, and entropy $S_i = S(p_i, T_i)$; states 1, 2, and 3 denote the ambient, shocked, and released states, respectively. The dashed line depicts the special case of an isentropic release. Note that the arrow signifying the shock-compression is intended only to guide the eye, as no meaningful path can be assigned to such a highly nonequilibrium process.

imply an overall increase in the sample's volume. Here, however, we observe that *every* Bragg peak shifts to lower 2θ, no matter its direction, meaning the targets really are less dense than ambient material.

of an isentropic, reversible release). To calculate the post-release temperature, we follow the release adiabat until it encounters the $p = p_1$ isobar. Since the gradient of the isobar in the entropy-temperature plane is always positive[23], the post-release temperature T_3 is strictly greater than T_1, which is to say that the sample is *always* hotter than it was pre-shock. However, the extent of the difference between T_3 and T_1 depends on the entropy change suffered by the sample on release: it assumes its minimum value when the release is isentropic, and increases the more entropic it is.

To calculate the temperature of a crystal from its diffraction image is conceptually simple: one first obtains the density of the target by measuring its scattering angles and employing Bragg's law to infer its interplanar spacings; then, one infers the temperature required to effect the observed change in density (relative to the ambient state) using the sample's known thermal expansion coefficient α_V. There are, however, a few subtleties that complicate the calculation for a shock-released metal. It was demonstrated in the previous chapter that under shock-compression conditions the two transverse components of stress σ_{xx} and σ_{yy} tend to 'lag behind' the longitudinal component σ_{zz} due to the crystal's strength (i.e. its ability to support shear stresses). There is good reason to believe that the same behaviour will manifest to some degree during shock release – while the free-surface boundary condition may compel σ_{zz} to vanish, one should not assume that σ_{xx} or σ_{yy} will do so. Not only, then, does the sample not truly release to the $p = 0$ isobar, but its stress state is not even hydrostatic. Under these circumstances, the volume change undergone by the crystal is not *exclusively* attributable to thermal expansion. In the following section, a more general prescription for converting diffraction peak positions to temperatures will be formulated for situations where small, residual, nonhydrostatic stresses may be present.

[23] One may show that $(\partial T/\partial p)_S = TV\alpha_V/C_p$, which is positive for any 'well-behaved' substance.

5.4 Temperature extraction algorithm

5.4.1 Calculating temperature from elastic strains

The defining property of the shock-released material is that it experiences no stress along the loading direction:

$$\sigma_{zz} = 0. \tag{5.1}$$

Fundamentally, this stress comprises two parts. The first is a compressive component owed to thermal motion of the atoms, which tends to cause the crystal to expand. The second is a tensile, 'cold' component due to the attractive interactive forces between nearby atoms, which counteracts the expansive effect of the 'thermal' stress. The cold component of σ_{zz} is essentially determined by the elastic strain state of the crystal. Once these strains have been determined from the sample's XRD image, and the cold stress calculated, one can ask: how hot must the crystal be to generate sufficient thermal pressure to balance exactly this tensile stress? One thus has a means of inferring the crystal's temperature T given its elastic strain ε. It is this balance between cold and thermal stresses (ordinarily encoded entirely by the thermal expansion coefficient) that we wish to formalise.

Usually, a state variable like σ_{zz} would be treated as a function of (say) V and T only. In order to allow for material strength, one must augment this description such that σ_{zz} is allowed to vary independently with each component of the crystal's elastic strain:

$$\sigma_{zz} = \sigma_{zz}(\varepsilon_{xx}, \varepsilon_{yy}, \varepsilon_{zz}, T). \tag{5.2}$$

A small change to σ_{zz} is therefore given by

$$d\sigma_{zz} = \underbrace{\left(\frac{\partial\sigma_{zz}}{\partial\varepsilon_{xx}}\right) d\varepsilon_{xx} + \left(\frac{\partial\sigma_{zz}}{\partial\varepsilon_{yy}}\right) d\varepsilon_{yy} + \left(\frac{\partial\sigma_{zz}}{\partial\varepsilon_{zz}}\right) d\varepsilon_{zz}}_{\text{cold component}} + \underbrace{\left(\frac{\partial\sigma_{zz}}{\partial T}\right) dT.}_{\text{thermal component}} \tag{5.3}$$

It is useful first to recast the various thermodynamic derivatives in Eq. (5.3) into forms containing material properties with which we are more familiar.

The derivatives of the form $\partial\sigma_{ij}/\partial\varepsilon_{kl}$ are simply the isothermal elastic constants:

$$d\sigma_{zz} = C_{13}d\varepsilon_{xx} + C_{23}d\varepsilon_{yy} + C_{33}d\varepsilon_{zz} + \left(\frac{\partial\sigma_{zz}}{\partial T}\right)dT. \tag{5.4}$$

These moduli depend on the sample's orientation, but may always be expressed as linear combinations of the three independent cubic elastic constants c_{11}, c_{12}, and c_{44}. As in the previous chapter, we will adopt the convention that the crystallographic directions aligned with the x, y, and z axes are [100], [01$\bar{1}$], and [011] respectively. In this case, one may show (see Appendix B) that the elastic constants in this frame are related to those in the $\langle 100\rangle$ frame (denoted by minuscule c's) via

$$C_{13} = c_{12}, \tag{5.5}$$

$$C_{23} = \frac{1}{2}(c_{11} + c_{12} - 2c_{44}), \tag{5.6}$$

$$C_{33} = \frac{1}{2}(c_{11} + c_{12} + 2c_{44}). \tag{5.7}$$

We turn now to the thermal derivative $(\partial\sigma_{zz}/\partial T)_V$. Tantalum is cubic, and so stress increases at the same rate in all directions when it is isochorically heated[24]. This allows us to make the replacement $(\partial\sigma_{zz}/\partial T)_V = (\partial p/\partial T)_V$, in which case we can exploit the thermodynamic triple product rule:

$$\left(\frac{\partial p}{\partial T}\right)_V \left(\frac{\partial T}{\partial V}\right)_p \left(\frac{\partial V}{\partial p}\right)_T = -1. \tag{5.8}$$

Using the volumetric thermal expansion coefficient $\alpha_V = 1/V\,(\partial V/\partial T)_p$ and the isothermal bulk modulus $K = -V(\partial p/\partial V)_T$, the above may be rewritten as

$$\left(\frac{\partial p}{\partial T}\right)_V = K\alpha_V. \tag{5.9}$$

The bulk modulus may in turn be expressed as $K = (c_{11} + 2c_{12})/3$.

We now integrate the differential $d\sigma_{zz}$ along the release path and demand that the result vanish, in accordance with the free-surface boundary condition [Eq. (5.1)].

[24] The notion that the thermal stress is isotropic is actually an approximation. If, as we anticipate, the crystal supports shear stress, its cubic symmetry is broken, and so the rate at which stress along a given axis increases when the crystal is isochorically heated depends on the direction of the axis. Under these circumstances, $(\partial\sigma_{zz}/\partial T)_V$ is orientation dependent. However, due to the lack of data on the anisotropy of tantalum's thermal properties, we will assume that the thermal pressure is indeed isotropic.

Re-expressing the thermodynamic derivatives in terms of the elastic constants $\{C_{ij}\}$ and the linear thermal expansion coefficient $\alpha_L = \alpha_V/3$, this condition may be expressed as

$$0 = \int \left[\frac{c_{12}}{c_{11}+2c_{12}} d\varepsilon_{xx} + \frac{c_{11}+c_{12}-2c_{44}}{2c_{11}+4c_{12}} d\varepsilon_{yy} + \frac{c_{11}+c_{12}+2c_{44}}{2c_{11}+4c_{12}} d\varepsilon_{zz} + \alpha_L dT \right]. \tag{5.10}$$

This expression of the free-surface boundary condition is the means by which we convert elastic strains to temperatures. As a sanity check, one can show that if the release is hydrostatic (i.e. $d\varepsilon_{xx} = d\varepsilon_{yy} = d\varepsilon_{zz}$), Eq. (5.10) reduces, as expected, to

$$\varepsilon(T) = -\int_{T_0}^{T} dT' \, \alpha_L. \tag{5.11}$$

To compute the line integral in Eq. (5.10) exactly would require knowledge of how α_L and $\{c_{ij}\}$ vary with both strain and temperature. To make the calculation tractable, some simplifying assumptions about these material properties will be made. First, the dependence of the thermal expansion coefficient and elastic moduli on density will be neglected entirely. The volumetric strain observed on release (relative to ambient density) is typically of order 1%. The variation of α_L and $\{c_{ij}\}$ over this density range is perhaps 2% at most for tantalum [115], meaning the errors introduced by using their ambient-volume values are largely negligible. By contrast, one cannot ignore their temperature dependence: the temperature after release may be a few thousand Kelvin (as will be shown), which can effect changes to α_L and $\{c_{ij}\}$ of several tens of percent [213, 214]. We can, however, treat the elastic constants as being *effectively* insensitive to temperature, for the following reason. Though tantalum's moduli decrease by up to 25% between 300 and 3000 K [214], the impact of their temperature dependence is tempered considerably by the fact that they only ever appear in ratios in Eq. (5.10). For illustration, consider a crystal with representative late-time elastic strains of $(\varepsilon_{xx}, \varepsilon_{yy}, \varepsilon_{zz}) = (-0.2, +0.4, -1.3)\%$. If one assumes its elastic moduli always assume their room-temperature values, one infers from Eq. (5.10) a release temperature of $T = 3010$ K. If instead one uses their values at 3010 K, one gets $T = 2820$ K. Therefore the 'true' temperature is presumably about midway between these two estimates, i.e. $T \approx 2915$ K. The error of 95 K

one introduces by making the room-temperature approximation of $\{c_{ij}\}$ amounts to only 3% of the final estimate of T in this case. Therefore the approximation of the moduli by their ambient values is adequate for our purposes.

In addition to these assumptions about its material properties, two further approximations will be made of the crystal's elastic deformation state. First, the residual shock-induced rotation ψ exhibited by the crystal following release (3° or so) will be neglected, meaning [011] is indeed parallel to compression axis, and Eqs. (5.5-7) for the elastic moduli are accurate. This approximation is justified because the corrections to the moduli go as $\psi^2 \approx 10^{-3}$ to leading order. The second assumption made is that the transverse strains ε_{xx} and ε_{yy} are approximately equal on release, which appears to be reasonable so far as one can tell from the diffraction data. Together, these two assumptions essentially state that the elastic deformation gradient is expected to take the form $F^e = I - \mathrm{diag}(\varepsilon_{xx}, \varepsilon_{xx}, \varepsilon_{zz})$.

After implementing these simplifications and substituting in the ambient elastic constant values of $c_{11} = 264$ GPa, $c_{12} = 160$ GPa and $c_{44} = 82$ GPa [105], Eq. (5.10) simplifies to

$$0.497\,\varepsilon_{xx} + 0.503\,\varepsilon_{zz} = -\int_{T_0}^{T} dT' \alpha_L(T'). \tag{5.12}$$

Note that the strains are combined quite differently to how one might have combined them naively, i.e. by simply taking their arithmetic mean $(2\varepsilon_{xx}+\varepsilon_{zz})/3$. In Sec. 5.4.3, it will be shown how great a difference doing the calculation carefully as above actually makes.

5.4.2 Calculating elastic strains from diffraction patterns

With x-ray diffraction, one can measure directly the spacing (and orientation) of any set of crystallographic planes, provided they satisfy the Bragg condition. Each one of these spacings encodes in some manner the crystal's underlying elastic deformation gradient F^e. By obtaining measurements of sufficiently many reflections, one can constrain the elements F^e, which may comprise up to nine independent components in general. The following section briefly describes a simple equation with which one can infer from a set of measured interplanar spacings a simplified deformation gradient $F^e = \mathrm{diag}(F_{xx}, F_{xx}, F_{zz})$.

Under the action of some real-space deformation gradient F^e, a crystal's reciprocal lattice transforms according to $[(F^e)^T]^{-1}$ [25]. An ambient reciprocal lattice vector $\mathbf{G}_0$ can therefore be related to its post-deformation value $\mathbf{G}$ via

$$\mathbf{G}_0 = (F^e)^T \mathbf{G}. \tag{5.13}$$

To introduce the interplanar spacing $d = 2\pi/G$, it is useful to 'square' both sides:

$$G_0^2 = \mathbf{G}^T F^e (F^e)^T \mathbf{G} \tag{5.14a}$$

$$= F_{xx}^2 (G_x^2 + G_y^2) + F_{zz}^2 G_z^2. \tag{5.14b}$$

Re-expressing the components of $\mathbf{G}$ in polar coordinates, one finds

$$G_0^2 = G^2 (F_{xx}^2 \sin^2\chi + F_{zz}^2 \cos^2\chi) \tag{5.15a}$$

$$= G^2 [F_{xx}^2 + (F_{zz}^2 - F_{xx}^2) \cos^2\chi], \tag{5.15b}$$

where χ is the angle made by the diffracting plane normals with the compression direction. To make this formula more convenient, the new polar angle χ can be expressed in terms of the planes' original polar angle χ_0. Given that $\cos\chi = G_z/G$ and $\cos\chi_0 = (F_{zz} G_z)/G_0$,

$$\cos\chi = \frac{G_0}{G} \frac{1}{F_{zz}} \cos\chi_0. \tag{5.16}$$

Substituting this expression into Eq. (5.15b) and collecting terms involving G_0/G, we find

$$\left(\frac{G_0}{G}\right)^2 = \frac{F_{xx}^2}{1 - (F_{zz}^2 - F_{xx}^2) F_{zz}^{-2} \cos^2\chi_0}. \tag{5.17}$$

Since both F_{xx} and F_{zz} will be close to unity even for reasonably strong shocks, the combination $F_{zz}^2 - F_{xx}^2$ is much less than unity, so the expression above can be approximated using the leading terms of its binomial expansion:

$$\left(\frac{G_0}{G}\right)^2 \approx F_{xx}^2 + (F_{zz}^2 - F_{xx}^2) \left(\frac{F_{xx}}{F_{zz}}\right)^2 \cos^2\chi_0. \tag{5.18}$$

By expanding the expression above to leading order in the shear strain $(F_{zz} - F_{xx})$,

[25] This follows almost trivially when one considers that the inner product of the real and reciprocal lattice vectors must by definition satisfy $\mathbf{a}_i^T \mathbf{b}_j = 2\pi\delta_{ij}$ (see Sec. 2.1.3).

it can further be shown that the ratio F_{xx}/F_{zz} can be approximated by unity. Replacing the magnitudes of the reciprocal lattice vectors G and G_0 with their corresponding interplanar spacings d and d_0, we arrive at our final expression to which to fit the experimental data:

$$\left(\frac{d}{d_0}\right)^2 \approx F_{xx}^2 + (F_{zz}^2 - F_{xx}^2)\cos^2\chi_0. \tag{5.19}$$

This formula provides a simple means of inferring F^e from the data. For each reflection (hkl), one calculates its ambient spacing and polar angle via $d_0 = 2\pi/\|(hkl)\|$ and $\cos\chi_0 = (hkl)\cdot(011)/[\|(hkl)\|\|(011)\|]$, and then measures its new spacing d using Bragg's law, $2d\sin\theta = \lambda$. A linear regression analysis may then be performed on the data using the equation above, allowing F_{xx} and F_{zz} to be extracted from the fitted intercept and gradient.

5.4.3 Demonstration of algorithm on synthetic diffraction

In the previous two sections, a prescription for calculating the release temperature of a crystal from its late-time diffraction image was derived: one first estimates the sample's longitudinal and transverse strains from the distribution of its scattering angles via Eq. (5.19), and then infers T by demanding that the tensile longitudinal stress associated with these elastic strains balance the temperature-dependent thermal pressure, using Eq. (5.12). It is natural to be dubious about the accuracy of these equations when one considers the number of approximations upon which they are reliant. Before applying it to real experimental data, this technique will first be applied to synthetic diffraction data from a simulated crystal, whose release temperature is of course known from its constituent atoms' velocity distribution. It will be shown that this temperature can be predicted very well (provided the elastic strains are determined accurately enough), thus validating the technique.

The crystal on which the temperature extraction algorithm was tested is essentially a scaled-up version of the single crystals described in the previous chapter. This larger crystal has dimensions of $33.1 \times 33.2 \times 5960$ nm^3, and contains some 362 million atoms. This crystal also differs in that it was modelled under the Ravelo Ta2 potential [54], whose thermal properties are more accurate than those of the

Ta1 potential employed in the previous chapter; the distinction is not too important for the purposes of verifying the temperature algorithm, but will become so when a detailed account of the crystal's temperature evolution is given in the next chapter. As before, a constant-velocity piston was used to compress the crystal, in this instance to approximately 100 GPa. The crystal was simulated for long enough that an appreciable fraction of it could release back to ambient pressure.

Fig. 5.6 shows the variation of the crystal's longitudinal stress σ_{zz} and temperature T as a function of distance from the piston at $t = 1.7$ ns (approximately 0.5 ns after breakout). The variation of σ_{zz} makes plain the structure of the rarefaction wave, and illustrates that, by this time, the last micron of material reaches the fully released state, for which $\sigma_{zz} \approx 0$. We see that the temperature of the sample in this released region is elevated considerably above room temperature, and is in fact only slightly lower than the on-shock temperature of 1750 K. We shall not dwell on the details of the temperature profile here; a full account will be given in the following chapter. The feature of interest here is the average temperature of the fully released material, which is $T_{\text{target}} = 1560$ K.

To emulate diffraction from this monocrystal's fibre-textured polycrystalline analogue, the FTFT described in Sec. 3.4.3 was used. Fig. 5.7 compares the syn-

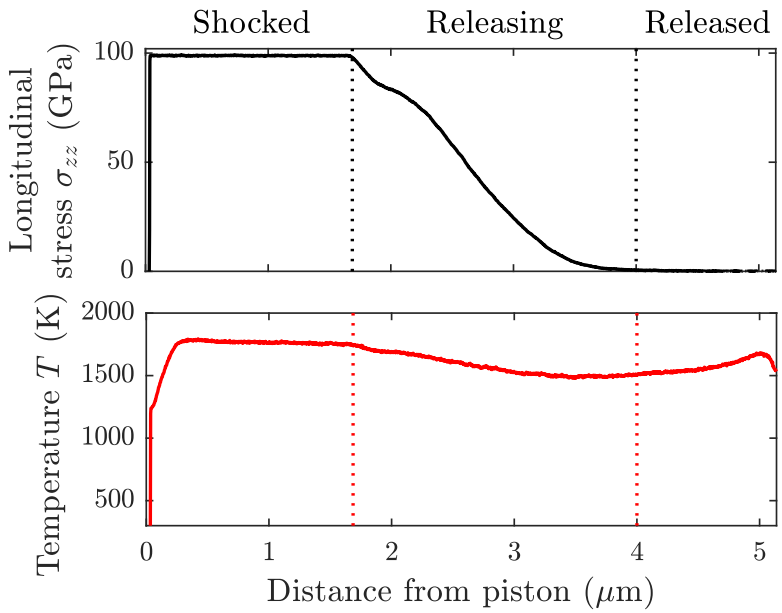

FIG. 5.6. Variation of longitudinal stress and temperature for a 6-μm-long tantalum monocrystal loaded along [011] to 100 GPa at around 0.5 ns after shock breakout.

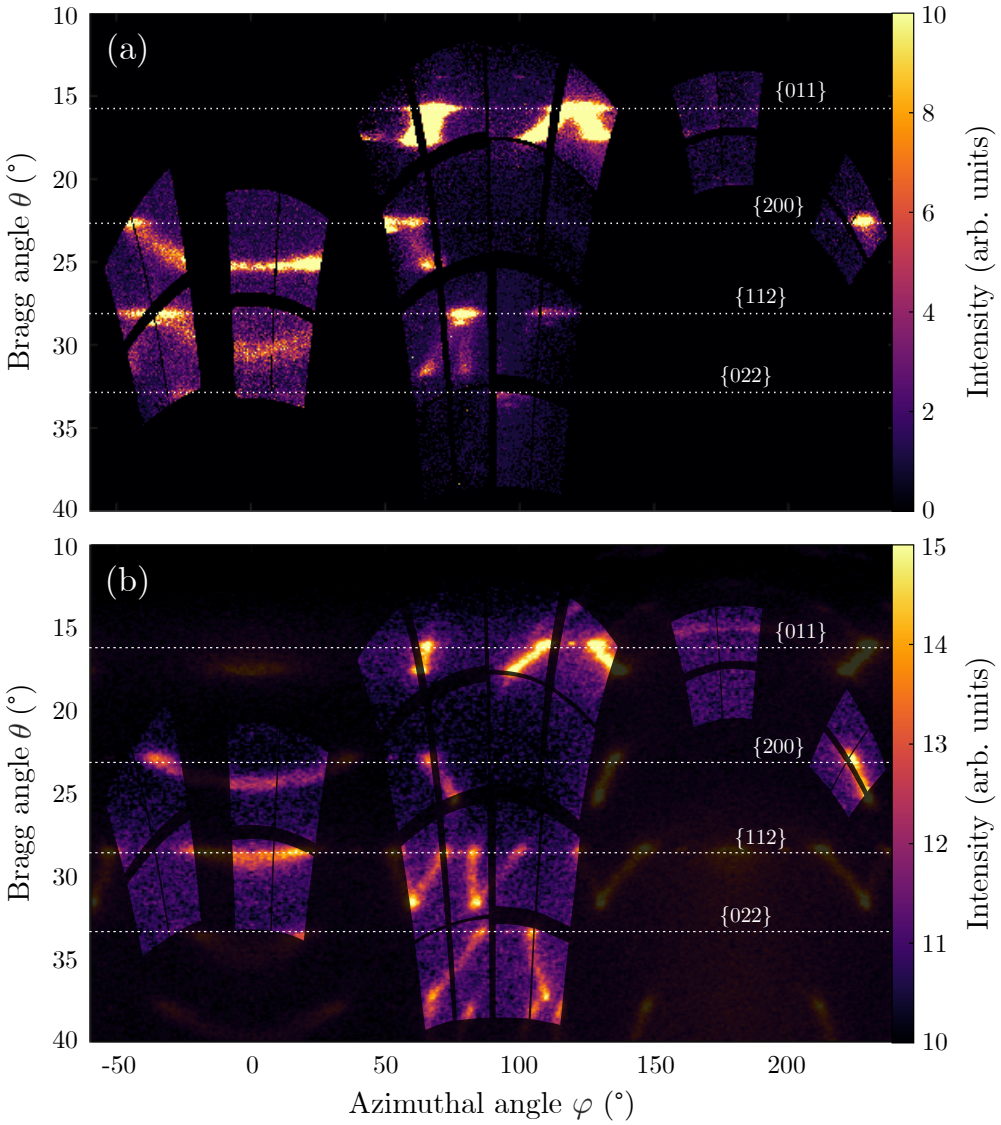

FIG. 5.7. Comparison of diffraction data (a) experimentally obtained from a shock-releasing fibre-textured tantalum foil using an XFEL and (b) synthesised from an MD simulation of a tantalum monocrystal using an augmented Fourier transform [see Eq. (3.15)]. Both the real and simulated crystals are releasing from around 100 GPa. A largely opaque mask has been added to the synthetic data to emulate the gaps between the detectors.

thetic diffraction pattern obtained from the 100 GPa shock-release simulation using Eq. (3.15) with experimental data taken from a shot at a comparable shock pressure. The synthetic pattern actually imitates the data reasonably well. Several differences are apparent: the experimental peaks are slightly wider in the azimuthal direction due to the foil's not having a perfect fibre texture; the 'splitting' of the peaks from the released material is greater in the synthetic data, which means the simulation predicts greater residual rotation than is observed experimentally; the

synthetic data does not exhibit the same attenuation with increasing Bragg angle, due to its omission of various elements like the atomic form factor; and there are no halo peaks in the synthetic data. These details aside, the qualitative agreement is good, meaning the simulated pattern can be treated as a fair representation of the kind of diffraction data obtained from experiment.

Let us now attempt to extract the crystal's elastic strains from its synthetic diffraction pattern via Eq. (5.19). First, a set of reflections from the {011}, {200}, and {112} families is chosen, as illustrated in Fig. 5.8(a). The scattering signal in the vicinity of these peaks is azimuthally integrated to yield a one-dimensional signal $f(\theta)$. The peak from the fully released material is fitted to a pseudo-Voigt profile, for which the intensity is assumed to vary with Bragg angle according to

$$f_{PV}(\theta) = w \underbrace{\frac{1}{1 + \left(\frac{2\tilde{\theta} - 2\theta}{\delta\theta}\right)^2}}_{\text{Lorentzian}} + (1 - w) \underbrace{\exp\left[-\ln 2 \left(\frac{2\tilde{\theta} - 2\theta}{\delta\theta}\right)^2\right]}_{\text{Gaussian}}, \tag{5.20}$$

where w determines the relative weights of the Lorentzian and Gaussian contributions, $2\tilde{\theta}$ is the peak centre, and $\delta\theta$ is the intrinsic linewidth. Note that the peak from the released material is markedly asymmetric due to bleeding of the diffraction signal from *nearly* released material near the foot of the rarefaction wave. To mitigate its influence, much of the right wing of the peak is excluded from the fitting routine, as shown in Figs. 5.8(b-i). The central scattering angle $2\tilde{\theta}$ is then used to infer the interplanar spacing d of the diffracting planes. Following Eq. (5.19), the dimensionless combination $(d/d_0)^2$ is finally plotted against $\cos^2\chi_0$ for each reflection and analysed using linear regression. This final step is shown in Fig. 5.8(j).

By inspecting the values assumed by the fit at $\chi_0 = 0°$ and 90°, it can be seen that the released portion of the simulated crystal has an average transverse elastic strain ε_{xx} close to zero, and a tensile longitudinal strain ε_{zz} of approximately 1%. The simulated crystal thus exhibits some degree of residual strength following release, and is also of slightly lower density than ambient, just as the true targets are. If one were to infer the crystal's release temperature using the average of the elastic strains extracted from the regression [$\varepsilon_{xx} = (0.07 \pm 0.05)\%$, $\varepsilon_{zz} = (-0.91 \pm 0.11)\%$] and the linear thermal expansion coefficient of Ta2 (4.02×10^{-6} K^{-1}), one would obtain a value

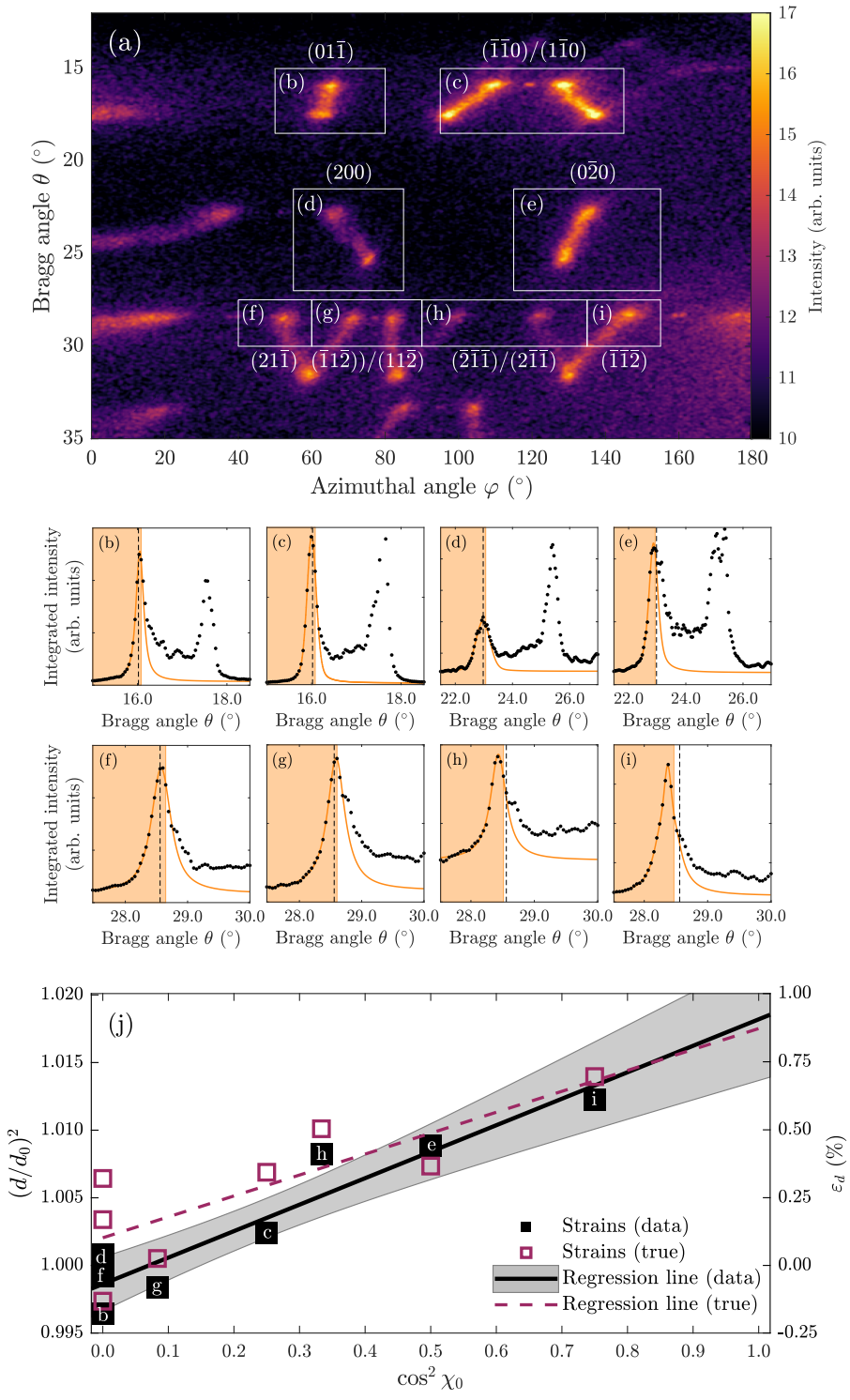

FIG. 5.8. The temperature extraction algorithm. (a) Sampling regions selected from the simulated diffraction pattern of a crystal releasing from 100 GPa. (b-i) Azimuthally integrated signals within each sampling region. Peaks from the released material are fitted to a pseudo-Voigt profile (orange curves) using mostly their left wing (orange regions). Vertical dashed lines mark the ambient Bragg angles. (j) Interplanar spacings d and strains ε_d inferred from either release peak positions (black points) or from the real-space elastic deformation gradient F^e (purple points) expressed as a function of the original angle made by the plane's normal with the target normal, χ_0. Strains extracted from the linear regression are converted to a release temperature using Eq. (5.12).

of $T_{\text{naive}} = (940 \pm 100)$ K. If instead one properly accounts for the nonhydrostaticity of the crystal's strain state using Eq. (5.12), one obtains $T_{\text{measured}} = (1350 \pm 130)$ K. This estimate is considerably closer to the known value of 1560 K, but still not quite consistent to within error.

To find out where the algorithm could be failing, the linear regression analysis and subsequent steps can be repeated using the 'known' elastic strains of the released portion of the crystal, obtained not from its synthetic diffraction pattern but directly from its real-space elastic deformation gradient. The true interplanar spacings obtained from the known strains of $(\varepsilon_{xx}, \varepsilon_{yy}, \varepsilon_{zz}) = (-0.32, +0.13, -0.87)\%$ are plotted alongside their respective values of $\cos^2 \chi_0$ in purple in Fig. 5.8(j). Note that the true spacings are almost always greater than the spacings inferred from diffraction. The strains extracted from the linear regression are $\varepsilon_{xx} = -0.10\%$ and $\varepsilon_{zz} = -0.87\%$. Using these strains, one infers from Eq. (5.12) a temperature of $T_{\text{cheat}} = (1510 \pm 210)$ K. This captures very well the target value of 1560 K.

If this algorithm has a flaw, then, it lies not in its conversion of the elastic strains to a temperature, but in the actual extraction of the elastic strains from the diffraction pattern. Fig. 5.8(j) shows that the peak fitting technique systematically underestimates the crystal's tensile strains, and thus underestimates the extent of the thermal expansion. This is surely caused by the asymmetry of the released peaks – the scattering intensity from material near the foot of rarefaction wave likely shifts each peak's centre to slightly higher values of θ, and thus gives the impression that the released material is a little more compressed than it really is. Indeed, when this entire calculation was repeated using diffraction data synthesised from the released portion of the crystal *only*, the release peaks were symmetric, and T_{measured} agreed with T_{target} to within error. This shortcoming of the temperature extraction algorithm, which is caused by its crude fitting of the diffraction signal to a single peak from a unique strain state, should be borne in mind in the section that follows. The upshot is that the release temperatures quoted, while likely correct to within a few hundred degrees, will tend to underestimate the true release temperature.

5.5 Temperatures from experiment

The release temperature extraction algorithm will now be applied to real data from targets shock compressed to between 1 and 2 Mbar. One additional step is required for the experimental data, and that is to determine the on-shot x-ray energy E_ν. This can be achieved by fitting the locations of the halo peaks using pseudo-Voigt profiles [see Eq. (5.20)] and using their associated plane spacings (known from the ambient lattice constant of tantalum) to calculate $E_\nu = hc/\lambda$ using Bragg's law. The uncertainty in λ combines with the uncertainty in the elastic strains to yield the full error on the temperature measurements.

In Fig. 5.9 is shown the release temperature inferred from XRD as a function of shock pressure for samples probed at the latest $\Delta t = 1.2$ ns after shock breakout – within this time, at most $C_0 \Delta t \approx 4$ μm of material has completely released (where C_0 is the ambient bulk sound speed [214, 217]), meaning the rarefaction fan is still propagating through the targets, and no reverberation from the ablator-foil interface should have taken place. Shown also in Fig. 5.9 is the locus of shock states and corresponding isentropic release states. Both loci were calculated by

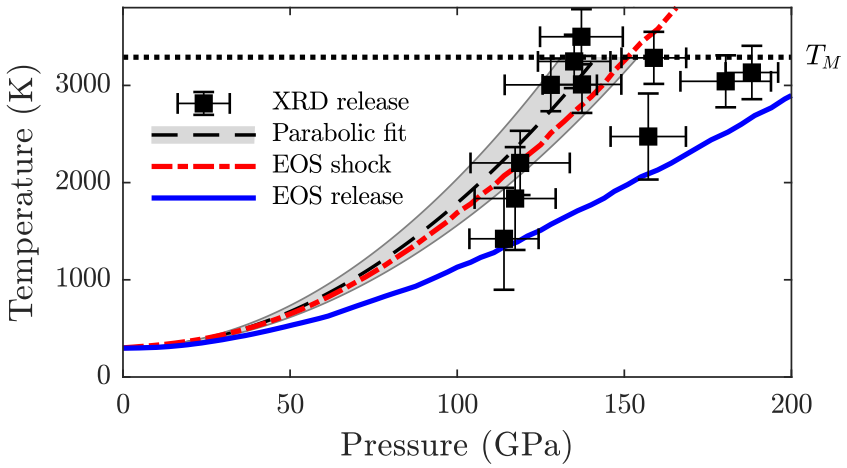

FIG. 5.9. Release temperature inferred from XRD as a function of shock pressure for tantalum foils probed less than 1.2 ns after shock breakout. The data for which $p <$ 150 GPa are fitted to a parabola whose 95% confidence interval is shaded grey. Shown also are the locus of shock and corresponding isentropic release states predicted from SESAME equation of state 3520 [215], and the value of tantalum's ambient-pressure melt temperature $T_M = 3270$ K [216].

solving the Rankine-Hugoniot equations[26] using a high-pressure equation of state for tantalum [215]. We observe that in all cases, the inferred release temperature exceeds the theoretical isentropic release temperature by some margin. In fact, the data follow more closely the Hugoniot itself (up to 150 GPa at least), suggesting that a substantial heating mechanism is active during shock release that largely counteracts expansive cooling.

To make more concrete the notion that the data statistically exclude the release isentrope, we can use Bayesian inference to calculate the confidence interval of a simple phenomenological fit to the data. The fit we will use is a parabolic one of the form $T_{\text{fit}}(p|\kappa) = 300\ \text{K} + \kappa p^2$. In Bayesian regression, the fit parameter κ is treated as a random variable whose distribution is informed by the data and their associated uncertainties. The posterior probability distribution of κ is given by

$$P(\kappa|\text{data}) \propto P(\text{data}|\kappa)P(\kappa), \tag{5.21}$$

where $P(\text{data}|\kappa)$ is the likelihood of observing the data for the given value of κ, and $P(\kappa)$ is the prior (i.e. uninformed) distribution of κ, which, given the absence of any readily available information about the phenomenological constant κ, we will simply take to be uniform. The likelihood function $P(\text{data}|\kappa)$ is given by

$$P(\text{data}|\kappa) \propto \prod_i \exp\left[-\frac{(T_i - \tilde{T}_i)^2}{2\sigma_{T_i}^2} - \frac{(p_i - \tilde{p}_i)^2}{2\sigma_{p_i}^2}\right], \tag{5.22}$$

where (p_i, T_i) is the location of the i^{th} data point, $(\tilde{p}_i, \tilde{T}_i)$ is its notional 'true' location, and σ_{p_i} and σ_{T_i} are its associated uncertainties. The uncertainty in the shock pressure σ_{p_i} was calculated for each shot using the variance of the pressures obtained by sampling different regions of the VISAR signal. The temperature uncertainty σ_{T_i} has two dominant components: there is first the error in the measurement of the elastic strains from the diffraction pattern, which is deduced using the residuals of the regression curve, as in the previous section; and there is appreciable uncertainty in the x-ray beam energy E_ν, which is derived from errors in the measurement of the halo peak locations. To estimate the true location of point i (the location it

[26] To calculate the isentropic release temperature using an EOS and the Rankine-Hugoniot equations, one essentially treats the release as a series of consecutive miniature shocks [218].

would have were it not displaced from the curve T_{fit} by statistical noise), an ellipse with major axes in the ratio $\sigma_{p_i} : \sigma_{T_i}$ is drawn centred on point i and expanded until it touches the curve; the tangential intersection is taken to be $(\tilde{p}_i, \tilde{T}_i)$. This 'true' position varies depending on the location of the curve, and thus varies with κ.

Iterating the calculation above over a set of values of κ yields the posterior probability distribution $P(\kappa|\text{data})$, which is approximately a Gaussian with some maximal (i.e. most likely) value κ_0. To calculate the fit parameter's confidence interval, the distribution was normalised and then integrated over the interval $[\kappa_0 - \delta\kappa, \kappa_0 + \delta\kappa]$ until the cumulative probability reached 0.95. The range of parabolic fits with values of κ between the limits $\kappa_0 \pm \delta\kappa$ is plotted in grey in Fig. 5.9, along with the most probable fit itself (for which $\kappa = \kappa_0$). Note that the fitting was only performed on data for which the shock pressure was less than 150 GPa, because the release temperature appears to saturate above this pressure (as will be discussed shortly). The confidence interval clearly excludes the locus of isentropic release states. From the experimental data we must therefore conclude that these tantalum foils undergo shock release in a strongly irreversible manner.

The conclusion that shock release is nonisentropic runs contrary to the textbook picture of the process, and should therefore be treated with some scepticism. The temperature extraction algorithm was verified in principle in Sec. 5.4.3. Although it was noted that it will generally tend to underestimate the target's release temperature, this is not a problem as far as our conclusion is concerned, as it means that the crystals are probably *at least* as hot as suggested. Even so, the data points are few, and rather scattered. To provide further confidence in our conclusion, we can turn once again to molecular dynamics. The final part of this chapter will present the results of some preliminary MD simulations that model a highly simplified version of release in monocrystalline tantalum. The purpose of the simulations is to test whether two conspicuous features of the experimental data can be reproduced, namely the release temperature's being markedly higher than the isentropic release temperature at each shock pressure, and its tendency to saturate at a value suspiciously close to the ambient melt temperature $T_M = 3270$ K [216].

5.6 Temperatures from small MD simulations

5.6.1 Simulation setup

The crystals modelled in these preliminary MD simulations were prepared as follows. Each sample starts as a fully periodic, defect-free crystal with dimensions of $26.1 \times 26.2 \times 26.6$ nm^3 and a population of just over one million atoms. The crystallographic orientation of the crystal is the standard [100]-[01$\bar{1}$]-[011]. After being equilibrated, the crystal is uniaxially compressed along the z axis (i.e. [011]) at a rate of 10^{10} s^{-1} until it reaches 25% compression, by which point the huge shear stress induced in the crystal by the loading has nucleated a dense dislocation network. The purpose of seeding these defects is to lower the yield stress of the crystal below its homogeneous nucleation limit, so that its elastic response during simulated release is minimised. The crystal is simulated under a microcanonical ensemble until the dislocation network spawned by the preloading relaxes – equilibrium is determined to have been reached once the average temperature of the crystal fluctuates by no more than 1 K over the course of 10 ps.

With its dislocations nominally stabilised, the crystal is then evolved under an isothermal-isobaric (NPT) ensemble to bring its temperature and pressure to match one of ten Hugoniot states between 45 and 220 GPa. The Hugoniot temperatures used here were taken from the MD study of Ravelo *et. al.* [54]. The sample is then released from the shock state to ambient pressure at a rate of 4×10^9 s^{-1}, which is representative of the local release rate at around one micron's distance from the experimental samples' rear surface (as will be shown in the following chapter). Two unloading scenarios are considered for each sample, the first being uniaxial expansion along z, the second volumetric expansion. In the latter scenario, almost no plastic deformation is induced by the unloading process, meaning the crystal releases reversibly. By comparing the latter and former release paths (henceforth referred to as the isentropes and adiabats, respectively), we can determine to what extent the uniaxially unloading targets release isentropically.

To unload these fully periodic samples, the dimensions of the computational cell ($\{L_i\}$, $i = x, y, z$) are evolved at a prescribed rate. Simultaneously, the coordinates

of the atoms are homogeneously remapped using an affine transformation, such that the distance between the atoms scales just as the cell dimensions do. One should note that if the atomistic configuration is evolved in this manner under the usual microcanonical ensemble, the rate of change of its internal energy $\dot{E}$ will differ from the applied work rate $\dot{W}$. That is to say that transforming the crystal in this way artificially heats it. To ensure the unloading is truly adiabatic, the equation of motion of each atom can be augmented to read thus [219]:

$$[\dot{\mathbf{x}}_\alpha]_i = \frac{[\mathbf{p}_\alpha]_i}{m_\alpha} + \frac{\dot{L}_i}{L_i}[\mathbf{x}_\alpha]_i, \tag{5.23}$$

$$[\dot{\mathbf{p}}_\alpha]_i = [\mathbf{f}_\alpha]_i - \frac{\dot{L}_i}{L_i}[\mathbf{p}_\alpha]_i. \tag{5.24}$$

Here, $\mathbf{x}_\alpha$ and $\mathbf{p}_\alpha$ are the position and momentum of atom α with mass m_α, and $\mathbf{f}_\alpha$ is the total force exerted upon it by its neighbours. The second term in Eq. (5.23) performs the affine remapping, while the second term in Eq. (5.24) is a per-atom force that prevents the remapping from heating the crystal.

5.6.2 Simulation results

Fig. 5.10 shows the simulated release isentropes and adiabats emanating from a set of ten Hugoniot states for fully periodic tantalum crystals released at 4×10^9 s^{-1}. Shown also for reference are the Hugoniot itself and the melt curve [54]. As expected, the temperature of samples releasing along an isentrope decreases monotonically and fairly quickly with pressure. The release adiabats, meanwhile, closely follow their corresponding isentrope at early times, but then suddenly diverge, and thence follow a much flatter trajectory through pressure-temperature space. In fact, at the lowest shock pressures, the adiabatically releasing crystals undergo net heating.

The early-time adherence of the adiabat to the isentrope followed by a sudden departure is exactly what one would expect from a two-phase elastoplastic release. During the initial phase of release, the shear stresses induced in the crystal by the uniaxial unloading are insufficient to cause any dislocation activity, so the release ensues reversibly (i.e. isentropically). Once the shear stress has built to such a level that dislocations become mobile, plastic flow ensues, and the considerable work

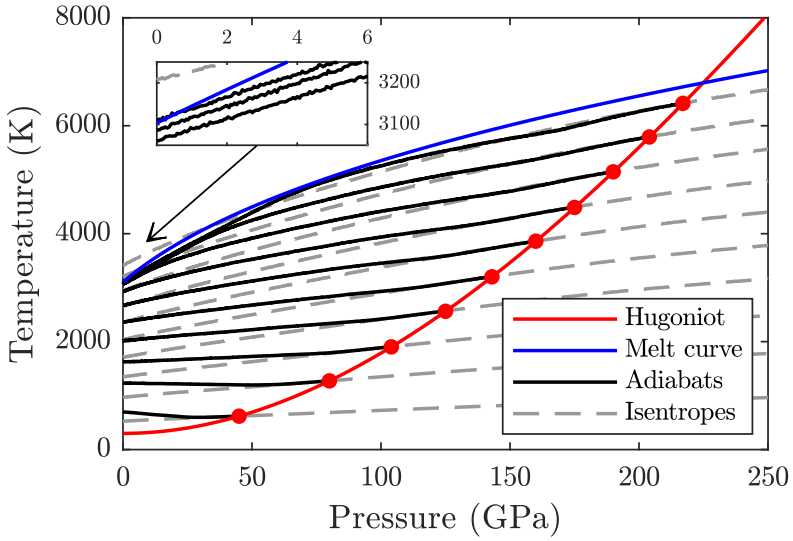

FIG. 5.10. Pressure-temperature space trajectories of tantalum monocrystals simulated under the Ravelo Ta2 EAM potential [54] evolving either volumetrically (isentropes) or uniaxially (adiabats) at strain rates of 4×10^9 s^{-1}. Shown also are the Hugoniot and solid-liquid phase boundary.

required to effect it is largely dissipated as heat. This would cause the adiabat to rise 'above' its corresponding isentrope as shown in Fig. 5.10, thus accounting for the unusually high release temperatures observed in experiment.

The second and even more promising feature of the simulated release adiabats is the interesting behaviour they exhibit at the highest shock pressures. The adiabats emanating from the 204 and 217 GPa shock states, it seems, are loath to cross the melt curve. In fact, during the latter stage of release (where $p < 50$ GPa), these uniaxially releasing crystals are so desperate to avoid the phase boundary that they cool even faster than the local isentropic cooling rate, despite their simultaneously suffering dissipative heating due to plastic work. Conspicuously, upon reaching ambient pressure, the three highest-pressure adiabats have converged to almost exactly the same temperature – the ambient melt temperature ($\approx$ 3080 K for Ta2 [54]). This is exactly what is observed experimentally.

To understand what is happening to the material undergoing uniaxial release in the proximity of the melt curve, it is useful to examine its synthetic x-ray diffraction signal. While generally more computationally expensive, reciprocal-space techniques tend to be considerably more robust than their real-space counterparts in the high-temperature regime [52], and are therefore extremely useful here. Shown in Fig. 5.11

is the azimuthally integrated scattering intensity from crystals releasing from the 204 GPa shock state at eleven points in phase space along the release path. The signals along the isentrope and the adiabat are shown in Figs. 5.11(b) and 5.11(c), respectively. While the Bragg peaks from the volumetrically releasing crystal remain sharp throughout, those of the uniaxially unloaded crystal soften considerably at late times. Broadening of this kind indicates that the latter crystal has at least partially melted. If the targets releasing from the very highest shock pressures do indeed begin to liquify on release, that would explain their tendency to follow the melt curve – the crystal's phase space trajectory would be prevented from easily crossing said boundary due to the barrier presented by the latent heat of fusion.

It is natural to ask: can any evidence of melting on release be discerned in the experiment? One can indeed see liquidlike diffraction from targets compressed above the shock-melt pressure [220] ($\sim$ 300 GPa for tantalum [192]). Unfortunately, the same signal is not readily visible for the notionally release-molten targets. There may be several reasons for this. First, the diffraction signal from molten material is considerably more diffuse than that from solid material. The signal will delocalise not only in θ, but also in φ, due to the loss of crystallographic texture that attends melting. Second, if the liquid phase exists, it must be found in a range of density states, just as its solid host is. This would cause further delocalisation of the liquid signal in θ. Third, the liquid phase might constitute only a small fraction of the sample: only part of the crystal needs to melt to cause its release path to adhere to the melt curve. Presumably, these three effects have conspired to give an extremely diffuse liquid signal that cannot easily be distinguished from the background.

It might be possible, in further work, to strengthen the liquid signal by carefully selecting the shock pressure. It so happens that for this experiment there is a paucity of data points between 200 GPa (where the saturation effect starts to manifest) and 300 GPa (where the material melts on shock). Were the experiment to be repeated, it would be prudent to explore this pressure region, because targets releasing from these higher pressures would encounter the melt curve sooner, spend longer following it, and therefore accumulate a greater liquid phase fraction before reaching ambient pressure. This would ideally amplify the liquid diffraction signal to such a level that it could be clearly observed, thus allowing us to experimentally confirm our intuition

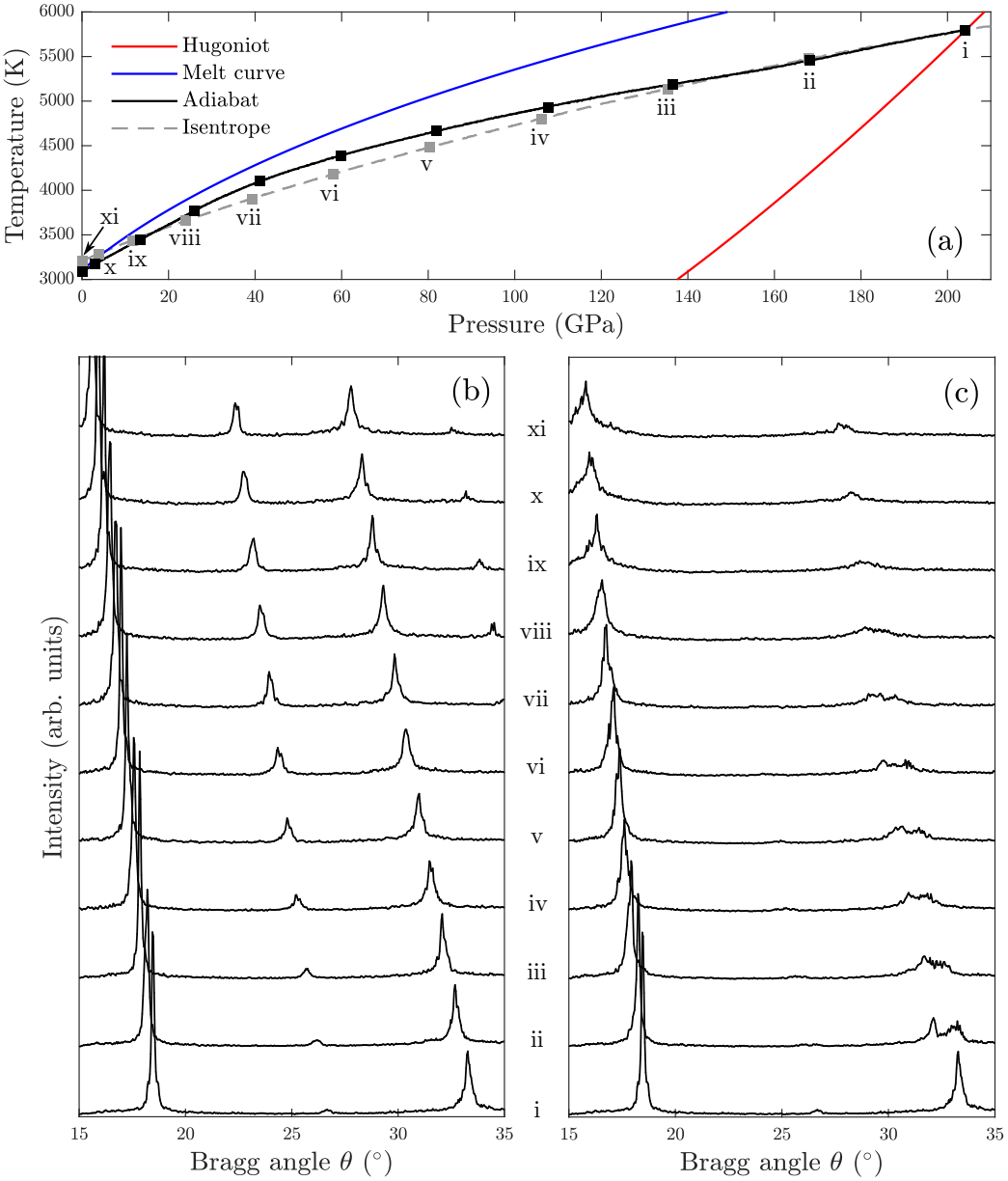

FIG. 5.11. (a) Release adiabat and isentrope of a tantalum monocrystal releasing from the 204 GPa Hugoniot state. (b) and (c) show the azimuthally integrated, fibrelike synthetic diffraction signals at states i to xi along the release paths for the isentropically and adiabatically releasing crystals, respectively.

about the temperature saturation effect.

At any rate, the small-scale simulations performed here reproduce both of the interesting features of the experimental data, namely that the targets are considerably hotter than they would be if their release proceeded isentropically, and that the release temperature saturates at the ambient melt temperature at high shock pressures. The simulations also provide hints at what the underlying physics might

be: the inferred heating that takes place during release appears to be consistent with plastic-work heating, and the saturation effect could conceivably be caused by the enthalpy barrier found at the melt curve. The simulations thus provide strong circumstantial evidence that the locus of shock release temperatures presented in Fig. 5.9 is correct, and give further assurance that the temperature extraction algorithm constructed in Secs. 5.4.1 and 5.4.2 is sound. Further weight is thus lent to the conclusion that shock release is not, in general, isentropic.

5.7 Conclusion

Micron-scale tantalum targets loaded to and subsequently allowed to release from megabar pressure states have been studied using time-resolved x-ray diffraction. A means of inferring the temperature they assume following release from their thermally induced tensile elastic strains was developed, and verified on simulant diffraction data generated from large-scale molecular dynamics simulations. The temperature extraction algorithm predicted that the post-breakout temperatures exhibited by the targets were substantially higher than those expected from a conventional isentrope release. It was further predicted that, at the highest shock pressures, the release temperature saturates at the ambient melt temperature. Both of these phenomena were borne out by small-scale molecular dynamics simulations of tantalum unloading from a megabar shock state at around 10^9 s^{-1}. These experimental results indicate that the shock release process is a highly nonisentropic one.

CHAPTER 6

Simulations of nonisentropic release in shocked tantalum

6.1 Introduction

In the previous chapter, it was shown experimentally that micron-scale tantalum crystals undergo substantial heating while unloading from a megabar shock state, contrary to the conventional picture of shock release. While it was speculated that internal dissipation (i.e. plastic work) was to blame, observing such a process in a shock compression experiment is challenging. To gain an insight into the microphysical processes at play during shock release, we can appeal once again to large-scale molecular dynamics (MD) simulations. In this chapter, MD simulations are used to study the detailed behaviour of micron-scale tantalum single crystals during shock compression and subsequent release. Their temperature history is interpreted using a heat equation, which can separate and quantify the heating and cooling mechanisms active during adiabatic deformation. Like the above-mentioned experiments, the simulations demonstrate dramatic heating during release, and confirm that plastic work is the primary source of heat. It is further shown that the amount of heating undergone by the crystal varies with distance from its rear surface, but that over the micron scale of the targets frequently used in laser-induced shock experiments, the release temperature is fairly uniform. These simulations thus give further reason to believe that the nonisentropic release observed in experiment is a real phenomenon.

6.1.1 Heating and cooling mechanisms

At any instant of time, there are several mechanisms competing to control the temperature of a shock-releasing material. Chief among them is the thermoelastic effect [184]. This refers to the reversible change in temperature undergone by a substance when its volume changes; heating is expected upon compression, cooling on expan-

sion. If a material releases isentropically (which to say, reversibly), its temperature T is governed exclusively by the thermoelastic effect, and therefore falls monotonically with volume. The typical magnitude of the thermoelastic effect (characterised by the Grüneisen parameter γ [203]) is such that a crystal releasing from a megabar pressure state is generally expected to cool by several hundred degrees.

While the crystal is expanding, it also inevitably undergoes plastic deformation – as illustrated in Chapter 4, it is principally by plastic flow that the elastic strains transverse to the loading direction are able to relax. Plastic deformation is an irreversible, dissipative process, which is to say that the work expended in bringing it about is converted almost completely to heat. The amount of work required to cause a given plastic strain scales with the strength (i.e. the flow stress τ) of the crystal. Conventionally, plastic-work heating is assumed to be negligible during shock release because it is a 'slow' process, and can therefore be realised with small flow stresses. However, while the strain rates present in a rarefaction fan are indeed far lower than those present in the shock front – and fall as the fan travels deeper into the crystal – within the first few microns of the rear surface they can exceed 10^9 s^{-1} (as will be shown). Laser-compression studies [202, 221, 222] and MD simulations performed on commensurate timescales [47, 223, 224] have shown that, in an ultra-high strain rate regime such as this, a metal will typically exhibit strength of order gigapascals. Strength of this magnitude is non-negligible. As shown in the computational studies of Swift *et. al.* [225] and of Kurosawa and Genda [226], the crystal's considerable strength will cause plastic-work heating not only during compression but also on release, directly opposing the thermoelastic cooling due to expansion and thus causing the release path to deviate markedly from the isentrope.

There is a second potential heating mechanism that is necessarily neglected by an isentropic treatment of release: recovery of energy from crystal defects. It has long been posited that defects must be created in huge numbers during shock compression in order to accommodate the extreme plastic strain rates induced at the shock front [227, 228], in accordance with Orowan's equation [91]. This prediction is supported by MD simulations, which consistently show copious homogeneous defect generation across the shock front (as shown in Chapter 4, and in Refs. [42, 43, 47, 54]). Such simulations have also shown that the huge defect densities created on shock can be

partially annihilated upon release [48, 59]. In fact, it has recently been demonstrated by *in situ* x-ray diffraction (XRD) measurements that both deformation twinning and lattice rotation induced by shock compression of tantalum [64] are largely reversed during rarefaction [59], which is consistent with such a defect annihilation. Studies performed over the past century have suggested that the energy stored by defects generally constitutes between 5% and 15% of the plastic work performed during compression [229–234]. Defect annihilation therefore allows a considerable amount of latent energy to be recovered during unloading and released as thermal energy, providing another source of heat that further opposes thermoelastic cooling.

The main aim of the following chapter is to see whether the release heating observed experimentally is borne out in simulations, and, if so, why? This question will be answered using a heat equation that allows us to quantify the three aforementioned heating and cooling mechanisms, namely expansive cooling due to the thermoelastic effect, heating due to plastic work, and the exchange of thermal energy with that of the material microstructure. Before tackling a true shock-release simulation, however, some time will be given to describing how the heat equation can be implemented in an atomistic simulation and how it was verified.

6.2 The heat equation

The following section describes how one evaluates the components of the heat equation for an MD simulation. Several small-scale tests of the heat equation will then be presented, to give an idea of how accurate it is expected to be in a shock-compression context. Only then will the equation be applied to a true shock-release simulation of a micron-scale target. Note that the superscript for elastic strain ε^e will henceforth be reinstated, so as to differentiate it from the plastic strain ε^p.

6.2.1 Formulation of the source terms

To quantify the effects of thermoelasticity, it is customary to use the Grüneisen parameter[27]. The Grüneisen parameter γ is the fundamental thermodynamic variable

[27] This is the convention in shock physics, at least – in engineering and materials science contexts, one often speaks instead of the 'thermoelastic constant' K. This is defined such that the frac-

that expresses how the vibrational properties of a solid vary with its volume. Among its definitions is

$$\gamma = V\left(\frac{\partial p}{\partial E}\right)_V, \tag{6.1}$$

where E is the internal energy of the solid. If the volume V of an isotropic material reversibly changes by δV, the concomitant temperature change δT expected within the Grüneisen formalism reads [203]

$$\delta T = -T\gamma\frac{\delta V}{V}. \tag{6.2}$$

Since γ is typically of order unity, the fractional decrease in temperature expected on release is approximately equal to the fractional increase in volume, which can be several tens of percent in the shock regime. When modelling an anisotropic material, it is advisable to promote γ to a tensor, and replace the definition above with

$$\gamma_{ij} = V\left(\frac{\partial \sigma_{ij}}{\partial E}\right)_V. \tag{6.3}$$

The thermoelastic heating (or cooling) rate becomes [236, 237]

$$\dot{T}_{\mathrm{TE}} = \sum_{i,j} T\gamma_{ij}\frac{d\varepsilon^e_{ij}}{dt} \tag{6.4a}$$

$$\equiv T\boldsymbol{\gamma} : \frac{d\boldsymbol{\varepsilon}^e}{dt}, \tag{6.4b}$$

where $\boldsymbol{\varepsilon}^e$ is the true elastic strain tensor. This more general formulation is better equipped to deal with low-symmetry crystal structures[28] undergoing non-volumetric deformation. We shall see that this distinction is important for shock release, during which the Grüneisen tensor can exhibit strong anisotropy.

To evaluate the heating due to plastic work, meanwhile, requires two terms. It is a simple matter to calculate the total amount of plastic work performed on a unit volume of material while it undergoes plastic strain. It reads

$$\dot{w}^p = \boldsymbol{\sigma} : \frac{d\boldsymbol{\varepsilon}^p}{dt}, \tag{6.5}$$

tional change in temperature upon a change in pressure Δp is $3K\Delta p$. In any case, K and γ are related by a constant of proportionality [235], and they describe the same underlying physics.

[28] A cubic crystal in a nonhydrostatic strain state also constitutes a low-symmetry structure.

where ε^p is the true plastic strain. In the simplest picture of plasticity, the entirety of this work is dissipated, suggesting a 'perfect plastic' heating rate of

$$\dot{T}_{\mathrm{PW}} = \frac{1}{c_V}\left(\sigma : \frac{d\varepsilon^p}{dt}\right), \tag{6.6}$$

c_V being the crystal's volumetric heat capacity. In reality, some fraction[29] of this plastic work is usually siphoned off to create the very dislocations mediating plastic flow. This is to say that, if defects are being created, the heating rate is somewhat less than the work rate. If the energy stored by the defects is E^s, then the amount of energy dissipated per unit volume actually reads $(\sigma : \dot{\varepsilon}^p - \dot{E}^s/V)$. This can be accounted for with the corrective term

$$\dot{T}_{\mathrm{MS}} = -\frac{1}{c_V}\left(\frac{1}{V}\frac{dE^s}{dt}\right). \tag{6.7}$$

Note, though, that this term cuts both ways: if the energy of the microstructure *decreases* (through dislocation annihilation, say), its latent energy is released and so causes heating additional to that provided by plastic work. In other words, defect energy can be exchanged for thermal energy. As will be shown, the changes in the dislocation density that take place during shock release are so huge that the exchange term $\dot{T}_{\mathrm{MS}}$ can cause perceptible changes to the material's temperature history.

6.2.2 Application to an atomistic simulation

To recap: the temperature T of a material element undergoing adiabatic deformation is notionally governed by the equation

$$\frac{dT}{dt} = \dot{T}_{\mathrm{TE}} + \dot{T}_{\mathrm{PW}} + \dot{T}_{\mathrm{MS}} \tag{6.8a}$$

$$= T\gamma : \frac{d\varepsilon^e}{dt} + \frac{1}{c_V}\left(\sigma : \frac{d\varepsilon^p}{dt} - \frac{1}{V}\frac{dE^s}{dt}\right), \tag{6.8b}$$

where γ is the Grüneisen parameter, ε^e is the true elastic strain, ε^p is the true plastic strain, σ is the Cauchy stress, c_V is the volumetric heat capacity, and E^s is

[29] The fraction of plastic work that must be invested in defects is often expressed via the *Taylor-Quinney factor* f_{TQ} [84]. In continuum modelling, one often amends the plastic work heating rate to $f_{\mathrm{TQ}}(\sigma : \dot{\varepsilon}^p)/c_V$, where f_{TQ} is canonically taken to be around 0.9 in the high strain rate regime [225]. With MD, however, we can evaluate the energy stored by the microstructure E^s directly, meaning we need not rely on the phenomenological constant f_{TQ}.

the energy stored by the element's defects. From left to right, these three source terms capture the thermoelastic heating or cooling caused by changes in volume, the heating due to plastic deformation, and the exchange of microstructure energy with thermal energy, respectively. In principle, every one of these macroscopic variables can be calculated for an atomistic material element, provided it is not too far from thermodynamic equilibrium. It is then possible to integrate numerically the heat equation at each timestep to generate its predicted temperature curve $T_f(t)$, which may then be compared with its true temperature $T(t)$. If the two are sufficiently similar, one can be confident that the 'thermal energy budget' expressed by Eq. (6.8) is accurate, and so explains the source of the heating observed on release.

While T, V, σ, ε^e and $c_V = 3nk_B$ represent fairly standard variables in the context of MD, the calculation of ε^p, γ, and E^s is arguably less routine. The following subsections explain how these latter macroscopic variables were extracted from the MD simulations; for details of the calculation of the standard variables, the reader is referred to Chapter 3.

Calculation of the plastic strains

When compared to ε^e_α, calculation of the per-atom plastic strain tensor ε^p_α is actually a somewhat involved process – unlike the elastic strain, the instantaneous plastic strain state cannot be deduced from the current atomistic configuration alone, because it depends on the material's deformation history. While there do exist algorithms for calculating the per-atom plastic strain using an elastoplastic decomposition of the total deformation gradient F_α (see the work by Stukowski and Arsenlis [238], for example), it transpires that the *macroscopic* plastic strain ε^p can be derived relatively painlessly from the element's macroscopic elastic strain ε^e, and certain boundary conditions that depend on the nature of the loading. Two loading scenarios (pictured in Fig. 6.1) will be considered here.

The first scenario to be considered is that in which the material element in question is a fully-periodic crystal. In this case, one can obtain the macroscopic plastic strains straightforwardly from the cell dimensions $\{L_i(t)\}$, which one knows exactly

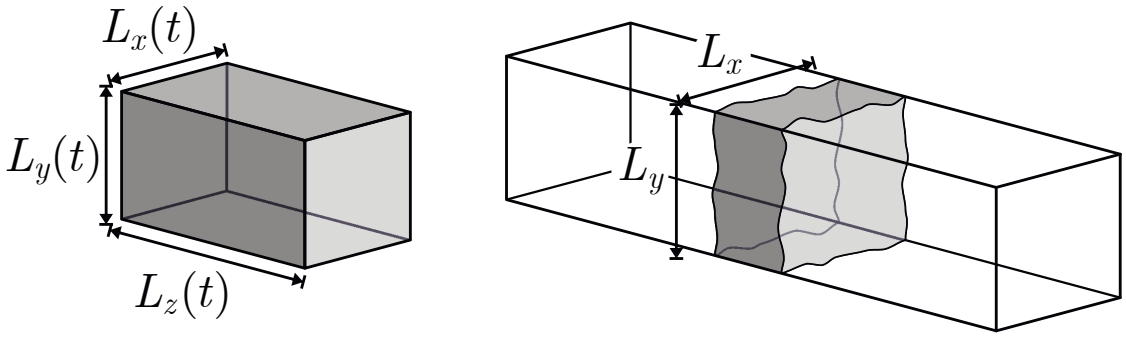

Loading scenario I Loading scenario II

FIG. 6.1. Depictions of two loading scenarios. Scenario I describes a fully periodic, orthogonal material element whose dimensions $\{L_i(t)\}$ are known at all times. Scenario 2 describes an element that straddles a uniaxially loaded crystal and has fixed transverse dimensions, but whose longitudinal extent is unconstrained.

at all times. By definition of the true strain ε (with our sign convention),

$$dL_i = -L_i d\varepsilon_{ii}. \tag{6.9}$$

In the differential limit, the strains decompose additively, hence

$$\frac{dL_i}{dt} = -L_i \left(\frac{d\varepsilon^e_{ii}}{dt} + \frac{d\varepsilon^p_{ii}}{dt} \right). \tag{6.10}$$

Given the cell dimensions and the average elastic strains, then, one can use the following system of equations to deduce $\dot{\varepsilon}^p$:

$$\frac{d\varepsilon^p_{xx}}{dt} = -\frac{1}{L_x}\frac{dL_x}{dt} - \frac{d\varepsilon^e_{xx}}{dt}, \tag{6.11a}$$

$$\frac{d\varepsilon^p_{yy}}{dt} = -\frac{1}{L_y}\frac{dL_y}{dt} - \frac{d\varepsilon^e_{yy}}{dt}, \tag{6.11b}$$

$$\frac{d\varepsilon^p_{zz}}{dt} = -\frac{1}{L_z}\frac{dL_z}{dt} - \frac{d\varepsilon^e_{zz}}{dt}. \tag{6.11c}$$

This set of equations for ε^p will be used for the tests of the heat equation performed on fully periodic crystals in Sec. 6.2.3.

The second loading scenario we consider is one in which the material element forms a cross-section of a uniaxially loaded, laterally confined monocrystal. In this case, one knows the transverse dimensions of the element L_x and L_y (which are constant throughout the simulation) but not necessarily its longitudinal extent L_z

(which is unconstrained). Indeed, given that the surface of the element is liable to change shape during plastic deformation, its thickness L_z likely varies over its cross-section. At any rate, one cannot simply use Eq. (6.11c) to infer ε^p_{zz}. Under certain circumstances, one might be justified in using the assumption of zero *plastic dilatation*. This states that, as a form of shear deformation, plastic flow is a volume-conserving process. If this is so,

$$\frac{d\varepsilon^p_{xx}}{dt} + \frac{d\varepsilon^p_{yy}}{dt} + \frac{d\varepsilon^p_{zz}}{dt} \equiv \dot{\varepsilon}^p_V = 0. \tag{6.12}$$

This constraint allows ε^p_{zz} to be inferred trivially from the other two components of plastic strain, which can in turn be deduced from the corresponding elastic strains via Eqs. (6.11a) and (6.11b). Here, however, we will not rely on any assumptions about the dilatancy ε^p_V of the element. While shear deformation is, in itself, an isochoric process, plasticity is also attended by the production of crystal defects. Since defective lattice sites do not necessarily occupy the same volume as crystalline ones, and because the number of defects generated by shock compression tends to be extremely large, there is no guarantee that the plastic flow should be volume-conserving. For this reason, we will adopt a more general approach that allows the volume change effected by plastic deformation to be non-zero.

Extending Eq. (6.9) to three dimensions, the change in volume attending changes in the average strains of $d\varepsilon_{xx}$, $d\varepsilon_{yy}$, and $d\varepsilon_{zz}$ is

$$dV = -V(d\varepsilon_{xx} + d\varepsilon_{yy} + d\varepsilon_{zz}). \tag{6.13}$$

By additively decomposing the strains as before, one finds

$$\frac{dV}{dt} = -V\left(\sum_i \frac{d\varepsilon^e_{ii}}{dt} + \sum_i \frac{d\varepsilon^p_{ii}}{dt}\right). \tag{6.14}$$

Hence, the dilatation can be expressed as

$$\dot{\varepsilon}^p_V = -\frac{1}{V}\frac{dV}{dt} - \sum_i \frac{d\varepsilon^e_{ii}}{dt}. \tag{6.15}$$

The element's volume V may be calculated using the Voronoi construction method

described in Sec. 3.4.1. Hence, the system of equations with which we can deduce the plastic strain state of a uniaxially loaded Lagrangian material element reads

$$\dot{\varepsilon}^p_{xx} = -\dot{\varepsilon}^e_{xx}, \tag{6.16a}$$

$$\dot{\varepsilon}^p_{yy} = -\dot{\varepsilon}^e_{yy}, \tag{6.16b}$$

$$\dot{\varepsilon}^p_{zz} = \dot{\varepsilon}^p_V + \dot{\varepsilon}^e_{xx} + \dot{\varepsilon}^e_{yy}. \tag{6.16c}$$

This latter set of equations for ε^p applies to the shock-release simulations proper described in Sec. 6.4.

Calculation of the Grüneisen parameter

The most practical formulation of the Grüneisen parameter is, for the purposes of MD, that given by Eq. (6.3): $\gamma = V(\partial\sigma/\partial E)_V$. To evaluate this derivative, one heats the crystal isochorically by some small amount[30] using an appropriate thermostat, waits for the crystal to equilibrate, and then evaluates the ratio of the resultant increase in its Cauchy stress $\delta\sigma$ to that of its energy density $\delta E/V$.

This sort of calculation is straightforward for a crystal in equilibrium, but a set of problems is immediately encountered when one tries to apply this method to a material element (or an isolated copy thereof) undergoing dynamic loading. First, such an element is unlikely to be in mechanical equilibrium, meaning the strain state and temperature of the element will evolve spontaneously while one tries to thermostat it. Second, if we are considering loading scenario II, the surface of the material element will generally be irregular, so finding appropriate boundary conditions to hold it at constant volume is non-trivial. For these reasons, it is often more practical to calculate instead the Grüneisen function of a 'surrogate' crystal, with the same temperature and average elastic strain state as the material element in question, but with fully periodic boundaries and none of the crystal defects. The volume of such a crystal is easily conserved, and the absence of dislocations means that, as long as the element's instantaneous shear stress is below the homogeneous yield stress, no plastic flow will ensue during thermostatting.

[30] The Grüneisen parameter is marginally temperature dependent, so the heating should be restricted to perhaps 100 K at most.

The assumption one makes when one replaces the crystal with its surrogate is that by removing the defects one does not appreciably alter the Grüneisen parameter. There are in fact a limited number of studies that cast some doubt on the universality of this premise – reportedly, the thermoelastic cooling rate of α-titanium [239–241] and stainless steel [242] can be changed by 5% – 10% by first plastically deforming the sample. Shortly, however, a simulation will be presented showing that under the loading conditions considered here, γ is apparently insensitive to dislocation density.

Calculation of the defect energy

To deduce the energy stored by an element's microstructure, we simply calculate the difference between its internal energy and that of its defect-free surrogate. That is, if the energy per atom in the surrogate is e_0, and the element contains N atoms, we say that $E^s = E - Ne_0$. The calculations of E^s and γ may be performed using the same surrogate crystal for efficiency.

6.2.3 Exercising the heat equation

Before applying it to a crystal undergoing shock compression and release, it is sensible first to verify that the heat equation can predict the temperature dynamics of atomistic systems experiencing more 'controlled' loading. By this, we mean loading conditions in which one or more of the source terms in Eq. (6.8) is absent. This allows us to isolate and assess the accuracy of each term in turn. The following section presents three simulations of fully-periodic crystals that test the various components of the heat equation. The first test assesses the thermoelastic cooling term $\dot{T}_{\mathrm{TE}}$, the second the anisentropic terms $\dot{T}_{\mathrm{PW}}$ and $\dot{T}_{\mathrm{MS}}$, and the third test verifies that the Grüneisen parameter is insensitive to dislocation density, justifying our use of the surrogate crystals to calculate γ.

Test 1: Elastic deformation of pristine crystal

The first test of the heat equation is designed to isolate the thermoelastic cooling term $\dot{T}_{\mathrm{TE}}$. The test involves unloading a crystal that is devoid of defects and is never

loaded above its yield stress. Such a crystal experiences neither plastic-work heating nor heating from dislocation annihilation, so its temperature evolution is governed exclusively by the thermoelastic effect. The test was conducted as follows.

A fully periodic, perfect crystal comprising one million atoms was equilibrated with an initial temperature and pressure of 1750 K and 100 GPa, respectively. This initial state matches the Hugoniot state from which the large-scale crystals we will eventually study in Sec. 6.4 undergo shock release. The elastic strain state of the crystal was then 'manually' evolved so as to simulate an anisotropic (i.e. nonvolumetric) release to ambient pressure. The strain state of the crystal was evolved by changing the dimensions of the computational cell $\{L_i\}$ while homogeneously remapping the coordinates of the atoms with an affine transformation. As in Sec. 5.6, the simulation was executed under an adiabatic integration scheme [219], which prevents the artificial heating that would otherwise result from the coordinate rescaling.

The prescribed elastic strain variation of the cell is pictured in Fig. 6.2(a). These profiles are representative of those one would expect of a material element undergoing shock release; a detailed discussion of their form will be given in Sec. 6.4.1. Note that while the shear stress associated with these profiles is generally nonzero, it is never large enough to precipitate plastic flow in this pristine crystal. This means there is no possibility of either plastic-work heating or exchange of thermal energy with a microstructure. Shown also for reference in Fig. 6.2(b) is the variation of the Grüneisen tensor components γ_{ij}. Wherever ε^e is anisotropic, so too is γ.

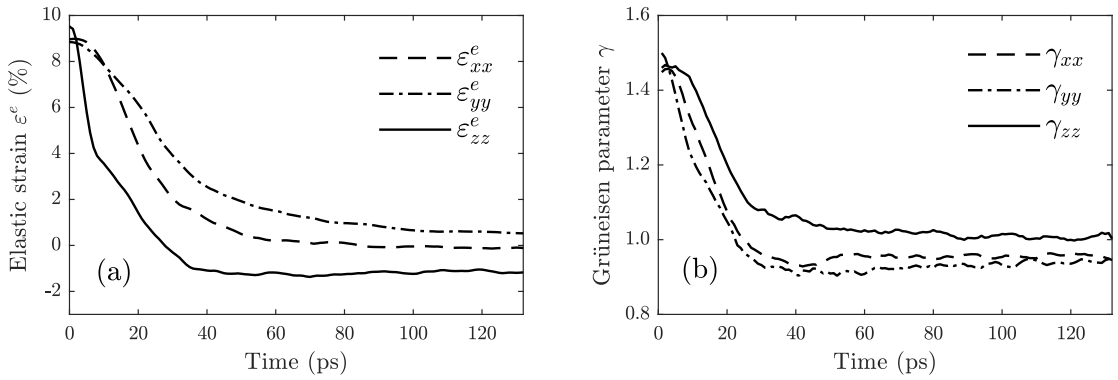

FIG. 6.2. (a) Elastic strain evolution of a fully periodic crystal undergoing simulated elastic release from the 100 GPa shock state via explicit evolution of its dimensions. (b) On-diagonal components of the Grüneisen tensor γ_{ij} during simulated release.

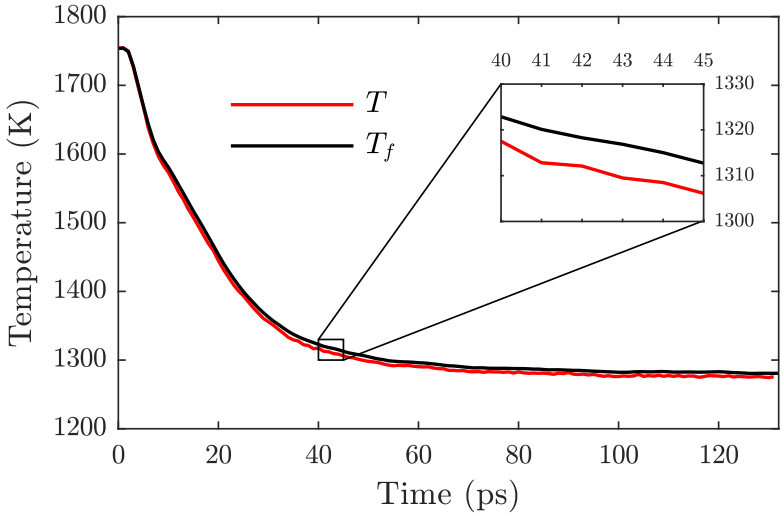

FIG. 6.3. Temperature T of a crystal undergoing simulated elastic release from the 100 GPa shock state via explicit evolution of its strains, compared with the predicted temperature T_f given by integration of the thermoelastic cooling rate [see Eq. (6.4).]

The actual temperature variation of the element and the temperature predicted based on the thermoelastic cooling rate $\dot{T}_{\mathrm{TE}}$ are plotted in Fig. 6.3. The agreement is very good: the two profiles differ by no more than 10 K throughout the simulation. On this basis, it appears that the heat equation can accurately quantify the thermoelastic effect, in the absence of plastic deformation at least.

Test 2: Plastic, isochoric deformation of defective crystal

The second test of the heat equation targets the two anisentropic terms $\dot{T}_{\mathrm{PW}}$ and $\dot{T}_{\mathrm{MS}}$. This is achieved by subjecting a defective crystal to plastic deformation, but in such a way that its volume remains constant – by loading the crystal isochorically, we eliminate the thermoelastic effect, leaving only the plastic-work heating and microstructure energy terms. The simulation is essentially similar to that presented in the study of Higginbotham *et. al.* [243], in which the authors used a simplified form of the heat equation (containing only the perfect plastic work term) to predict the temperature evolution of copper single crystals undergoing pure shear; the salient difference between this simulation and theirs is that the defect density is likely to change appreciably here. The simulation was executed as follows.

A fully periodic, pristine crystal was first uniaxially compressed along z at a rate

of $\approx 10^{10}$ s^{-1} in order to nucleate a dense dislocation network. When the volumetric compression reached 25% the loading was arrested, but the system continued to be simulated under a microcanonical ensemble until the dislocations equilibrated – equilibrium was determined to have been reached once the temperature of the crystal, which slowly increases due to dislocation relaxation, drifted by no more than 1 K over a 10 ps interval. The crystal was subsequently cooled to ≈ 1700 K using an NVT thermostat to bring the crystal close to the 100 GPa shock state. This equilibrated, defective crystal was then expanded by 33% along z over the course of 100 ps, while simultaneously being compressed along x and y at such a rate as to keep the volume of the cell constant. The atoms' coordinates were remapped under an adiabatic integration scheme as before to prevent artificial heating.

Shown in Fig. 6.4 is the variation of the crystal's elastic strain, plastic strain and stress state over the course of its volume-conserving deformation. We see that, at early times, the elastic strain along z decreases while those along x and y increase, mimicking the behaviour of the macroscopic strains applied to the cell. Meanwhile, the plastic strains remain at zero, indicating that the crystal can initially accommo-

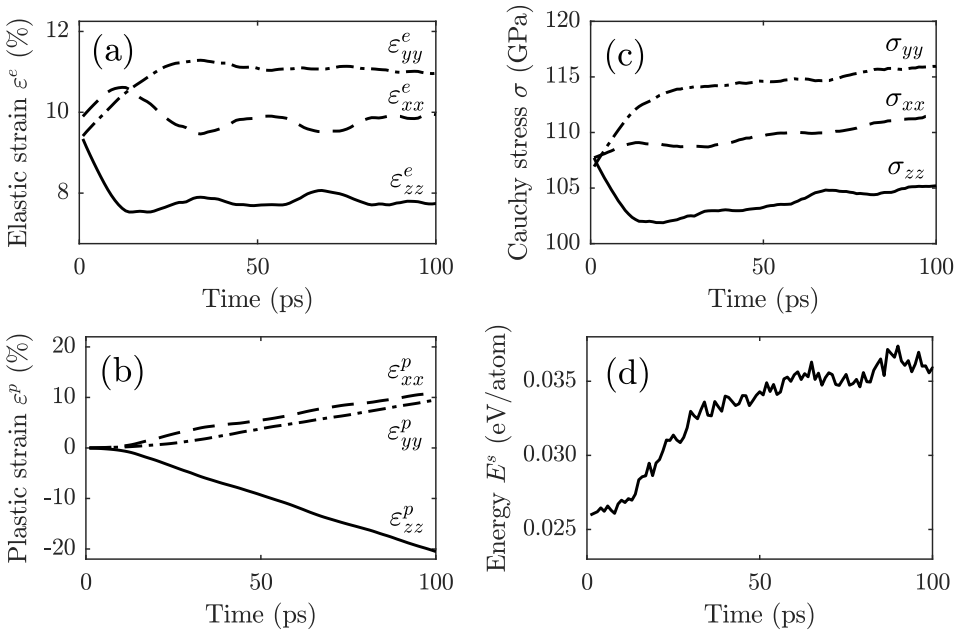

FIG. 6.4. Evolution of (a) the elastic strain state ε^e, (b) the plastic strain state ε^p, (c) the stress state σ and (d) the stored energy E^s of a fully-periodic crystal undergoing plastic, isochoric deformation at around 100 GPa. The crystal was expanded along z at a rate of 10^9 s^{-1} while simultaneously being compressed along x and y so as to conserve its volume.

date the applied strains elastically. Once the shear stresses have built to 2.5 GPa, the crystal yields. Thereafter, the crystal enters a period of steady plastic flow, during which shear stress and strain are prevented from further accumulating by continuous dislocation motion.

Shown also in Fig. 6.4 is the time dependence of the stored energy E^s. Following the onset of plastic flow ($t \approx 10$ ps), we observe that the energy stored by the crystal's microstructure increases by some 40%. This energy increase is evidence of dislocation nucleation or multiplication. Some fraction of the plastic work, then, is not converted directly to heat, but is instead invested in creating new crystal defects. The correction to the heat equation is encoded by the microstructure term $\dot{T}_{\mathrm{MS}} = -(dE^s/dt)/(Vc_V) < 0$.

The temperature of the isochorically loaded crystal is plotted in Fig. 6.5, along with two other curves: the first, T_p, is obtained by integrating $\dot{T}_{\mathrm{PW}}$ only, i.e. assuming perfect conversion of plastic work to heat; the second, T_f, includes the correction from $\dot{T}_{\mathrm{MS}}$. We see that once the crystal yields, plastic work continually heats the crystal at a rate well predicted by the heat equation. Note, however, that T_p slightly overestimates the heating suffered by the crystal overall, because it neglects the plastic work 'sopped up' by the new dislocations formed during the early stages of loading. The full solution T_f, meanwhile, provides an excellent prediction of

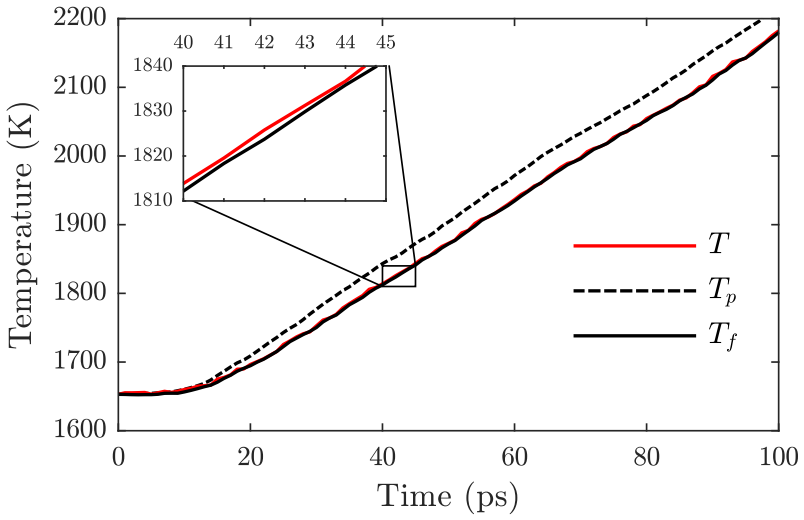

FIG. 6.5. Temperature T of a crystal suffering volume-conserving, plastic deformation, compared with two predictions from the heat equation; T_p assumes perfect conversion of plastic work to heat, while T_f contains the correction from the microstructural term $\dot{T}_{\mathrm{MS}}$.

the crystal's temperature variation: over the entire course of the crystal's 530 K temperature rise, T and T_f differ by no more than 5 K. On this basis, it seems the heat equation can correctly account for the effects of plastic work, at least under isochoric conditions.

Test 3: Volumetric expansion of defective crystal

The final test of the heat equation verifies that, in the temperature and pressure range of interest, the defect content of the crystal does not significantly alter its thermoelastic properties. This test involves elastically unloading two crystals from the same initial temperature and elastic strain state. The first crystal is free of defects, but the second contains a dense dislocation network. By comparing their temperature evolution, one can assess whether the latter crystal's being defective has any bearing on its Grüneisen parameter.

The defective crystal was prepared in the same manner as in the previous test. This crystal and its nondefective surrogate were then unloaded to approximately ambient pressure using coordinate remapping under an adiabatic integration scheme as usual. In contrast to previous tests, the dimensions of the crystals were varied such that $\dot{\varepsilon}_{xx} = \dot{\varepsilon}_{yy} = \dot{\varepsilon}_{zz}$. This was done in an effort to prevent the accumulation of

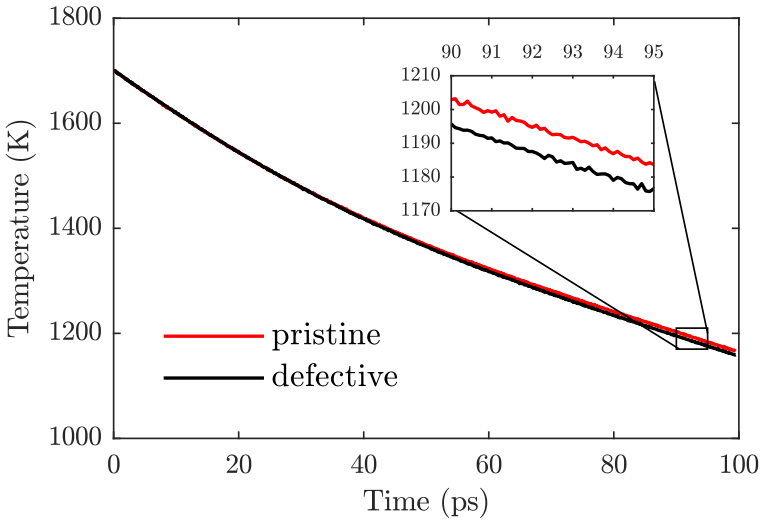

FIG. 6.6. Temperatures of two crystals undergoing isentropic, volumetric expansion from approximately 100 GPa. One crystal is defect-free, while the other contains a dense dislocation network.

any shear stress, particularly in the defective crystal, which is susceptible to plastic deformation due to its dislocation content. The purpose of this test is to compare the thermoelastic cooling rates only, so we wish to avoid the complication of having to account for plastic-working heating too.

Fig. 6.6 shows the temperature variation of the two crystals as functions of time. The difference in final temperatures between the two crystals amounts to only 1.5% of the total temperature drop. The dependence of γ on dislocation density is therefore so small in this regime that it is not worth the trouble to correct for, and our use of surrogates to estimate γ is reasonable.

6.3 Simulation setup

Having tested the individual components of the heat equation, we are now in a position to apply it to micron-scale tantalum crystals undergoing shock compression and release. We do so with a view to examining 'in real time' the heating and cooling processes active during shock release that cannot be resolved experimentally.

The EAM interatomic potentials constructed by Ravelo *et. al.* were tailored to reproduce the behaviour of tantalum under pressures of order 100 GPa and above. Indeed, they successfully predict the experimentally determined pressure-volume curve at ambient temperature [163, 164] and the Hugoniot in the U_S-U_P plane [165], in addition to many mechanical properties determined from first-principles calculations, such as the cold curve (i.e. the zero-temperature equation of state) and the pressure-dependent elastic constants [54]. However, the authors note that these two potentials largely fail to capture the *thermal* properties of tantalum: notably, the two potentials (known as Ta1 and Ta2) underestimate the ambient Grüneisen parameter γ by approximately 60% and 40%, respectively [54]. It would seem at first glance, then, that even Ta2 (the more faithful of the two potentials in this regard, and the one that will be used in this chapter's simulations) would significantly underestimate the amount of thermoelastic cooling the crystal suffers upon release, artifically inflating the release temperature and so hampering a meaningful comparison with the experiment described in the previous chapter.

It so happens, however, that the pressure dependence of γ for Ta2 is such that

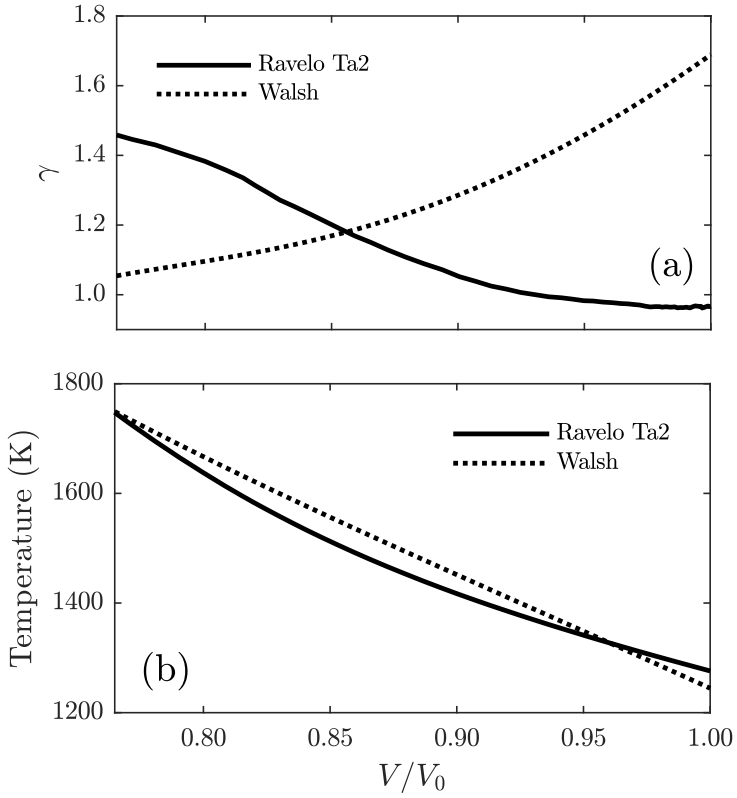

FIG. 6.7. (a) Scalar Grüneisen parameter γ versus volume for the Ta2 potential along a release path from 100 GPa, and determined experimentally along the Hugoniot [12]. (b) Release paths from the 100 GPa shock state to ambient volume V_0 according to integration of the cooling rate $\dot{T} = -T\gamma\,\dot{V}/V$.

the total amount of cooling it predicts for release from around 100 GPa differs only slightly from that expected experimentally. This can be understood from Fig. 6.7(a), which shows the variation of the scalar Grüneisen parameter with volume V as predicted by the Ta2 potential[31], and as determined using velocimetric measurements of explosively driven tantalum by Walsh *et. al.* [12]. While the experimental value of γ is the higher of the two at ambient volume, the Grüneisen parameter for the Ta2 potential *increases* with pressure (contrary to what is observed experimentally), such that its 'average' value over the pressure range 0 to 100 GPa is actually close to the experimental average. When we compare the temperature drops that would result from release from the 100 GPa Hugoniot state [shown in Fig. 6.7(b)], we find the simulated and experimental results differ by only 40 K. So, although the spurious dependence of the Grüneisen parameter on pressure for Ta2 means we probably

[31] The Ta2 curve was calculated along a release adiabat from 100 GPa, while the experimental curve was measured on the Hugoniot. There is therefore some additional variation in γ due to its dependence on T, but this dependence is far weaker than the volume dependence [115].

should not perform a wide pressure scan (as was done in the experiment), if we choose a shock pressure of 100 GPa, the total amount of expansive cooling predicted during shock release should be of approximately the correct magnitude. It is for this reason that only this single shock pressure will be considered in this chapter.

The crystals we will study are identical to the single crystals described in Chapter 4; the essential details will be recapped here. As illustrated in Fig. 6.8, the crystals have dimensions of $24.8 \times 24.8 \times 1121$ nm^3, and are subjected to periodic boundaries on their transverse faces. The crystallographic directions aligned with the x, y, and z axes are [100], [01$\bar{1}$], and [011], respectively, where again [011] was aligned with z in order to emulate the fibre-textured targets studied in the previous chapter. As before, compression of the crystal is realised with a constant-velocity piston instantaneously accelerated to constant velocity $\mathbf{U}_P = (0, 0, U_P)$, where $U_P = 1.2$ kms^{-1} (yielding a shock pressure of 100 GPa). In contrast to previous simulations, the system was simulated beyond shock breakout in order to allow the crystal to release. The crystal was equilibrated prior to compression as described in Sec. 4.2.

In previous chapters, we have typically calculated material properties at an instant of time as a function of a static spatial coordinate. That is, we have been employing an Eulerian description of the crystal. Given that the central focus in

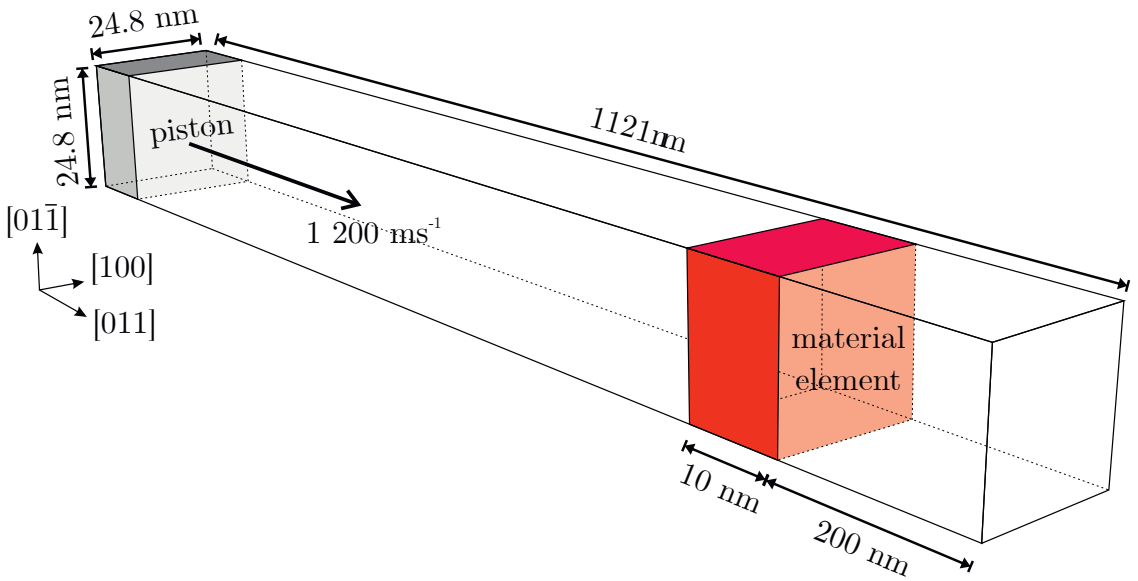

FIG. 6.8. Schematic illustration of the computational cell used in MD simulations of shock-releasing tantalum single crystals. Analysis was focused on a Lagrangian element of material (shown in red) initially situated 200 nm from the rear surface of the crystal.

this chapter is the application of the adiabatic heat equation [Eq. 6.8], it is more natural to move to a Lagrangian picture, in which one instead monitors the properties of a set of evolving material elements as functions of time. The elements in question are distributed along the length of the crystal, each with a thickness of 10 nm along z and a cross-section equal to that of the computational cell. Each element comprises around 340 000 atoms. By examining the stress, strain, and microstructural evolution effected in these material elements by the release process, we hope to be able to account for the heating and cooling mechanisms that govern their temperature evolution, and thus provide a microphysical basis for the highly nonisentropic release observed experimentally in the previous chapter. We will consider first the gross qualitative features of the shock-release cycle, before providing a detailed account of the temperature dynamics that ensue during release.

6.4 Results

6.4.1 Overview of shock-release cycle

Shown in Fig. 6.9(a) are the temperature T and elastic components of strain ε^e of a material element found 0.2 μm below the rear surface of the crystal, and Fig. 6.9(b) shows the concurrent evolution of its dislocation density ρ_D and twin fraction ρ_t. Four distinct periods of evolution can be distinguished: the ambient period ($t <$ 185 ps), before the shock front has reached the element; the shock period ($185 \leq t < 247$ ps), during which the element relaxes in the wake of the shock; the elastic period ($247 \leq t < 254$ ps), during which the element begins to release without yielding; and the plastic period ($t \geq 254$ ps), when the element undergoes full plastic release back to ambient pressure. These four periods are labelled in Fig. 6.9, and all subsequent figures, as A, S, E, and P, respectively.

The shock-release cycle proceeds as follows. First, the shock strikes the element at 185 ps. The compression wave heats the material to 1750 K and generates a short-lived population of deformation twins. The twins rapidly 'evaporate', and are replaced by a dense network of perfect dislocations. The Hugoniot temperature of 1750 K at this pressure is in fair agreement with *ab initio* calculations [244], and

the induced dislocation density of order 10^{13} cm^{-2} matches the densities inferred from compression experiments on [001] tantalum crystals [245]. The element suffers compression for a total of 62 ps, during which time the shear strain induced in it by the shock relaxes to a limiting value of $\Delta\varepsilon^e = \varepsilon^e_{zz} - (\varepsilon^e_{xx} + \varepsilon^e_{yy})/2 = 0.6\%$, and the dislocation network steadily decreases in density while it relaxes. Meanwhile, the shock traverses the remaining 200 nm of the crystal, breaks out from the rear surface, and launches a rarefaction wave back into the crystal that encounters the element at $t = 247$ ps. The ensuing release proceeds in two phases.

Initially, we see that the elastic strain along z rapidly decreases in response to the tensile release wave, but the transverse elastic strains remain largely unchanged. The loading conditions to which the material element is subjected are such that

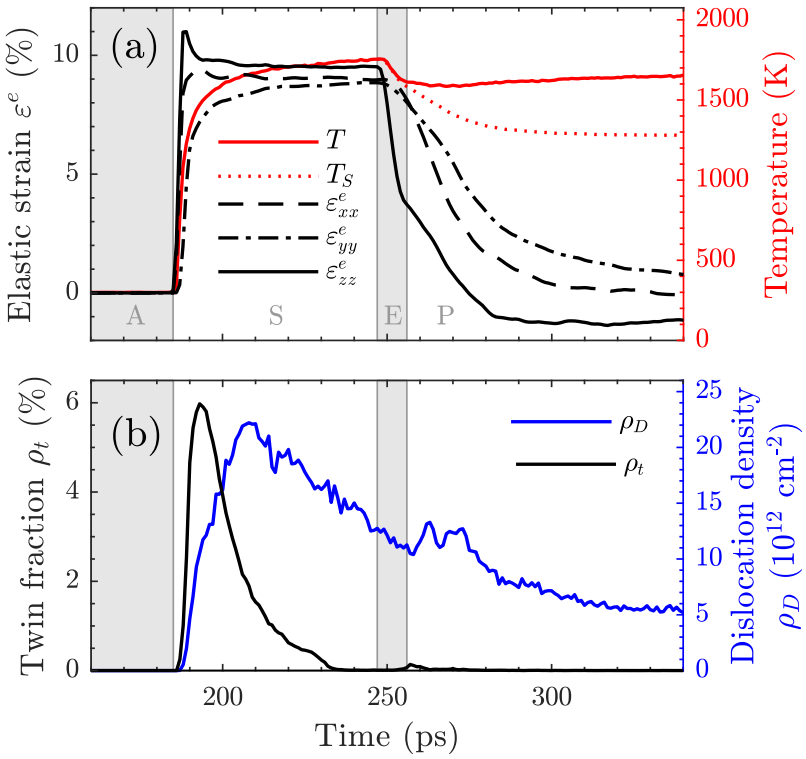

FIG. 6.9. Time evolution of a 10-nm-thick Lagrangian material element initially situated 200 nm below the rear surface of a single crystal shock compressed along z to 100 GPa. (a) Temperature T and true elastic strain ε^e. Shown also for reference is T_s, the predicted temperature along the release isentrope emanating from the shock state at $t = 247$ ps. (b) Dislocation density ρ_D (calculated using the dislocation extraction algorithm [123, 124]) and twin fraction ρ_t. Regions A, S, E, and P denote when the crystal was under ambient conditions, shock compressed, elastically releasing, and plastically releasing, respectively.

macroscopic plastic flow cannot take place without causing changes to ε^e_{xx} and ε^e_{yy} – this constraint is expressed mathematically in Eqs. (6.16a) and (6.16b). We must conclude, then, that the first phase of release is largely elastic, and is therefore also isentropic. One should expect a substance undergoing isentropic expansion to cool, and indeed we observe that the temperature of the element briefly drops by 123 K between 247 and 254 ps. As a preliminary test of the heat equation, one can estimate the thermoelastic cooling that should attend a decrease of the longitudinal elastic strain ε^e_{zz} from 9.5% to 4.3%. Using the cooling rate $\dot{T}_{\mathrm{TE}} = T\gamma : \dot{\varepsilon}^e$, the change in temperature δT may be approximated as

$$\delta T \approx (T_0 + \delta T/2)\, \gamma_{zz} \delta\varepsilon^e_{zz} \tag{6.17}$$

where T_0 is the initial temperature. Given that $\gamma_{zz} \approx 1.5$ at 100 GPa and that $\delta\varepsilon^e_{zz} = (4.3 - 9.5)\%$, we find $\delta T = -131$ K. The expansive cooling during the elastic release can therefore be predicted reasonably well within the Grüneisen formalism.

By 254 ps, the shear strain $\Delta\varepsilon^e$ has reached 4.2%. At this point, the corresponding shear stress $\tau = [\sigma_{zz} - (\sigma_{xx} + \sigma_{yy})/2]/2 \approx -5$ GPa has built to such a level that the crystal yields. The plastic deformation that ensues allows ε^e_{xx} and ε^e_{yy} to start decreasing, as can be seen in Fig. 6.9(a). It is at this moment that the release path departs from the isentrope. In fact, the temperature of the element practically stagnates, signalling the presence of a substantial heating mechanism that counteracts the thermoelastic cooling suffered by the material as it expands. Note also that when the crystal yields, the dislocation density ρ_D, which was previously undergoing something close to an exponential decay, suddenly jumps by some 25% in response to the renewed plastic strain rate of order 4×10^9 s^{-1} [see Fig. 6.9(b)]. Following a plateau of around 15 ps duration, ρ_D then drops, and resumes its decay to a limiting value of 5×10^{12} cm^{-2}. Given that the dislocation density undergoes a net decrease during release (as illustrated in Fig. 6.10), we should expect that some part of the heating during release is attributable to recovery of microstructure energy.

Before attempting to interpret the temperature evolution, we shall first look at two other interesting aspects of the load cycle. First, the assumption that thermal conductivity need not be considered in the heat equation (i.e. that the crystal really

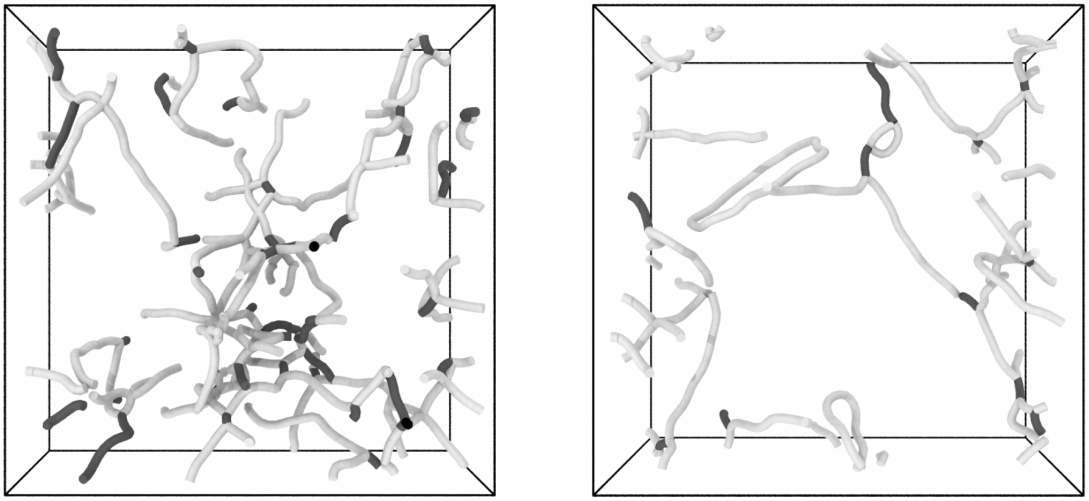

Before release (247 ps) After release (378 ps)

FIG. 6.10. Dislocation network within a material element releasing from a 100 GPa shock state (left) immediately before release and (right) long after release. Light grey dislocations have Burgers vectors of the type $\frac{1}{2}\langle 111\rangle$, dark grey $\langle 100\rangle$. Dislocations were identified using the dislocation extraction algorithm [123, 124].

does release adiabatically) will be verified by directly evaluating the heat flux into the material. We will then assess the magnitude of the plastic dilatation ε_V^p [which is needed to calculate the macroscopic plastic strains with Eq. (6.16)], and identify which species of crystal defect are responsible for it.

6.4.2 Test of adiabaticity

The heat equation constructed in Sec. 6.2.1 describes a material undergoing adiabatic deformation. That is, it accounts only for heating or cooling attributable to thermodynamic work (either elastic or plastic), not for temperature changes caused by the direct flow of heat in or out of the system. While thermal radiation is not modelled in these simulations, and thermal convection is precluded by construction (we are treating a Lagrangian material element here), it is perhaps not immediately obvious that thermal *conduction* should be negligible. Indeed, it transpires that there is actually a temperature gradient along the release fan both during and after release (as will be demonstrated in Sec. 6.4.5), which could in principle cause a flow of heat. Fortunately, we can use the first law of thermodynamics to show directly that the crystal experiences a negligible amount of heat flux.

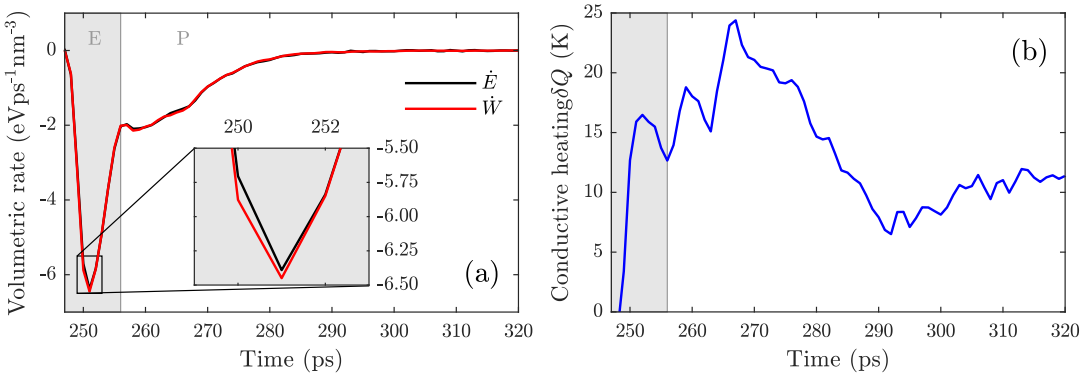

FIG. 6.11. (a) Rate of change of internal energy $\dot{E}$ and total work rate $\dot{W}$ (expressed per unit volume) for a material element in a single crystal releasing from the 100 GPa shock state. (b) The inferred conductive heating $\delta Q = \int dt' \, (\dot{E} - \dot{W})$ as a function of time.

The first law states any change to the internal energy of a closed system, δE, can be expressed as the sum of the mechanical work performed upon it, δW, and the heat supplied to it, δQ:

$$\delta E = \delta W + \delta Q. \tag{6.18}$$

So, if one knows both the internal energy variation of a given element *and* the rate at which mechanical work was performed upon it, one can infer how much heat (if any) is required to make up the shortfall. The internal energy of each material element is readily obtained from its constituent atoms' velocities and potential energies, while the total work rate $\dot{W}$ can be found if one knows its stress-strain state [246]:

$$\dot{W} = V \left(\sigma : D \right). \tag{6.19}$$

D is the so-called *stretching tensor*, and is related to the total deformation gradient F via $D = \frac{1}{2}(\dot{F}F^{-1} + [\dot{F}F^{-1}]^T)$. The macroscopic deformation gradient for this uniaxial loading scenario is simply $F = \mathrm{diag}(1, 1, V/V_0)$, so the total work rate reduces as expected to

$$\dot{W} = \sigma_{zz} \times \frac{dV}{dt}. \tag{6.20}$$

To deduce δQ, one simply integrates the difference between $\dot{E}$ and $\dot{W}$:

$$\delta Q(t) = \int^t dt' \, \left(\dot{E} - \sigma_{zz} \frac{dV}{dt} \right). \tag{6.21}$$

Fig. 6.11(a) shows the time dependence of $\dot{E}$ and $\dot{W}$ during release for the material element located 0.2 μm from the rear surface of the crystal. Plotted on the opposite graph is the cumulative amount of heat transferred, $\delta Q(t)$, expressed in terms of the change in temperature it would produce. We see that the difference between $\dot{E}$ and $\dot{W}$ is generally extremely small, indicating that the overwhelming majority of changes to the element's internal energy can be ascribed to mechanical work. The inferred change in temperature owed to thermal conduction during release [plotted in Fig. 6.11(b)] amounts to only 10 K. Even if this temperature change is physically meaningful (i.e. not just due to the noisiness of the profiles of $\dot{E}$ and $\dot{W}$), it is so small in comparison to the other terms in the heat equation that it is likely not worth the trouble to correct for. It seems that the duration of the release process for the crystal simulated here is so short that there is simply not enough time for appreciable thermal conduction to take place. The question of whether the conduction can be ignored in *experiment* will be visited in Sec. 6.4.5.

6.4.3 Origin of the plastic dilatation

To calculate the crystal's macroscopic plastic strain state ε^p via Eq. (6.16), one needs to know its plastic dilatation $\dot{\varepsilon}^p_V = \sum_i \dot{\varepsilon}^p_{ii}$. This is the fractional change in volume produced purely by plastic deformation. Per Eq. (6.15), ε^p_V may be calculated by finding the difference between the true volume of the region of interest, V, and the volume that it would have if all of its constituent atoms had a perfectly crystalline environment with strain state ε^e. As any atom located near one of the myriad defects in a shock-loaded crystal does *not* occupy an ideal lattice site, one should in general anticipate that ε^p_V will be non-zero. In the following section, the magnitude and origin of the element's observed dilatancy will be explored.

Fig. 6.12(a) shows the variation of the element's plastic dilatation, calculated using Eq. (6.15), during shock and subsequent release. The dilatation reaches a local maximal value of 0.3% a few picoseconds after the arrival of the shock, before undergoing an exponential decay as the element relaxes (much as ρ_D and ρ_t do). At the onset of plastic release, ε^p_V experiences a small 'bump' (somewhat like ρ_D and ρ_t), but then increases linearly until around 300 ps, after which the dilatation appears to

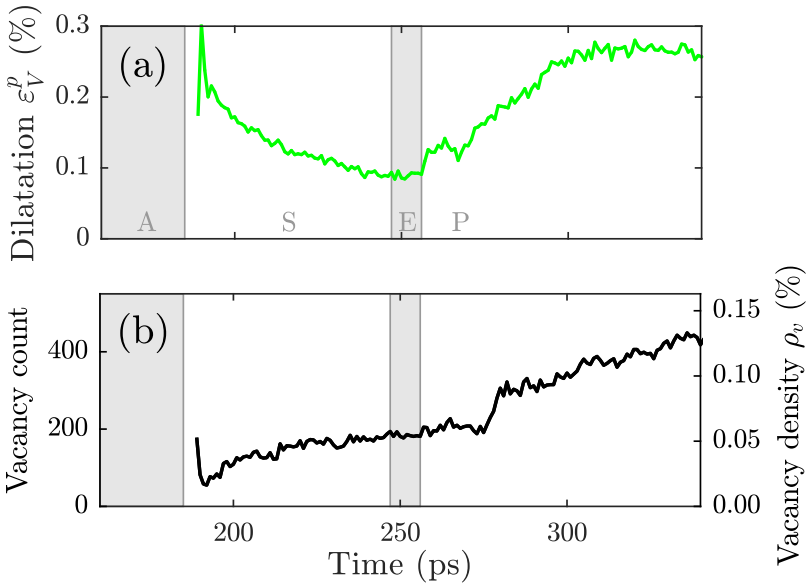

FIG. 6.12. (a) Variation of the plastic dilatation for a material element releasing from the 100 GPa shock state. (b) Approximation of the number of vacancies present in the element, expressed as both a raw count (left axis), and as a fraction of the element's atomic population (right axis).

saturate at a limiting value of 0.27%. We note first that the dilatation is small (i.e. sub-percent), but not so small as to be negligible. Second, the time dependence of ε_V^p has a definite and rather interesting structure. However, the structure is not easily explicable in terms of either the dislocation density or the twin fraction, neither of which increases as ε_V^p does during plastic release. The culprit is a proliferation of a third species of crystal defects we have not yet considered: vacancies.

In Chapter 3, it was shown how point vacancies (and aggregates thereof) could be indirectly detected and counted by examining the spectrum of atomic cluster populations. Vacancies tend to be associated with clusters with populations between 10 and 100: an isolated single vacancy creates a connected group of 14 defective atoms, a divacancy between 22 and 28 defective atoms, and so on. Defective clusters with populations exceeding 100 or so tend to belong to far larger defect structures, e.g. dislocations or twin boundaries, which comprise hundreds to thousands of connected, noncrystalline atoms. This stratification of the spectrum means aggregates of point vacancies have a fairly conspicuous signal. Even so, reliably identifying and counting vacancies in this shock-released crystal is challenging because of its high tempera-

ture[32] – thermal noise causes many atoms to be misidentified as defective by the a-CNA routine, which hampers both visualisation of the defects and interpretation of the cluster population spectrum. To facilitate accurate counting of the vacancies, one can *quench* the atomistic configuration (that is, drain it of its kinetic energy) before partitioning it into clusters. This was achieved as follows.

First, the instantaneous deformation state of the element $F^e(t)$ was obtained. The element was then isolated, and the coordinates of its constituent atoms were scaled using the operator $[F^e(t)]^{-1}$, which effectively 'undoes' the elastic deformation imposed on the element by the loading process and brings it to an approximately hydrostatic stress state. The element was then allowed to evolve under an NVE ensemble, but with an additional viscous damping force applied to each atom. The idea is to allow each atom to settle dynamically to its equilibrium position, but first to relieve as far as possible any shear stress that could cause it to undergo plastic flow while it does so. It is only once the temperature of the element has dropped to a sufficiently low value (< 0.1 K, say) that we apply the cluster analysis and count the vacancies using the cluster population spectrum. By applying this process at each instant of time, we can construct the vacancy population profile.

Fig. 6.12(b) shows the inferred variation of the vacancy count for $t > 190$ ps alongside the dilatation profile. The vacancies cannot be counted during the first 5 ps of shock compression (185 ps $\leq t <$ 190 ps) due to the element's being highly defective, but after this period a meaningful profile emerges. We see that approximately 200 vacancies are created during compression, and another 200 or so form during release. The crystal is thus left surprisingly porous – given that this material element's population is 340 000, this means just over one in every thousand lattice sites is unoccupied. Fig. 6.13 shows that the vacancies and vacancy clusters are distributed evenly throughout the element, and that only 65% of the vacancies are found in complete isolation – the remainder form groups of two or more. Though a discussion of the details of the vacancy nucleation mechanism is beyond the remit of this chapter, it is noted that screw dislocations gliding through a simulated bcc crystal under high shear stress have previously been observed generating copious point vacancies via the so-called *cross-kink* mechanism – the interested reader is

[32] The typical post-breakout temperature, ~ 1650 K, constitutes half of tantalum's ambient melt temperature T_M [216].

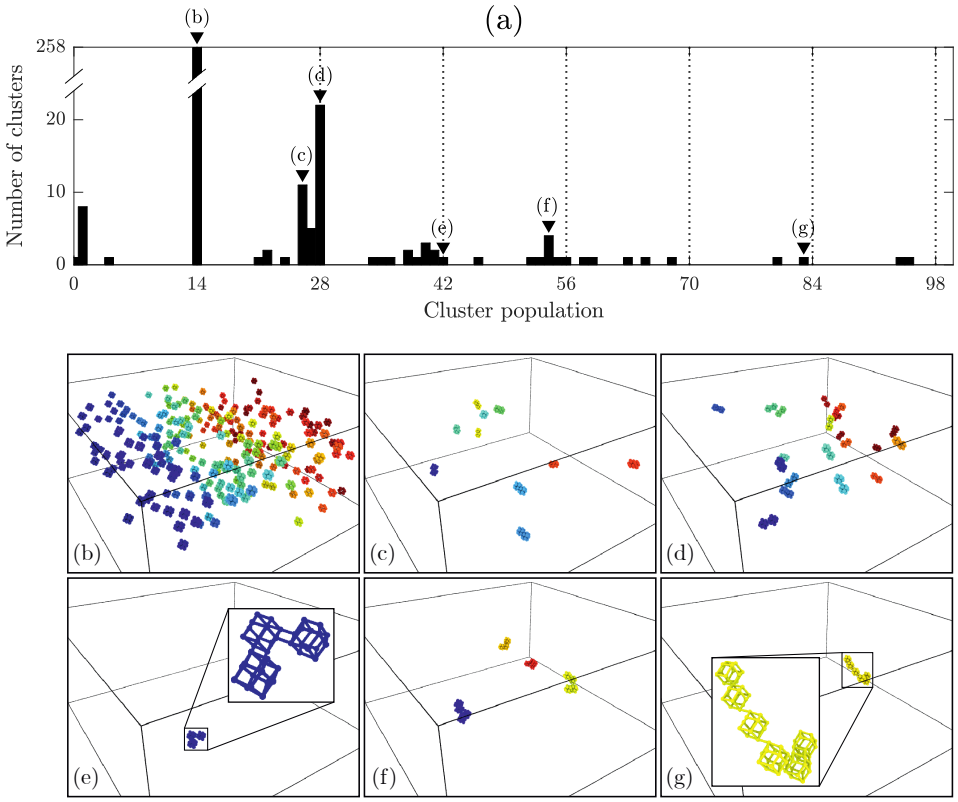

FIG. 6.13. Vacancy detection algorithm applied to a Lagrangian material element after complete shock release from the 100 GPa shock state (t = 378 ps). (a) Distribution of defective atomic cluster populations. Isolated vacancies generate clusters of 14 defective atoms; aggregates of vacancies form groups with populations slightly below integer multiples of 14. (b–g) Groups of vacancies from selected peaks in the cluster spectrum. Single vacancies are abundant, but chains of up to six or seven vacancies exist too.

referred to Ref. [247] for a detailed description of the nucleation process.

One question that naturally arises from this analysis is: where are all the self-interstitials? The atoms that vacate their lattice sites must go somewhere, after all. One's first thought might be that some of the point vacancies shown in Fig. 6.13 are actually interstitials that have been misidentified – indeed, the 'vacancy'-counting technique described in Sec. 3.5.2 is so crude that it cannot tell the difference between different types of point defect. When the material element under consideration is systematically viewed plane-by-plane, however, only one interstitial defect can be found: a single ⟨111⟩ *crowdion*, in which five atoms are distributed between four lattice sites. That is, the point defects shown really are almost exclusively vacancies. How is so great an asymmetry between the vacancies and the interstitials possible?

The answer may lie in their mobilities. Under the Ravelo Ta2 potential, the

migration energy of an isolated vacancy is 1.08 eV [54]. At the temperatures characteristic of this shock pressure ($T \approx 1700$ K $\equiv 0.15$ eV), vacancies are therefore practically immobile over the picosecond timescale of the shock-release process. The migration energy of a self-interstitial, meanwhile, might only be a fraction of an electronvolt[33], meaning its diffusivity can be several orders of magnitude greater than that of a vacancy [250], such that it can move through many lattice spacings over tens of picoseconds. Where, then, will the interstitials 'choose' to go? It is now understood that, given enough time, self-interstitials tend to migrate towards one another and form platelike clusters called *interstitial loops*[34]. The boundary separating this loop from the rest of the crystal may in fact be a perfect dislocation; the loop itself is nondefective. In this way, any interstitials nucleated by the cross-kink mechanism can be rapidly reintegrated into the host crystal. The disparity between the migration energies of vacancies and self-interstitials may thus explain why only the former are visible following release from the shock state.

The most promising feature of the vacancy density profile shown in Fig. 6.12 is that it *increases* during the unloading phase, just as the dilatation does. To gain an idea of whether the late-time dilatation's being attributable to the vacancies is plausible, we can use the following crude reasoning. Imagine taking a pristine crystal comprising N atoms, and generating a vacancy by plucking a single atom out of the bulk and placing it on the crystal's surface. Where once the crystal occupied N lattice sites, each with some effective volume Ω_0, it now takes up approximately $N+1$ sites. The fractional volume change effected by the creation of this vacancy is $[(N+1)\Omega_0 - N\Omega_0]/(N\Omega_0) = 1/N$. If one makes N_v vacancies, the volume change is N_v/N, which we will define as the vacancy density ρ_v:

$$[\varepsilon_V^p]_{\text{vacancies}} \approx \rho_v. \tag{6.22}$$

At late times in Fig. 6.12, we observe a dilatation of 0.27%, and a vacancy density of 0.13%. The porosity owed to the vacancies is therefore, at the very least, of the

[33] Self-interstitial migration energies for the Ta2 potential are not quoted in the original paper [54], but first-principles calculations place their value at between 0.4 and 0.6 eV [248, 249].

[34] There is strong motivation to understand the behaviour of interstitials and the aggregates they form from the nuclear power industry: the structure surrounding a reactor is continually bombarded by a flux of neutrons capable of blasting its constituent atoms from their lattice sites, causing a *displacement cascade* that results in the generation of many vacancies and interstitials, and, ultimately, damage to the material. Self-healing nanomaterials that capture and recombine interstitials with vacancies are being explored as a potential means of solving this problem [251].

correct order of magnitude to account for the observed dilatation. The 0.14% of the dilatation that remains unaccounted for could be explained by the fact that the crude cluster counting algorithm almost always underestimates the vacancy density: any vacancy 'attached' to a much larger defective structure (like a dislocation or a surface) is absorbed into its associated cluster, and thus evades detection. A more sophisticated algorithm than the one used here could easily circumvent this issue.

To give as full an account as possible of the dilatation observed during the shock-release cycle, we can attempt to express ε_V^p as a sum of dilatations from each defect species, and compare the prediction with the known dilatation. Suppose each vacancy, each length of dislocation, and each volume of twinned material brings about some constant amount of plastic dilatation. If this is so, ε_V^p can be expressed as

$$\tilde{\varepsilon}_V^p(t) = \alpha_v \rho_v(t) + \alpha_t \rho_t(t) + \alpha_D \rho_D(t), \tag{6.23}$$

where α_v, α_t and α_D are constants to be determined. We make this constant-dilatancy assumption for convenience, and with the express understanding that it is almost certainly false – it would be surprising if the dilatation per defect did not vary with pressure to some degree. The assumption that a given volume of twinned material occupies a constant excess volume is also suspect[35]. Pressing on regardless, we can find the dilatancy coefficients that minimise the sum of the squared residuals, $\sum_i [\tilde{\varepsilon}_V^p(t_i) - \varepsilon_V^p(t_i)]^2$, where the sum is conducted over the set of timesteps $\{t_i\}$ at which the system is characterised.

Fig. 6.14 shows the measured dilatation ε_V^p, the modelled dilatation obtained from the best fit $\tilde{\varepsilon}_V^p$, and the contributions to the excess volume from each species of defect. We see that while the fit struggles in several places (likely due to the shortcomings of the vacancy detection algorithm), the gross features of the dilatation can be accounted for: the rapid peak and subsequent decay during shock compression are owed to the short-lived deformation twins that nucleate on shock, and the steady increase during shock release, as suggested above, is owed to the vacancies. The dislocations, meanwhile, apparently contribute very little to the dilatancy.

In summary, the proliferation of point vacancies generated during deformation

[35] Any dilatation caused by a twin is presumably associated with its boundaries, rather than the twinned material itself (which is non-defective).

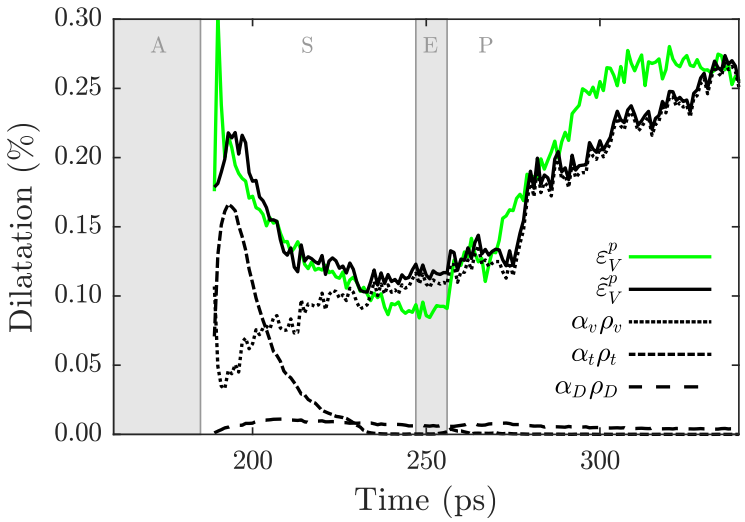

FIG. 6.14. Comparison of the calculated plastic dilatation ε_V^p and a simple modelled dilatation $\tilde{\varepsilon}_V^p$, in which the dilatation is expressed as sum of contributions from point vacancies ($\alpha_v\rho_v$), deformation twins ($\alpha_t\rho_t$), and full dislocations ($\alpha_D\rho_D$).

can in principle provide a physical origin for the plastic dilatation of 0.27% observed following release. If one substitutes the expression for the plastic strains [Eq. (6.16)] into that for the rate of plastic work [Eq. (6.5)], one obtains the following:

$$\dot{w}^p = (\sigma_{xx} - \sigma_{zz})(-\dot{\varepsilon}^e_{xx}) + (\sigma_{yy} - \sigma_{zz})(-\dot{\varepsilon}^e_{yy}) - \sigma_{zz}(-\dot{\varepsilon}^p_V). \tag{6.24}$$

Given that $|\delta\varepsilon_V^p| \approx 0.1\%$ during release, and that $\sigma_{zz} \approx 50$ GPa on average, the correction to the plastic work heating provided by the plastic dilatation will be of order 15 K – small, but not entirely negligible.

6.4.4 Interpretation of the temperature evolution

We can now piece everything together, and apply Eq. (6.8) to the Lagrangian material element undergoing shock release. To make more apparent the effect of each mechanism, we will consider various solutions to the heat equation in which certain source terms are 'switched off'. The isentropic solution, T_s, is obtained simply by integrating the thermoelastic cooling term:

$$T_s(t) = \int^t dt'\ \dot{T}_{\mathrm{TE}}(t'). \tag{6.25}$$

The perfect-plastic solution, T_p, is obtained by summing the thermoelastic and plastic-work heating contributions:

$$T_p(t) = \int^t dt' \left(\dot{T}_{\mathrm{TE}}(t') + \dot{T}_{\mathrm{PW}}(t') \right). \tag{6.26}$$

This is the temperature evolution that would result if plastic work were converted purely to heat, i.e. if work could neither be invested in nor recovered from crystal defects. The full solution, T_f, includes all mechanisms and accounts for microstructural energy exchange:

$$T_f(t) = \int^t dt' \left(\dot{T}_{\mathrm{TE}}(t') + \dot{T}_{\mathrm{PW}}(t') + \dot{T}_{\mathrm{MS}}(t') \right). \tag{6.27}$$

Henceforth, we will focus exclusively on the release portion of the load cycle.

Plotted in Fig. 6.15(a) are the heating rates resulting from plastic work and from defect energy recovery alongside the thermoelastic cooling rate, and in Fig. 6.15(b) we compare the various release paths inferred from these rates with the observed release temperature, T. During the elastic phase of release, the thermoelastic cooling overwhelmingly dominates the element's temperature evolution, and, as expected, the release path closely follows the release isentrope, T_s. As the crystal transitions from the elastic to the plastic phase, the plastic-work heating rate $\dot{T}_{\mathrm{PW}}$ ramps up to about 15 $\mathrm{K\,ps^{-1}}$, and in fact draws approximately equal with $\dot{T}_{\mathrm{TE}}$ for $t > 265$ ps. As a result, when we combine the plastic-work heating and thermoelastic cooling rates to give the perfect-plastic solution T_p, the predicted temperature is practically stagnant during the plastic phase of release. The simulation predicts, then, that plastic-work heating can largely compensate for the cooling effect of expansion, and thus explains the height of the temperature profile.

However, the *shape* of T_p leaves something to be desired: it departs far too quickly from the isentrope when plastic flow begins, and it does not capture the slow temperature rise observed at late times. To resolve these features of the release path, we must appeal to the microstructural term $\dot{T}_{\mathrm{MS}}$. Fig. 6.15(a) shows that shortly after plastic flow begins, $\dot{T}_{\mathrm{MS}} < 0$, i.e. it brings about a cooling effect. This reflects the fact that the dislocation density briefly rises when the crystal yields [see Fig. 6.9(b)], meaning some fraction of the plastic work must be siphoned off and

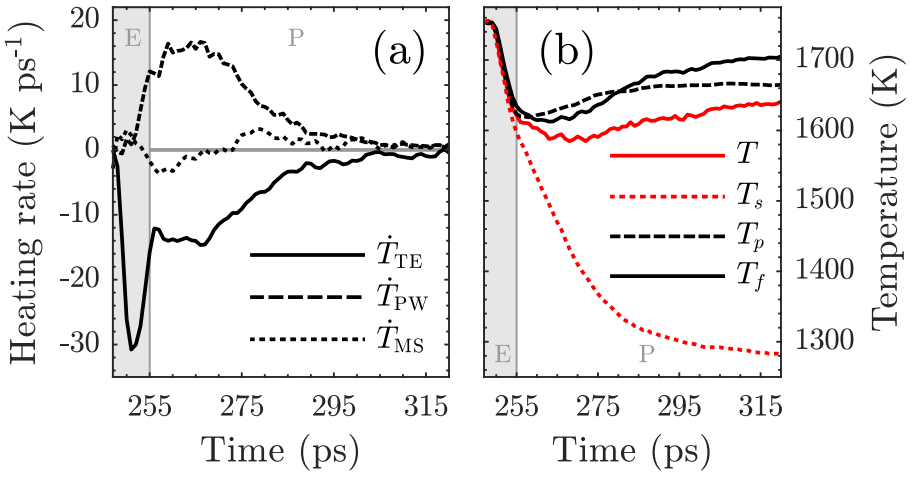

FIG. 6.15. Thermal analysis of a material element 200 nm below the free surface of a single crystal releasing from the 100 GPa shock state to ambient pressure. (a) Heating rates resulting from the thermoelastic effect ($\dot{T}_{\mathrm{TE}}$), plastic work ($\dot{T}_{\mathrm{PW}}$), and recovery of microstructure energy ($\dot{T}_{\mathrm{MS}}$). (b) Comparison of the observed release path T and the corresponding isentrope T_s with paths predicted from various terms in the heat equation; T_f contains the correction from the microstructural term $\dot{T}_{\mathrm{MS}}$, while T_p does not. Periods of elastic and plastic release are labelled E and P, respectively.

invested in making new defects. This is why T_p overestimates the heating rate early on. Conversely, $\dot{T}_{\mathrm{MS}} > 0$ at late times, meaning the evolution of the defects brings about a heating effect. This is because the dislocation density decays after 275 ps, and the energy that was previously stored by these defects is released into the crystal as heat. By accounting for the energy content of the defects, we are thus able to reproduce the shape of the release path with greater fidelity.

Overall, the agreement between the predicted and measured release paths, T_f and T, is fair, insofar as the height and shape of the profile are approximately correct. There is, however, a rather conspicuous gap between the two. The late-time disparity between the two profiles is 64 K, which constitutes about 18% of the magnitude of the difference between the isentropic and observed release paths. This is surprising given that the tests in Sec. 6.2.3 suggested that the thermoelastic and plastic-work heating mechanisms can be modelled accurately, at least individually. Assuming all of the ingredients of the heat equation have been calculated correctly, it would seem that some additional physics manifests when the material undergoes true shock release. It is difficult to speculate on the source of the disparity without additional investigation. It should be noted, though, that the Grüneisen formalism is

reliant on the crystal's being in thermodynamic equilibrium at all times. However, if dislocations are nucleated or annihilated quickly enough, the crystal's phonon spectrum will assume a nonequilibrium distribution [252], and could thus cause the Grüneisen formalism to fail. A thorough exploration of this intriguing issue could form the basis of further work.

All this being said, the agreement between T and T_f, while imperfect, is good enough that we can state with some confidence that the bulk of the heating we observe on release is indeed due to plastic-work heating, owing to the high strength exhibited by the crystal.

6.4.5 Depth-dependent heating

We have been able to give a fair account of the temperature evolution of a single material element undergoing shock release. The final point we will explore in this chapter is how the local temperature evolution varies with depth below the rear surface of the sample. It is known that the strain rate associated with a release wave falls as it propagates, due to the top of the wave travelling faster than its tail. It is further known that material strength generally decreases with decreasing strain rate. One might expect, then, that the heating suffered by the material during release falls as one looks deeper into the crystal. This is exactly what is observed, as will now be shown.

Fig. 6.16 shows the variation of the plastic shear strain rate $\dot{\varepsilon}^p_{xz} = \frac{1}{2}\left(\dot{\varepsilon}^p_{xx} - \dot{\varepsilon}^p_{zz}\right)$ and the corresponding shear stress $\tau_{xz} = \frac{1}{2}\left(\sigma_{xx} - \sigma_{zz}\right)$ during release for material elements initially situated up to 200 nm from the crystal's rear surface. The quantities τ_{xz} and $\dot{\varepsilon}^p_{xz}$ characterise the shear stress and shear strain rate experienced by crystal planes with normals along $(\pm 1, 0, 1)$, i.e. those that sit at 45° to the loading direction. As expected, we see that material further from the rear surface suffers a lower peak plastic strain rate due to the gradual broadening of the release fan. The decreasing strain rate can be accommodated by slower-moving dislocations, which can in turn be driven by lower shear stresses, as shown in Fig. 6.16(b). The attenuation of the peak flow stress with depth is quite dramatic over the distance considered here, falling from 6 GPa to 4 GPa over the course of only 0.2 μm. Since the local

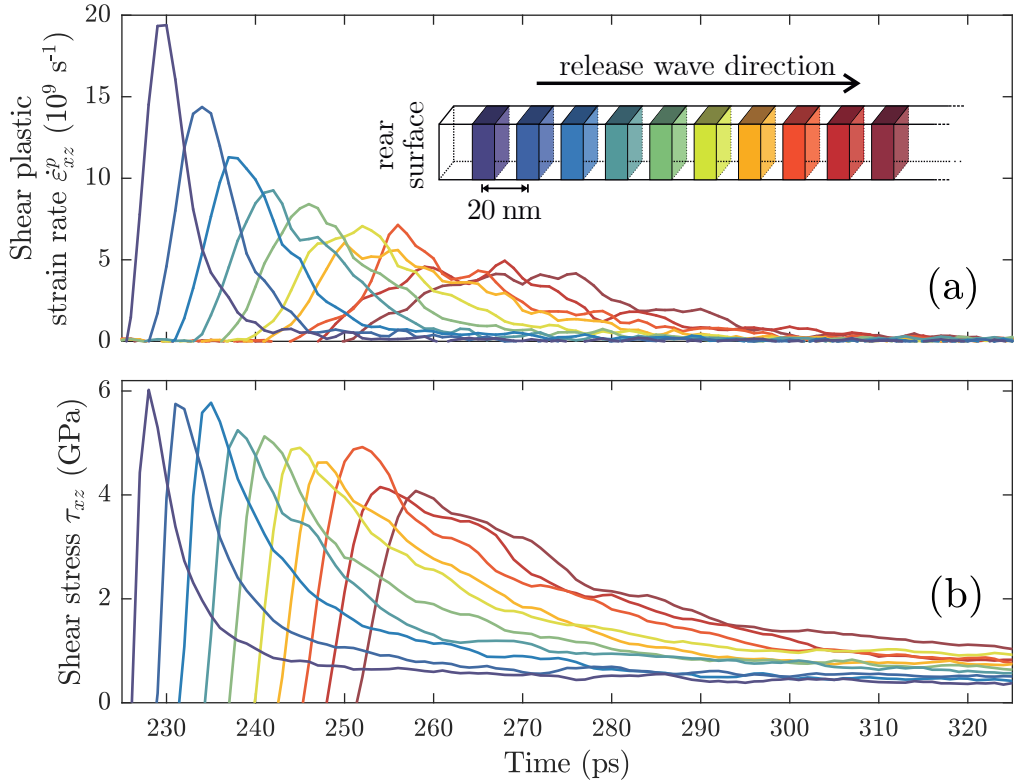

FIG. 6.16. Time evolution of (a) shear plastic strain rate $\dot{\varepsilon}^p_{xz}$ and (b) corresponding shear stress τ_{xz} of a set of releasing material elements initially spaced at regular 20 nm intervals from the rear surface. Curves coloured according to the element they correspond to [see inset diagram in (a)].

strain rate within the rarefaction wave falls monotonically with distance, one should expect this decay of the local shear strength to continue as one moves further and further from the target's rear surface.

It is readily observed from Eq. (6.24) that the material further from the rear surface undergoing deformation at lower shear stress should suffer less plastic-work heating. This is confirmed in Fig. 6.17(b), in which the total plastic work $T_{\mathrm{PW}} = \int dt\, \dot{T}_{\mathrm{PW}}$ performed on each material element during release is plotted as a function of its Lagrangian distance from the rear surface. Shown also in Fig. 6.17(a) are the time-averaged stresses and (inverse) strain rates, $\langle \tau_{xz} \rangle$ and $\langle \dot{\varepsilon}^p_{xz} \rangle^{-1}$, for reference. We see that the local plastic-work heating T_{PW} generally increases as one moves towards the rear surface (though it is slightly reduced in the immediate vicinity of this surface, as will be explained momentarily).

The heat analysis performed in the previous section indicated that it is plastic

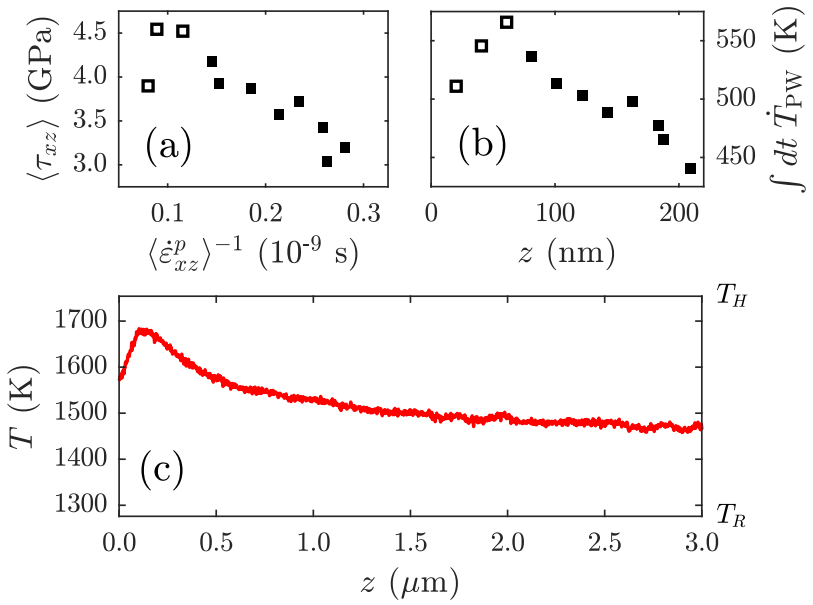

FIG. 6.17. (a) Time-averaged shear stress $\langle \tau_{xz} \rangle$ on planes at 45° to the loading direction against inverse plastic shear strain rate $\langle \dot{\varepsilon}^p_{xz} \rangle^{-1}$ for a set of material elements releasing from a 100 GPa shock. (b) Plastic-work heating versus Lagrangian distance from the rear surface, z. (c) Temperature profile for a 6-μm-long crystal unloading from 100 GPa at 1.3 ns after breakout. T_H and T_R denote the shock and isentropic release temperatures, respectively. Lagrangian material elements found in the cooler region immediately below the rear surface are marked by hollow data points.

work that provides the bulk of the heating observed on release. We should therefore expect that material nearer the rear surface will be hotter. To confirm this, the spatial temperature profile of a much larger crystal some 6 μm long is shown in Fig. 6.17(c) at 1.3 ns after shock breakout. The sample length is comparable to those of the targets described in the previous chapter, as is the time at which it is 'probed', so a direct comparison with the experiment is warranted. One can see that the release temperature of the crystal falls as one moves away from the surface material into the bulk. Note, however, that the length scale over which the temperature decays is of order microns: the average temperature of the last 3 μm of material is 1520 K, which is still some 250 K above the isentrope. So, although the release heating mechanism diminishes with increasing distance into the crystal, it does so sufficiently slowly that a micron-scale target will suffer substantial plastic-work heating throughout its length. The simulation is therefore consistent with the experimental observations described in the previous chapter.

It is interesting to note that the release temperature does not decrease mono-

tonically with depth, but actually has a global maximum approximately 100 nm below the free surface. There appear to be two reasons for this. First, we see from Fig. 6.17(b) that the plastic work performed on release starts to fall once one is less than 50 nm from the rear surface. Given that the speed of the shock and the top of the release wave is approximately 5 kms^{-1} at this shock pressure, material less than 50 nm below the surface is compressed for at most 20 ps before it starts to release. We see from Fig. 6.9(a) that before 20 ps have elapsed the crystal is still undergoing plastic deformation – the elastic strain along y (i.e. $[01\bar{1}]$) is particularly slow to relax, as we saw in Chapter 4. This means that, for material in proximity to the rear surface, there is less plastic deformation to 'undo' during release, so less work is performed upon release. The second (and related) reason for the surface being marginally cooler is that less plastic work is performed on this shallow material on *shock*, again because the plastic deformation process precipitated by the shock is never completed. The hottest material, then, is close enough to the surface to experience maximal flow stress on release, but sufficiently far away that it experiences the maximum amount of cumulative plastic flow possible over the shock-release cycle for the given shock pressure.

There is a final point to be made here about length scales and timescales. It was noted above that the extent of the heating experienced by the material is smaller further into the target. One can imagine that if the target were much longer (on the scale of a millimetre, say), the strain rate in the rarefaction fan could eventually fall so far that the flow stress in the fan could reassume its quasistatic limit[36]. In this limit, the plastic-work heating during release would (presumably) be negligible compared to the expansive cooling. The crystal bulk would therefore release isentropically, in accordance with the textbook picture of release. A temperature difference of hundreds of degrees would thus exist between the crystal's surface and its interior. It is therefore important to consider, for a given experiment, whether thermal conduction has sufficient time to iron out the temperature gradient.

From Fig. 6.17(c), we see that the characteristic distance L over which the temperature varies in the vicinity of the free surface is of order one micron. The thermal diffusivity D of tantalum is approximately 23 mm^2s^{-1} [253]. The timescale t_D over

[36] Note that 'quasistatic' is not quite the same as 'ambient' – the dense dislocation network left in the wake of the shock could still enhance the flow strength on release above its ambient value due to the effects of work hardening [98]. Pressure hardening, too, would likely be non-negligible.

which the excess surface temperature would dissipate is therefore $t_D = (1\ \mu\text{m})^2/D \approx 50$ ns. This diffusion time greatly exceeds the implicit nanosecond timescale of laser-compression experiments using micron-scale foils. In other words, the duration of these experiments is so short that the temperature gradient owed to the decay strain rate is effectively 'frozen into' the sample. By contrast, gas-gun experiments often use millimetre-scale projectiles and targets, and are therefore typically conducted over the course of a microsecond or so. This is ample time for the high surface temperature to diffuse into the bulk. So, while the rear surface of a 'macroscopic' target would still release nonisentropically, one might be hard-pushed to detect this unless one deliberately probed within the first few tens of nanoseconds of shock breakout. In conclusion, while the last few microns of material will always release nonisentropically (if it is sufficiently strong), it is the timescale of the experiment that dictates whether this is observable.

6.5 Beyond tantalum

It should be borne in mind that this result (that shock release is highly nonisentropic for sufficiently strong targets) is not necessarily peculiar to tantalum. To gain an idea of whether a given target will release nonisentropically, one can use Eq. (6.8) to estimate the instantaneous ratio of the magnitudes of the plastic-work heating and thermoelastic cooling terms. If for simplicity one assumes that both γ_{ij} and $\dot{\varepsilon}^e_{ij}$ are scalars (i.e. tensors proportional to δ_{ij}), it can be shown that the ratio reads

$$R = \frac{4}{3}\left(\frac{\tau}{c_V T}\right)\frac{1}{\gamma}, \tag{6.28}$$

where $\tau = (\sigma_{xx,yy} - \sigma_{zz})/2$ is the flow stress. Any material for which this dimensionless figure of merit R approaches or exceeds unity will release nonisentropically. Clearly, the greater the strength of the material, the more likely this is.

6.6 Conclusion

In summary, large-scale molecular dynamics of shock release in tantalum single crystals have been performed, and have demonstrated that the temperature following

shock release greatly exceeds what one would expect were the release to be isentropic. The heat equation was used to quantify the massive plastic-work heating suffered by the crystal, which compensated almost entirely for the expansive cooling owed to the thermoelastic effect. The prodigious heating was ultimately owed to the crystal's exceptional strength during release (typically 5 GPa) that was in turn due to the extreme rate at which it is forced to deform. These simulations were consistent with the experimental observations of highly nonisentropic release in shock-loaded tantalum foils described in the previous chapter. These results challenge the textbook understanding of shock release, and illustrate the power of combined computational and experimental studies of lattice response under high strain rate.

CHAPTER 7

Conclusion

It is the hope of the author that the results of this thesis have demonstrated not only the rich physics owed to material strength under shock conditions, but also the immense power of the molecular dynamics simulation technique, as both a predictive and as an interpretative tool. This final chapter summarises the main findings of Chapters 4 to 6, and speculates upon possible routes for further work.

7.1 Summary

In Chapter 4, the role of grain interactions under shock conditions was investigated by means of large-scale molecular dynamics simulations. First, the response of a control group of tantalum single crystals shocked along [011] was examined. These monocrystals showed marked stress anisotropy in the plane normal to the shock (due to their twofold rotational symmetry about the loading axis). Elementary polycrystals built from several such crystals were then simulated under elastic loading conditions. It was shown that stress anisotropy at the level of each grain causes stress gradients to form over the grain boundaries, and thus causes grains to exert gigapascal-scale stresses on one another. The influence of these interactions under shock conditions was then explored. It was found that the deformation intergranular forces cause can replace conventional plastic deformation, and thus alter the defect content of the polycrystal. The deformation further allows grains to relax to a state of lower shear stress than would ordinarily be permitted by material strength, provided the grains are coordinated in such a way that they can relax cooperatively. This study demonstrates that the grain dynamics taking place in the wake of the shock are complex and dramatic, and have measurable effects on the polycrystal's elastic strain state that can in principle be detected by x-ray diffraction.

Chapter 5 presented the results of an experiment conducted at LCLS in which the temperature of tantalum foils following shock release from a megabar pressure

state was measured *in situ* using x-ray diffraction. The data showed that, following a shock-release load cycle, the foils were less dense than they were pre-shock, indicating they had thermally expanded. An algorithm to convert the elastic strains obtained from a diffraction pattern to a release temperature while properly accounting for material strength was derived, and then verified on synthetic diffraction data generated from molecular dynamics simulations. When the algorithm was applied to experimental data, the inferred release temperatures exceeded that expected from a purely isentropic release by a considerable margin. The algorithm further suggested that the release temperature saturated at the ambient melt temperature above shock pressures of about 150 GPa. Both of these qualitative features of the experimental data were reproduced by small-scale molecular dynamics simulations of tantalum monocrystals undergoing quasistatic release.

The physical origin of the highly nonisentropic release observed experimentally was identified in Chapter 6, which details the results of large-scale molecular dynamics simulations wherein the temperature evolution of a micron-scale tantalum crystal undergoing shock release was interpreted by use of a heat equation. The equation accounted for the effects of thermoelastic cooling, plastic-work heating, and changes in the energy of the crystal's dislocation network; the accuracy of each of these terms was verified using small-scale simulations of single crystals undergoing quasistatic deformation. Full simulations of micron-scale tantalum crystals in shock and release were then performed. These too showed unexpectedly high release temperatures, which the heat equation attributed to the massive plastic-work heating resulting from the crystal's exceptionally high strength during release. The high strength was a direct consequence of the extremely high release rate, a conclusion consistent with the observation that material deeper into the crystal experiencing a slower rarefaction was cooler. Together, Chapters 5 and 6 contradict the textbook picture of shock release as an isentropic process.

7.2 Further work

There are a number of routes for further work that might shed further light on the physics of grain interactions under shock-loading conditions, and bring us closer

to detecting such interactions in experiment. It would first be useful to conduct a search of the 'parameter space' of polycrystals for a target in which the effects of grain interactions are maximised. One might start, for example, with a systematic study of polycrystals with a wider range of morphological and crystallographic textures (rather than just the two presented here). The simulations indicate that the efficiency of the cooperative relaxation mode is dictated by the configuration of the grains. A deeper, more intuitive understanding of how each grain frustrates the relaxation of its neighbours might make it possible to predict the efficiency of elastic deformation in a real polycrystal with a known texture. It is also likely that there exists a particular element whose mechanical properties are such as to amplify grain interactions further. Desirable properties would include high material strength (as this would make elastic relaxation effects more conspicuous), and a *Zener ratio* far from unity (which would ensure that large stress gradients were induced over the grain boundaries upon shock compression).

It would also be fascinating to study the role of grain size. It was noted in Chapter 4 that, at shock pressures of around 50 GPa, the elastic deformation owed to grain interactions is able to replace ordinary transverse slip because the former takes place very quickly – the response time is essentially the time taken for sound waves to traverse the grain, which for a nanocrystal is only a few picoseconds. If instead the grains were a *micron* across, there would probably not be enough time for the stress waves generated at the grain boundaries to propagate into the bulk and relieve the shear stress generated by shock compression before plastic deformation could do so. One can therefore imagine the grain would possess an 'acoustically insulated' core, with much the same dislocation content as a single crystal, surrounded by a mantle of markedly lower dislocation density. Observing this kind of stratification in a simulation would make for a beautiful illustration of grain interaction physics.

Finally, it would be instructive to identify and quantify the diffraction signatures of grain interaction effects. The simulations show that, if the arrangement of the grains is conducive to cooperative relaxation, the difference between the transverse elastic strains is much smaller than would be expected from the crystal's strength. In principle, these strains can be measured directly using a diffraction pattern, provided one has access to sufficiently many reflections. With a simple model for how the

structure or position of the diffraction peaks changes due to interactions between grains, one could set about identifying the experimental setup in which sensitivity to such interactions is maximized. Studies of this kind could thus inform the design of experiments, and facilitate the observation of grain interactions during a shock.

The study of nonisentropic release, too, naturally suggests several routes for further investigation. It is first important to establish whether the same phenomenon can be experimentally observed in metals other than tantalum. As noted at the end of the previous chapter, nonisentropic release should manifest in any metal that is sufficiently strong, and the tendency of solids to become stronger at higher strain rates is apparently a universal one. It would be particularly interesting to investigate metals with crystal structures differing from that of tantalum – the plastic deformation modes available to a crystal, and so its inherent strength, are governed to a great extent by its structure. Copper, for example, tends to accommodate plastic strain primarily (though not exclusively) by slip due to its being fcc, while zinc, a hexagonal-closed-packed crystal, is expected to respond principally by twinning.

It would also be useful to resolve the discrepancy between the temperature evolution measured in the simulation and the temperature predicted using the heat equation. Although the individual terms in the heat equation appear to be accurate, something causes one or more of them to fail under the rapid shock release conditions explored here. Is the release process really so fast that it cannot be understood using thermodynamics, and so is fundamentally unamenable to the kind of analysis we are trying to perform? If so, do the predictions of the heat equation become more accurate at lower release rates? In what regime is the equation actually applicable? More rigorous testing will be required to answer these questions.

Perhaps the most important avenue of further investigation, though, would be towards a direct experimental measurement of material strength during shock release. The simulations in Chapter 6 suggest that the micron-scale tantalum crystals exhibiting temperatures far exceeding the isentropic release temperature do so because they become extremely strong when forced to unload rapidly. These same excessively high release temperatures were measured experimentally, meaning the experiment is at least *consistent* with the high-strength story. However, no attempt was made to 'close the loop', and measure the flow stress in the release fan directly

directly from the shear strain that could potentially be deduced from the diffraction. This is possible in principle, but by no means easy. The task is made nontrivial by the fact that the x-ray diffraction measurement is not spatially resolved, in the sense that the beam enters the target at an oblique angle and thus scatters from a continuum of strain states – one cannot easily tell which parts of the scattering signal come from which parts of the sample. One could imagine solving this inverse problem by building a 'forward model' that simulates the diffraction pattern generated by a crystal with known elastic strain and rotation profiles, and then iteratively adjusting the profiles until the simulated and experimental signals match (much like the method used in Ref. [59]). With these profiles, one could measure directly the shear strain throughout the release fan, and so its strength.

APPENDIX A

Fibre-texture Fourier transform

This section derives an analytic approximation for the Fourier transform of a fibre-textured polycrystal, given the atomistic configuration of one of its many grains.

Let $\{\mathbf{x}_\alpha^{(0)}\}$ be the configuration of the grain in question. The idea is to emulate the presence of a continuum of 'image' grains whose orientations are related to that of the original grain by rotations about the fibre direction, which we will take to be z. The atomistic configuration of the full polycrystal is easily parametrised: each atom α has an infinite number of images with position

$$\mathbf{x}_\alpha^{(g)} = R_z(\phi_g)\,\mathbf{x}_\alpha^{(0)} + \mathbf{d}_g, \tag{A.1}$$

where ϕ_g is the angle expressing the relative orientation of image grain g and the original grain, and $\mathbf{d}_g$ is their displacement. The Fourier transform of the polycrystal is obtained by summing over every atom and all of its images:

$$F(\mathbf{q}) = \sum_g \sum_\alpha e^{-i\mathbf{q}\cdot\mathbf{x}_\alpha^{(g)}} \tag{A.2a}$$

$$= \sum_g \left[e^{-i\mathbf{q}\cdot\mathbf{d}_g} \sum_\alpha e^{-i\mathbf{q}\cdot R_z(\phi_g)\mathbf{x}_\alpha^{(0)}} \right]. \tag{A.2b}$$

To calculate such a sum by brute force would be extremely expensive. However, it is possible to evaluate the sum analytically *if* one ignores the fact that the grains are displaced from one another, i.e. if one identically sets $\mathbf{d}_g$ to zero:

$$F(\mathbf{q}) \approx \sum_g \sum_\alpha e^{-i\mathbf{q}\cdot R_z(\phi_g)\mathbf{x}_\alpha^{(0)}}. \tag{A.3}$$

In this crude approximation, atom α and all of its images are found on a circle with height z_α and radius $\rho_\alpha = \sqrt{x_\alpha^2 + y_\alpha^2}$. It transpires that the sum over grains can, in the continuous limit, can be calculated analytically.

Writing out the exponent in Eq. (A.3) in full gives

$$F(\mathbf{q}) = \sum_g \sum_\alpha \exp\left[-i \begin{pmatrix} q_x \\ q_y \\ q_z \end{pmatrix} \cdot \begin{pmatrix} \cos\phi_g & -\sin\phi_g & 0 \\ \sin\phi_g & \cos\phi_g & 0 \\ 0 & 0 & 1 \end{pmatrix} \begin{pmatrix} x_\alpha \\ y_\alpha \\ z_\alpha \end{pmatrix}\right], \tag{A.4}$$

Rearranging the above, one finds

$$F(\mathbf{q}) = \sum_\alpha \Bigg[e^{-iq_z z_\alpha} \underbrace{\sum_g \exp\left\{-i[(q_x x_\alpha + q_y y_\alpha)\cos\phi_g + (q_y x_\alpha - q_x y_\alpha)\sin\phi_g]\right\}}_{C_\alpha(\mathbf{q})} \Bigg]. \tag{A.5}$$

If for brevity we relabel the grain-independent coefficients as

$$q_x x_\alpha + q_y y_\alpha = A_\alpha, \tag{A.6}$$

$$q_y x_\alpha - q_x y_\alpha = B_\alpha, \tag{A.7}$$

the function C_α may be written

$$C_\alpha(\mathbf{q}) = \sum_g \exp[-i(A_\alpha \cos\phi_g + B_\alpha \sin\phi_g)]. \tag{A.8}$$

It is that this point that we promote the discrete sum over a finite number of grains to a continuous integral:

$$C_\alpha(\mathbf{q}) \to \frac{\mathcal{G}}{2\pi} \int_0^{2\pi} d\phi \, e^{-i(A_\alpha \cos\phi + B_\alpha \sin\phi)}, \tag{A.9}$$

where $\mathcal{G}$, the number of grains, serves as a normalisation constant whose value does not matter for our purposes. The integral above is actually a standard one:

$$C_\alpha(\mathbf{q}) = \frac{\mathcal{G}}{2\pi} \times 2\pi I_0\left[\sqrt{(-iA_\alpha)^2 + (-iB_\alpha)^2}\right] \tag{A.10a}$$

$$= \mathcal{G} I_0\left(i\sqrt{A_\alpha^2 + B_\alpha^2}\right), \tag{A.10b}$$

where I_0 is a zeroth-order, modified Bessel function of the first kind. Given the identity $I_n(x) \equiv i^{-n} J_n(ix)$, and the fact that the Bessel function is even for even n,

the above can be rewritten as

$$C_\alpha(\mathbf{q}) = \mathcal{G} J_0\left(\sqrt{A_\alpha^2 + B_\alpha^2}\right), \tag{A.11}$$

where J_0 is an unmodified Bessel function. This is where the computational saving is made – the sum over the aggregate of grains can be performed automatically by evaluating a Bessel function with the appropriate argument.

To get the Fourier transform into the form quoted in Eq. (3.15), we note that the combination $A_\alpha^2 + B_\alpha^2$ can be rewritten as

$$\begin{aligned} A_\alpha^2 + B_\alpha^2 &= (q_x x_\alpha + q_y y_\alpha)^2 + (q_y x_\alpha - q_x y_\alpha)^2 && \text{(A.12a)} \\ &= q_x^2 x_\alpha^2 + q_y^2 y_\alpha^2 + q_y^2 x_\alpha^2 + q_x^2 y_\alpha^2 && \text{(A.12b)} \\ &= (q_x^2 + q_y^2)(x_\alpha^2 + y_\alpha^2) && \text{(A.12c)} \\ &= q_\rho^2 \rho_\alpha^2, && \text{(A.12d)} \end{aligned}$$

where q_ρ is the radial coordinate of the scattering vector $\mathbf{q}$. On substituting this expression into that for $C_\alpha(\mathbf{q})$ and inserting the result in Eq. (A.5), we arrive at

$$F(\mathbf{q}) = \mathcal{G} \sum_\alpha J_0\left(q_\rho \rho_\alpha\right) e^{-i q_z z_\alpha}. \tag{A.13}$$

As noted above, Eq. (A.13) is in fact the Fourier transform of a set of continuous rings of atoms, where ring α has height z_α and radius ρ_α. One should expect the Fourier transform of the cylindrically symmetric system formed by the rings to be cylindrically symmetric itself, and this is indeed the case, as is readily seen from the fact that F depends only on the radius of the scattering vector, q_ρ, and not on its individual transverse components q_x and q_y. By dispensing with the peculiar grain displacements $\{\mathbf{d}_g\}$, we have been able to calculate the numerical sum over different grain orientations analytically, which reduces the computational cost of doing so by at least an order of magnitude. However, in doing so, one also artificially forces the grains to overlap one another and thus diffract 'coherently'. It is stressed that the shortcut above is not necessarily being endorsed – it was utilised in this thesis out of convenience in order to circumvent the prohibitively massive computational cost

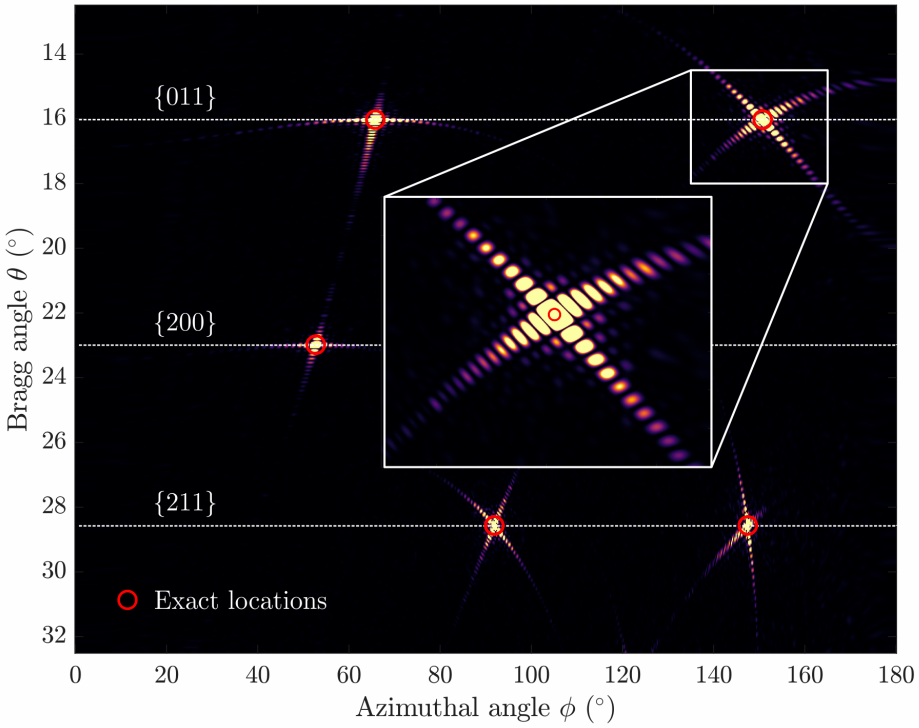

FIG. A.1. Diffraction simulated using the fibre-texture Fourier transform of an ambient block of ⟨100⟩ bcc tantalum, showing {011}, {200}, and {211} peaks. Peaks locations expected from the geometrical solution of the Laue condition are superimposed as circles.

of simulating diffraction from a 6-μm-long crystal.

To reassure the reader that the fibre-texture Fourier transform (FTFT) correctly predicts diffraction peak positions, the results of a simple test are presented. A fully periodic block of bcc tantalum with its ⟨100⟩ directions aligned with the computational cell axes was constructed with cubic lattice constant $a = 3.308$ Å and allowed to thermalise at 300 K for a few picoseconds. Its atomic coordinates were subsequently written out and fed into the FTFT. The transform was evaluated at a set of $\mathbf{q}$-points on an Ewald sphere so as to simulate a diffraction pattern, with an incident beam angle of $\omega = 35°$ and energy of $E_\nu = 9.6$ keV. The resulting diffraction pattern is shown in Fig. A.1. Shown also are the expected locations of the {011}, {200}, and {211} diffraction peaks calculated by finding geometrically the intersection between the Ewald sphere and the various reciprocal-lattice rings on the Polanyi surface (see Sec. 2.2.5). Every peak is exactly where it is expected to be. So, while one should perhaps not read too much into the *structure* of the peaks in the FTFT, one can at least be sure that their positions are correct.

APPENDIX B

Stiffness tensor rotation

This section briefly explains the origin of the values taken by the elastic constants in the standard $[100]/[01\bar{1}]/[011]$ frame.

For a cubic crystal like tantalum whose $\langle 100 \rangle$ directions are aligned with the coordinate axes, the stiffness tensor reads

$$C = \begin{pmatrix} c_{11} & c_{12} & c_{12} & 0 & 0 & 0 \\ c_{12} & c_{11} & c_{12} & 0 & 0 & 0 \\ c_{12} & c_{12} & c_{11} & 0 & 0 & 0 \\ 0 & 0 & 0 & c_{44} & 0 & 0 \\ 0 & 0 & 0 & 0 & c_{44} & 0 \\ 0 & 0 & 0 & 0 & 0 & c_{44} \end{pmatrix}, \tag{B.1}$$

where c_{11}, c_{12}, and c_{44} are the independent cubic elastic constants. We can calculate the stiffness tensor in another frame by applying a transformation of the form

$$C \to MCM^T, \tag{B.2}$$

where the rotation matrix M encodes the relative orientation of the two frames. To move to the standard frame, in which directions of the type $\langle 011 \rangle$ are aligned with the y and z axes, we can imagine applying an active rotation about the x-direction by 45°. For a rotation about x through angle θ, the transformation matrix

M assumes a reasonably simple form [254]:

$$M = \begin{pmatrix} 1 & 0 & 0 & 0 & 0 & 0 \\ 0 & \cos^2\theta & \sin^2\theta & 2\cos\theta\sin\theta & 0 & 0 \\ 0 & \sin^2\theta & \cos^2\theta & -2\cos\theta\sin\theta & 0 & 0 \\ 0 & -\cos\theta\sin\theta & \cos\theta\sin\theta & \cos^2\theta - \sin^2\theta & 0 & 0 \\ 0 & 0 & 0 & 0 & \cos\theta & -\sin\theta \\ 0 & 0 & 0 & 0 & \sin\theta & \cos\theta \end{pmatrix}. \tag{B.3}$$

For $\theta = \pi/4$, the above becomes

$$M = \begin{pmatrix} 1 & 0 & 0 & 0 & 0 & 0 \\ 0 & \frac{1}{2} & \frac{1}{2} & 1 & 0 & 0 \\ 0 & \frac{1}{2} & \frac{1}{2} & -1 & 0 & 0 \\ 0 & -\frac{1}{2} & \frac{1}{2} & 0 & 0 & 0 \\ 0 & 0 & 0 & 0 & \frac{1}{\sqrt{2}} & -\frac{1}{\sqrt{2}} \\ 0 & 0 & 0 & 0 & \frac{1}{\sqrt{2}} & \frac{1}{\sqrt{2}} \end{pmatrix}. \tag{B.4}$$

So,

$$C \to \begin{pmatrix} 1 & 0 & 0 & 0 & 0 & 0 \\ 0 & \frac{1}{2} & \frac{1}{2} & 1 & 0 & 0 \\ 0 & \frac{1}{2} & \frac{1}{2} & -1 & 0 & 0 \\ 0 & -\frac{1}{2} & \frac{1}{2} & 0 & 0 & 0 \\ 0 & 0 & 0 & 0 & \frac{1}{\sqrt{2}} & -\frac{1}{\sqrt{2}} \\ 0 & 0 & 0 & 0 & \frac{1}{\sqrt{2}} & \frac{1}{\sqrt{2}} \end{pmatrix} \begin{pmatrix} c_{11} & c_{12} & c_{12} & 0 & 0 & 0 \\ c_{12} & c_{11} & c_{12} & 0 & 0 & 0 \\ c_{12} & c_{12} & c_{11} & 0 & 0 & 0 \\ 0 & 0 & 0 & c_{44} & 0 & 0 \\ 0 & 0 & 0 & 0 & c_{44} & 0 \\ 0 & 0 & 0 & 0 & 0 & c_{44} \end{pmatrix} M^T \tag{B.5a}$$

$$\to \begin{pmatrix} c_{11} & c_{12} & c_{12} & 0 & 0 & 0 \\ c_{12} & \frac{c_{11}+c_{12}}{2} & \frac{c_{11}+c_{12}}{2} & c_{44} & 0 & 0 \\ c_{12} & \frac{c_{11}+c_{12}}{2} & \frac{c_{11}+c_{12}}{2} & -c_{44} & 0 & 0 \\ 0 & \frac{c_{12}-c_{11}}{2} & \frac{c_{11}-c_{12}}{2} & 0 & 0 & 0 \\ 0 & 0 & 0 & 0 & \frac{c_{44}}{\sqrt{2}} & -\frac{c_{44}}{\sqrt{2}} \\ 0 & 0 & 0 & 0 & \frac{c_{44}}{\sqrt{2}} & \frac{c_{44}}{\sqrt{2}} \end{pmatrix} \begin{pmatrix} 1 & 0 & 0 & 0 & 0 & 0 \\ 0 & \frac{1}{2} & \frac{1}{2} & -\frac{1}{2} & 0 & 0 \\ 0 & \frac{1}{2} & \frac{1}{2} & \frac{1}{2} & 0 & 0 \\ 0 & 1 & -1 & 0 & 0 & 0 \\ 0 & 0 & 0 & 0 & \frac{1}{\sqrt{2}} & \frac{1}{\sqrt{2}} \\ 0 & 0 & 0 & 0 & -\frac{1}{\sqrt{2}} & \frac{1}{\sqrt{2}} \end{pmatrix} \tag{B.5b}$$

$$\rightarrow \begin{pmatrix} c_{11} & c_{12} & c_{12} & 0 & 0 & 0 \\ c_{12} & \frac{c_{11}+c_{12}}{2}+c_{44} & \frac{c_{11}+c_{12}}{2}-c_{44} & 0 & 0 & 0 \\ c_{12} & \frac{c_{11}+c_{12}}{2}-c_{44} & \frac{c_{11}+c_{12}}{2}+c_{44} & 0 & 0 & 0 \\ 0 & 0 & 0 & \frac{c_{11}-c_{12}}{2} & 0 & 0 \\ 0 & 0 & 0 & 0 & c_{44} & 0 \\ 0 & 0 & 0 & 0 & 0 & c_{44} \end{pmatrix}. \tag{B.5c}$$

We thus arrive at the quoted results

$$C_{13} = c_{12}, \tag{B.6}$$

$$C_{23} = \frac{1}{2}(c_{11} + c_{12}) - c_{44}, \tag{B.7}$$

$$C_{33} = \frac{1}{2}(c_{11} + c_{12}) + c_{44}. \tag{B.8}$$

Note that for an isotropic material, for which the Zener ratio $A = 2c_{44}/(c_{11}-c_{12}) = 1$, the transformed and original stiffness tensors are identical, as expected.

References

[1] T. Mashimo, R. Chau, Y. Zhang, T. Kobayoshi, K. Fukuoka, Y. Syono, M. Kodama, and W. Nellis, "Transition to a Virtually Incompressible Oxide Phase at a Shock Pressure of 120 GPa (1.2 Mbar): $Gd_3Ga_5O_{12}$," Physical Review Letters **96**, 105504 (2006).

[2] D. Valencia, R. J. O'Connell, and D. D. Sasselov, "The role of high-pressure experiments on determining super-Earth properties," Astrophysics and Space Science **322**, 135 (2009).

[3] D. Kraus, A. Ravasio, M. Gauthier, D. Gericke, J. Vorberger, S. Frydrych, J. Helfrich, L. Fletcher, G. Schaumann, B. Nagler, B. Barbrel, B. Bachmann, E. Gamboa, S. Göde, E. Granados, G. Gregori, H. J. Lee, P. Neumayer, W. Schumaker, and M. Roth, "Nanosecond formation of diamond and lonsdaleite by shock compression of graphite," Nature Communications **7**, 10970 (2016).

[4] D. Keefe, "Inertial Confinement Fusion," Annual Review of Nuclear and Particle Science **32**, 391 (1982).

[5] G. E. Duvall, "Shock Waves in Solids," in *Modern Science and Technology*, edited by R. Colborn (Van Nostrand, 1963) p. 80.

[6] W. J. M. Rankine, "XV. On the thermodynamic theory of waves of finite longitudinal disturbance," Philosophical Transactions of the Royal Society of London **160**, 277 (1870).

[7] P. H. Hugoniot, "Memoire sur la propagation du mouvement dans les corps et plus spécialement dans les gaz parfaits, 1e Partie," Journal de l'École polytechnique **57**, 3 (1887).

[8] J. W. Taylor, "Thunder in the Mountains," in *Shock Waves in Condensed Matter - 1983*, edited by J. R. Asay, R. A. Graham, and G. K. Straub (Elsevier, New York, 1983) pp. 3–15.

[9] J. M. Walsh and R. H. Christian, "Equation of State of Metals from Shock Wave Measurements," Physical Review **97**, 1544 (1955).

[10] S. Minshall, "Properties of Elastic and Plastic Waves Determined by Pin Contactors and Crystals," Journal of Applied Physics **26**, 463 (1955).

[11] D. Bancroft, E. L. Peterson, and S. Minshall, "Polymorphism of Iron at High Pressure," Journal of Applied Physics **27**, 291 (1956).

[12] J. M. Walsh, M. H. Rice, R. G. McQueen, and F. L. Yarger, "Shock-Wave Compressions of Twenty-Seven Metals. Equations of State of Metals," Physical Review **108**, 196 (1957).

[13] M. Rice, R. McQueen, and J. Walsh, in *Advances in Research and Applications*, Solid State Physics, Vol. 6, edited by F. Seitz and D. Turnbull (Academic Press, 1958) pp. 1 – 63.

[14] P. W. Bridgman, "High Pressure Polymorphism of Iron," Journal of Applied Physics **27**, 659 (1956).

[15] A. S. Balchan and H. G. Drickamer, "High Pressure Electrical Resistance Cell, and Calibration Points above 100 Kilobars," Review of Scientific Instruments **32**, 308 (1961).

[16] P. W. Bridgman, *Solids Under Pressure*, edited by W. Paul and D. M. Warschauer (McGraw-Hill, 1963) pp. 1–13.

[17] K. K. M. Lee, L. R. Benedetti, R. Jeanloz, P. M. Celliers, J. H. Eggert, D. G. Hicks, S. J. Moon, A. Mackinnon, L. B. Da Silva, D. K. Bradley, W. Unites, G. W. Collins, E. Henry, M. Koenig, A. Benuzzi-Mounaix, J. Pasley, and D. Neely, "Laser-driven shock experiments on precompressed water: Implications for icy giant planets," The Journal of Chemical Physics **125**, 014701 (2006).

[18] R. G. McQueen and S. P. Marsh, "Equation of State for Nineteen Metallic Elements from Shock-Wave Measurements to Two Megabars," Journal of Applied Physics **31**, 1253 (1960).

[19] W. D. Crozier and W. Hume, "High-Velocity, Light-Gas Gun," Journal of Applied Physics **28**, 892 (1957).

[20] B. Lexow, M. Wickert, K. Thoma, F. Schäfer, M. H. Poelchau, and T. Kenkmann, "The extra-large light-gas gun of the Fraunhofer EMI: Applications for impact cratering research," Meteoritics & Planetary Science **48**, 3 (2013).

[21] D. Alfè, M. J. Gillan, and G. D. Price, "Temperature and composition of the Earth's

core," Contemporary Physics **48**, 63 (2007).

[22] A. H. Jones, W. M. Isbell, and C. J. Maiden, "Measurement of the Very-High-Pressure Properties of Materials using a Light-Gas Gun," Journal of Applied Physics **37**, 3493 (1966).

[23] D. Strickland and G. Mourou, "Compression of amplified chirped optical pulses," Optics Communications **56**, 219 (1985).

[24] R. F. Smith, J. H. Eggert, R. Jeanloz, T. S. Duffy, D. G. Braun, J. R. Patterson, R. E. Rudd, J. Biener, A. E. Lazicki, A. V. Hamza, J. Wang, T. Braun, L. X. Benedict, P. M. Celliers, and G. W. Collins, "Ramp compression of diamond to five terapascals," Nature **511**, 330 (2014).

[25] R. Cauble, D. W. Phillion, T. J. Hoover, N. C. Holmes, J. D. Kilkenny, and R. W. Lee, "Demonstration of 0.75 Gbar planar shocks in x-ray driven colliding foils," Physical Review Letters **70**, 2102 (1993).

[26] P. Mason, M. Divoký, K. Ertel, J. Pilař, T. Butcher, M. Hanuš, S. Banerjee, J. Phillips, J. Smith, M. D. Vido, A. Lucianetti, C. Hernandez-Gomez, C. Edwards, T. Mocek, and J. Collier, "Kilowatt average power 100 J-level diode pumped solid state laser," Optica **4**, 438 (2017).

[27] Q. Johnson, R. N. Keeler, and J. W. Lyle, "X-ray Diffraction Experiments in Nanosecond Time Intervals," Nature **213**, 1114 (1967).

[28] Q. Johnson, A. Mitchell, R. N. Keeler, and L. Evans, "X-Ray Diffraction During Shock-Wave Compression," Physical Review Letters **25**, 1099 (1970).

[29] D. W. Phillion and C. J. Hailey, "Brightness and duration of x-ray line sources irradiated with intense 0.53-μm laser light at 60 and 120 ps pulse width," Physical Review A **34**, 4886 (1986).

[30] J. S. Wark, R. R. Whitlock, A. A. Hauer, J. E. Swain, and P. J. Solone, "Sub-nanosecond x-ray diffraction from laser-shocked crystals," Physical Review B **40**, 5705 (1989).

[31] D. H. Kalantar, J. F. Belak, G. W. Collins, J. D. Colvin, H. M. Davies, J. H. Eggert, T. C. Germann, J. Hawreliak, B. L. Holian, K. Kadau, P. S. Lomdahl, H. E. Lorenzana, M. A. Meyers, K. Rosolankova, M. S. Schneider, J. Sheppard, J. S. Stölken, and J. S. Wark, "Direct Observation of the $\alpha-\epsilon$ Transition in Shock-

Compressed Iron via Nanosecond X-Ray Diffraction," Physical Review Letters **95**, 075502 (2005).

[32] M. S. Schneider, B. Kad, D. H. Kalantar, B. A. Remington, E. Kenik, H. Jarmakani, and M. A. Meyers, "Laser shock compression of copper and copper-aluminum alloys," International Journal of Impact Engineering **32**, 473 (2005).

[33] D. Milathianaki, D. C. Swift, J. Hawreliak, B. S. El-Dasher, J. M. McNaney, H. E. Lorenzana, and T. Ditmire, "In situ lattice measurement of the bcc phase boundary in Mg on the principal shock Hugoniot," Physical Review B **86**, 014101 (2012).

[34] D. Milathianaki, S. Boutet, G. J. Williams, A. Higginbotham, D. Ratner, A. E. Gleason, M. Messerschmidt, M. M. Seibert, D. C. Swift, P. Hering, J. Robinson, W. E. White, and J. S. Wark, "Femtosecond Visualization of Lattice Dynamics in Shock-Compressed Matter," Science **342**, 220 (2013).

[35] A. Paskin and G. J. Dienes, "Molecular Dynamic Simulations of Shock Waves in a Three-Dimensional Solid," Journal of Applied Physics **43**, 1605 (1972).

[36] B. L. Holian and G. K. Straub, "Molecular Dynamics of Shock Waves in Three-Dimensional Solids: Transition from Nonsteady to Steady Waves in Perfect Crystals and Implications for the Rankine-Hugoniot Conditions," Physical Review Letters **43**, 1598 (1979).

[37] B. L. Holian, "Modeling shock-wave deformation via molecular dynamics," Physical Review A **37**, 2562 (1988).

[38] P. A. Taylor and B. W. Dodson, "Propagating lattice instabilities in shock-loaded metals," Physical Review B **42**, 1200 (1990).

[39] D. H. Robertson, D. W. Brenner, and C. T. White, "Split shock waves from molecular dynamics," Physical Review Letters **67**, 3132 (1991).

[40] N. J. Wagner, B. L. Holian, and A. F. Voter, "Molecular-dynamics simulations of two-dimensional materials at high strain rates," Physical Review A **45**, 8457 (1992).

[41] B. L. Holian and R. Ravelo, "Fracture simulations using large-scale molecular dynamics," Physical Review B **51**, 11275 (1995).

[42] B. L. Holian and P. S. Lomdahl, "Plasticity Induced by Shock Waves in Nonequilibrium Molecular-Dynamics Simulations," Science **280**, 2085 (1998).

[43] T. C. Germann, B. L. Holian, P. S. Lomdahl, and R. Ravelo, "Orientation De-

pendence in Molecular Dynamics Simulations of Shocked Single Crystals," Physical Review Letters **84**, 5351 (2000).

[44] K. Kadau, T. Germann, P. Lomdahl, and B. Holian, "Microscopic View of Structural Phase Transitions Induced by Shock Waves," Science **296**, 1681 (2002).

[45] E. M. Bringa, J. U. Cazamias, P. Erhart, J. Stölken, N. Tanushev, B. D. Wirth, R. E. Rudd, and M. J. Caturla, "Atomistic shock Hugoniot simulation of single-crystal copper," Journal of Applied Physics **96**, 3793 (2004).

[46] T. C. Germann, B. L. Holian, P. S. Lomdahl, D. Tanguy, M. Mareschal, and R. Ravelo, "Dislocation structure behind a shock front in fcc perfect crystals: Atomistic simulation results," Metallurgical and Materials Transactions A **35**, 2609 (2004).

[47] E. M. Bringa, K. Rosolankova, R. E. Rudd, B. A. Remington, J. S. Wark, M. Duchaineau, D. H. Kalantar, J. Hawreliak, and J. Belak, "Shock deformation of face-centred-cubic metals on subnanosecond timescales," Nature Materials **5**, 805 (2006).

[48] H. N. Jarmakani, E. M. Bringa, P. Erhart, B. A. Remington, Y. M. Wang, N. Q. Vo, and M. A. Meyers, "Molecular dynamics simulations of shock compression of nickel: From monocrystals to nanocrystals," Acta Materialia **56**, 5582 (2008).

[49] T. Germann and K. Kadau, "Trillion-atom molecular dynamics becomes a reality," International Journal of Modern Physics C **8**, 1315 (2008).

[50] T. Germann, "Large-scale classical molecular dynamics simulations of shock-induced plasticity in bcc niobium," AIP Conference Proceedings **1195**, 761 (2009).

[51] M. J. Cawkwell, K. J. Ramos, D. E. Hooks, and T. D. Sewell, "Homogeneous dislocation nucleation in cyclotrimethylene trinitramine under shock loading," Journal of Applied Physics **107**, 063512 (2010).

[52] A. Higginbotham, J. Hawreliak, E. M. Bringa, G. Kimminau, N. Park, E. Reed, B. A. Remington, and J. S. Wark, "Molecular dynamics simulations of ramp-compressed copper," Physical Review B **85**, 024112 (2012).

[53] A. Higginbotham, M. J. Suggit, E. M. Bringa, P. Erhart, J. A. Hawreliak, G. Mogni, N. Park, B. A. Remington, and J. S. Wark, "Molecular dynamics simulations of shock-induced deformation twinning of a body-centered-cubic metal," Physical Review B **88**, 104105 (2013).

[54] R. Ravelo, T. C. Germann, O. Guerrero, Q. An, and B. L. Holian, "Shock-induced plasticity in tantalum single crystals: Interatomic potentials and large-scale molecular-dynamics simulations," Physical Review B **88**, 134101 (2013).

[55] N. Gunkelmann, E. M. Bringa, and H. M. Urbassek, "Influence of phase transition on shock-induced spallation in nanocrystalline iron," Journal of Applied Physics **118**, 185902 (2015).

[56] E. N. Hahn, T. C. Germann, R. Ravelo, J. E. Hammerberg, and M. A. Meyers, "On the ultimate tensile strength of tantalum," Acta Materialia **126**, 313 (2017).

[57] M. X. Tang, J. C. E, L. Wang, and S. N. Luo, "Loading-path dependent deformation of nanocrystalline Ta under single- and double-shock, and quasi-isentropic compression," Journal of Applied Physics **121**, 115901 (2017).

[58] L. Zepeda-Ruiz, A. Stukowski, T. Oppelstrup, and V. Bulatov, "Probing the limits of metal plasticity with molecular dynamics simulations," Nature **550**, 492 (2017).

[59] M. Sliwa, D. McGonegle, C. Wehrenberg, C. A. Bolme, P. G. Heighway, A. Higginbotham, A. Lazicki, H. J. Lee, B. Nagler, H. S. Park, R. E. Rudd, M. J. Suggit, D. Swift, F. Tavella, L. Zepeda-Ruiz, B. A. Remington, and J. S. Wark, "Femtosecond X-Ray Diffraction Studies of the Reversal of the Microstructural Effects of Plastic Deformation during Shock Release of Tantalum," Physical Review Letters **120**, 265502 (2018).

[60] G. Li, Y. Wang, K. Wang, M. Xiang, and J. Chen, "Shock induced plasticity and phase transition in single crystal lead by molecular dynamics simulations," Journal of Applied Physics **126**, 075902 (2019).

[61] B. L. Holian, W. G. Hoover, B. Moran, and G. K. Straub, "Shock-wave structure via nonequilibrium molecular dynamics and Navier-Stokes continuum mechanics," Physical Review A **22**, 2798 (1980).

[62] G. Kimminau, P. Erhart, E. M. Bringa, B. Remington, and J. S. Wark, "Phonon instabilities in uniaxially compressed fcc metals as seen in molecular dynamics simulations," Physical Review B **81**, 092102 (2010).

[63] A. Higginbotham, P. Stubley, A. Comley, J. Eggert, J. Foster, D. Kalantar, D. McGonegle, S. Patel, L. Peacock, S. Rothman, R. Smith, M. Suggit, and J. Wark, "Inelastic response of silicon to shock compression," Scientific Reports **6**, 24211

(2016).

[64] C. E. Wehrenberg, D. McGonegle, C. Bolme, A. Higginbotham, A. Lazicki, H. J. Lee, B. Nagler, H.-S. Park, B. A. Remington, R. E. Rudd, M. Sliwa, M. Suggit, D. Swift, F. Tavella, L. Zepeda-Ruiz, and J. S. Wark, "In situ X-ray diffraction measurement of shock-wave-driven twinning and lattice dynamics," Nature **550**, 496 (2017).

[65] H.-S. Park, B. A. Remington, R. C. Becker, J. V. Bernier, R. M. Cavallo, K. T. Lorenz, S. M. Pollaine, S. T. Prisbrey, R. E. Rudd, and N. R. Barton, "Strong stabilization of the Rayleigh-Taylor instability by material strength at megabar pressures," Physics of Plasmas **17**, 056314 (2010).

[66] E. McBride, A. Krygier, A. Ehnes, E. Galtier, M. Harmand, Z. Konôpková, H. J. Lee, H.-P. Liermann, B. Nagler, A. Pelka, M. Rödel, A. Schropp, R. Smith, C. Spindloe, D. Swift, F. Tavella, S. Toleikis, T. Tschentscher, J. Wark, and A. Higginbotham, "Phase Transition Lowering in Dynamically Compressed Silicon," Nature Physics **15**, 89 (2019).

[67] P. G. Heighway, D. McGonegle, N. Park, A. Higginbotham, and J. S. Wark, "Molecular dynamics simulations of grain interactions in shock-compressed highly textured columnar nanocrystals," Physical Review Materials **3**, 083602 (2019).

[68] P. G. Heighway, M. Sliwa, D. McGonegle, C. Wehrenberg, C. A. Bolme, J. Eggert, A. Higginbotham, A. Lazicki, H. J. Lee, B. Nagler, H.-S. Park, R. E. Rudd, R. F. Smith, M. J. Suggit, D. Swift, F. Tavella, B. A. Remington, and J. S. Wark, "Nonisentropic Release of a Shocked Solid," Physical Review Letters **123**, 245501 (2019).

[69] S. H. Simon, *The Oxford Solid State Basics* (Oxford University Press, Oxford, 2013).

[70] S. H. Akhtar S. Khan, *Continuum Theory of Plasticity* (John Wiley & Sons, New York, 1995).

[71] D. Hull and D. J. Bacon, *Introduction to Dislocations*, 5th ed. (Elsevier, 2011).

[72] Y. B. Zel'dovich and Y. P. Raizer, *Physics of Shock Waves and High-Temperature Hydrodynamic Phenomena* (Dover Publications, New York, 2002).

[73] D. C. Rapaport, *The Art of Molecular Dynamics Simulation*, 2nd ed. (Cambridge University Press, Cambridge, 2004).

[74] A. Bravais, "Mémoire sur les systèmes formés par des points distribués régulièrment

sur un plan ou dans l'espace," Journal de l'École polytechnique **19**, 1 (1850).

[75] C. Giacovazzo, H. L. Monaco, G. Artioli, D. Viterbo, G. Ferraris, G. Gilli, G. Zanotti, and M. Catti, *Fundamentals of Crystallography*, 2nd ed. (Oxford University Press, New York, 2002) pp. 1–32.

[76] Z. Dauter and M. Jaskolski, "How to read (and understand) Volume A of *International Tables for Crystallography*: an introduction for nonspecialists," Journal of Applied Crystallography **43**, 1150 (2010).

[77] H.-R. Wenk and P. V. Houtte, "Texture and anisotropy," Reports on Progress in Physics **67**, 1367 (2004).

[78] J. Frenkel, Zeitschrift für Physik **37**, 572 (1926).

[79] H. W. Gene Simmons, *Single crystal elastic constants and calculated aggregate properties: a handbook*, 2nd ed. (M. I. T. Press, Minnesota, 1971).

[80] D. H. Lassila, A. Goldberg, and R. Becker, "The effect of grain boundaries on the athermal stress of tantalum and tantalum-tungsten alloys," Metallurgical and Materials Transactions A **33**, 3457 (2002).

[81] J. H. Bechtold, "Tensile properties of annealed tantalum at low temperatures," Acta Metallurgica **3**, 249 (1955).

[82] E. Orowan, "Zur Kristallplastizität: Über den Mechanismus des Gleitvorganges," Zeitschrift für Physik **89**, 634 (1934).

[83] M. Polanyi, "Über eine Art Gitterstörung, die einen Kristall plastisch machen könnte," Zeitschrift für Physik **89**, 660 (1934).

[84] G. I. Taylor, "The mechanisms of plastic deformation of crystals," Proceedings of the Royal Society A **145**, 362 (1934).

[85] I. V. Obreimov and A. V. Shubnikov, Zhurnal Russkogo Fiz.-Khim. Obshchestva **58**, 817 (1926).

[86] I. V. Obreimov and A. V. Shubnikov, Zeitschrift für Physik **41**, 907 (1927).

[87] A. F. Joffé and L. B. Ioeb, *The Physics of Crystals*, 1st ed. (McGraw Hill Book Company Inc., New York, 1928) p. 47.

[88] P. Hirsch, D. Cockayne, J. Spence, and M. Whelan, "50 Years of TEM of dislocations: Past, present and future," Philosophical Magazine **86**, 4519 (2006).

[89] F. C. Frank, "LXXXIII. Crystal dislocations - Elementary concepts and definitions,"

The London, Edinburgh, and Dublin Philosophical Magazine and Journal of Science **42**, 809 (1951).

[90] J. M. Burgers, "Geometrical considerations concerning the structural irregularities to be assumed in a crystal," Proceedings of the Physical Society **52**, 23 (1940).

[91] E. Orowan, "Problems of plastic gliding," Proceedings of the Physical Society **52**, 8 (1940).

[92] C. Pellegrini, "The history of X-ray free-electron lasers," The European Physical Journal H **37**, 659 (2012).

[93] C. Pellegrini, "X-ray free-electron lasers: from dreams to reality," Physica Scripta **T169**, 014004 (2016).

[94] G. Margaritondo and P. Rebernik Ribic, "A simplified description of X-ray free-electron lasers," Journal of Synchrotron Radiation **18**, 101 (2011).

[95] D. R. Bland, "On Shock Structure in a Solid," IMA Journal of Applied Mathematics **1**, 56 (1965).

[96] D. J. Steinberg, S. G. Cochran, and M. W. Guinan, "A constitutive model for metals applicable at high-strain rate," Journal of Applied Physics **51**, 1498 (1980).

[97] D. L. Preston, D. L. Tonks, and D. C. Wallace, "Model of plastic deformation for extreme loading conditions," Journal of Applied Physics **93**, 211 (2003).

[98] N. R. Barton, J. V. Bernier, R. Becker, A. Arsenlis, R. Cavallo, J. Marian, M. Rhee, H.-S. Park, B. A. Remington, and R. T. Olson, "A multiscale strength model for extreme loading conditions," Journal of Applied Physics **109**, 073501 (2011).

[99] J. Colvin and J. Larsen, *Extreme Physics: Properties and Behavior of Matter at Extreme Conditions* (Cambridge University Press, Cambridge, 2014) pp. 66–69.

[100] D. Batani, H. Stabile, A. Ravasio, G. Lucchini, F. Strati, T. Desai, J. Ullschmied, E. Krousky, J. Skala, L. Juha, B. Kralikova, M. Pfeifer, C. Kadlec, T. Mocek, A. Präg, H. Nishimura, and Y. Ochi, "Ablation pressure scaling at short laser wavelength," Physical Review E **68**, 067403 (2003).

[101] J. Lindl, "Development of the indirect-drive approach to inertial confinement fusion and the target physics basis for ignition and gain," Physics of Plasmas **2**, 3933 (1995).

[102] J. S. Wark, *Plasma Physics – Short Option* (University of Oxford, Oxford, 2016) pp

134 – 139.

[103] M. M. Siddick, G. J. Ackland, and C. A. Morrison, "Constrained dynamics and extraction of normal modes from ab initio molecular dynamics: Application to ammonia," The Journal of Chemical Physics **125**, 064707 (2006).

[104] G. J. Ackland and I. B. Magdău, "Appraisal of the realistic accuracy of molecular dynamics of high-pressure hydrogen," Cogent Physics **2** (2015), 10.1080/23311940.2015.1049477.

[105] W. L. Stewart, J. M. Roberts, N. G. Alexandropolous, and K. Salama, "Effect of hydrogen on the temperature dependence of the elastic constants of tantalum single crystals," Journal of Applied Physics **48**, 75 (1977).

[106] M. S. Daw and M. I. Baskes, "Embedded-atom method: Derivation and application to impurities, surfaces, and other defects in metals," Physical Review B **29**, 6443 (1984).

[107] S. Nosé, "A molecular dynamics method for simulations in the canonical ensemble," Molecular Physics **52**, 255 (1984).

[108] S. Plimpton, "Fast Parallel Algorithms for Short-Range Molecular Dynamics," Journal of Computational Physics. **117**, 1 (1995).

[109] A. Stukowski, "Structure identification methods for atomistic simulations of crystalline materials," Modelling and Simulation in Materials Science and Engineering **20**, 045021 (2012).

[110] A. Stukowski, "Computational Analysis Methods in Atomistic Modeling of Crystals," JOM **66**, 399 (2014).

[111] D. Li, W. Feng-Chao, Y. Zhen-Yu, and Z. Ya-Pu, "How to identify dislocations in molecular dynamics simulations?" Science China: Physics, Mechanics and Astronomy **57**, 2177 (2014).

[112] K. Rosolankova, J. S. Wark, E. M. Bringa, and J. Hawreliak, "Measuring stacking fault densities in shock-compressed FCC crystals using in situ x-ray diffraction," Journal of Physics: Condensed Matter **18**, 6749 (2006).

[113] K. Huang, *Statistical Mechanics*, 2nd ed. (John Wiley & Sons, New York, 1987) pp. 136–138.

[114] R. J. Swenson, "Comments on virial theorems for bounded systems," American

Journal of Physics **51**, 940 (1983).

[115] Z.-L. Liu, L.-C. Cai, X.-R. Chen, Q. Wu, and F.-Q. Jing, "Ab initio refinement of the thermal equation of state for bcc tantalum: the effect of bonding on anharmonicity," Journal of Physics: Condensed Matter **21**, 095408 (2009).

[116] C. S. Hsu and A. Rahman, "Interaction potentials and their effect on crystal nucleation and symmetry," The Journal of Chemical Physics **71**, 4974 (1979).

[117] E. A. Lazar, J. Han, and D. J. Srolovitz, "Topological framework for local structure analysis in condensed matter," Proceedings of the National Academy of Sciences **112**, E5769 (2015).

[118] P. M. Larsen, S. Schmidt, and J. Schiøtz, "Robust structural identification via polyhedral template matching," Modelling and Simulation in Materials Science and Engineering **24**, 055007 (2016).

[119] C. H. Rycroft, "VORO++: A three-dimensional Voronoi cell library in C++," Chaos: An Interdisciplinary Journal of Nonlinear Science **19**, 041111 (2009).

[120] A. Higginbotham and D. McGonegle, "Prediction of Debye-Scherrer diffraction patterns in arbitrarily strained samples," Journal of Applied Physics **115**, 174906 (2014).

[121] D. McGonegle, D. Milathianaki, B. A. Remington, J. S. Wark, and A. Higginbotham, "Simulations of in situ x-ray diffraction from uniaxially compressed highly textured polycrystalline targets," Journal of Applied Physics **118**, 065902 (2015).

[122] J. D. Honeycutt and H. C. Andersen, "Molecular Dynamics Study of Melting and Freezing of Small Lennard-Jones Clusters," The Journal of Physical Chemistry **91**, 4950 (1987).

[123] A. Stukowski and K. Albe, "Extracting dislocations and non-dislocation crystal defects from atomistic simulation data," Modelling and Simulation in Materials Science and Engineering **18**, 085001 (2010).

[124] A. Stukowski, V. V. Bulatov, and A. Arsenlis, "Automated identification and indexing of dislocations in crystal interfaces," Modelling and Simulation in Materials Science and Engineering **20**, 085007 (2012).

[125] J. A. Zimmerman, C. L. Kelchner, P. A. Klein, J. C. Hamilton, and S. M. Foiles, "Surface Step Effects on Nanoindentation," Physical Review Letters **87**, 165507

(2011).

[126] A. Stukowski, "A triangulation-based method to identify dislocations in atomistic models," Journal of the Mechanics and Physics of Solids **70**, 314 (2014).

[127] R. Becker, "Analysis of texture evolution in channel die compression - I. Effects of grain interaction," Acta Metallurgica et Materialia **39**, 1211 (1991).

[128] S. Kalidindi, C. Bronkhorst, and L. Anand, "Crystallographic texture evolution in bulk deformation processing of FCC metals," Journal of the Mechanics and Physics of Solids **40**, 537 (1992).

[129] R. Becker and S. Panchanadeeswaran, "Effects of grain interactions on deformation and local texture in polycrystals," Acta Metallurgica et Materialia **43**, 2701 (1995).

[130] A. Beaudoin, P. Dawson, K. Mathur, and U. Kocks, "A hybrid finite element formulation for polycrystal plasticity with consideration of macrostructural and microstructural linking," International Journal of Plasticity **11**, 501 (1995).

[131] S. Panchanadeeswaran, R. Doherty, and R. Becker, "Direct observation of orientation change by channel die compression of polycrystalline aluminum - Use of a split sample," Acta Materialia **44**, 1233 (1996).

[132] G. Sarma, B. Radhakrishnan, and T. Zacharia, "Finite element simulations of cold deformation at the mesoscale," Computational Materials Science **12**, 105 (1998).

[133] F. Delaire, J. Raphanel, and C. Rey, "Plastic heterogeneities of a copper multicrystal deformed in uniaxial tension: experimental study and finite element simulations," Acta Materialia **48**, 1075 (2000).

[134] A. Bhattacharyya, E. El-Danaf, S. R. Kalidindi, and R. D. Doherty, "Evolution of grain-scale microstructure during large strain simple compression of polycrystalline aluminum with quasi-columnar grains: OIM measurements and numerical simulations," International Journal of Plasticity **17**, 861 (2001).

[135] H. Toda, T. Kamiko, Y. Tanabe, M. Kobayashi, D. Leclere, K. Uesugi, A. Takeuchi, and K. Hirayama, "Diffraction-amalgamated grain boundary tracking for mapping 3D crystallographic orientation and strain fields during plastic deformation," Acta Materialia **107**, 310 (2016).

[136] G. Sarma and P. Dawson, "Effects of interactions among crystals on the inhomogeneous deformations of polycrystals," Acta Materialia **44**, 1937 (1996).

[137] D. P. Mika and P. R. Dawson, "Effects of grain interaction on deformation in polycrystals," Materials Science and Engineering: A **257**, 62 (1998).

[138] F. Barbe, S. Forest, and G. Cailletaud, "Intergranular and intragranular behavior of polycrystalline aggregates. Part 2: Results," International Journal of Plasticity **17**, 537 (2001).

[139] U. Lienert, T.-S. Han, J. Almer, P. Dawson, T. Leffers, L. Margulies, S. Nielsen, H. Poulsen, and S. Schmidt, "Investigating the effect of grain interaction during plastic deformation of copper," Acta Materialia **52**, 4461 (2004).

[140] M. F. Ashby, "The deformation of plastically non-homogeneous materials," Philosophical Magazine **21**, 399 (1970).

[141] L. Evers, D. Parks, W. Brekelmans, and M. Geers, "Crystal plasticity model with enhanced hardening by geometrically necessary dislocation accumulation," Journal of the Mechanics and Physics of Solids **50**, 2403 (2002).

[142] T. Ohashi, R. Barabash, J. Pang, G. Ice, and O. Barabash, "X-ray microdiffraction and strain gradient crystal plasticity studies of geometrically necessary dislocations near a Ni bicrystal grain boundary," International Journal of Plasticity **25**, 920 (2009).

[143] P. Littlewood, T. Britton, and A. Wilkinson, "Geometrically necessary dislocation density distributions in Ti-6Al-4V deformed in tension," Acta Materialia **59**, 6489 (2011).

[144] J. W. Hutchinson and R. Hill, "Elastic-plastic behaviour of polycrystalline metals and composites," Proceedings of the Royal Society of London A: Mathematical, Physical and Engineering Sciences **319**, 247 (1970).

[145] S. Harren and R. Asaro, "Nonuniform deformations in polycrystals and aspects of the validity of the Taylor model," Journal of the Mechanics and Physics of Solids **37**, 191 (1989).

[146] G. I. Taylor, "Plastic Strain in Metals," Journal of the Institute of Metals **62**, 307 (1937).

[147] J. Bishop and R. Hill, "XLVI. A theory of the plastic distortion of a polycrystalline aggregate under combined stresses." The London, Edinburgh, and Dublin Philosophical Magazine **42**, 414 (1951).

[148] H. Honneff and H. Mecking, in *Proceedings of the 5th International Conference on Texture of Materials*, edited by G. Gottstein and K. Lucke (Springer, 1978) pp. 265–275.

[149] U. F. Kocks and G. R. Canova, in *Deformation of Polycrystals*, edited by N. Hansen (Risø National Laboratory, 1980) p. 35.

[150] E. Kröner, "Zur plastischen verformung des vielkristalls," Acta Metallurgica **9**, 155 (1961).

[151] B. Budiansky and T. T. Wu, in *Proc. 4th U.S. Natn. Congr. Appl. Mech.* (American Society of Mechanical Engineers, 1962) p. 1175.

[152] R. Hill, "A self-consistent mechanics of composite materials," Journal of the Mechanics and Physics of Solids **13**, 213 (1965).

[153] F. Roters, P. Eisenlohr, T. Bieler, and D. Raabe, *Crystal Plasticity Finite Element Methods* (Wiley-VCH, Weinheim, Germany, 2010).

[154] K. Kadau, T. C. Germann, P. S. Lomdahl, R. C. Albers, J. S. Wark, A. Higginbotham, and B. L. Holian, "Shock Waves in Polycrystalline Iron," Physical Review Letters **98**, 135701 (2007).

[155] N. Park, *Modelling Shocks using Molecular Dynamics*, Ph.D. thesis, Cranfield University (2009).

[156] S.-N. Luo, T. Germann, D. L. Tonks, and Q. An, "Shock wave loading and spallation of copper bicrystals with asymmetric $\Sigma 3\langle 110\rangle$ tilt grain boundaries," Journal of Applied Physics **108**, 093526 (2010).

[157] H. Pham, B. Arman, S.-N. Luo, and T. Cagin, "Shock compression and spallation of palladium bicrystals with a $\Sigma 5$ grain boundary," Journal of Applied Physics **109**, 086107 (2011).

[158] E. Lin, H. Shi, L. Niu, and E. Jin, "Shock response of copper bicrystals with a $\Sigma 3$ asymmetric tilt grain boundary," Computational Materials Science **59**, 94 (2012).

[159] W. Han, Q. An, S.-N. Luo, T. Germann, D. L. Tonks, and W. Goddard, "Deformation and spallation of shocked Cu bicrystals with 3 coherent and symmetric incoherent twin boundaries," Physical Review B **85**, 024107 (2012).

[160] N. Gunkelmann, E. M. Bringa, D. R. Tramontina, C. J. Ruestes, M. J. Suggit, A. Higginbotham, J. S. Wark, and H. M. Urbassek, "Shock waves in polycrystalline

iron: Plasticity and phase transitions," Physical Review B **89**, 140102 (2014).

[161] L. Wang, J. E, Y. Cai, F. Zhao, D. Fan, and S.-N. Luo, "Shock-induced deformation of nanocrystalline Al: Characterization with orientation mapping and selected area electron diffraction," Journal of Applied Physics **117**, 084301 (2015).

[162] C. E. Wehrenberg, D. McGonegle, C. Bolme, A. Higginbotham, A. Lazicki, H. J. Lee, B. Nagler, H.-S. Park, B. A. Remington, R. E. Rudd, M. Sliwa, M. Suggit, D. Swift, F. Tavella, L. Zepeda-Ruiz, and J. S. Wark, "In situ X-ray diffraction measurement of shock-wave-driven twinning and lattice dynamics," Nature **550**, 496 (2017).

[163] H. Cynn and C.-S. Yoo, "Equation of state of tantalum to 174 GPa," Physical Review B **59**, 8526 (1998).

[164] A. Dewaele, P. Loubeyre, and M. Mezouar, "Equations of state of six metals above 94 GPa," Physical Review B **70**, 094112 (2004).

[165] A. C. Mitchell and W. J. Nellis, "Shock compression of aluminium, copper, and tantalum," Journal of Applied Physics **52**, 3363 (1981).

[166] A. Dewaele, M. Mezouar, N. Guignot, and P. Loubeyre, "High Melting Points of Tantalum in a Laser-Heated Diamond Anvil Cell," Physical Review Letters **104**, 255701 (2010).

[167] A. Stukowski, "Visualization and analysis of atomistic simulation data with OVITO–the Open Visualization Tool," Modelling and Simulation in Materials Science and Engineering **18**, 015012 (2009).

[168] D. Tramontina, C. Ruestes, Y. Tang, and E. Bringa, "Orientation-dependent response of defective Tantalum single crystals," Computational Materials Science **90**, 82 (2014).

[169] C.-H. Lu, E. N. Hahn, B. A. Remington, B. R. Maddox, E. M. Bringa, and M. A. Meyers, "Phase Transformation in Tantalum under Extreme Laser Deformation," Scientific Reports **5**, 15064 (2015).

[170] B. Pang, S. Case, I. P. Jones, J. C. F. Millett, G. Whiteman, Y. L. Chiu, and C. A. Bronkhorst, "The defect evolution in shock loaded tantalum single crystals," Acta Materialia **148**, 482 (2018).

[171] J. Florando, N. Barton, B. S. El-Dasher, J. Mcnaney, and M. Kumar, "Analysis of deformation twinning in tantalum single crystals under shock loading conditions,"

Journal of Applied Physics **113**, 083522 (2013).

[172] C. Ruestes, A. Stukowski, Y. Tang, D. Tramontina, P. Erhart, B. Remington, H. Urbassek, M. Meyers, and E. Bringa, "Atomistic simulation of tantalum nanoindentation: Effects of indenter diameter, penetration velocity, and interatomic potentials on defect mechanisms and evolution," Materials Science and Engineering: A **613**, 390 (2014).

[173] W. Voigt, "Ueber die Beziehung zwischen den beiden Elasticitätsconstanten isotroper Körper," Annalen der Physik **274**, 573 (1889).

[174] A. Reuss, "Berechnung der Fließgrenze von Mischkristallen auf Grund der Plastizitätsbedingung für Einkristalle ." Zeitschrift für Angewandte Mathematik und Mechanik **9**, 49 (1929).

[175] D. R. Lide, *CRC Handbook of Chemistry and Physics*, 84th ed. (CRC Press, Florida, USA, 2003-2004).

[176] V. Dremov, A. Rykounov, F. A Sapozhnikov, A. Karavaev, S. V Yakovlev, G. V Ionov, and M. V Ryzhkov, "Cold melting of beryllium: Atomistic view on Z-machine experiments," Journal of Applied Physics **118**, 035901 (2015).

[177] R. F. Smith, J. H. Eggert, R. Jeanloz, T. S. Duffy, D. G. Braun, J. R. Patterson, R. E. Rudd, J. Biener, A. E. Lazicki, A. V. Hamza, J. Wang, T. Braun, L. X. Benedict, P. M. Celliers, and G. W. Collins, "Ramp compression of diamond to five terapascals," Nature **511**, 330 (2014).

[178] G. I. Taylor, "The Deformation of Crystals of β-Brass," Proceedings of the Royal Society of London A: Mathematical, Physical and Engineering Sciences **118**, 1 (1928).

[179] G. Sainath and B. K. Choudhary, "Orientation dependent deformation behaviour of BCC iron nanowires," Computational Materials Science **111**, 406 (2016).

[180] J.-Y. Kim, D. Jang, and J. R. Greer, "Crystallographic orientation and size dependence of tension-compression asymmetry in molybdenum nano-pillars," International Journal of Plasticity **28**, 46 (2012).

[181] D. K. Bowen, J. W. Christian, and G. Taylor, "Deformation properties of niobium single crystals," Canadian Journal of Physics **45**, 903 (1967).

[182] E. O. Hall, "The Deformation and Ageing of Mild Steel: III Discussion of Results," Proceedings of the Physical Society. Section B **64**, 747 (1951).

[183] N. J. Petch, "The Cleavage Strength of Polycrystals," The Journal of the Iron and Steel Institute **174**, 25 (1953).

[184] W. Thomson, "On the Dynamical Theory of Heat, with numerical results deduced from Mr Joule's Equivalent of a Thermal Unit, and M. Regnault's Observations on Steam," Transactions of the Royal Society of Edinburgh **20**, 261 (1853).

[185] Y. B. Zel'dovich and Y. P. Raizer, *Physics of Shock Waves and High-Temperature Hydrodynamic Phenomena* (Dover Publications, New York, 2002) p. 716.

[186] M. A. Meyers, *Dynamic Behavior of Materials* (John Wiley & Sons, Inc., New York, 1994) p. 146.

[187] J. W. Forbes, *Shock Wave Compression of Condensed Matter* (Springer, Berlin, 2012) p. 38.

[188] L. Davison, *Fundamentals of Shock Wave Propagation in Solids* (Springer, Berlin, 2008) p. 55.

[189] J. R. Asay, "Shock and release behavior of porous 1100 aluminium," Journal of Applied Physics **46**, 197 (1974).

[190] D. V. Minakov, P. R. Levashov, K. V. Khishchenko, and V. E. Fortov, "Quantum molecular dynamics simulation of shock-wave experiments in aluminium," Journal of Applied Physics **115**, 223512 (2014).

[191] A. A. Bakanova, I. P. Dudoladov, M. V. Zhernokletov, V. N. Zubarev, and G. V. Simakov, "Vaporization of shock-compressed metals on expansion," Journal of Applied Mechanics and Technical Physics **24**, 204 (1983).

[192] C. Dai, J. Hu, and H. Tan, "Hugoniot temperatures and melting of tantalum under shock compression determined by optical pyrometry," Journal of Applied Physics **106**, 043519 (2009).

[193] G. I. Kanel, J. Baumung, D. Rush, J. Singer, S. V. Razorenov, and A. V. Utkin, "Melting of shock-compressed metals in release," AIP Conference Proceedings **429**, 155 (1998).

[194] M. G. Gorman, R. Briggs, E. E. McBride, A. Higginbotham, B. Arnold, J. H. Eggert, D. E. Fratanduono, E. Galtier, A. E. Lazicki, H. J. Lee, H. P. Liermann, B. Nagler, A. Rothkirch, R. F. Smith, D. C. Swift, G. W. Collins, J. S. Wark, and M. I. McMahon, "Direct Observation of Melting in Shock-Compressed Bismuth

With Femtosecond X-ray Diffraction," Physical Review Letters **115**, 095701 (2015).

[195] T. Ye, Y. Y-Ying, D. Cheng-Da, Y. Ji-Dong, W. Qing-Song, and T. Hua, "Release melting of bismuth," Acta Physica Sinica **62**, 036401 (2013).

[196] J. D. Colvin, M. Legrand, B. A. Remington, G. Schurtz, and S. V. Weber, "A model for instability growth in accelerated solid metals," Journal of Applied Physics **93**, 5287 (2003).

[197] J. Colvin and J. Larsen, *Extreme Physics: Properties and Behavior of Matter at Extreme Conditions* (Cambridge University Press, Cambridge, 2014) pp. 149–150.

[198] A. Dewaele and P. Loubeyre, "Mechanical properties of tantalum under high pressure," Physical Review B **72**, 134106 (2005).

[199] S. Merkel, H. R. Wenk, J. Shu, G. Shen, P. Gillet, H.-k. Mao, and R. J. Hemley, "Deformation of polycrystalline MgO at pressures of the lower mantle," Journal of Geophysical Research: Solid Earth **107**, ECV 3 (2002).

[200] D. He, S. R. Shieh, and T. S. Duffy, "Strength and equation of state of boron suboxide from radial x-ray diffraction in a diamond cell under nonhydrostatic compression," Physical Review B **70**, 184121 (2004).

[201] R. J. Hemley, H.-k. Mao, G. Shen, J. Badro, P. Gillet, M. Hanfland, and D. Häusermann, "X-ray Imaging of Stress and Strain of Diamond, Iron, and Tungsten at Megabar Pressures," Science **276**, 1242 (1997).

[202] W. J. Murphy, A. Higginbotham, G. Kimminau, B. Barbrel, E. M. Bringa, J. Hawreliak, R. Kodama, M. Koenig, W. McBarron, M. A. Meyers, B. Nagler, N. Ozaki, N. Park, B. Remington, S. Rothman, S. M. Vinko, T. Whitcher, and J. S. Wark, "The strength of single crystal copper under uniaxial shock compression at 100 GPa," Journal of Physics: Condensed Matter **22**, 065404 (2010).

[203] A. M. Molodets, "Use of the Grüneisen Coefficient in Calculations of Temperature along the Isentrope of Elementary Substances," Combustion, Explosion and Shock Waves **37**, 455 (2001).

[204] B. Yaakobi, T. R. Boehly, D. D. Meyerhofer, T. J. B. Collins, B. A. Remington, P. G. Allen, S. M. Pollaine, H. E. Lorenzana, and J. H. Eggert, "EXAFS Measurement of Iron bcc-to-hcp Phase Transformation in Nanosecond-Laser Shocks," Physical Review Letters **95**, 075501 (2005).

[205] W. J. Murphy, A. Higginbotham, J. S. Wark, and N. Park, "Temperature measurements of shocked crystals by use of nanosecond x-ray diffraction," AIP Conference Proceedings **955**, 325 (2007).

[206] W. J. Murphy, A. Higginbotham, J. S. Wark, and N. Park, "Molecular dynamics simulations of the Debye-Waller effect in shocked copper," Physical Review B **78**, 014109 (2008).

[207] E. E. McBride, T. G. White, A. Descamps, L. B. Fletcher, K. Appel, F. P. Condamine, C. B. Curry, F. Dallari, S. Funk, E. Galtier, M. Gauthier, S. Goede, J. B. Kim, H. J. Lee, B. K. Ofori-Okai, M. Oliver, A. Rigby, C. Schoenwaelder, P. Sun, T. Tschentscher, B. B. L. Witte, U. Zastrau, G. Gregori, B. Nagler, J. Hastings, S. H. Glenzer, and G. Monaco, "Setup for meV-resolution inelastic X-ray scattering measurements and X-ray diffraction at the Matter in Extreme Conditions endstation at the Linac Coherent Light Source," Review of Scientific Instruments **89**, 10F104 (2018).

[208] H. T. Philipp, M. Hromalik, M. Tate, L. Koerner, and S. M. Gruner, "Pixel array detector for X-ray free electron laser experiments," Nuclear Instruments and Methods in Physics Research Section A: Accelerators, Spectrometers, Detectors and Associated Equipment **649**, 67 (2011).

[209] L. M. Barker and R. E. Hollenbach, "Laser interferometer for measuring high velocities of any reflecting surface," Journal of Applied Physics **43**, 4669 (1972).

[210] J. Als-Nielsen and D. McMorrow, *Elements of Modern X-ray Physics* (John Wiley & Sons, Chichester, 2011) p. 21.

[211] J. H. Hubbell and S. M. Seltzer, "X-Ray Mass Attenuation Coefficients". *NIST Standard Reference Database 126* (2004).

[212] S. J. Turneaure and Y. M. Gupta, "Real time synchrotron x-ray diffraction measurements to determine material strength of shocked single crystals following compression and release," Journal of Applied Physics **106**, 033513 (2009).

[213] K. Wang and R. R. Reeber, "The role of defects on thermophysical properties: Thermal expansion of V, Nb, Ta, Mo and W," Materials Science and Engineering: R: Reports **23**, 101 (1998).

[214] D. Orlikowski, P. Söderlind, and J. Moriarty, "First-principles thermoelasticity of

transition metals at high pressure: Tantalum prototype in the quasiharmonic limit," Physical Review B **74**, 054109 (2006).

[215] B. Bennett, Sandia National Laboratories Report No. SC-RR-70-28 (1983).

[216] L. Malter and D. B. Langmuir, "Resistance, Emissivities and Melting Point of Tantalum," Physical Review **55**, 743 (1939).

[217] R. G. McQueen, J. W. Hopson, and J. N. Fritz, "Optical technique or determining rarefaction wave velocities at very high pressures," Review of Scientific Instruments **53**, 245 (1982).

[218] M. D. Knudson and M. P. Desjarlais, "Adiabatic release measurements in α-quartz between 300 and 1200 GPa: Characterisation of α-quartz as a shock standard in the multimegabar regime," Physical Review B **88**, 184107 (2013).

[219] R. Ravelo, B. L. Holian, and T. C. Germann, "High strain rates effects in quasi-isentropic compression of solids," AIP Conference Proceedings **1195**, 825 (2009).

[220] M. Sliwa, Ph.D. thesis, University of Oxford, 2019.

[221] M. A. Meyers, F. Gregori, B. K. Kad, M. S. Schneider, D. H. Kalantar, B. A. Remington, G. Ravichandran, T. Boehly, and J. S. Wark, "Laser-induced shock compression of monocrystalline copper: characterisation and analysis," Acta Materialia **51**, 1211 (2003).

[222] A. J. Comley, B. R. Maddox, R. E. Rudd, S. T. Prisbrey, J. A. Hawreliak, D. A. Orlikowski, S. C. Peterson, J. H. Satcher, A. J. Elsholz, H. S. Park, B. A. Remington, N. Bazin, J. M. Foster, P. Graham, N. Park, P. A. Rosen, S. R. Rothman, A. Higginbotham, M. Suggit, and J. S. Wark, "Strength of Shock-Loaded Single-Crystal Tantalum [100] Determined using In Situ Broadband X-Ray Laue Diffraction," Physical Review Letters **110**, 115501 (2013).

[223] E. M. Bringa, A. Caro, Y. Wang, M. Victoria, J. M. McNaney, B. A. Remington, R. F. Smith, B. R. Torralva, and H. Van Swygenhoven, "Ultrahigh Strength in Nanocrystalline Materials Under Shock Loading," Science **309**, 1838 (2005).

[224] R. E. Rudd, "High-Rate Plastic Deformation of Nanocrystalline Tantalum to Large Strains: Molecular Dynamics Simulation," Materials Science Forum **633-634**, 3 (2009).

[225] D. C. Swift, A. Seifter, D. B. Holtkamp, and D. A. Clark, "Shock and release

temperatures in molybdenum: Experiment and theory," Physical Review B **76**, 054122 (2007).

[226] K. Kurosawa and H. Genda, "Effects of Friction and Plastic Deformation in Shock-Comminuted Damaged Rocks on Impact Heating," Geophysical Research Letters **45**, 620 (2018).

[227] C. S. Smith, Trans. TMS-AIME **212**, 574 (1958).

[228] M. A. Meyers, "A mechanism for dislocation generation in shock-wave deformation," Scripta Metallurgica **12**, 21 (1978).

[229] W. S. Farren and G. I. Taylor, "The heat developed during plastic extension of metals," Proceedings of the Royal Society of London A: Mathematical, Physical and Engineering Sciences **107**, 422 (1925).

[230] G. I. Taylor and H. Quinney, "The latent energy remaining in a metal after cold working," Proceedings of the Royal Society of London A: Mathematical, Physical and Engineering Sciences **143**, 307 (1934).

[231] M. Bever and L. Ticknor, "The energy stored during the cold working of a gold-silver alloy," Acta Metallurgica **1**, 116 (1953).

[232] M. Bever, D. Holt, and A. Titchener, "The stored energy of cold work," Progress in Materials Science **17**, 5 (1973).

[233] J. Mason, A. Rosakis, and G. Ravichandran, "On the strain and strain rate dependence of the fraction of plastic work converted to heat: an experimental study using high speed infrared detectors and the Kolsky bar," Mechanics of Materials **17**, 135 (1994).

[234] P. Rosakis, A. Rosakis, G. Ravichandran, and J. Hodowany, "A thermodynamic internal variable model for the partition of plastic work into heat and stored energy in metals," Journal of the Mechanics and Physics of Solids **48**, 581 (2000).

[235] A. Wong, R. Jones, and J. Sparrow, "Thermoelastic constant or thermoelastic parameter?" Journal of Physics and Chemistry of Solids **48**, 749 (1987).

[236] J. Clayton, "Dynamic plasticity and fracture in high density polycrystals: Constitutive modeling and numerical simulation," Journal of the Mechanics and Physics of Solids **53**, 261 (2005).

[237] P. Longère and A. Dragon, "Adiabatic heat evaluation for dynamic plastic localiza-

tion," Journal of Theoretical and Applied Mechanics **45** (2007).

[238] A. Stukowski and A. Arsenlis, "On the elastic–plastic decomposition of crystal deformation at the atomic scale," Modelling and Simulation in Materials Science and Engineering **20**, 035012 (2012).

[239] C. E. Bottani and P. M. Ossi, "Plastic deformation, anharmonicity and Grüneisen parameter of α-titanium," Philosophical Magazine A **41**, 943 (1980).

[240] P. M. Ossi, "Plastic-deformation dependence of the Grüneisen parameter strain derivatives," Il Nuovo Cimento D **2**, 953 (1983).

[241] S. Punnose and A. Mukhopadhyay, "Influence of residual plastic strain on the thermoelastic behavior of a titanium alloy," Journal of Applied Physics **125**, 125103 (2019).

[242] A. Robinson, J. Dulieu-Barton, S. Quinn, and R. Burguete, "Thermoelastic investigation of residual stress: Plastic deformation and the change in thermoelastic constant," The European Physical Journal Conferences **6**, 38016 (2010).

[243] A. Higginbotham, E. M. Bringa, J. Marian, N. Park, M. Suggit, and J. S. Wark, "Simulations of copper single crystals subjected to rapid shear," Journal of Applied Physics **109**, 063530 (2011).

[244] J. A. Moriarty, J. F. Belak, R. E. Rudd, P. Söderlind, F. H. Streitz, and L. H. Yang, "Quantum-based atomistic simulation of materials properties in transition metals," Journal of Physics: Condensed Matter **14**, 2825 (2002).

[245] C. E. Wehrenberg, A. J. Comley, N. R. Barton, F. Coppari, D. Fratanduono, C. M. Huntington, B. R. Maddox, H. S. Park, C. Plechaty, S. T. Prisbrey, B. A. Remington, and R. E. Rudd, "Lattice-level observation of the elastic-to-plastic relaxation process with subnanosecond resolution in shock-compressed Ta using time-resolved in situ Laue diffraction," Physical Review B **92**, 104305 (2015).

[246] A. Norris, "Eulerian conjugate stress and strain," Journal of Mechanics of Materials and Structures **3**, 243 (2007).

[247] J. Marian, W. Cai, and V. V. Bulatov, "Dynamic transitions from smooth to rough to twinning in dislocation motion," Nature Materials **3**, 158 (2004).

[248] R. Thetford, Ph.D. thesis, University of Oxford, 1989.

[249] L. H. Yang, J. A. Moriarty, and P. Söderlind, "Accurate atomistic simulation of

(a/2)⟨100⟩ screw dislocations and other defects in bcc tantalum," Philosophical Magazine A **81**, 1355 (2001).

[250] N. Soneda and T. D. de la Rubia, "Defect production, annealing kinetics and damage evolution in α-Fe: at atomic-scale computer simulation," Philosophical Magazine A **78**, 995 (1998).

[251] G. Ackland, "Controlling Radiation Damage," Science **327**, 1587 (2010).

[252] D. E. Grady, "Principles underlying the fourth power nature of structured shock waves," AIP Conference Proceedings **1979**, 070014 (2018).

[253] F. Cverna, ed., *ASM Ready Reference: Thermal Properties of Metals* (ASM International, Materials Park, OH, 2002).

[254] T. C. T. Ting, *Anisotropic Elasticity: Theory and Applications* (Oxford University Press, New York, 1996).